
Monitoring permafrost environments with Synthetic Aperture Radar (SAR) sensors

Dissertation

an der Fakultät für Geowissenschaften

der Ludwig - Maximilians - Universität München

vorgelegt von

Lingxiao Wang

aus Anhui, P.R.China

München, den 11.09.2018

1. Gutachter: Prof. Dr. Ralf Ludwig, Department of Geography, LMU Munich

2. Gutachter: Prof. Dr. Monique Bernier, Institut National de la Recherche Scientifique (INRS), Québec

Tag der Disputation: 20.12.2018

Preface

This work is the result of a long journey, a mixture of many excited, depressed, joyful and sad moments, but full of passion and gratitude all the way.

This work would not have been possible without the support of two of my supervisors: Prof. Dr. Ralf Ludwig (LMU) and Prof. Dr. Monique Bernier (INRS). I am more than grateful to them for giving me this wonderful and unique opportunity to work on such an interesting research topic. I appreciate the endless support and patience they gave me throughout the years. I am deeply grateful to them for the large time spent on improving my every manuscript, with revision word by word. I want to thank Prof. Dr. Ralf Ludwig in particular, who always gave me the largest freedom to work on my interests and supported me to explore new ideas. I have learned a lot from his enthusiasm for research work and working experience. I also want to express my deepest gratitude to my co-supervisor Prof. Dr. Monique Bernier, who always inspired and motivated me. I am sincerely appreciated that she provided me valuable opportunities to communicate with the experts during my every visit at the Institute (INRS) in Quebec City and deeply thankful for the tremendous effort she investigated for organizing every field campaign.

The largest gratitude also goes to the funders of my PhD work:

- CSC-LMU doctoral program cooperated by the China Scholarship Council (CSC) and the international office of the Ludwig-Maximilians-Universität (LMU). I sincerely appreciate the opportunity to be founded by this program.
- Bavarian Research Alliance (Bayerischen Forschungsallianz BayFOR) Studentenmobilität program for providing travel funds for two field campaigns conducted in northern Quebec.
- Centre d'Études Nordiques (CEN) for allocating helicopter flight times and providing logistical support during the fieldwork.
- Helmholtz Research School of Mechanisms and Interactions of Climate Change in Mountain Regions (MICMoR) for providing financial support for the devices installed in the field.

I am very grateful to two of my mentors Prof. Dr. Irena Hajsek (ETH- Zürich and DLR) and Prof. Dr. Harald Kunstmann (KIT/IMK-IFU and Uni Augsburg) of the MICMoR Graduate Programme. I really appreciate that they listen to my progress, difficulties and give lots of valuable suggestions during every one of our mentoring meetings.

I also would like to sincerely thank Prof. Dr. Michel Allard (Laval University-CEN) and Denis Sarrazin (research professional at Laval University-CEN) for introducing permafrost research and sharing field datasets. I would like to thank Jimmy Poulin (professional at INRS-CEN) in particular, who accompanies me to the two field campaigns. He provides tremendous help in the field and data collection throughout the years. I also

would like to express deep thanks to Dr. Andres Jacome (INRS), Yueli Chen (student at LMU), and Chaima Touati (student at INRS) for providing valuable fieldwork assistance.

Many thanks to my nice colleagues from the LMU who always gave me unconditional help in the past years. With whom I spent some many joyful and great moments. Special thanks go to Dr. Philip Marzahn for the great introduction of radar remote sensing and endless beneficial discussions, Josef \Seppo Schmid and Juliana Braun who gave me the detailed introduction of the hydro-thermal model, Vera Erfurth who manage all the logistical affairs. I also want to say many thanks to the great colleagues from INRS-ETE who gave me a warm welcome during my visits. I really enjoyed every one of my stays in Quebec. Special thanks go to Dr. Yannick Duguay and Laurence Provencher-Nolet who gave me the great introduction of the related researches in the study area, Dr. Parvin Kalantari and Sophie Roberge for making my stay in Quebec City very happy. I am so lucky that I could work with you all.

Meanwhile, I also express my deep thanks to many scientists and researchers for the numerous inspiring thoughts, valuable discussions and constructive suggestions. They are Dr. Jörg Schulla, Dr. Anna K. Liljedahl, Dr. Ronald P. Daanen, Dr. Anne Gädeke, Dr. Maxime Jolivel, Dr. Anne-Marie Leblanc, Dr. Simon Zwieback, Dr. Lin Bai, Dr. Xiaowen Wang, Dr. Panpan Tang. Of course, I would also like to thank all my friends who accompany me all the way and bring me joy.

Last but not least, I would like to thank my parents for their endless love, great understanding and unlimited support. Without them, this would not have been possible.

Summary

Permafrost occupies approximately 24% of the exposed land area in the Northern Hemisphere. It is an important element of the cryosphere and has strong impacts on hydrology, biological processes, land surface energy budget, and infrastructure.

For several decades, surface air temperatures in the high northern latitudes have warmed at approximately twice the global rate. Permafrost temperatures have increased in most regions since the early 1980s, the averaged warming north of 60°N has been 1-2°C.

In-situ measurements are essential to understanding physical processes in permafrost terrain, but they have several limitations, ranging from difficulties in drilling to the representativeness of limited single point measurements. Remote sensing is urgently needed to supplement ground-based measurements and extend the point observations to a broader spatial domain.

This thesis concentrates on the sub-arctic permafrost environment monitoring with SAR datasets. The study site is selected in a typical discontinuous permafrost region in the eastern Canadian sub-Arctic. Inuit communities in Nunavik and Nunatsiavut in the Canadian eastern sub-arctic are amongst the groups most affected by the impacts of climate change and permafrost degradation. Synthetic Aperture Radar (SAR) datasets have advantages for permafrost monitoring in the Arctic and sub-arctic regions because of its high resolution and independence of cloud cover and solar illumination. To date, permafrost environment monitoring methods and strategies with SAR datasets are still under development.

The variability of active layer thickness is a direct indication of permafrost thermal state changes. The Differential SAR Interferometry (D-InSAR) technique is applied in the study site to derive ground deformation, which is introduced by the thawing/freezing depth of active layer and underlying permafrost. The D-InSAR technique has been used for the mapping of ground surface deformation over large areas by interpreting the phase difference between two signals acquired at different times as ground motion information. It shows the ability to detect freeze/thaw-related ground motion over permafrost regions. However, to date, accuracy and value assessments of D-InSAR applications have focused mostly on the continuous permafrost region where the vegetation is less developed and causes fewer complicating factors for the D-InSAR application, less attention is laid on the discontinuous permafrost terrain. In this thesis, the influencing factors and application conditions for D-InSAR in the discontinuous permafrost environment are evaluated by using X- band and L-band data. Then, benefit from by the high-temporal resolution of C-band Sentinel-1 time series, the seasonal displacement is derived from small baseline subsets (SBAS)-InSAR.

Landforms are indicative of permafrost presence, with their changes inferring modifications to permafrost conditions. A permafrost landscape mapping method was developed which uses multi-temporal TerraSAR-X backscatter intensity and interferometric coherence information. The land cover map is generated through the combined use of object-based image analysis (OBIA) and classification and regression tree analysis (CART). An overall accuracy of 98% is achieved when classifying rock and water bodies, and an accuracy of 79% is achieved when discriminating between different vegetation types with one year of single-polarized acquisitions. This classification strategy can be transferred to other time-series SAR datasets, e.g., Sentinel-1, and other heterogeneous environments.

One predominant change in the landscape tied to the thaw of permafrost is the dynamics of thermokarst lakes. Dynamics of thermokarst lakes are developed through their lateral extent and vertical depth changes. Due to different water depth, ice cover over shallow thermokarst ponds/lakes can freeze completely to the lake bed in winter, resulting in grounded ice; while ice cover over deep thermokarst ponds/lakes cannot, which have liquid water persisting under the ice cover all winter, resulting in floating ice. Winter ice cover regimes are related to water depths and ice thickness. In the lakes having floating ice, the liquid water induces additional heat in the remaining permafrost underneath and surroundings, which contributes to further intensified permafrost thawing. SAR datasets are utilized to detect winter ice cover regimes based on the character that liquid water has a remarkably high dielectric constant, whereas pure ice has a low value. Patterns in the spatial distribution of ice-cover regimes of thermokarst ponds in a typical discontinuous permafrost region are first revealed. Then, the correlations of these ice-cover regimes with the permafrost degradation states and thermokarst pond development in two historical phases (Sheldrake catchment in the year 1957 and 2009, Tasiapik Valley 1994 and 2010) were explored. The results indicate that the ice-cover regimes of thermokarst ponds are affected by soil texture, permafrost degradation stage and permafrost depth. Permafrost degradation is difficult to directly assess from the coverage area of floating-ice ponds and the percentage of all thermokarst ponds consisting of such floating-ice ponds in a single year. Continuous monitoring of ice-cover regimes and surface areas is recommended to elucidate the hydrological trajectory of the thermokarst process.

Several operational monitoring methods have been developed in this thesis work. In the meanwhile, the spatial distribution of seasonal ground thaw subsidence, permafrost landscape, thermokarst ponds and their winter ice cover regimes are first revealed in the study area. The outcomes help understand the state and dynamics of permafrost environment.

Zusammenfassung

Der Permafrostboden bedeckt etwa 24% der exponierten Landfläche in der nördlichen Hemisphäre. Es ist ein wichtiges Element der Kryosphäre und hat starke Auswirkungen auf die Hydrologie, die biologischen Prozesse, das Energie-Budget der Landoberfläche und die Infrastruktur.

Seit mehreren Jahrzehnten erhöhen sich die Oberflächenlufttemperaturen in den nördlichen hohen Breitengraden etwa doppelt so stark wie die globale Rate. Die Temperaturen der Permafrostböden sind in den meisten Regionen seit den frühen 1980er Jahren gestiegen. Die durchschnittliche Erwärmung nördlich von 60° N beträgt 1-2°C.

In-situ-Messungen sind essentiell für das Verständnis der physischen Prozesse im Permafrostgelände. Es gibt jedoch mehrere Einschränkungen, die von Schwierigkeiten beim Bohren bis hin zur Repräsentativität begrenzter Einzelpunktmessungen reichen. Fernerkundung ist dringend benötigt, um bodenbasierte Messungen zu ergänzen und punktuelle Beobachtungen auf einen breiteren räumlichen Bereich auszudehnen.

Diese Dissertation konzentriert sich auf die Umweltbeobachtung der subarktischen Permafrostböden mit SAR-Datensätzen. Das Untersuchungsgebiet wurde in einer typischen diskontinuierlichen Permafrostzone in der kanadischen östlichen Sub-Arktis ausgewählt. Die Inuit-Gemeinschaften in den Regionen Nunavik und Nunatsiavut in der kanadischen östlichen Sub-Arktis gehören zu den Gruppen, die am stärksten von den Auswirkungen des Klimawandels und Permafrostdegradation betroffen sind. Synthetische Apertur Radar (SAR) Datensätze haben Vorteile für das Permafrostmonitoring in den arktischen und subarktischen Regionen aufgrund der hohen Auflösung und der Unabhängigkeit von Wolkendeckung und Sonnenstrahlung. Bis heute sind die Methoden und Strategien mit SAR-Datensätzen für Umweltbeobachtung der Permafrostböden noch in der Entwicklung.

Die Variabilität der Auftautiefe der aktiven Schicht ist eine direkte Indikation der Veränderung des thermischen Zustands der Permafrostböden. Die Differential-SAR-Interferometrie(D-InSAR)-Technik wird im Untersuchungsgebiet zur Ableitung der Bodendeformation, die durch Auftau- / und Gefriertiefe der aktiven Schicht und des unterliegenden Permafrostbodens eingeführt wird, eingesetzt. Die D-InSAR-Technik wurde für Kartierung der Landoberflächendeformation über große Flächen verwendet, indem der Phasenunterschied zwischen zwei zu verschiedenen Zeitpunkten als Bodenbewegungsinformation erfassten Signalen interpretiert wurde. Es zeigt die Fähigkeit, tau- und gefrierprozessbedingte Bodenbewegungen über Permafrostregionen zu detektieren. Jedoch fokussiert sich die Genauigkeit und Wertschätzung der D-InSAR-Anwendung bis heute hauptsächlich auf kontinuierliche Permafrostregion, wo die Vegetation wenig entwickelt ist und weniger komplizierte Faktoren für D-InSAR-Anwendung verursacht. Das diskontinuierliche Permafrostgelände wurde nur weniger

berücksichtigt. In dieser Dissertation wurden die Einflussfaktoren und Anwendungsbedingungen für D-InSAR im diskontinuierlichen Permafrostgebiet mittels X-Band und L-Band Daten ausgewertet. Dann wurde die saisonale Verschiebung dank der hohen Auflösung der C-Band Sentinel-1 Zeitreihe von „Small Baseline Subsets (SBAS)-InSAR“ abgeleitet.

Landformen weisen auf die Präsenz des Permafrosts hin, wobei deren Veränderungen auf die Modifikation der Permafrostbedingungen schließen. Eine Kartierungsmethode der Permafrostlandschaft wurde entwickelt, dabei wurde Multi-temporal TerraSAR-X Rückstreuungsintensität und interferometrische Kohärenzinformationen verwendet. Die Landbedeckungskarte wurde durch kombinierte Anwendung objektbasierter Bildanalyse (OBIA) und Klassifikations- und Regressionsbaum Analyse (CART) generiert. Eine Gesamtgenauigkeit in Höhe von 98% wurde bei Klassifikation der Gesteine und Wasserkörper erreicht. Bei Unterscheidung zwischen verschiedenen Vegetationstypen mit einem Jahr einzelpolarisierte Akquisitionen wurde eine Genauigkeit von 79% erreicht. Diese Klassifikationsstrategie kann auf andere Zeitreihen der SAR-Datensätzen, z.B. Sentinel-1, und auch anderen heterogenen Umwelten übertragen werden.

Eine vorherrschende Veränderung in der Landschaft, die mit dem Auftauen des Permafrosts verbunden ist, ist die Dynamik der Thermokarstseen. Die Dynamik der Thermokarstseen ist durch Veränderungen der seitlichen Ausdehnung und der vertikalen Tiefe entwickelt. Aufgrund der unterschiedlichen Wassertiefen kann die Eisdecke über den flachen Thermokarstteichen/-seen im Winter bis auf den Wasserboden vollständig gefroren sein, was zum geerdeten Eis führt, während die Eisdecke über den tiefen Thermokarstteichen/-seen es nicht kann. In den tiefen Thermokarstteichen/-seen bleibt den ganzen Winter flüssiges Wasser unter der Eisdecke bestehen, was zum Treibeis führt. Das Wintereisdeckenregime bezieht sich auf die Wassertiefe und die Eisdicke. In den Seen mit Treibeis leitet das flüssige Wasser zusätzliche Wärme in den restlichen Permafrost darunter oder in der Umgebung, was zur weiteren Verstärkung des Permafrostauftauens beiträgt. Basiert auf den Charakter, dass das flüssige Wasser eine bemerkenswert hohe Dielektrizitätskonstante besitzt, während reines Eis einen niedrigen Wert hat, wurden die SAR Datensätzen zur Erkennung des Wintereisdeckenregimes verwendet. Zunächst wurden Schemen in der räumlichen Verteilung der Eisdeckenregimes der Thermokarstteiche in einer typischen diskontinuierlichen Permafrostregion abgeleitet. Dann wurden die Zusammenhänge dieser Eisdeckenregimes mit dem Degradationszustand des Permafrosts und der Entwicklung der Thermokarstteiche in zwei historischen Phasen (Sheldrake Einzugsgebiet in 1957 und 2009, Tasiapik Tal in 1994 und 2010) erforscht. Die Ergebnisse deuten darauf, dass die Eisdeckenregimes der Thermokarstteiche von der Bodenart, dem Degradationszustand des Permafrosts und der Permafrosttiefe beeinflusst werden. Es ist schwer, die Permafrostdegradation in einem einzelnen Jahr direkt durch den Abdeckungsbereich der Treibeis-Teiche und die Prozentzahl aller aus solchen Treibeis-Teichen bestehenden Thermokarstteiche abzuschätzen. Ein kontinuierliches Monitoring der Eisdeckenregimes und -oberflächen ist empfehlenswert, um den hydrologischen Verlauf des Thermokarstprozesses zu erläutern.

In dieser Dissertation wurden mehrere operativen Monitoringsmethoden entwickelt. In der Zwischenzeit wurden die räumliche Verteilung der saisonalen Bodentauabsenkung, die Permafrostlandschaft, die Thermokarstteiche und ihre Wintereisdeckenregimes erstmals in diesem Untersuchungsgebiet aufgedeckt. Die Ergebnisse tragen dazu bei, den Zustand und die Dynamik der Permafrostumwelt zu verstehen.

Contents

Preface	i
Summary	iii
Zusammenfassung	v
Contents	viii
List of Figures	x
List of Tables	xii
List of Abbreviations	xiii
1 Introduction	1
1.1 Background and motivation	1
1.1.1 Permafrost	1
1.1.2 Climate change in the Arctic	3
1.1.3 Impacts of climate warming on permafrost terrain	4
1.1.4 Threats by permafrost degradation in the eastern Canadian sub-arctic	7
1.1.5 Study area	10
1.1.5.1 Climate	10
1.1.5.2 Geomorphology	11
1.1.5.3 Vegetation	12
1.1.5.4 Village and research station history	13
1.2 Monitoring permafrost environments	14
1.2.1 In-situ monitoring of permafrost	14
1.2.2 Monitoring permafrost environments with remote sensing	15
1.3 Monitoring permafrost environments with SAR datasets	17
1.3.1 The SAR system	17
1.3.1.1 Spaceborne SAR sensors and imaging geometry	17
1.3.1.2 Backscattering signal	20
1.3.1.3 SAR Interferometry	23
1.3.1.3.1 DEM generation	23
1.3.1.3.2 Surface deformation monitoring	24
1.3.2 Ground surface movement detected by D-InSAR technique	26
1.3.3 Permafrost landscape characterization and land cover classification	28
1.3.4 Monitoring ice cover regimes of thermokarst ponds/lakes	30

1.4 Research objectives	32
1.5 Thesis outline and scientific publications	33
2 Comparison of TerraSAR-X and ALOS PALSAR Differential Interferometry with Multi-Source DEMs for Monitoring Ground Displacement in a Discontinuous Permafrost Region	38
3 High temporal resolution deformation monitoring over discontinuous permafrost terrain using Sentinel-1 time series	59
4 Mapping permafrost landscape features using object-based image classification of multi-temporal SAR images.....	94
5 Thermokarst pond dynamics in subarctic environment monitoring with radar remote sensing	115
6 Conclusions and Outlook.....	131
6.1 Conclusions	131
6.2 Outlook	134
7 Bibliography	136
8 Curriculum Vitae	147

List of Figures

Figure 1. 1: Circum-Arctic map of permafrost (Brown et al. 1997).....	2
Figure 1. 2: Typical permafrost landforms. (1) ice-wedge polygons and an eroding shoreline at Cape Halkett on the Beaufort Sea coast of Alaska, photo is from webpage (soundwavesUSGS). (2) One pingo in the Pingo Canadian Landmark, Northwest Territories, Canada, photo is from webpage (TheTuktoyaktukPingos). (3) One collapsed palsa site in northern Quebec, Canada. (4) Lithalsas and thermokarst ponds in northern Quebec, Canada. 3	3
Figure 1. 3: Patterns of warming and precipitation change from the Coupled Model Inter-comparison Project Phase 5 (CMIP5) (Collins et al. 2013).....	4
Figure 1. 4: Location maps of the North Polar region, the Nunavik in the eastern Canadian sub-Arctic are marked in the figure. (Map is drawn by P. Fretwell, British Antarctic Survey). The borehole temperatures shown in Figure 1. 5 are also marked with numbers in this figure.	7
Figure 1. 5: Ground temperatures at three Nunavik villages (1) Umiujaq (56.5421 N, 76.5216 W), borehole into the basalt rock; (2) Apupaluk (59.2993 N, 69.5996 W), borehole into marine sand/gravel, about 40 m west of the village airport runway; (3) Tasiujaq (58.7 N, 69.9167 W), borehole into schist rock, a few kilometers northeast of the airport; (4) Tasiujaq (58.6699 N, 69.9522 W), borehole into sand embankment (terrace), about 40 m west of the airport runway. Ground temperature data is obtained through Nordicana-D online database (Allard et al. 2016).....	9
Figure 1. 6: Location of the study area of Umiujaq, Northern Quebec, Canada. (a) Canada Map, red rectangle marks the region shown in Figure 1.6 (b). (b) The red box indicates the study area.	10
Figure 1. 7: (a) Mean annual air temperatures (MAATs) in the period 1960–2017 at three meteorological stations. (b) Annual precipitation in the period 1960–2017 at three meteorological stations. The solid line is a non-parametric local regression applied to the original line curve of points.	11
Figure 1. 8: Land cover map based on Sentinel-2 images in 2017.....	13
Figure 1. 9: Illustration of the SAR imaging geometry, adapted from (Zhou et al. 2009). 20	20
Figure 1. 10: Simplified schematic illustration of the dominant backscatter mechanisms for short (e.g. X/C) and long (e.g. P/L) wavelength electromagnetic signals for various surface cover conditions.	22
Figure 1. 11: Conceptual representation of satellite interferometric SAR system.	23

Figure 1. 12: Conceptual representation of differential InSAR system..... 24

Figure 1. 13: Position of the papers, and the topics they are covering within this PhD thesis..... 34

List of Tables

Table 1. 1: Frequency bands for radar systems.	17
Table 1. 2: List of spaceborne SAR sensors and their parameters.	18
Table 1. 3: Studies that employed InSAR for ground surface motion monitoring in Arctic and sub-Arctic permafrost-affected terrain.	26
Table 1. 4: Studies that employ spaceborne SAR data for the characterization of the Arctic and sub-Arctic permafrost (tundra) landscapes.	28
Table 1. 5: Studies that employ spaceborne SAR data for ice cover and bathymetric features of thermokarst ponds/lakes.	30
Table 1. 6: Overview of journals in which the papers of this thesis are published or are submitted to (2017 Journal Citation Reports (ClarivateAnalytics 2018)).	36

List of Abbreviations

Abbreviation	Description
ALT	Active Layer Thickness
ALOS	Advanced Land Observing Satellite
ASAR	Advanced Synthetic Aperture Radar
CMIP5	The Coupled Model Intercomparison Project Phase 5
CALM	Circumpolar Active Layer Monitoring
DEM	Digital Elevation Model
D-InSAR	Differential Interferometric Synthetic Aperture Radar
Envisat	Environmental Satellite
ERS	European Remote Sensing Satellite
ERT	Electrical Resistivity Tomography
ESA	European Space Agency
GPR	Ground Penetrating Radar
GRACE	Gravity Recovery and Climate Experiment
GTN-P	Global Terrestrial Network for Permafrost
InSAR	Interferometric Synthetic Aperture Radar
IPCC	Intergovernmental Panel on Climate Change
JERS	Japanese Earth Resources Satellite
LiDAR	Light Detection And Ranging
LST	Land Surface Temperature
NDVI	Normalized Difference Vegetation Index
PALSAR	Phased Array type L-band Synthetic Aperture Radar
RCP	Representative Concentration Pathways
SAR	Synthetic Aperture Radar
TanDEM-X	TerraSAR-X-Add-on for Digital Elevation Measurements

1 Introduction

1.1 Background and motivation

1.1.1 Permafrost

Permafrost is defined as ground (soil or rock and included ice or organic material) that remains at or below 0°C for at least two consecutive years (Harris et al. 1988). It can occur beneath the seafloor (subsea permafrost), and beneath the land surface (terrestrial permafrost), which is the focus of this study. The thickness of permafrost varies from less than one meter to more than 1500 meters. It is an important element of the cryosphere and has strong impacts on hydrology, biological processes, land surface energy budget, and infrastructure.

The surface layer of ground, on top of the perennially frozen permafrost, is subject to annual thawing and freezing. This layer is named as active layer (Burn 1998; Harris et al. 1988). Energy and water are exchanged between the atmosphere and underlying permafrost across this layer. The active layer plays a critical ecological role in permafrost regions because most biological, chemical and hydrological processes are constrained in this layer. The active layer thickness (ALT) is highly variable in time and over space. The boundary of the active layer (permafrost table) could shift upwards or downwards following climate variations; one exceptionally warm summer may lead to a thicker active layer. Variations in vegetation, surface organic layer, substrate properties, surface temperature, and water content can result in very large differences in ALT, even over small distances (Nelson et al. 1999).

In the Northern Hemisphere, permafrost occupies approximately 24 % of the exposed land area (Zhang et al. 2008). The large extent of permafrost is found in Siberia, Alaska, the Arctic and sub-arctic Canada. Permafrost is also found at high elevations of many mountain regions, e.g., the Qinghai Tibetan Plateau, European Alps, the Rocky Mountains of North America and the Andes.

Based on the estimated geographic continuity of subsurface permafrost in the landscape, lowland permafrost regions are divided into several zones (Brown et al. 1997), shown in Figure 1.1:

- Continuous zone (more than 90% of the area underlain by permafrost),
- Discontinuous (50-90% of the area),
- Sporadic (less than 50% of the area),
- Isolated zone (only small patches).

By its temperature, permafrost can be distinguished as cold permafrost and warm permafrost. Cold permafrost is defined by mean annual ground temperatures below -2°C,

and warm permafrost at temperatures above -2°C . Warm permafrost is found mostly in the discontinuous permafrost zone, while cold permafrost exists in the continuous permafrost zone and only occasionally in the discontinuous permafrost zone (Romanovsky et al. 2010; Smith et al. 2010).

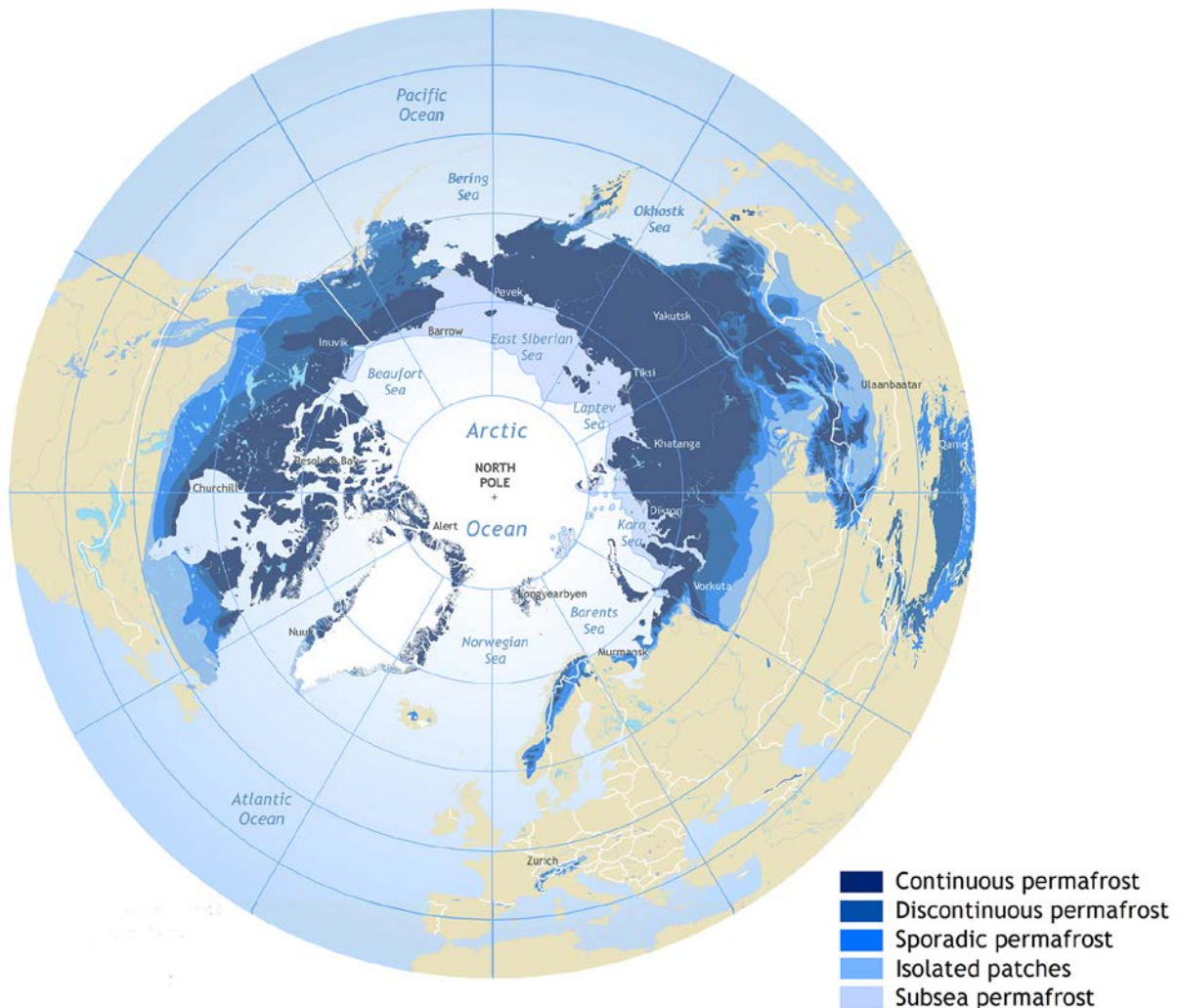


Figure 1. 1: Circum-Arctic map of permafrost (Brown et al. 1997).

Distinctive landforms are associated with permafrost. These landforms include ice wedges, pingos and the palsa family (Ballantyne 2018). Figure 1.2 shows typical permafrost landforms. Polygonal ice wedge networks are common in areas of continuous permafrost (Mackay 2000). Ice wedges result from the ground cracking in winter, followed by the cracks being filled with snow and meltwater during spring and summer. The resulting wedges of ice create interconnected, polygonal shapes on the Earth's surface called polygonal ground. Pingos are ice-cored hills with height up to 100 m and a diameter between 30 to 1000 meters. Most pingos are circular in shape; they are significant landforms on the flat tundra of the Arctic. Palsas and lithalsas belong to the palsa family; they are most common in the discontinuous permafrost zone. They are low frost mounds standing several meters (generally 3 to 5 m) above the surrounding terrain,

with cores of layered segregated ice formed by cryosuction of soil water in freezing fine-grained, frost-susceptible soils (like silt) (Pissart 2002). Palsas and lithalsas are very similar in shape, size, and origin; however, the palsas have a cover of peat which is absent for lithalsas.

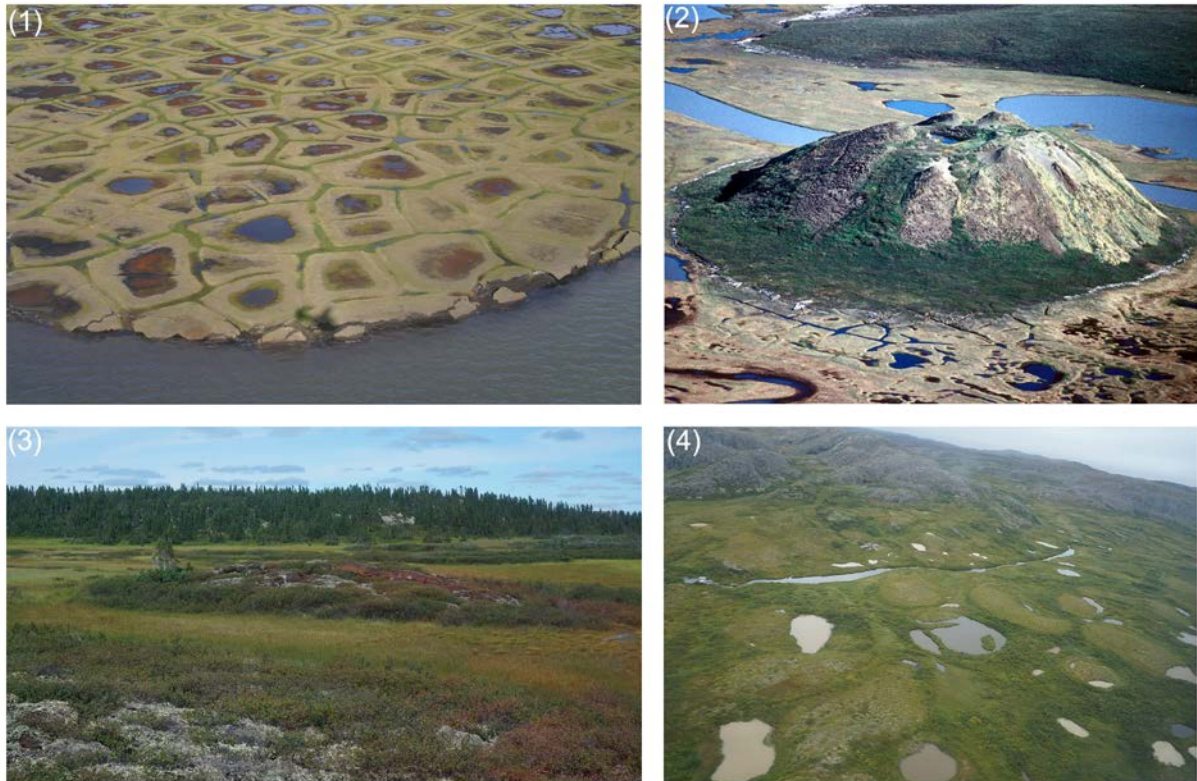


Figure 1. 2: Typical permafrost landforms. (1) ice-wedge polygons and an eroding shoreline at Cape Halkett on the Beaufort Sea coast of Alaska, photo is from the webpage (soundwavesUSGS). (2) One pingo in the Pingo Canadian Landmark, Northwest Territories, Canada, photo is from the webpage (TheTuktoyaktukPingos). (3) One collapsed palsa site in northern Quebec, Canada. (4) Lithalsas and thermokarst ponds in northern Quebec, Canada.

1.1.2 Climate change in the Arctic

For several decades, surface air temperatures in the high northern latitudes have warmed at approximately twice the global rate (Anisimov et al. 2007). The averaged warming north of 60°N has been 1-2°C since a temperature minimum in the 1960s and 1970s (Anisimov et al. 2007; Serreze and Barry 2011).

According to the IPCC report 2007 and 2013, the most recent (1980 to present) warming of much of the Arctic is strongest (about 1°C/decade) in winter and spring, and smallest in autumn. Precipitation in the Arctic shows signs of an increase over the past century, although the trends are small (about 1% per decade), highly variable in space, and highly uncertain because of deficiencies in the precipitation measurement network and the difficulty in obtaining accurate measurements of rain and snow in windy polar regions (Anisimov et al. 2007; Collins et al. 2013).

Long-term projections of climate change for the end of the 21st also exhibit that the Arctic region is projected to suffer from great climatic changes. Figure 1.3 shows the patterns of warming and precipitation change from the Coupled Model Inter-comparison Project Phase 5 (CMIP5) (using 46 General Circulation Models and four RCPs) (Collins et al. 2013).

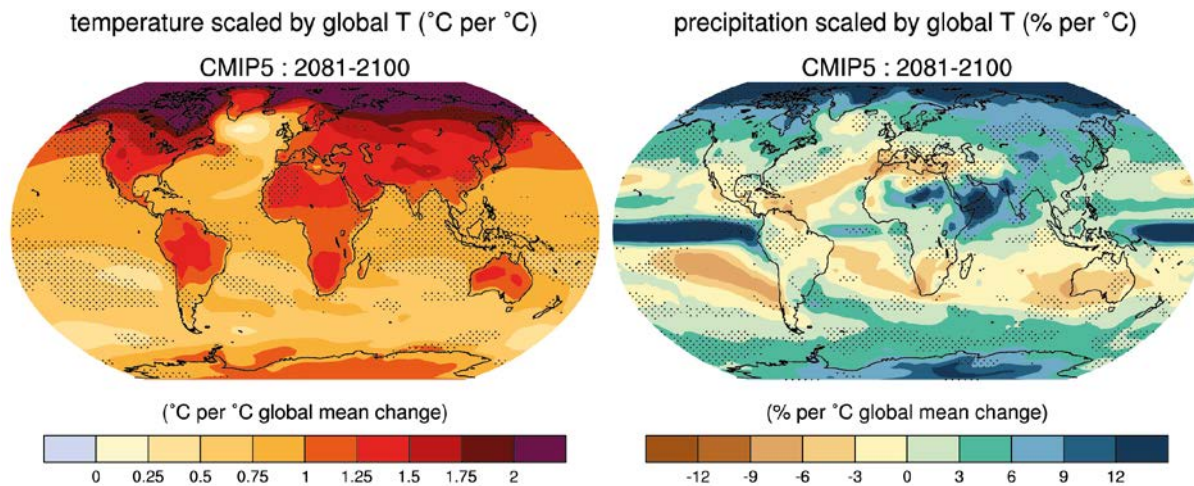


Figure 1. 3: Patterns of warming and precipitation change from the Coupled Model Inter-comparison Project Phase 5 (CMIP5) (Collins et al. 2013)

1.1.3 Impacts of climate warming on permafrost terrain

Permafrost temperatures have increased in most regions since the early 1980s (Vaughan et al. 2013). Permafrost warming is mainly in response to increased air temperature and variability in snow cover. Permafrost temperature increases are greater in cold permafrost than in warm permafrost, especially in tundra regions with low ice content, where permafrost warming rates have been greatest (Romanovsky et al. 2010; Smith et al. 2010; Wu et al. 2012). Cold permafrost in northern Siberia, northern Alaska and northwest Canada have shown the largest magnitude of temperature increases, up to 4°C in some regions. For warm ice-rich permafrost, due to heat absorbed by partial melting of interstitial ice, the temperature change is slowed and attenuated. Temperatures of warm permafrost have also increased over the last three decades, but generally by less than 2°C (Callaghan et al. 2010; Smith et al. 2010; Wu et al. 2012). In some areas in the southern margins of discontinuous permafrost regions, permafrost temperatures have shown little or no change, indicating that permafrost is thawing internally but remaining very close to the melting point (Smith et al. 2010).

Regional warming in the high northern latitudes leads to a decrease in thickness and/or areal extent of permafrost, referred to as permafrost degradation (Streletskiy et al. 2015a). Manifestations of permafrost degradation include geomorphologic changes such as talik and thermokarst development (Grosse et al. 2013; Liljedahl et al. 2016), ground surface subsidence (Streletskiy et al. 2017) and slope instability. By the end of the 21st

century, the area of permafrost near the surface (upper 3.5 m) is projected to decrease by 37% (RCP2.6) to 81% (RCP8.5) for the model average (Collins et al. 2013).

Permafrost degradation brings significant changes in landscapes (Rowland et al. 2010), ecosystems and hydrological processes. Permafrost degradation could directly affect the lives of people through impacts on the landscape, vegetation and civil infrastructure. The influence of permafrost degradation is stated in the following four aspects.

- Landscape and ecosystem

Changes in vegetation have been recorded in the arctic and sub-arctic over the last 20 years (Elmendorf et al. 2012a; Elmendorf et al. 2012b; Myers-Smith et al. 2015). It was pointed out that the groups that increased most were graminoids (grasses and grass-like plants) in cold regions and primarily shrubs in warm regions of the tundra. Increased growth of deciduous shrubs and graminoids is at the loss of decreased cover of mosses and lichens and decreased species diversity and evenness (Elmendorf et al. 2012a). Tall graminoids and shrubs are expected to alter snow distribution and its persistence on the ground, which provides thermal insulation in winter. Changes in vegetation affect the permafrost thermal state, and in turn, permafrost degradation alters the vegetation.

Another predominant change in the landscape tied to permafrost thaw is the change in abundance and characteristics of thermokarst lakes (Jones et al. 2011; Payette et al. 2004; Smith et al. 2005; Yoshikawa and Hinzman 2003). Thermokarst lakes which are abundant in the Arctic and sub-arctic permafrost lowlands are closed depressions formed by ground subsidence following the thawing of ice-rich permafrost or ground ice (Kokelj and Jorgenson 2013). Expansion of thermokarst lakes is caused by climate-induced thermal erosion, while shrinkage of thermokarst lakes is caused by evaporation or talik development. Once thermal erosion is initiated, the presence of a water body on permafrost serves as positive feedback to permafrost degradation.

Thawing of the permafrost also changes the topography, e.g., provoking landslides and active layer detachment failure, or creating thermo-erosion gullies in regions where ice-wedge polygons are widespread. Along the ice-rich permafrost coastal bluffs, rapid and accelerating coastal retreat is evident (Lantuit et al. 2013). These landscape changes affect animal populations as well, such as caribou feeding habits and migration patterns.

- Greenhouse gases

Permafrost holds considerable quantities of carbon in the frozen organic soils, about twice the amount currently in the atmosphere (Zimov et al. 2006). By increasing microbial activity in the thickening active layer, carbon and nitrogen previously stabilized in the frozen substrates are released into the atmosphere (Schuur et al. 2015). In the coming decades, permafrost carbon and nitrogen release (methane (CH₄), carbon dioxide (CO₂) and nitrous oxide (N₂O)) are likely to be a major contributor to atmospheric greenhouse gas concentrations.

Development of thermokarst ponds caused by thawing of permafrost is carbon source. However, the concurrent rapid terrestrialization of drained thermokarst lakes favors carbon-sink conditions. Thus the two processes tend to balance the local carbon budget in some peatland ecosystems (Payette et al. 2004).

- Hydrology and aquatic ecosystem

Permafrost degradation can lead to changes in the terrestrial water cycle, including alteration of water storage in surface reservoirs (including lakes/ponds, and wetlands), hydrological connectivity (ponds are becoming interconnected) (Connon et al. 2014) and surface water-groundwater interaction. Thawing permafrost also promotes transport of sediment, nutrients, carbon, and nitrate in the stream water (Frey and McClelland 2009; Walvoord and Striegl 2007).

In permafrost terrain, the interaction between groundwater and surface water is restricted. With permafrost degradation, groundwater storage and groundwater recharge is anticipated to increase (Bense et al. 2012). In several rivers in the pan-arctic, variability in river discharge has been detected, and an increase in winter baseflow is a major trend (McClelland et al. 2004; St. Jacques and Sauchyn 2009). Permafrost degradation has been associated as a potential cause for the increased winter streamflow (McClelland et al. 2006; Streletskiy et al. 2015b). However, evaluating the effects of permafrost degradation on river flow is a challenging task because a large number of possible influencing factors besides changing permafrost conditions interact, e.g., precipitation, evaporation, lakes and grounded ice. The spatiotemporal dynamics of groundwater flow and hydrogeological regime response to permafrost degradation are not well understood yet (Bense et al. 2012).

- Infrastructure stability

Permafrost provides a solid base for supporting man-made infrastructures, but thawing permafrost turns into soft ground or even into the mud. Permafrost threatens the stability of infrastructures in two ways: 1) through ground subsidence induced by thawing of ice-rich permafrost and, 2) through terrain destabilization by active layer slides and thermal erosion (Allard et al. 2012; Anisimov et al. 2007; Nelson et al. 2001). Over permafrost terrain, infrastructures are designed to either preserve permafrost or be adapted to the loss of frozen ground support. Permafrost degradation presents an additional challenge to the construction and maintenance of northern infrastructure, which calls for a better understanding of local permafrost conditions under climate change.

1.1.4 Threats by permafrost degradation in the eastern Canadian sub-arctic

Inuit communities in Nunavik and Nunatsiavut (locations are marked in Figure 1.4) in the eastern Canadian sub-Arctic are amongst the groups most affected by the impacts of climate change and permafrost degradation (Allard et al. 2012).

According to the temperature recordings by Historical Climate Data Canada, the Mean annual air temperature (MAAT) in Nunavik remained stable in the 1960s-1990s; then, there was strong warming in the 1990s-2010s (with MAAT increasing by 2°C). After peaking in 2010, MAAT continuously dropped from 2010 to 2015, with the most recent two years (2016-2017) again exhibiting warming (Figure 1.7 (a)).

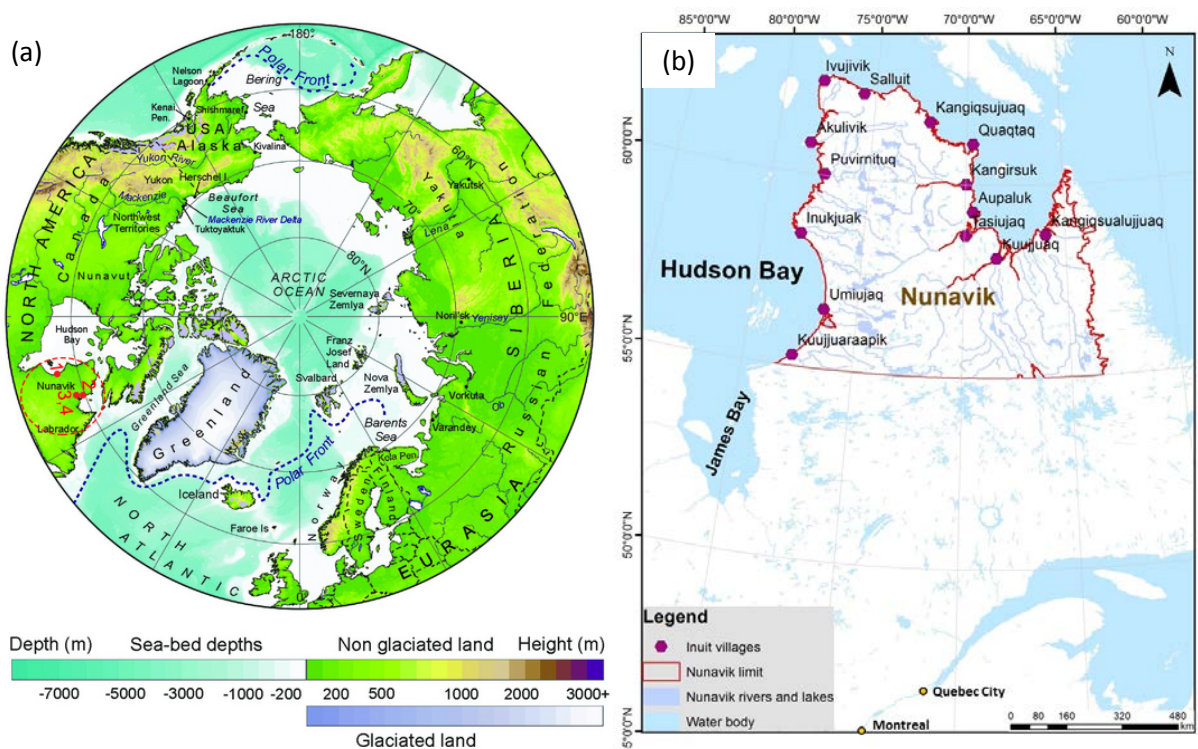


Figure 1. 4: (a) North Polar region, the Nunavik in the eastern Canadian sub-Arctic are marked with right circle. (Map is drawn by P. Fretwell, British Antarctic Survey). The borehole temperatures shown in Figure 1. 5 are also marked with numbers on this figure. (b) Nunavik map.

The warming has induced a widespread and fast permafrost degradation in the eastern Canadian sub-Arctic (Jolivel and Allard 2013; Payette et al. 2004). In-situ monitoring shows significant increases in active layer depth and ground temperature. Figure 1.5 shows ground temperature measurements at four borehole stations in Nunavik. Boreholes into the basalt rock Figure 1.5 (1) and schist rock Figure 1.5 (3) show very large seasonal fluctuations, which is related to the high heat conductivity of the rock. At site Figure 1.5 (1), the ground temperature at a depth of 20 m increased from -1.2°C in 1998 to -0.4°C in 2015. At site Figure 1.5 (3), the ground temperature at a depth of 20 m increased from -2.9°C in 1994 to -1.5°C in 2010, then decreased from -1.2°C in 2011 to -

1.5°C in 2016. Ground temperatures below 6 m all show a slight decrease after 2011. At site Figure 1.5 (2), borehole into marine sand/gravel has a much shallower active layer, which is around 2.1 m. Since 2011, the permafrost table also arises along with the MAAT decreases during the period 2010-2015. The ground temperature at a depth of 19.1 m, however, shows a continuous warming trend from -3.6°C in 1995 to -2.2°C in 2016. At site Figure 1.5 (4), a sandy road embankment, the seasonal fluctuations continuously enlarged. The change is not only due to the climate change but also the snow accumulation along the road embankment which insulates the ground surface in winter and prevents further ground freezing (Fortier and Bolduc 2008).

In the meanwhile, the population growth of Inuit communities is amongst the highest in the world. Nunavik and Nunatsiavut residents are largely affected by climate change and permafrost degradation because resources and conditions traditionally available for them are changing, such as vegetation, water bodies and soil drainage (Allard et al. 2012). For example, the growth of berries is shaded by the expansion of shrubs. In many Nunavik communities, permafrost thawing has begun to impact the stability of some runway sections (Allard et al. 2012). The rapid population growth also leads to a raised need for residential, municipal and transportation infrastructures. Knowledge of sub-arctic environmental conditions including permafrost, freezing of active layer, the impacts of permafrost thaw and seasonal hydrological conditions are needed for infrastructure maintenance and development as well as construction plans.

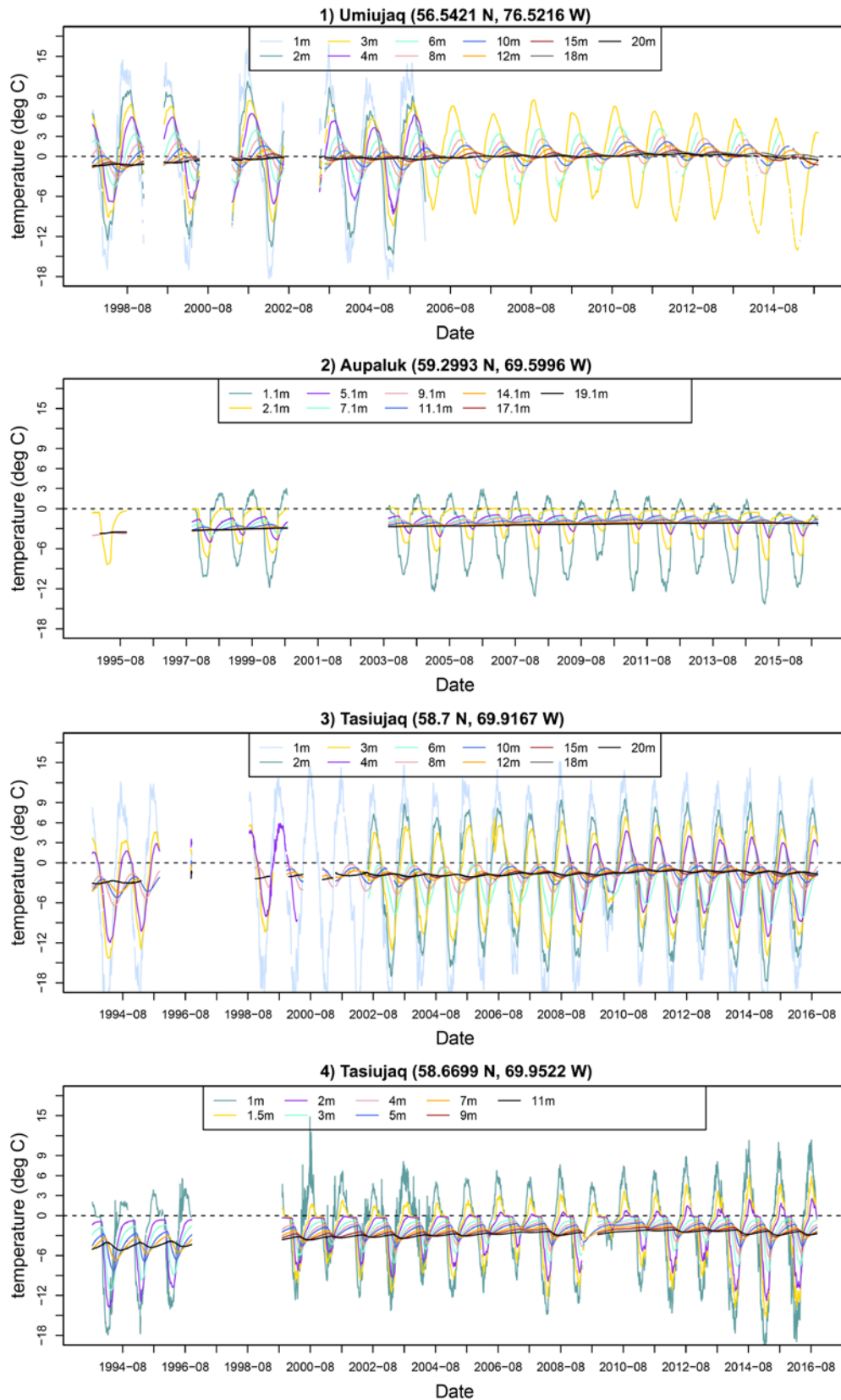


Figure 1. 5: Ground temperatures at three Nunavik villages (1) Umiujaq (56.5421 N, 76.5216 W), borehole into the basalt rock; (2) Aupaluk (59.2993 N, 69.5996 W), borehole into marine sand/gravel, about 40 m west of the village airport runway; (3) Tasiujaq (58.7 N, 69.9167 W), borehole into schist rock, a few kilometers northeast of the airport; (4) Tasiujaq (58.6699 N, 69.9522 W), borehole into sand embankment (terrace), about 40 m west of the airport runway. Ground temperature data is obtained through Nordicana-D online database (Allard et al. 2016).

1.1.5 Study area

The study area is in the Umiujaq region in Nunavik, situated on the eastern shore of Hudson Bay ($56^{\circ}33' \text{ N}$, $76^{\circ}31' \text{ W}$), shown in Figure 1.6. This region is situated in the transitional area from the isolated and sporadic permafrost zone (2-50% area cover) to the widespread discontinuous permafrost zone (50-90%) (Allard and Seguin 1987b). The temperature of permafrost is precariously close to above freezing. The study area was selected because of its susceptibility to climate change, and long research focused on permafrost studies, coastal geology, and geomorphological characterization of the region (Elger et al. 2012).

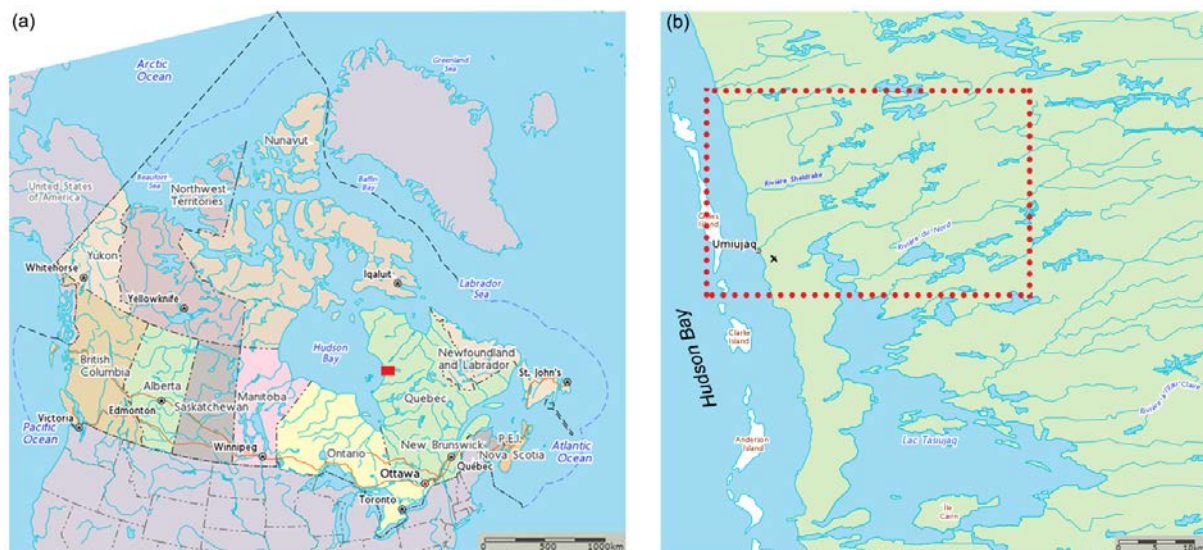


Figure 1. 6: Location of the study area of Umiujaq, Northern Quebec, Canada. (a) Canada Map, red rectangle marks the region shown in Figure 1.6 (b). (b) The red box indicates the study area.

1.1.5.1 Climate

The climate is sub-Arctic, with a mean annual air temperature (MAAT) of approximately -2.9°C ; the area experiences cold winters (-20.3°C in January, -21.4°C in February) and cool summers (11.4°C in July, 11.7°C in August). Wind speed is in an average of 5.9 m/s , and could reach a maximum of 30.8 m/s in winter.

The continuous weather observation in Umiujaq starts in the 1990s. However, the long-term climate trend could be referred to two other stations (Kuujjuarapik, $55^{\circ}17' \text{ N}$, $77^{\circ}45' \text{ W}$, 150 km south of the study area; and Inukjuak, $58^{\circ}28' \text{ N}$, $78^{\circ}05' \text{ W}$, 200 km north of the study area), which have long climate records since the 1950s. The locations of these three stations can be found in Figure 1.4 (b). Figure 1.7 shows MAATs and annual precipitation in the period 1960-2017.

Figure 1.7 (a) exhibits the warming starts in the 1990s and reaches the peak in 2010. In the most recent two years (2016-2017), the weather again exhibits a warming signal.

Accurate measurements of rain and snow are difficult in the Arctic and sub-Arctic regions. Based on the records in station Kuujjuarapik and Inukjuak, the yearly precipitation in Umiujaq region is speculated to be around 550 mm. However, according to the reanalysis dataset ERA-Interim, the Umiujaq region has yearly precipitation around 700 mm; according to the reanalysis dataset North American Regional Reanalysis (NARR), the range is in around 800 mm. According to the Umiujaq SILA weather station installed in the Tasiapik valley (SILA 2018), yearly precipitation is around 800 mm (Figure 1.7 (b)).

Snow cover thickness varies spatially from several centimeters to about two meters according to the field measurements. In winter, the prevailing westerly and northwesterly winds affect snow distribution, shifting snow from the top of plateaus into low depressions and gulleys (Ménard et al. 1998; Pelletier 2015).

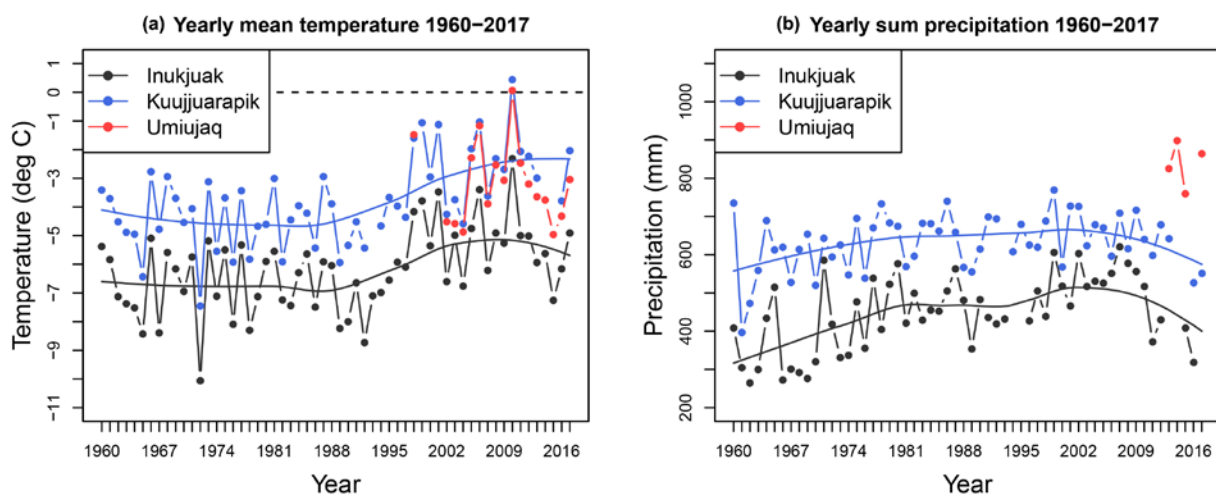


Figure 1. 7: (a) Mean annual air temperatures (MAATs) in the period 1960–2017 at three meteorological stations. (b) Annual precipitation in the period 1960–2017 at three meteorological stations. The solid line is a non-parametric local regression applied to the original line curve of points.

1.1.5.2 Geomorphology

The region was covered by ice during the Wisconsin glacialiation. The ice sheet load caused isostatic depression of the crust; following the receding front of the Laurentide Ice Sheet eastward and inland, between 8000 and 7400 calendar years before present (cal BP) (Lajeunesse 2008; Lavoie et al. 2012; Lavoie et al. 2002), the Tyrrell Sea flooded a large band of coastline up to 204 m - 220 m in elevation (Allard and Seguin 1985; Lajeunesse and Allard 2003) in the study area.

The marine transgression leaves the deep-water sediments (silt and clay) and coarse shore sediments (sand, gravel, pebbles and boulders) lying over the bedrock and on glacial drift (Lévesque et al. 1988).

The postglacial land emergence rate was 10 m/century immediately after deglaciation, then has decreased to the present-day rate of 1.3 m/century (Allard and Seguin 1985; Lavoie et al. 2012). After land emergence, about 5800 BP, the ground is invaded by

permafrost during cold climate periods. The formation of segregation ice lenses in fine-grained marine sediments produces a variety of landforms such as cryogenic mounds and palsas (Allard and Seguin 1987a; Calmels et al. 2008; Cyr and Payette 2010).

1.1.5.3 Vegetation

The maritime influence of Hudson Bay generates a west-east climate gradient from the shoreline inward; has created a tree line approximately 15 km inland parallel to the coastline, with the shrub-tundra to the west and the forest-tundra to the east (Payette 1983; Payette and Gagnon 1979). The landscape exhibits high spatial heterogeneity with regards to the vegetation type, vegetation structure, and hydrologic properties. The expansion of shrub communities is observed in the study area (Allard and Pollard 2011; Provencher-Nolet 2014), particularly near the tree-line, where increased summer temperature and snow cover favors shrubification of the tundra sites.

The narrow coastal plain (~3 km) along the eastern shore of Hudson Bay is covered by a range of tundra plant communities dominated by herbaceous species (e.g., sedges and grasses), prostrate dwarf shrubs (*Vaccinium uliginosum* and *Vaccinium vitis-idea*), lichens and mosses.

The shrub tundra landscape further inland is dominantly covered by lichens and low to high shrubs, primarily willows (*Salix planifolia*), dwarf birch (*Betula glandulosa*) and green alder (*Alnus Crispa*). The taller shrub species grow mainly in sheltered areas such as in low depressions and gullies. krummholz-shaped black spruce (*Picea mariana*) patches can also be found in the shrub tundra environment but within small, isolated tree islands.

The forest-tundra environment is composed of clusters of black spruces, tundra plants, peatland, and fen/bog vegetation.

A land cover map based on Sentinel-2 optical satellite images, shown in Figure 1.8. It is generated through a maximum likelihood supervised classification based on three Sentinel-2 images acquired on 2017-07-29, 2017-08-23 and 2017-10-02. First, classification is individually applied to three Sentinel-2 images. Then, the majority of the three classification results are taken to guarantee a higher accuracy (overall accuracy is 94.8%).

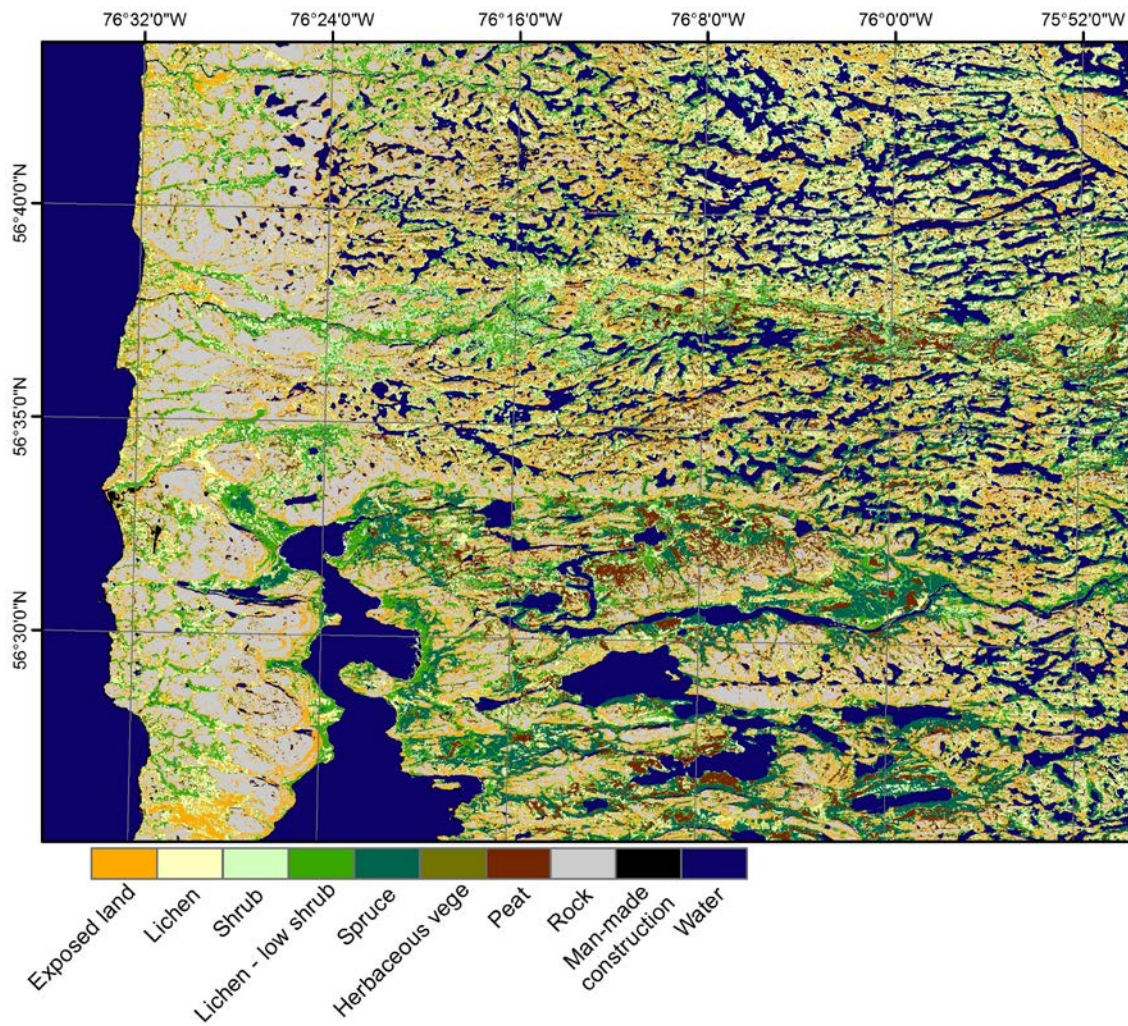


Figure 1. 8: Land cover map based on Sentinel-2 images in 2017.

1.1.5.4 Village and research station history

The Umiujaq village was established in 1986 by Inuit from Kuujjuarapik, 160 km to the south, who decided to relocate in the region where they hoped to better preserve their traditional lifestyle in an area where fish and game were not threatened by development. Today, Umiujaq has a population of about 500 inhabitants, mainly Inuit. Centre d'études Nordiques (CEN: Centre for Northern Studies) has conducted research here since 1980. In 2010, CEN undertook major station upgrades.

1.2 Monitoring permafrost environments

1.2.1 In-situ monitoring of permafrost

In-situ measurements are essential to understanding physical processes in permafrost terrain. The detection of permafrost presence is generally established by in-situ ground measurements of active layer thickness (ALT) and borehole temperatures. The Global Terrestrial Network for Permafrost (GTN-P), developed in the 1990s, is the primary international program concerned with the monitoring of permafrost parameters. The monitoring sites are spread in the permafrost regions, from Polar regions to mid-latitude mountain environments. The program has two international monitoring components: (a) long-term monitoring of the thermal state of permafrost in an extensive borehole network; and (b) monitoring of active-layer thickness and processes at representative locations (Circumpolar Active layer monitoring-CALM) (Shiklomanov et al. 2012).

-Temperature

Permafrost temperature measurements are obtained from temperature sensors installed in the borehole. The depth of boreholes varies from less than 10m to greater than 100m. Measurements may be recorded manually or by data loggers. Data loggers are utilized to reduce the frequency of site visits and provide continuous records.

- Active layer thickness (ALT)

Several methods are used to determine the active layer thickness, such as annual mechanical probing, frost tubes (or thaw tubes), and the interpolation of soil temperatures (Humlum and Matsuoka 2004).

Thaw/frost tubes contain a rigid outer tube which is anchored vertically in permafrost and serves as a stable reference; a flexible inner tube is filled with deionized water. The approximate position of the thawed active layer is indicated by the presence of ice in the inner tube. The heave and settlement is recorded by a scriber, attached to a sleeve, which scratches the outer tube as it moves up and down with a metal grill resting on the ground surface. Thaw/frost tube can deliver information on (1) the maximum seasonal thaw depth (2) and the maximum heave and settlement of the ground surface (Mackay 1973).

Recently, Ground Penetrating Radar (GPR) and Electrical Resistivity Tomography measurements (ERT) have been employed in the field surveys to map active-layer thickness along transects (Fortier et al. 2008; Fortier et al. 2011; Hinkel et al. 2001; Kneisel et al. 2008).

In-situ measurements provide vital parameters of permafrost, but they have several limitations, ranging from difficulties in drilling to the representativeness of limited single point measurements. It also requires regular site visits, e.g. for downloading records in the dataloggers and readings on the thaw tubes.

1.2.2 Monitoring permafrost environments with remote sensing

Remote sensing is urgently needed to supplement ground-based measurements and extend the point observations to a broader spatial domain. Mapping the depths of soil freezing/thawing or properties of permafrost directly from remote sensing is challenging because satellite and airborne sensors do not adequately penetrate the ground. However, many surface and subsurface features related to the permafrost active layer properties are observable or can be proxied by a variety of sensors at various wavelengths (Jorgenson and Grosse 2016; Westermann et al. 2015a). State of the art in permafrost environment monitoring with remote sensing is highlighted in the following four aspects.

-Landscape

Landforms are indicative of permafrost presence, with their changes inferring modifications to permafrost conditions. Vegetation cover has an impact on soil temperature and moisture regimes and therefore permafrost conditions (Juszk et al. 2016; Kelley et al. 2004). Based on in-situ ground measurements and meteorological data, together with remotely-sensed datasets, permafrost conditions and potential degradation are often extrapolated to the landscape scale. Vegetation properties (e.g., species, composition, NDVI) derived from optical remote sensing (Gangodagamage et al. 2014; Nguyen et al. 2009) or radar remote sensing (Widhalm et al. 2017) has been used to derive the permafrost extent and active layer thickness (ALT) at a local scale. Although vegetation is a function of the parameters that determine the ground thermal regime, plant type and structure are not directly proportional to permafrost extent. Any vegetation-permafrost relationship, established from field measurements, is only valid locally. Also, vegetation and permafrost changes occur on different timescales, where the former does not necessarily result in the latter (Myers-Smith et al. 2011).

The distribution of some permafrost landforms, e.g., above-ground permafrost mounds, pingos, and polygon morphology in the ice wedge polygonal ground, can be mapped directly on very high resolution aerial or satellite optical infrared images (Beck et al. 2015a; Jolivel and Allard 2013; May 2011; Provencher-Nolet 2014), or in combination with a high-resolution elevation model (Grosse and Jones 2011).

Thermokarst lake development is a direct indicator of thermokarstic processes in the permafrost terrain. The distribution and morphology of these lakes (Riordan et al. 2006), winter lake ice regimes (grounded ice versus floating ice cover) (Arp et al. 2012) and ice phenology (freeze/break-up and duration) (Olthof et al. 2015) have been monitored and mapped with satellite data.

-Topographic change (thaw slumps and thaw settlement)

Retrogressive thaw slumps and active layer detachment slides are prominent features of permafrost degradation, which occur in environments with high excess ground ice contents in near-surface permafrost and a sufficient slope gradient. Locations prone to

thaw slump, active layer detachment slides and coastal erosion have been detected with very high-resolution remote sensing images (Lantuit and Pollard 2008).

Through differencing of multi-temporal precise Digital Elevation Models (DEMs), which are generated by LiDAR imaging, stereoscopic aerial photography or interferometry technique, ground surface deformation can be obtained at different time phases (Günther et al. 2015; Jones et al. 2013b).

In addition to the methods mentioned above, ground surface deformation caused by permafrost activity can also be detected through Differential Interferometric SAR (D-InSAR) technique (Liu et al. 2015; Rykhus and Lu 2008; Short et al. 2014).

-Water storage

Permafrost degradation alters surface water-groundwater interactions. Groundwater recharge is anticipated to increase with permafrost degradation. The Gravity Recovery And Climate Experiment (GRACE) satellite is able to map time variations in the Earth's gravity field. Several studies have used GRACE data to detect spatiotemporal changes of water equivalent mass in the Arctic river basins (Im and Kharuk 2015; Muskett and Romanovsky 2011; Velicogna et al. 2012).

-Land surface temperature (LST) and freeze/thaw cycle

Land surface temperature or freeze-thaw state of the surface is especially connected with the thermal state of permafrost-affected terrain. The land surface temperature (LST) can be provided by infrared - optical remote sensing, derived from sensors of low spatial resolution (e.g., MODIS, AATSR, AVHRR) to medium spatial resolution (e.g., Sentinel-2, LANDSAT, ASTER). However, cloud contamination over the Arctic is a limitation for LST products derived by infrared - optical remote sensing. Cloud detection over snow and ice in the Arctic is a big challenge. Passive microwave emission can penetrate non-precipitating clouds, thus LST data derived from passive microwave sensors, like SSM/I, AMSR-E, AMSR2, SMMIS, provides a better representation of LST under nearly all sky conditions, but at much coarse resolution (on the order of 25-50 km). Some studies employ LST data as inputs for semi-empirical equilibrium permafrost models (e.g., TTOP, CryoGrid) to map permafrost extent and to simulate thawing depths (Westermann et al. 2015b).

The near-surface soil freeze/thaw cycle can be detected in both passive and active microwave remote sensing because of dielectric contrast. Relative permittivity is around 80 for water and below 10 for both ice and typical soil minerals, so that freezing of soil leads to a drastic decrease of its relative permittivity. Passive microwave remote sensing sensors have the advantage of high temporal resolution. They have been widely used for detecting the timing and duration of near-surface soil freeze/thaw cycles (Derksen et al. 2017; Kalantaria et al. 2015; Kim et al. 2012; Xu et al. 2016).

1.3 Monitoring permafrost environments with SAR datasets

1.3.1 The SAR system

1.3.1.2 Spaceborne SAR sensors and imaging geometry

SAR is an active microwave imaging system. It provides high-resolution, day-and-night and weather-independent images. Microwave imagery has a distinct advantage over optical imagery in high-latitude areas because it allows data to be acquired independently of cloud cover and solar illumination. Today, more than 15 spaceborne SAR systems are being operated for innumerable applications. Commonly used frequency bands in radar systems and the associated wavelength ranges are shown in Table 1.1. Most used frequency bands of spaceborne SAR systems are L-, C- and X- band. Table 1.2 provides an overview of spaceborne SAR sensors.

Table 1. 1: Frequency bands for radar systems.

Band	Ka	Ku	X	C	S	L	P
Frequency (Ghz)	40–25	17.6–12	12–7.5	7.5–3.75	3.75–2	2–1	0.5–0.25
Wavelength (cm)	0.75–1.2	1.7–2.5	2.5–4	4–8	8–15	15–30	60–120

Table 1. 2: List of spaceborne SAR sensors and their parameters.

Satellite mission	Wavelength (cm)	Life status	Resolution range x az. (m)	Repeat cycle (days)	Swath width (km)	Incident angle (°)	Institution, Country
X - band							
COSMOSkyMED (4 Sat)	3.1	2007 -	1	2/4/8/16	10 (spot) single pol.	20 - 60	ASI/MiD, Italy
			3		40 (strip) single pol.		
			30 / 100		100 / 200 (scan) single pol.		
TerraSAR - X Tandem - X	3.1	2007- 2010 -	1	1/11	10 (spot)	20 - 55	DLR/Astrium, Germany
			3		30 (strip)		
			15		100 (scan)		
COSMOSkyMED-2 (2 Sat)	3.1	2015 -	0.8	14 13/16	10 (spot) single pol.	20 - 60	ASI/MiD, Italy
			1		10 (spot) dual pol.		
			3		40 (spot) dual pol.		
			3		15 (spot) quad pol.		
			4 x 20		100 (scan) single/dual pol.		
			6 x 40		200 (scan) single/dual pol.		
PAZ	3.1	2018 -	1	t_0 with TSX, t_{0+5} with PAZ, t_{0+11} with TSX	10 (spot)	15 - 60	CDTI, Spain
			3		30 (strip)		
			15		100 (scan)		
C - band							
ERS-1/2	5.6	1992 - 2001	26 x 6 - 30	35	100	23	ESA, Europe
ENVISAT	5.6	2003 - 2010	26 x 6 - 30	35	100	19 - 44	ESA, Europe
RADARSAT - 1	5.6	1995 -	8	24	45 (strip)	20 - 50	CSA,

			30		100 / 150 (strip)		Canada
			50 / 100		300 / 500 (scan)		
RADARSAT - 2	5.6	2007 -	1 - 8	24	18 - 125 single pol.	20 - 50	CSA, Canada
			8		50 / 150 (strip) single/dual pol.		
			25		100 / 150 (strip) single/dual pol.		
			50 / 100		300 / 500 (scan) single/dual pol.		
			12 / 25		25 / 50 (polarimetric) quad pol.		
Sentinel - 1A/B	5.6	2016 -	5	6/12	80 (SM)	30 - 46	ESA, Europe
			5 x 20		250 (IW)		
			20 x 40		400 (EW)		
RADARSAT Constellation Mission (3 Sat)	5.5	2019	1 - 100	3/12	20 - 500	20 - 55	CSA, Canada
L - band							
J - ERS	23.5	1992 - 1998	18	44	75	35	JAXA, Japan
ALOS PALSAR	23.6	2006 - 2011	7 - 44	46	40 - 70 (fine) single pol.	8 - 60	JAXA, Japan
			14 - 88		40 - 70 (fine) dual pol.		
			100		250 - 350 (scan) single pol.		
			24 - 89		20 - 65 (polarimetric) quad pol.		
ALOS PALSAR - 2	22.9	2014 -	3 x 1	14	25 (spot)	8 - 70	JAXA, Japan
			3 - 10		30 - 70 (strip)		
			100 / 60		350 / 490 (scan)		
SAOCOM (2 Sat)	23.5	2019	10 - 50	8/16	20 - 150	20 - 50	CONAE, Argentina
Tandem - L		2024					DLR/Astrium, Germany

Future missions are shown in gray

SAR systems have a side-looking imaging geometry (Figure 1.9). The SAR makes use of the radar principle to form an image by utilizing the time delay of the backscattered signals. In the SAR system, the transmitted pulse interacts with the Earth surface and some of the energy is reflected back towards the receiving antenna.

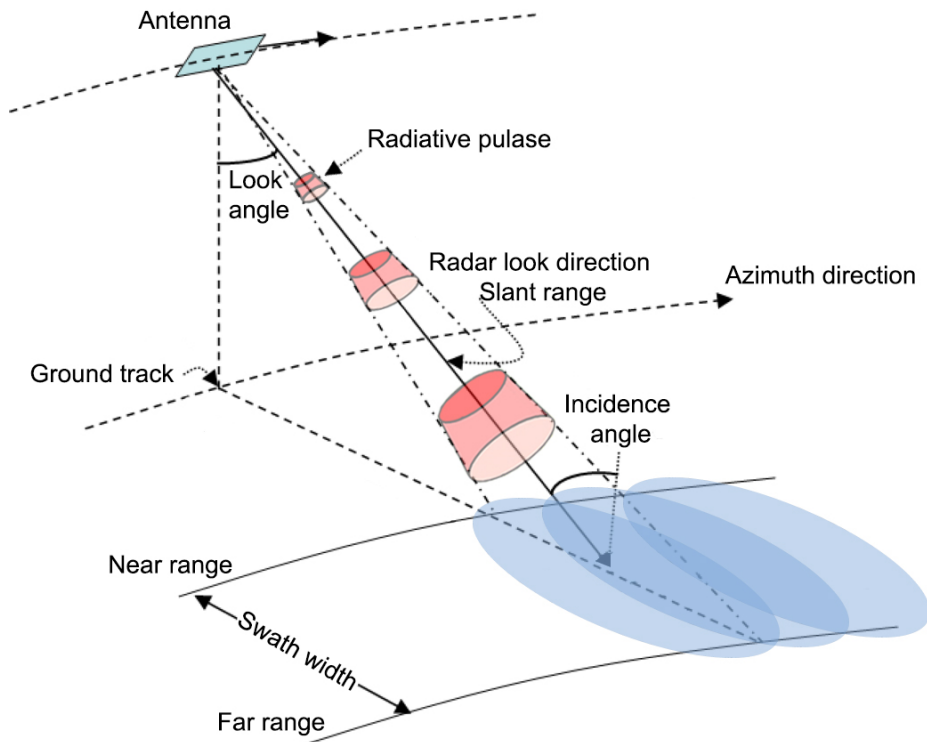


Figure 1. 9: Illustration of the SAR imaging geometry, adapted from (Zhou et al. 2009).

1.3.1.2 Backscattering signal

The backscattering signal is a function of SAR sensor configuration (wavelength, polarization, resolution and incidence angle) and surface target characteristics (roughness, geometric shape and dielectric properties).

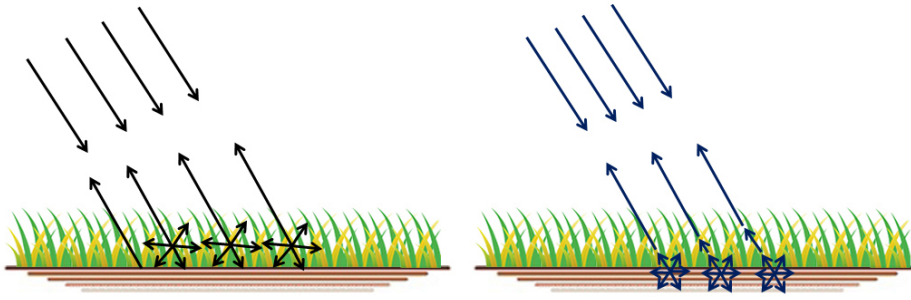
The frequency of the transmitted pulse determines the penetration depth into the target as well as the relative roughness of the target surface. Penetration depth tends to be longer with longer wavelengths. For example, in the forest area, the X-band radiation will only penetrate the first leaves on top of the trees, the backscattering signal contains the information of the top layer and the crown of the trees; however, the L-band radiation penetrates leaves and small branches, the backscattering signal contains the information of the branches and tree trunks. Roughness is a relative concept depending upon wavelength and incidence angle. A surface is considered "rough" if its surface structure has dimensions that are comparable to the incident wavelength. Polarization describes the orientation of the electric field component of an electromagnetic wave. Linear polarization configurations HH, VV, HV, VH are most commonly used. The first term corresponds to the polarization of the emitted radiation, the second term to the received

radiation, for example, HV refers to H transmitted, and V received. Polarization provides information on the form and the orientation of small scattering elements that compose the surface or target. Another important parameter which influences the scattering mechanism is the incidence angle, which describes the angle between the radar beam and the direction to the intercepting surface. Smaller incidence angles can better penetrate the vegetation layer. Figure 1.10 shows a schematic illustration of the dominant backscatter mechanisms.

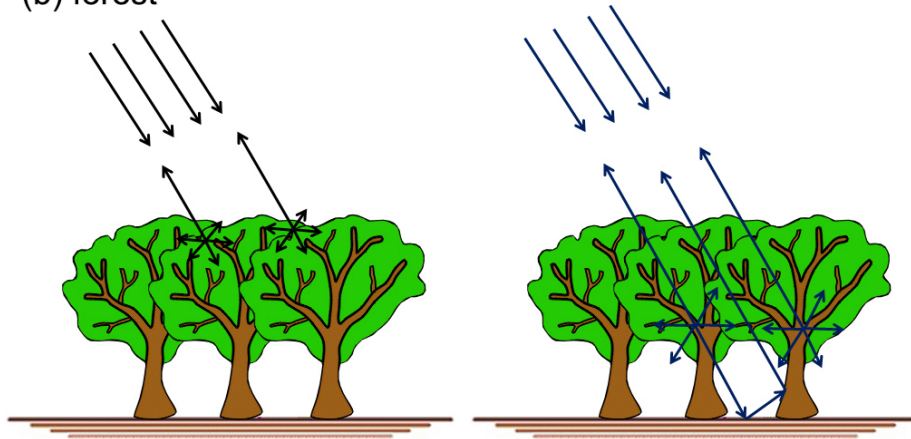
Four surface cover conditions are illustrated in Figure 1.10. Figure 1.10 (a) Short vegetation/soil, e.g., herbaceous vegetation and tundra landscape. Over bare ground, surface reflection is the dominant scattering mechanism; when the surface is smooth, the reflection becomes specular. Over vegetated terrain, vegetation layer results in volume scattering at short wavelengths. Longer wavelengths show a deeper penetration into the soil. Thus scattering from the vegetation layer in combination with volume scattering within the soil contribute to the overall backscattering signal. (b) Forests. The shortwave signal mainly interacts with leaves, twigs, and small branches. At shorter wavelengths, volume scattering within canopies is the dominated. The longwave signal penetrates the crown cover. Scattering from branches and tree structures in combination with double-bounce effect contribute to the overall backscattering signal. (c) Water. Specular scattering is dominated, assuming a calm smooth water surface. (d) Urban regions. The 'double-bounce' effect is the dominated at short and long wavelengths.

Dielectric properties of the ground target depend on its moisture content. Water has a high dielectric constant, several times higher than other natural materials in dry conditions. As a result, a change in moisture content generally provokes a significant change in the dielectric properties of natural materials; increasing moisture is associated with an increased SAR backscatter. Water content also influences the electromagnetic wave penetration. The electromagnetic wave penetration in an object is an inverse function of water content. In the specific case of vegetation, penetration depth depends on moisture, density and geometric structure of the plants (leaves, branches).

(a) short vegetation



(b) forest



(c) water



(d) Urban

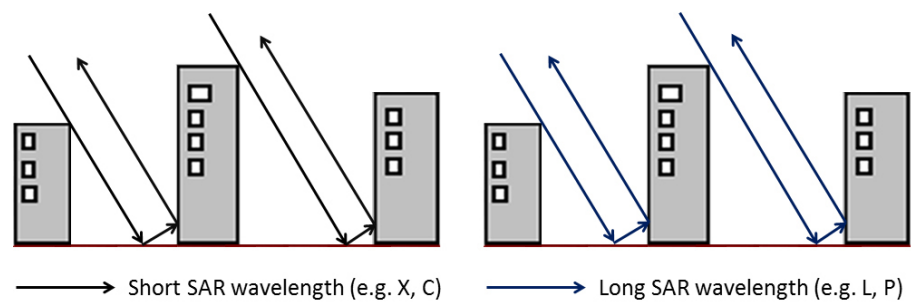


Figure 1. 10: Simplified schematic illustration of the dominant backscatter mechanisms for short (e.g. X/C) and long (e.g. P/L) wavelength electromagnetic signals for various surface cover conditions.

1.3.1.3 SAR Interferometry

The SAR system also records the phase of the reflected pulse, which is a measurement of travel path length from ground scatterer to satellite. By using this information, the Interferometric SAR (InSAR) technique has been developed to generate DEM or measure surface deformation of the terrain; the latter is named as Differential InSAR (D-InSAR) technique.

1.3.1.3.1 DEM generation

For DEM generation (Figure 1.11), the height of a point on the Earth surface can be reconstructed from the phase difference between two signals received from two SAR antennae of slightly different positions (S_1 and S_2 as illustrated in Figure 1.11). If the positions of the antennae are known accurately, the path difference received from two antennae can be used to infer the position of the target point on the Earth surface.

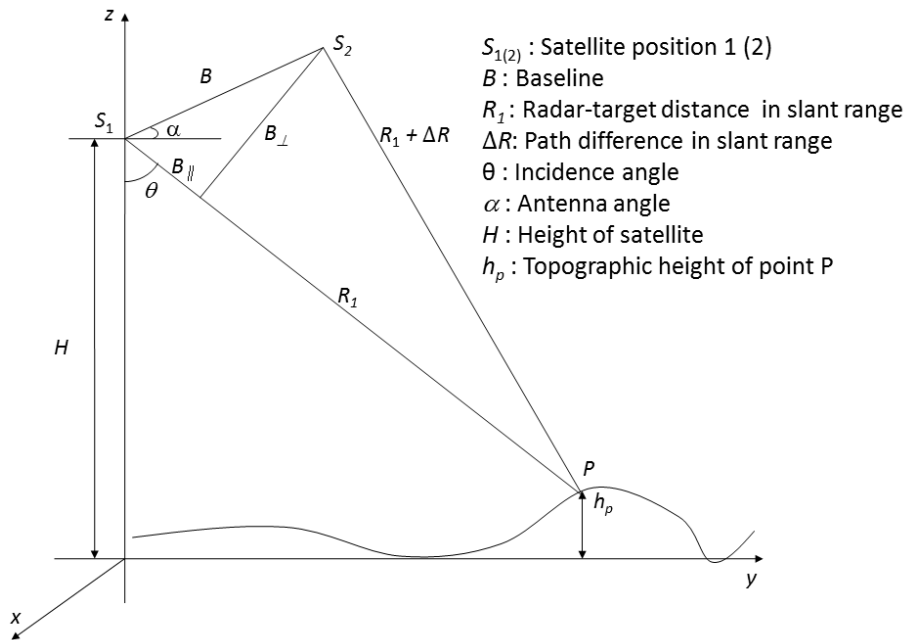


Figure 1. 11: Conceptual representation of satellite interferometric SAR system.

Phase - height relationship (for DEM generation) can be obtained from Figure 1.11:

$$B_{\perp} = B \cos(\theta - \alpha) \quad \text{Eq.1}$$

$$B_{\parallel} = B \sin(\theta - \alpha) \quad \text{Eq.2}$$

$$\Delta R \approx B \sin(\theta - \alpha) \approx B_{\parallel} \quad \text{Eq.3}$$

The interferometric phase between the two acquisitions can be written as

$$\varphi_p = -\frac{4\pi}{\lambda} \Delta R = -\frac{4\pi}{\lambda} [B \sin(\theta - \alpha)] = -\frac{4\pi}{\lambda} B_{\parallel} \quad \text{Eq.4}$$

$$h_p = H - R_1 \cos\theta \quad \text{Eq.5}$$

Differentiating on both sides of Eq.4 and Eq.5:

$$\Delta\varphi = -\frac{4\pi}{\lambda} B \cos(\theta - \alpha) \Delta\theta = -\frac{4\pi}{\lambda} B_{\perp} \Delta\theta \quad \text{Eq.6}$$

$$\Delta h = R_1 \sin\theta \Delta\theta - \Delta R_1 \cos\theta \quad \text{Eq.7}$$

Combining Eq.6 and Eq.7, the Eq.8 can be found.

$$\Delta\varphi = -\frac{4\pi}{\lambda} \frac{B_{\perp}}{R_1 \sin\theta} \Delta h - \frac{4\pi}{\lambda} \frac{B_{\perp}}{R_1 \tan\theta} \Delta R_1 \quad \text{Eq.8}$$

Where

$\frac{4\pi}{\lambda} \frac{B_{\perp}}{R_1 \sin\theta} \Delta h$ represents the phase caused by elevation change, and

$\frac{4\pi}{\lambda} \frac{B_{\perp}}{R_1 \tan\theta} \Delta R_1$ represents the phase term for the “flat earth,” i.e. in the absence of any topography.

1.3.1.3.2 Surface deformation monitoring

For surface terrain deformation monitoring, the phase difference between two signals acquired at different times contains the ground motion information. After removing the topographic phase from an interferogram, the resulting differential interferogram presents the smaller motion effects. Figure 1.12 illustrates how phase - deformation relationship (deformation monitoring) can be obtained from differential interferogram.

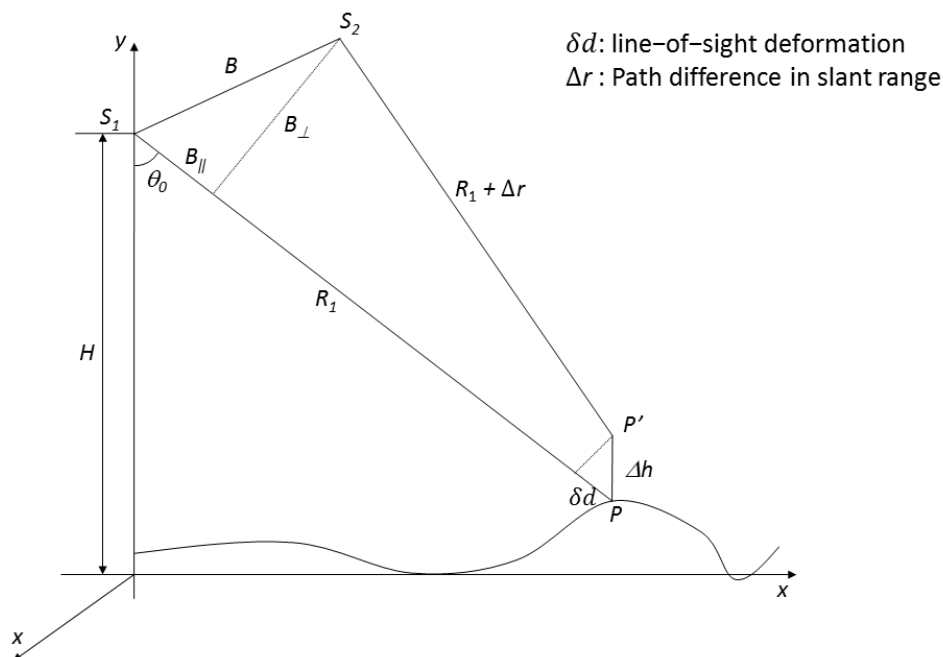


Figure 1. 12: Conceptual representation of differential InSAR system.

Phase - deformation relationship can be obtained by differential interferometry using the following steps (Figure 1.12):

Suppose that the surface deformed slightly in an amount of Δh between the first and second acquisitions in such a way that the range changed by an amount of Δr :

$$\Delta r \approx \Delta R_0 + \delta d \approx B_{\parallel} + \delta d \quad \text{Eq.9}$$

The interferometric phase between the first and second acquisition can be written as:

$$\varphi = -\frac{4\pi}{\lambda}\Delta r = -\frac{4\pi}{\lambda}(B_{\parallel} + \delta d) \quad \text{Eq.10}$$

After removing the flat earth and topographic phase component $\varphi_0 = -\frac{4\pi}{\lambda}B_{\parallel}$, the so-called differential phase φ_{def_h} is obtained in Eq.11:

$$\varphi_{\text{def}_h} = \varphi - \varphi_0 = -\frac{4\pi}{\lambda}\delta d \quad \text{Eq.11}$$

Differential InSAR has been applied to map small surface movements in the order of centimeters caused by earthquakes (Massonnet et al. 1993), volcanoes (Massonnet et al. 1995), urban deformation (Lanari et al. 2004), landslides, or glacier advancement (Mohr et al. 1998). Limitations of D-InSAR application are essentially due to noises, atmospheric effects and decorrelation. Interferometric coherence, the signal coherence between two datasets, indicates the accuracy and effectiveness of deformation monitoring. Noise, geometric baselines, temporal decorrelations, and volume decorrelations all contribute to a reduction of interferometric coherence (Moreira et al. 2013). With the increasing availability of datasets, several improvements have been introduced in the interferometric processing to overcome the limitations of decorrelation and noise contamination, e. g, small baseline subsets (SBAS) strategy (Berardino et al. 2002; Usai 2003), persistent scatterers interferometry (PSI) ((Ferretti et al. 2001)), and synergistic usage of SBAS and PS, which is Multi-temporal InSAR (MT-InSAR) (Hooper 2008). SBAS strategy takes advantage of high-quality interferograms which have small temporal and spatial baselines; persistent scatterer takes advantage of coherent radar scatterers exhibiting high phase stability over the entire observation period, MT-InSAR increases the spatial density of coherent radar scatterers in non-urban areas.

However, the degree of decorrelation could be used for change detection and land cover classification. Some land cover types keep high coherence over long time spans, such as civil construction and rock, but some land cover types are quickly decorrelated over short time spans, such as higher vegetation (Bruzzone et al. 2004; Tanase et al. 2010). The spatial variation of the degree of decorrelation allows for the identification of different land covers, as well as different forest and crop types.

1.3.2 Ground surface movement detected by D-InSAR technique

Seasonal freeze-thaw cycles in the active layer cause seasonal upward and downward ground motion due to the phase transitions of water during the freeze-thaw cycle. Disturbances caused by climate change or anthropogenic activities also introduce a long-term ground motion.

Several studies have demonstrated the capability of D-InSAR technique in detecting this freeze/thaw-related ground motion over permafrost terrain in the Arctic (Antonova et al. 2018; Liu et al. 2014a; Liu et al. 2015; Liu et al. 2014b; Liu et al. 2012; Liu et al. 2010; Rudy et al. 2018; Rykhus and Lu 2008; Short et al. 2011; Short et al. 2014), sub-Arctic (Beck et al. 2015b; Wolfe et al. 2014) and in Qinghai-Tibet Plateau (Chang and Hanssen 2015; Chen et al. 2012; Chen et al. 2013; Daout et al. 2017; Li et al. 2015; Zhao et al. 2016). The studies are listed in Table 1. 3. Generally, SAR datasets of long wavelength, e.g., of L-band ALOS PALSAR, have advantages in the tundra environment, because it keeps higher interferometric coherence due to the deeper penetration through the vegetation canopy layer.

Most of the studies listed in Table 1. 3 are conducted in the Arctic or Qinghai-Tibet Plateau, only two studies are conducted in the sub-Arctic discontinuous permafrost terrain. The discontinuous permafrost environment shares some landscape properties with Arctic continuous permafrost environments, e.g., tundra environment, but the discontinuous permafrost environment has a more heterogeneous landscape with scattered frozen ground and more developed vegetation cover (tall shrubs and coniferous stands). The unique landscape results in more complicating factors for D-InSAR applications (Wolfe et al. 2014).

Table 1. 3: Studies that employed InSAR for ground surface motion monitoring in Arctic and sub-Arctic permafrost-affected terrain.

Study area	Sensor	Method and monitoring content	Author and year
Brooks Range, Alaska Arctic	ERS -1 SAR	D-InSAR to detect winter frost heave	(Wang and Li 1999)
Alaska north slope 69°N, 150°W Arctic	JERS -1 SAR	D-InSAR to derive seasonal ground movement	(Rykhus and Lu 2008)
Alaska north slope coast 70°12'N, 148°15'W Arctic	ERS -1/2 SAR	SBAS-InSAR to derive seasonal and inter-annual movements using a conceptual deformation model which takes into account the accumulated degree days of thawing	(Liu et al. 2010)
Herschel Island, off the northern Yukon coast in the southern Beaufort Sea 69°35'N, 139°06'W Arctic	TerraSAR-X RADARSAT-2 ALOS-PALSAR	D-InSAR to derive seasonal cumulative ground movement, compare the difference of three sensors	(Short et al. 2011)

Qinghai-Tibet Plateau	ALOS-PALSAR Envisat ASAR	MT-InSAR to derive movements of the Qinghai–Tibet railway	(Chen et al. 2012)
Alaska north slope Arctic lowland coast 70°12'N, 148°15'W Arctic	ERS -1/2 SAR	SBAS-InSAR to derive seasonal and inter-annual movement using a conceptual deformation model which takes into account the accumulated degree days of thawing; Use thaw-season surface subsidence to estimate long-term average active layer thickness	(Liu et al. 2012)
Qinghai-Tibet Plateau 34°28'N, 92°61'E	ALOS PALSAR	SBAS-InSAR to derive seasonal and inter-annual ground movements	(Chen et al. 2013)
Anaktuvuk River, Alaska north slope 69.1°N, 150.8°W Arctic	ALOS PALSAR	SBAS-InSAR to derive averaged thaw-season subsidence during pre-fire years and post-fire years using a conceptual deformation model which takes into account the accumulated degree days of thawing	(Liu et al. 2014a)
Alaska north slope 70°8'20" N, 148°38'58" W Arctic	ALOS PALSAR	SBAS-InSAR to derive thaw-season subsidence over drained thermokarst lake basins (DTLBs) using a conceptual deformation model which takes into account the accumulated degree days of thawing. Use thaw-season surface subsidence in a combination of GPR-based volumetric water content to estimate long-term average active layer thickness	(Liu et al. 2014b)
Head of Frobisher Bay on the southeast Baffin Island 63°45'N and 68°33'W Arctic	RADARSAT-2	D-InSAR to derive seasonal cumulative ground movement	(Short et al. 2014)
Mouth of the Yellowknife River, on the north shore of Great Slave Lake 62°26' N, 114°24' W sub-Arctic	RADARSAT-2	D-InSAR to derive seasonal cumulative ground movement	(Wolfe et al. 2014)
Eastern shoreline of Hudson Bay in northern Quebec, Canada 56°33' N, 76°33' W sub-Arctic	TerraSAR-X	D-InSAR to derive seasonal ground movement	(Beck et al. 2015b)
Alaska north slope coast 70.082° N, 148.57° W Arctic	ALOS-PALSAR	SBAS-InSAR to derive thermokarst-induced and seasonal subsidence using a conceptual deformation model which takes into account the accumulated degree days of thawing	(Liu et al. 2015)
Qinghai-Tibet Plateau 30°18'N, 90°48'E	Envisat ASAR	SBAS-InSAR to derive seasonal and inter-annual ground movements using a sinusoidal deformation model	(Li et al. 2015)
Qinghai-Tibet Plateau	Envisat ASAR	PS-InSAR to derive movements of the Qinghai-Tibet railway	(Chang and Hanssen 2015)
Qinghai-Tibet Plateau 30° N, 91° E	Envisat ASAR	SBAS-InSAR to derive seasonal and inter-annual ground movements using an improved deformation model which takes into account the temperature and precipitation	(Zhao et al. 2016)

Qinghai-Tibet Plateau	Envisat ASAR	SBAS-InSAR to derive seasonal and inter-annual ground movements using a sinusoidal deformation model and Stefan model	(Daout et al. 2017)
Southern Melville Island 75°55' N, 109°35'W Arctic	RADARSAT-2	D-InSAR to derive seasonal cumulative ground movement	(Rudy et al. 2018)
Yedoma, Northern Siberia 72°N, 126°E Arctic	TerraSAR-X	D-InSAR to derive seasonal cumulative ground movement	(Antonova et al. 2018)

The main shortcoming of D-InSAR application in permafrost areas is the lack of coherence between scenes, due to snow accumulation, snowmelt, and changes in soil moisture, vegetation or the general heterogeneity of ground surface conditions (Liu et al. 2014a; Short et al. 2014; Wolfe et al. 2014). To date, accuracy and value assessments of D-InSAR results have focused mostly on the continuous permafrost region where the vegetation is less developed and causes fewer complicating factors for the D-InSAR application (Wolfe et al. 2014). D-InSAR applications in the lowlands of the Arctic and sub-Arctic are still not entirely operational.

1.3.3 Permafrost landscape characterization and land cover classification

Several studies have applied SAR datasets for the characterization of land cover in the Arctic and sub-Arctic environment. Table 1.4 provides an overview of the studies that use SAR data for the characterization of Arctic and sub-Arctic permafrost landscapes. All the studies listed in Table 1.4 use SAR polarimetric information for land cover classification; however, the ability to employ interferometric information for permafrost landscape mapping has not been employed.

Table 1. 4: Studies that employ spaceborne SAR data for the characterization of the Arctic and sub-Arctic permafrost (tundra) landscapes.

Study area	Sensor	Objective and method	Author and year
Richards Island, and Tuktoyaktuk Harbour, in the Mackenzie Delta coastal region, Northwest Territories, Canada southern Arctic	RADARSAT-2 polarized quad -	Land cover classification using Maximum Likelihood classifier along with polarimetric analyses, jointly use SPOT-4 optical image, assess the impact of incidence angle on class separability and classification accuracy	(Banks et al. 2014a)
Richards Island, and Tuktoyaktuk Harbour, in the Mackenzie Delta coastal region,	RADARSAT-2 polarized quad -	Assess the potential of unsupervised polarimetric SAR classifiers, analyze scattering behavior of shore and near-shore land cover types	(Banks et al. 2014b)

Northwest Territories, Canada southern Arctic			
Richards Island, and Ivvavik, Yukon Territory, Canada southern Arctic	RADARSAT-2 polarized	quad -	Land cover classification using pixel-based Maximum Likelihood classifier and hierarchical object-based classifier along with polarimetric analyses, jointly use SPOT-4 optical image and DEM (Demers et al. 2015)
Richards Island, 69°N, 133°W southern Arctic	TerraSAR-X polarized RADARSAT polarized	HH/VV - -2 quad -	Land cover classification using supervised Maximum-Likelihood classifier/unsupervised classifier along with polarimetric analyses, jointly use Landsat 8 optical image (Ullmann et al. 2014)
Coronation Gulf, Dease Strait, and Bathurst Inlet, in the Kitikmeot region of Nunavut 68°N, 110°W southern Arctic	RADARSAT polarized	-2 quad -	Land cover classification using random forest classifier along with polarimetric analyses in the Arctic marine shorelines, jointly use Landsat 5 optical image and DEM (Banks et al. 2015)
Umiujaq, eastern shoreline of Hudson Bay in northern Quebec, Canada 56.55°N, 76.55°W sub-Arctic	RADARSAT-2 polarized	quad-	Land cover classification using support vector machine (SVM) classification along with polarimetric analyses (Duguay et al. 2016)
Mackenzie Delta Region, 69°N, 134°W southern Arctic	RADARSAT-2 and TerraSAR-X HH/VV - polarized		Investigate a two component decomposition technique for HH/VV-polarized data, analyze the separability over the tundra environment (Ullmann et al. 2016)
Tuktoyaktuk Peninsula, Northwest Territories, Canada 69°32' N, 132°55' W southern Arctic	TerraSAR-X polarized RADARSAT - 2 quad - polarized ALOS PALSAR polarized ALOS PALSAR -2 quad- polarized	HH/VV - - 2 - -2 quad-	Analyze the separability of polarimetric features at each wavelength over the tundra environment (Ullmann et al. 2017)

(Widhalm et al. 2017) tested the possibility of using SAR backscatter intensity for active layer thickness estimation. The concept is to use a relationship between vegetation cover and ALT, as applied in the optical remote sensing (Gangodagamage et al. 2014; Nguyen et al. 2009). Backscatter intensity is related to vegetation coverage, due to volume scattering; an increase of ALT is associated with increasing backscatter. A range of 5 dB was observed for an ALT range of 100 cm (40–140 cm). Widhalm et al. (2017) build a linear relationship between X-band backscatter intensity and ALT and an R^2 of 0.66 is determined over the calibration sites.

1.3.4 Monitoring ice cover regimes of thermokarst ponds/lakes

In addition to surface extent monitoring of thermokarst ponds/lakes, SAR allows detecting their ice cover regimes in winter, which are related to water depths and ice thickness. Some thermokarst ponds/lakes are shallow, and ice can freeze completely to the bottom in winter; no liquid water remains when the seasonal ice thickness is at a maximum, resulting in grounded ice. Some ponds/lakes are deeper than the ice thickness, liquid water persists under the ice cover all winter, resulting in floating ice (Engram et al. 2013). In the lakes which ice is grounded in winter, the energy and gas fluxes as well as biological activity within the frozen sediments are suppressed. In the lakes having liquid water beneath the ice cover, the liquid water induces additional heat in the remaining permafrost underneath surroundings, which contributes to further intensified permafrost thawing. Therefore, distinguishing grounded ice from floating ice areas in high latitude lakes is essential for permafrost science (Arp et al. 2012).

Liquid water has a remarkably high dielectric constant, whereas pure ice has a low value. Floating pond/lake ice has high backscatter intensities because liquid water beneath the ice cover provides a high dielectric contrast, causing most of the radar signal to reflect. In contrast, in the case of grounded lake ice, the microwaves pass through the snow and lake ice, and most of the radar signal is transmitted below the lake bed, resulting in backscatter of low intensity (Engram et al. 2013). SAR datasets of different wavelengths have been applied to distinguish between these two ice-cover regimes due to the difference in the backscatter intensities. Some of the studies are listed in Table 1.5. The change of thermokarst ponds/lakes from grounded- to floating-ice regimes or vice versa, can be a result of lake drainage or lake expansion, thus indicating climate variability as well as permafrost state (Arp et al. 2012). The depth of shallow thermokarst lakes/ponds (i.e., less deep than the maximum ice thickness) can also be estimated via SAR-derived timing of ice grounding in combination with the numerical ice-growth model (Antonova et al. 2016; Hirose et al. 2008; Jeffries et al. 1996; Kozlenko and Jeffries 2000).

Table 1. 5: Studies that employ spaceborne SAR data for ice cover and bathymetric features of thermokarst ponds/lakes.

Study area	Sensor	Objective	Author and year
near Barrow, Alaska Arctic	ERS-1 SAR	Use time series of backscatter to monitor lake ice growth and decay process	(Jeffries et al. 1994)
Alaska north slope, interior of Alaska near Fort Yukon, Yukon Delta, near Bristol Bay, Tazlina Lake, Great Bear Lake Arctic and sub-Arctic	ERS-1 SAR	Use time series of backscatter to monitor lake ice growth and decay process	(Morris et al. 1995)

In the vicinity of Barrow and 100 km south of Barrow Arctic	ERS-1 SAR	Combine SAR and numerical model for lake depth determination	(Jeffries et al. 1996)
near Barrow Alaska north slope Arctic	ERS-1 SAR	Develop a semi-automated procedure for bathymetric mapping of water up to 2 m deep in thermokarst lakes. Steps are: discriminate between floating ice and grounded ice in the SAR images to define raw isobaths; assign an ice thickness or water depth to each isobath from the simulated ice-growth curve, and interpolate to create equally spaced isobaths	(Kozlenko and Jeffries 2000)
East of Churchill, Manitoba, Canada 58°45' N, 94°04' W sub-Arctic	RADARSAT-1	Monitor ice growth and decay, and related processes of shallow sub-Arctic lakes	(Duguay et al. 2002)
near Churchill, Hudson Bay Lowland, Manitoba, Canada 58°42' N, 93°52' W sub-Arctic	ERS-1 SAR	Determine lake depth and ice thickness of shallow lakes and ponds, in combination with Landsat-5 TM optical images	(Duguay and Lafleur 2003)
Mackenzie Delta, east of the Mackenzie River, north of Inuvik, and south of Tuktoyaktuk, Northwest Territories, Canada southern Arctic	RADARSAT-1	Identify the location of the grounded ice-floating ice boundary, determine the lake depth at the grounded ice-floating ice boundaries with a one-dimensional thermodynamic lake ice thickness model	(Hirose et al. 2008)
Midway between Barrow and Prudhoe Bay on the Alaska northern coastal plain Arctic	RADARSAT -1	Differentiate between grounded-ice and floating ice	(Arp et al. 2011)
near Barrow Alaska north slope coastal plain 70.1°N, 152°W Arctic	ENVISAT ASAR and airborne radar SLAR	Compare the ice-cover regime during the 2003-2011 period with the regime in 1980	(Arp et al. 2012)
Fish Creek watershed, Alaska north slope coastal plain 70°17' N, 151°24' W Arctic	TerraSAR - X	Identify and characterize floating ice and grounded ice conditions in lakes, ponds, beaded stream pools, and an alluvial river channel	(Jones et al. 2013a)
Northern Seward Peninsula, and Arctic coastal plain, Alaska	ALOS PALSAR ERS-1/2 SAR	Analyze the scattering mechanism of floating-ice-lake at L-band, compare with C-band data	(Engram et al. 2013)

Arctic			
Southern central part of the Lena River Delta, northern Siberia, Russia 72°N, 126°E Arctic	TerraSAR-X RADARSAT-2	Evaluate the performance of the unsupervised k-means classification for dividing ice and water fractions on lakes and river channels	(Sobiech and Dierking 2013)
Barrow region, Alaska north slope coastal plain 71°31' N, 156°45' W Arctic	ERS-1/2 SAR	Detect ice cover changes from 1991 to 2011. Use a time series of SAR images to determine the monthly fraction of grounded ice.	(Surdu et al. 2014)
Barrow region, Alaska north slope coastal plain 71°31' N, 156°45' W Arctic	ENVISAT ASAR Wide Swath and RADARSAT-2 ScanSAR Wide Swath	Evaluate the ability of combined ENVISAT ASAR and RADARSAT-2 observations for detecting the timing of the initial ice formation, beginning of melt and end of the ice season of shallow lakes based on the temporal evolution of backscatter intensity, assess SAR-observed lake-ice parameters against results obtained with a numerical lake-ice model	(Surdu et al. 2015)
Nunavut, Canada 70° ~ 82°30' N, 92°W Arctic	RADARSAT-1/2 ScanSAR Wide Swath, and ENVISAT ASAR Wide Swath	Detect lake ice cover changes from 1997 to 2011 in the Canadian High Arctic, in combination with Landsat optical images	(Surdu et al. 2016)
Lena River Delta, Siberia 72°25' N, 126°10' E Arctic	TerraSAR - X	use time-series backscatter intensity data to derive the timing of ice grounding of shallow thermokarst lakes (with grounded ice), retrieve their ice thicknesses (water depths) by combining the SAR-derived date of ice grounding and a numerical of lake ice growth	(Antonova et al. 2016)

1.4 Research objectives

SAR-based monitoring has become increasingly important for understanding the state and dynamics of permafrost environment at the regional scale. Currently, most of the researches regarding permafrost environment monitoring involved SAR datasets is focused on the Arctic permafrost, and less attention is paid to the sub-Arctic permafrost environment (Table 1.3, Table 1.4 and Table 1.5). The sub-Arctic environment has different landscapes and different permafrost thermal states compared to the Arctic permafrost environment. Sub-Arctic permafrost is more vulnerable to changes in climatic and environmental conditions. Thus, there is a high demand for developing SAR-based monitoring methods in the sub-Arctic permafrost environment, which is the predominant research objective of this thesis.

As mention earlier, the selected study area is placed in the Canadian Eastern Sub-Arctic, on the eastern shore of Hudson Bay in northern Quebec (Nunavik). The following research questions are to be answered through the development of monitoring methods. The environment characteristics are also waited to be revealed.

Regarding with SAR-based monitoring methods:

1) Is the D-InSAR or MT-InSAR technique able to monitor surface ground motion caused by permafrost activities in the sub-Arctic environment? What are the influencing factors limiting the application of these techniques? What are suitable datasets regarding wavelength and resolution (temporal and spatial)?

2) Are multi-temporal SAR backscatter and interferometric coherence information able to classify heterogeneous sub-Arctic permafrost environments? How can we classify heterogeneous discontinuous permafrost environments by using multi-temporal SAR images? What are the most efficient features for classification?

Regarding with sub-Arctic permafrost environment characteristics:

3) What is the distribution pattern of permafrost-caused seasonal thaw subsidence? Which area has larger seasonal thaw subsidence?

4) Liquid water beneath the floating ice cover contributes to further intensified permafrost thawing underneath. Thus one hypothesis is made that the numbers of ponds or the coverage areas of floating-ice ponds could be used to assess permafrost degradation state. In this study, the ice-cover regime characteristic in the sub-Arctic discontinuous permafrost zone is detected, and the hypothesis is tested.

1.5 Thesis outline and scientific publications

In total, this cumulative thesis encompasses four manuscripts, three of them have already been published in peer-reviewed journals, and one is under review. Each manuscript is reprinted in one single chapter. The first two papers focus on the surface ground movements monitoring, and the latter two papers focus on the permafrost landscape features mapping. Figure 1.13 illustrates the connection and contribution of each paper to this thesis as well as to the scientific areas, including 1) monitoring surface ground motion caused by permafrost activities 2) mapping landscape features in a sub-Arctic permafrost environment. The journals' impact factors and rankings are listed in Table 1.6.

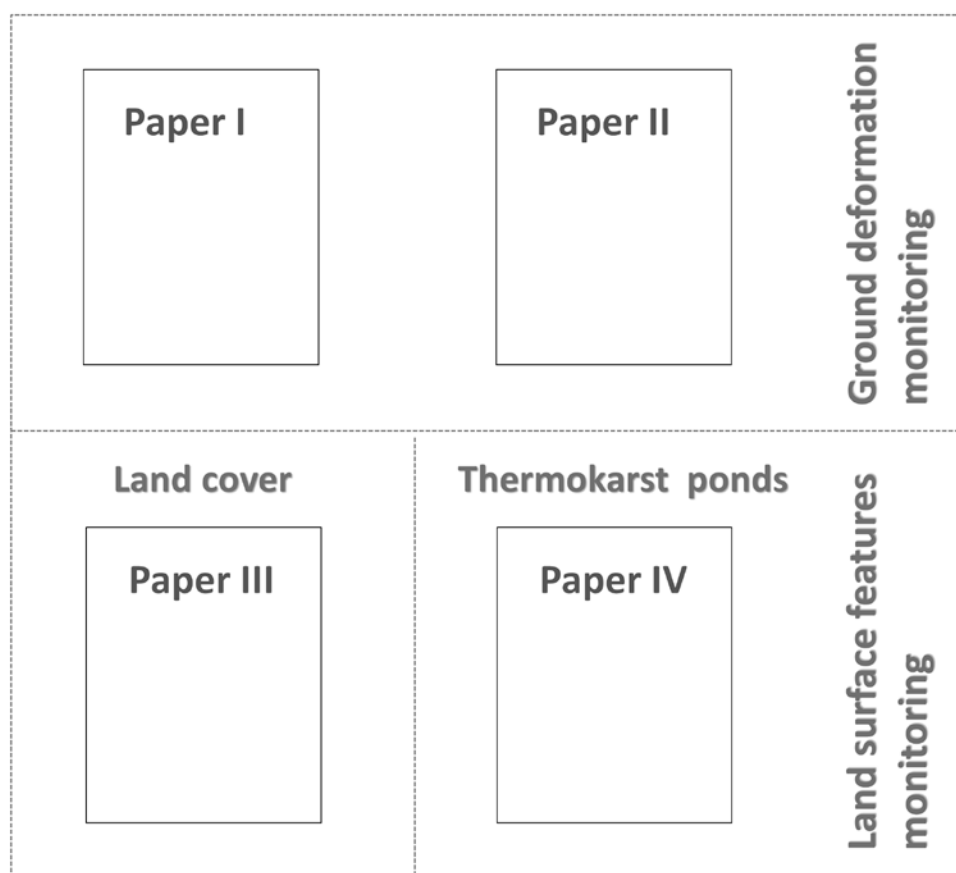


Figure 1. 13: Position of the papers, and the topics they are covering within this PhD thesis.

Paper 1: Publication in the journal *IEEE Journal of Selected Topics in Applied Earth Observations and Remote Sensing*

Wang, L., Marzahn, P., Bernier, M., Jacome, A., Poulin, J. and Ludwig, R., (2017). Comparison of TerraSAR-X and ALOS PALSAR differential interferometry with multisource DEMs for monitoring ground displacement in a discontinuous permafrost region. *IEEE Journal of Selected Topics in Applied Earth Observations and Remote Sensing*, 10 (9), pp.4074-4093.

L. Wang designed the study, conducted image and in-situ data analysis, results interpretation, as well as manuscript writing. P. Marzahn participated to the results interpretation and revised the manuscript. M. Bernier, research co-director, designed the study, defined the research plan, participated to the field campaign and the results interpretation and revised the manuscript. A. Jacome and J. Poulin organized and did the field work as well as data and results interpretation. R. Ludwig, research director, designed the study, defined the research plan, participated to the results interpretation and revised the manuscript.

Paper 2: Submitted to the journal Remote Sensing of Environment

Wang, L., Marzahn, P., Bernier, M., and Ludwig, R.. High temporal resolution deformation monitoring over discontinuous permafrost terrain using Sentinel-1 time series. *Remote Sensing of Environment*, under review.

L. Wang designed the study, conducted for image analysis, results interpretation, as well as manuscript writing. P. Marzahn, participated to the results interpretation. M. Bernier, research co-director, designed the study, defined the research plan, participated to the field campaign and the results interpretation and revised the manuscript. R. Ludwig, research director, designed the study, defined the research plan, participated to the results interpretation and revised the manuscript.

Paper 3: Publication in the journal ISPRS Journal of Photogrammetry and Remote Sensing

Wang, L., Marzahn, P., Bernier, M. and Ludwig, R., 2018. Mapping permafrost landscape features using object-based image classification of multi-temporal SAR images. *ISPRS Journal of Photogrammetry and Remote Sensing*, 141, pp.10-29.

L. Wang designed the study, conducted ground measurements, image analysis, results interpretation, as well as manuscript writing. P. Marzahn participated to the results interpretation and revised the manuscript. M. Bernier, research co-director, designed the study, defined the research plan, participated to the field campaigns and the results interpretation and revised the manuscript. R. Ludwig, research director, designed the study, defined the research plan, participated to the results interpretation and revised the manuscript.

Paper 4: Publication in the journal Permafrost and Periglacial Processes

Wang, L., Jolivel, M., Marzahn, P., Bernier, M. and Ludwig, R., 2018. Thermokarst pond dynamics in subarctic environment monitoring with radar remote sensing. *Permafrost and Periglacial Processes*, 1-15. DOI: 10.1002/ppp.1986

L. Wang designed the study, conducted image analysis, results interpretation, as well as manuscript writing. M. Jolivel conducted ground measurements and data analysis, participated to the results interpretation and revised the manuscript. P. Marzahn participated to the results interpretation. M. Bernier, research co-director, designed the study, defined the research plan, participated to the field campaigns and the results interpretation and revised the manuscript. R. Ludwig, research director, designed the study, defined the research plan, participated to the results interpretation and revised the manuscript.

Table 1. 6: Overview of journals in which the papers of this thesis are published or are submitted to (2017 Journal Citation Reports (ClarivateAnalytics 2018)).

	IEEE Journal of Selected Topics in Applied Earth Observations and Remote Sensing	Remote Sensing of Environment	ISPRS Journal of Photogrammetry and Remote Sensing	Permafrost and Periglacial Processes
Impact Factor 2017	2.777	6.457	5.994	3.529
5-year Impact Factor	3.156	7.737	6.592	3.426
Journal ranking in the category	Remote Sensing 12/30 Imaging science & Photographic technology 8/27 Geography, physical 18/49 Engineering, electrical & electronic 78/260	Environmental sciences 12/241 Remote Sensing 1/30 Imaging science & Photographic technology 1/27	Remote Sensing 2/30 Imaging science & Photographic technology 3/27 Geography, physical 1/49 Geosciences, multidisciplinary 5/189	Geography, physical 11/49 Geology 5/47
Status	published	under review	published	published

Paper I evaluates the influencing factors and application conditions for D-InSAR in the discontinuous permafrost environment. Analysis of DEM influences and temporal decorrelation are based on a large number of interferograms generated from two radar systems: X-band TerraSAR-X and L-band ALOS PALSAR. The displacement velocities of the two sensors are compared with the referencing in situ measurements. It is demonstrated that L-band has strong advantages over the X-band in monitoring displacements in discontinuous permafrost environments. The ALOS PALSAR results capture the permafrost-induced terrain movement in the correct range; whereas TerraSAR-X results largely underestimate the deformation values. The X-band differential phase links to the canopy rather than the topography in tundra environment, and temporal decorrelation over more than 22 days is very strong in more developed vegetation (such as shrubs and spruce).

Paper II is built on Paper I and is an extension of Paper I's work. The recent launch of C-band Sentinel-1A/B has a shorter revisit time (6 days combining Sentinel-1A and 1B). The study explores the potential improvements in permafrost monitoring using this high temporal resolution C-band dataset. It implements SBAS-InSAR method with Sentinel-1 time series to calculate the deformation time series in a permafrost environment for the first time. Based on the derived displacement time series, two different thaw subsidence patterns are observed over the wet terrain (covered by herbaceous vegetation) and the dry terrain (covered by lichen and prostrate shrubs). The wet region has larger thaw

subsidence and reaches the maximum subsidence in October before the ground freezes; the drier region has a smaller thaw subsidence and reaches maximum subsidence in August when the surface air temperature reaches its maximum. This phenomenon is suspected to be related with the transient zone at the bottom of the active layer and above the permafrost table. There is normally abundant of ice in the transient zone; an increase in the energy budget is required to thaw such amounts of ice, which may explain why there is no distinctive subsidence between August and the beginning of October over the lichen-dominated terrain. The study demonstrated the ability of C-band Sentinel-1 A/B with shorter revisit time (6 days combining Sentinel-1A and 1B) in monitoring deformation over sub-Arctic tundra plain, also discussed the application limitations over developed shrub-tundra and forest tundra environment.

Paper III presents a permafrost landscape mapping method which uses multi-temporal SAR images. It is the first time that temporal backscatter intensity and interferometric coherence information are both employed for land cover classification in a permafrost environment. Through the combined use of object-based image analysis (OBIA) and classification and regression tree analysis (CART), a land cover map is generated. The permafrost-affected areas can be inferred from the relationship between vegetation cover and the existence of permafrost, and thermokarst ponds distributions are directly inherited from the land cover map.

During the classification procedure, to reduce the noise in the classification results brought by the speckle noise within the radar imagery, the spatial-temporal filtering of time-series images is firstly applied, then, the segmentation was implemented on the stacked mean backscatter intensity image. A regression tree analysis (CART) is applied to find the most effective variables for classification among lots of candidates derived from multi-temporal backscatter intensity and coherence analysis. Such a processing and classification strategy with multi-temporal SAR images could be transferred to other heterogeneous environments and other SAR datasets.

Paper IV studies the development process of thermokarst ponds. SAR backscatter images acquired during winter are used to map ice-cover regimes of thermokarst ponds. Liquid water beneath floating-ice cover induces additional heat in the remaining permafrost underneath surroundings, which contributes to further intensified permafrost thawing. Thus it is hypothesized that the coverage of floating-ice ponds among all the thermokarst ponds could be used to assess permafrost degradation state. The study tested the hypothesis by correlating the mapped ice-cover regimes with the permafrost degradation states and thermokarst pond development in two historical phases (Sheldrake catchment in the year 1957 and 2009, Tasiapik Valley 1994 and 2010). Results indicate that the ice-cover regime of thermokarst pond is controlled by the combined effects of soil texture, permafrost degradation stage and permafrost depth. It is difficult to assess permafrost degradation directly from the numbers and coverage areas of floating-ice ponds as percentages of all thermokarst ponds in a single year.

2 Comparison of TerraSAR-X and ALOS PALSAR Differential Interferometry with Multi-Source DEMs for Monitoring Ground Displacement in a Discontinuous Permafrost Region

Comparison of TerraSAR-X and ALOS PALSAR Differential Interferometry With Multisource DEMs for Monitoring Ground Displacement in a Discontinuous Permafrost Region

Lingxiao Wang, Philip Marzahn, *Member, IEEE*, Monique Bernier, *Senior Member, IEEE*, Andres Jacome, Jimmy Poulin, and Ralf Ludwig

Abstract—Differential synthetic aperture radar interferometry (DInSAR) has shown its capability in monitoring ground displacement caused by the freeze-thaw cycle in the active layer of permafrost regions. However, the unique landscape in the discontinuous permafrost zone increases the difficulty of applying DInSAR to detect ground displacements. In this study, datasets from two radar systems, X-band TerraSAR-X and L-band ALOS PALSAR, were used to evaluate the influencing factors and application conditions for DInSAR in the discontinuous permafrost environment based on a large number of analyzed interferograms. Furthermore, the impact of different DEMs on the application of DInSAR was illustrated by comparing the high-resolution LiDAR-DEM, TanDEM-X DEM, and SRTM DEM. The results demonstrate that temporal decorrelation and strong volume decorrelation in areas with developed vegetation highly constrains the application of X-band data. In terrain with more developed vegetation (such as shrubs and spruce), the X-band differential phase becomes linked to the canopy rather than the topography, whereas L-band data show promising results in retrieving topography-related displacement. By comparing the displacement velocity maps of the two sensors and referencing *in situ* measurements, we demonstrated that the ALOS PALSAR results capture the permafrost-induced terrain movement characteristics and values in the correct range. Moreover, the influence of soil moisture and vegetation phenology on the accuracy of displacement retrievals using the L-band data are illustrated and discussed. The analyses confirm that the L-band has strong advantages over the X-band in monitoring displacements in discontinuous permafrost environments.

Index Terms—ALOS PALSAR, coherence, decorrelation, discontinuous permafrost, ground movement, interferometric SAR (InSAR), northern Québec, TanDEM-X DEM, TerraSAR-X.

I. INTRODUCTION

PERMAFROST is defined as all ground types, including soil, rock, ice, and organic material, that remains at or below 0 °C for two or more consecutive years [1]. It is overlain by an active layer that undergoes seasonal freezing and thawing [2]. Permafrost represents one of the main components of the cryosphere in northern regions and has an influence on hydrological processes, energy exchanges, natural hazards, and carbon budgets. Under climate warming, permafrost degradation, which is a decrease in the thickness and/or areal extent of permafrost, is inevitable [3]. In recent years, widespread permafrost degradation has been reported in North America, Russia, Northern Europe, and the Tibetan Plateau [3], [4], and the rate of degradation is notably high in the discontinuous permafrost zone [5], [6]. In the discontinuous permafrost zone, degradation accelerates thermokarst processes, which results in significant landscape changes. In the continuous zone, the change occurs through active layer thickening and more frequent slope processes [7], and these changes significantly alter vegetation, water bodies, and soil drainage. Permafrost degradation has an adverse effect on traditionally available resources for northern residents [7], and it has become problematic for the integrity of certain transportation infrastructures.

Differential synthetic aperture radar interferometry (DInSAR) has been used for large-coverage surface deformation monitoring [8]–[12]. The approach is based on the measurements of the phase difference between two SAR observations in a given time interval. The phase difference primarily covers ground displacement and other distortion phase terms [13]–[17]. With the increasing availability of radar data, advanced time-series InSAR techniques, such as permanent/persistent scatterer interferometry (PSI) and small baseline subsets (SBAS) have been developed from analyzing a series of SAR images. These techniques are used to reduce the influence of factors other than the target movement and analyze the evolution of monitored deformations [13]–[17].

Manuscript received November 12, 2016; revised March 23, 2017; accepted May 9, 2017. This work was supported in part by grants and contributions from the Bavarian Research Alliance (BayFOR), in part by the Canadian Space Agency (CSA, grant number: 14SUSMAPIN), in part by the Helmholtz Research School of Mechanisms and Interactions of Climate Change in Mountain Regions (MICMoR), and in part by the Centre d'Études Nordiques (CEN). (Corresponding author: Lingxiao Wang.)

L. Wang, P. Marzahn, and R. Ludwig are with the Department of Geography, Ludwig-Maximilians-Universität München, Munich 80333, Germany (e-mail: l.wang@iggf.geo.uni-muenchen.de; p.marzahn@iggf.geo.uni-muenchen.de; r.ludwig@lmu.de).

M. Bernier and J. Poulin are with the Centre Eau, Terre & Environment, Institut National de la Recherche Scientifique, QC G1K 9A9, Canada (e-mail: Monique.Bernier@ete.inrs.ca; Jimmy.Poulin@ete.inrs.ca).

A. Jacome is with the Financière Agricole du Québec-Development International, Saint-Romuald (Québec) G6W 8K7, Canada (e-mail: Andres.Jacome@fadq.qc.ca).

Color versions of one or more of the figures in this paper are available online at <http://ieeexplore.ieee.org>.

Digital Object Identifier 10.1109/JSTARS.2017.2707337

The freeze-thaw cycle in the active layer (or the phase transition of the ice-water cycle) results in ground surface movement. The persistent thawing of permafrost (permafrost degradation) can lead to ground subsidence and active-layer detachment slide [3], [18], [19]. Ground displacement creates a window through which the inner thermal states of permafrost can be explored because the displacement is generally determined by two factors: the freeze/thaw depth and the water/ice content at the corresponding depth.

The DInSAR and advanced time-series InSAR methods have been tested recently for monitoring permafrost thaw subsidence and frost heave [18], [20]–[26]. One of the main limitations of DInSAR applications is the signal loss caused by insufficient interferometric coherence, which describes the degree of correlation between two SAR observations [17]. This feature indicates the quality of the DInSAR results. The loss of phase coherence can be explained by a number of reasons, including thermal noise from the antenna, large interferometric baseline, topographic effects, and misregistration between SAR images, and atmospheric effects; however, it can also be caused by land surface changes that occur between two SAR acquisitions [27]. Permafrost regions are usually difficult to access because of their remoteness and harsh environmental conditions; therefore, the availability of ground-truth data for these regions is limited. Although quantitatively validating DInSAR displacements over permafrost is difficult, several efforts have been reported. Short *et al.* first used *in situ* thaw tubes [21], [28], [29] to obtain ground observation data to evaluate RADARSAT-2 DInSAR products at the Iqaluit Airport, Baffin Island, Canada [21]. The thaw/frost tube is a classical method used to record thaw settlements and frost heave in permafrost areas. In this method, a tube is anchored vertically in permafrost, a metal grill is placed on the ground surface, and a scribe scratches the tube when it moves with the upward and downward movement of the metal grill [21], [28], [29]. In the work undertaken by Short *et al.*, DInSAR-derived seasonal ground displacement patterns aligned well with *in situ* measurements. In dry areas, the data showed subcentimeter consistency. However, in low-lying wet areas, the DInSAR stack significantly underestimated the true thawing settlement because the combination of high phase gradients and poor coherence over intermittently flooded surfaces increases the difficulty of preserving reliable phase measurements [21]. Subject to saturation and flooding, changes in soil moisture between two radar acquisitions can also influence DInSAR displacements [10], [30].

Almost all DInSAR applications in permafrost environments have been limited to the continuous permafrost zone except for the studies by Beck *et al.* [31] and Wolfe *et al.* [32]. Compared with the continuous permafrost zone, the discontinuous permafrost zone is characterized by a heterogeneous landscape, numerous scattered frozen ground types accompanied by thermokarst ponds caused by thawing, a deeper active layer, and more developed vegetation cover (tall shrubs and coniferous stands) [32]. All of these elements increase the difficulty of preserving reliable phase measurements because they strongly decorrelate the stability of the phase signal. Tall shrubs grow in the gullies between frozen grounds. The disconnection of coher-

ent frozen grounds, i.e., the scattered permafrost pattern, is more likely to introduce errors in the unwrapped interferogram in the form of 2π jumps [33]. Beck *et al.* [31] tested TerraSAR-X data on three frost mounds near the village of Umiujaq (northern Quebec) and revealed that notably low coherence limited the ability of InSAR to quantify the vertical motion of these mounds. Wolfe *et al.* [32] showed that C-band RADARSAT-2 DInSAR data stack can yield patterns of seasonal displacement, but areas of forest and shrub in discontinuous permafrost regions can cause incoherence or higher errors.

Although these tests have already been conducted in the discontinuous permafrost zone, information remains scarce on the DInSAR application conditions and constraint factors in the discontinuous permafrost environment. In this study, we tested two datasets from two radar systems: X-band TerraSAR-X data and L-band ALOS PALSAR data. The interferogram quality, influencing factors, and application conditions were compared and established by testing a large number of interferogram pairs.

The new TanDEM-X DEM produced by DLR (German Aerospace Centre) is expected to produce pole-to-pole coverage with unprecedented accuracy and should eventually replace the SRTM DEM for large-scale applications [34]. We also evaluated the capability of improvements that this new application brings to the DInSAR results compared with the SRTM DEM for topographic phase removal in the DInSAR procedure and geocoding of InSAR products.

II. STUDY AREA

The study area is located in a typical discontinuous permafrost region in northern Quebec, Canada, near the Inuit village of Umiujaq (56°32' N, 76°31' W) at the eastern shore of the Hudson Bay (see Fig. 1). This region is situated in the transitional area from the isolated and sporadic permafrost zone (2–50% area cover) to the widespread discontinuous permafrost zone (50–90%) [35]. Under a warming climate, the region transitions from a widespread discontinuous permafrost zone to an isolated and sporadic permafrost zone, and this transition is currently in progress. The test site was selected because of its susceptibility to climate change and long research history.

The climate is subarctic, with a mean annual air temperature near -3 °C, and the area experiences cold winters (-24 °C in January) and cool summers (10 °C in August) [36]. However, the region is currently experiencing climate warming as confirmed by a meteorological station located 150 km south of the study area (Kuujuuarapik 55° 17' N, 77° 45' W). This station has recorded a significant rise in air temperatures since 1990, with mean annual air temperatures (MAATs) increasing from -4 to -2 °C over the past two decades. The same trend was also recorded at a station located 200 km north of the study area (Inukjuak 58° 28' N, 78° 05' W), where the MAAT also rose by 2 ° over the past two decades. Fig. 2 reveals the trend for the two meteorological stations. Soil temperature data from boreholes into the volcanic rock in the study area also showed a strong ground temperature rise. At a depth of 20 m, the ground temperature increased from -2.5 °C in 1998 to 0.5 °C in 2013 [37].

The landscape in the study area is heterogeneous. A mosaic of rock outcrops, lichen tundra patches, shrub thickets, forest

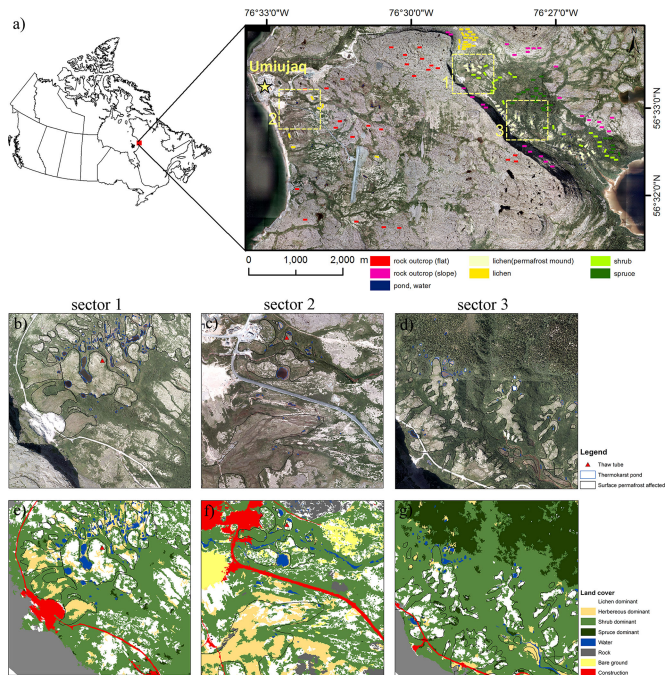


Fig. 1. Study area. (a) Map and location of study area. Sectors and ROIs used in the analyses are indicated in the right figure. The base map shows a 15-cm resolution aerial photograph taken in summer 2010. (b)–(d) Views for the three selected sectors. Permafrost-affected regions and thermokarst ponds are outlined in black and blue, respectively, and thaw tube locations are marked with red triangles. (e)–(g) Corresponding land-cover maps interpreted from aerial photographs.

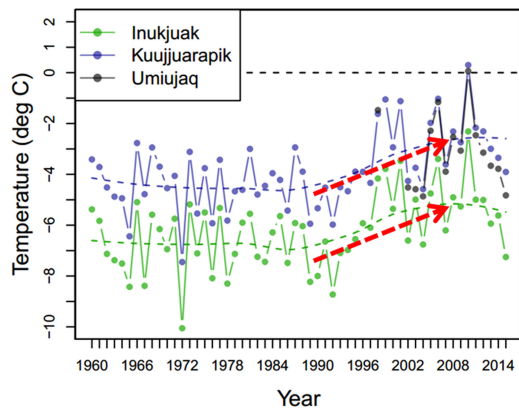


Fig. 2. Mean annual air temperatures in two stations.

stands, and thermokarst ponds is spread over a small region [38]. Lithalsas [39], mineral permafrost mounds with an ice-rich core, constitute the dominant component of the periglacial landscape in the study area. The top of these periglacial features stands a few meters (generally 3–5 m) above the surrounding ground due to frost heaving, which is caused by the formation of segregated ice fed by cryosuction in frost-susceptible fine-grained soils [40]. The permafrost thickness in the frozen mounds and plateaus typically varies from 10 to 15 m [41]. The active layer is approximately 1.5 m to 3 m thick in the study area, and it is currently thickening [6], [39], [42]. For simplicity, lithalsas, permafrost plateaus (elongated and wide mineral permafrost landforms), peat-covered permafrost mounds, and frozen spurs

(spurs that were in place before the inception of permafrost) are considered permafrost mounds in this study.

Lichen is the dominant vegetation cover on such permafrost mounds, and dense shrubs or spruce colonize the areas between and on the edge of these mounds. Tall shrubs and spruce are usually linked to a notably deep permafrost table. Permafrost degradation accompanies natural environmental changes. The major trends are shrubification, an increase in tall vegetation (spruce and tall shrubs) at the expense of low vegetation (lichens, prostrate shrubs, herbaceous vegetation), and the appearance of new thermokarst ponds and the shrinkage of older ponds [43], [44].

Based on the features of the permafrost landscape in the study area, three test sectors and regions of interest (ROIs) were selected and analyzed to determine the differences between the DEM and the variations in displacement retrieved from the X-band and L-band SAR data. Sectors 1 and 3 are located in the Tasiapik Valley, and sector 2 is situated near Umiujaq. *In situ* ground displacements are available from two thaw tubes located inside sector 1 and sector 2 (see Fig. 1). The following seven categories of ROIs represent the different topographic regimes and land-cover types that were chosen and applied in the comparison analysis:

- 1) rock outcrop on flat terrain;
- 2) rock outcrop on slope terrain;
- 3) lichen with scattered short shrubs (~20 cm);
- 4) lichen-dominant surface permafrost-affected terrain (permafrost mound) with scattered short shrubs (~20 cm);
- 5) shrub-dominant terrain (>50 cm);
- 6) spruce-dominant terrain; and
- 7) thermokarst ponds.

The distributions are shown in Fig. 1(a). For each category, 25 same-sized polygons (92 m long and 41 m wide) were delineated.

III. DATASETS AND METHOD

A. SAR Data

Two different SAR sensors were used to monitor the permafrost-induced ground movements: TerraSAR-X (X-band SAR with a 3.1 cm wavelength) and ALOS PALSAR (L-band SAR with a 23.62 cm wavelength). The characteristics of the two SAR systems and the acquisition dates are summarized in Table I. The orbits are nearly identical for the two datasets (see Table I), and only slight differences occur between the incidence angles from the two sensors. Copolarization offers higher coherence for ground surface measurements than cross polarization [45], [46]; thus, we adapted VV polarization for TerraSAR-X and HH polarization for ALOS PALSAR data to retrieve the displacements. Before comparing the TerraSAR-X and ALOS PALSAR results directly, outputs of TerraSAR-X HH polarization and large multi-look factors were analyzed.

In winter, freeze and thaw cycles at the soil surface as well as the accumulation and melting of snow cover greatly decrease the coherence of interferograms and increase the difficulty of image coregistration and phase unwrapping [18], [23], [46]. Thus, winter images were excluded. Climate data indicate that the average air temperatures are above the freezing point from

TABLE I
CHARACTERISTICS OF THE SENSORS AND ACQUISITION DATE FOR THE TWO DATASETS

Year	TerraSAR-X	ALOS PALSAR	
Launch Termination	2007-06 to	2006-01 to 2011-04	
Revisit Time	11 days	46 days	
Frequency (GHz)	9.65	1.27	
Wavelength (cm)	3.1	23.62	
Mode	StripMap	Fine Beam Dual Mode	
Pass	Ascending/right, Orbit 165	Ascending/right, Orbit 127	Ascending/right, Orbit 128
Heading	349.81°	349.28°	349.87°
Incidence Angle	40.69°	38.74°	38.75°
Acquired Time	22:47 UTC, 18:47 Local time	03:16 UTC, 23:19 Local time	03:19 UTC, 23:19 Local time
Data Level	L1B	L1.5	L1.5
Pixel spacing	Range: 0.91 m; Azimuth: 2.44 m	Range: 9.37 m; Azimuth: 3.14 m	Range: 9.37 m; Azimuth: 3.13 m
Acquisition Date	2009-08-03, 2009-08-14, 2009-08-25, 2009-09-27, 2009-10-08, 2009-10-19, 2010-08-01, 2010-08-12, 2010-08-23, 2010-10-28	2007-07-08, 2007-08-23, 2008-08-25, 2008-10-10, 2009-07-13, 2010-05-31, 2010-07-16, 2010-08-31, 2010-10-16	2007-06-09, 2007-07-25, 2009-06-14, 2009-07-30, 2010-06-17, 2010-08-02, 2010-09-17, 2010-11-02
Polarization	VV HH (three acquisitions on dates of 2010-08-01, 2010-08-12, 2010-08-23) VV VH (other acquisitions)	HH HV (all acquisitions)	HH HV (all acquisitions)

May to October [37]; thus, only scenes acquired in this period were processed.

B. Elevation Data

To identify the displacement component, the topographic phase must be removed from differential interferometry. In this study, the topographic phase was simulated from the external DEM. Although it was assumed that a high-precision DEM should greatly improve the final products, the effectiveness needs to be evaluated by experimental analyses. In this paper, three DEM products with different resolutions and precisions were compared: LiDAR-based DEM, TanDEM-X-based DEM, and C-band SRTM DEM with 1 arc-s resolution.

The C-band SRTM DEM was developed based on the 2000 shuttle radar topography mission from C-band interferometric radar data. Interferometric SAR (InSAR) data were acquired from 2000-02-11 to 2000-02-22 by radar systems mounted on the space shuttle [47]. The coverage of this SRTM DEM is principally limited to a latitude range of 56° S to 60° N because of the inclined orbit of the space shuttle and its mapping geometry. The product has a 16 m (90% linear error) absolute vertical height accuracy and a 20 m (90% circular error) absolute horizontal accuracy [48], [49]. The elevation step is 1 m. Because of the nature of the interferometric height response, the SRTM dataset represents the scattering phase center height [50]. The heights include vegetation canopy heights; thus, the DEM is not a “bare-earth” digital terrain model (DTM) [34]. In areas where extensive tree and/or shrub cover is present (e.g., boreal and Amazon regions), a significant positive bias in the data is observed [51], [52]. It has also been found that the slope is positively correlated with a positive bias [52].

The X-band TanDEM-X-based DEM was also developed based on interferometric radar data [53], [54]. The entire land-mass of Earth will be covered in this mission. Similar to a SRTM, TanDEM-X measures the height to the top of the canopy; thus, it is a digital surface model (DSM) from which vegetation heights

must be removed to create a DTM [34]. In this paper, we use the WorldDEMcore product, which is an unedited version of the DSM distributed by Airbus DS. The influence of vegetation and man-made objects was not removed [53], [54]. The grid spacing of the WorldDEMcore product is 0.4 arc-s in latitude, which equals approximately 12 m [53]. In longitude, the pixel spacing depends on the latitude [53], and it is 0.6 arc-s in our study area. The absolute vertical accuracy is less than 4 m (90% linear error), and the absolute horizontal accuracy is less than 6 m (90% circular error). The elevation step is 0.000001 m.

The local LiDAR-based bare-earth elevation model delivers detailed terrain elevation. In certain locations, data gaps are filled with CanVec digital cartographic reference product [55]. The LiDAR DEM is created at a 1 m resolution with an elevation step of 0.000001 m.

For the elevation height comparison analysis, three DEMs were projected to the same projection (Datum: WGS_1984, Project: UTM, zone 18). The grid spacing was 30 m for the SRTM DEM, 15 m for the TanDEM-X DEM, and 1 m for the LiDAR DEM. The C-band SRTM was obtained more than 10 years before the generation of the LiDAR DEM and X-band DEM; thus, vegetation has grown and the water level of thermokarst ponds has changed since it was obtained [43], [44]. We did not use the X-band SRTM DEM because it was not available for our study area. X-band SRTM DEM is discontinuous and only supplies partial (40%) coverage of the targeted area between 60° north and 57° south latitude [51]. Toward the lower latitudes, the availability of the X-band SRTM DEM is expected to increase [47].

Fig. 3 shows the general topography of the study area and tiles of the three DEMs for the three sectors. As expected, the three DEMs have a similar elevation, although an obvious difference is the degree to which the topographic features can be depicted, which is primarily determined by the grid spacing. The LiDAR DEM and TanDEM-X DEM allow for a more detailed description of topographic features. For example, the black ellipses

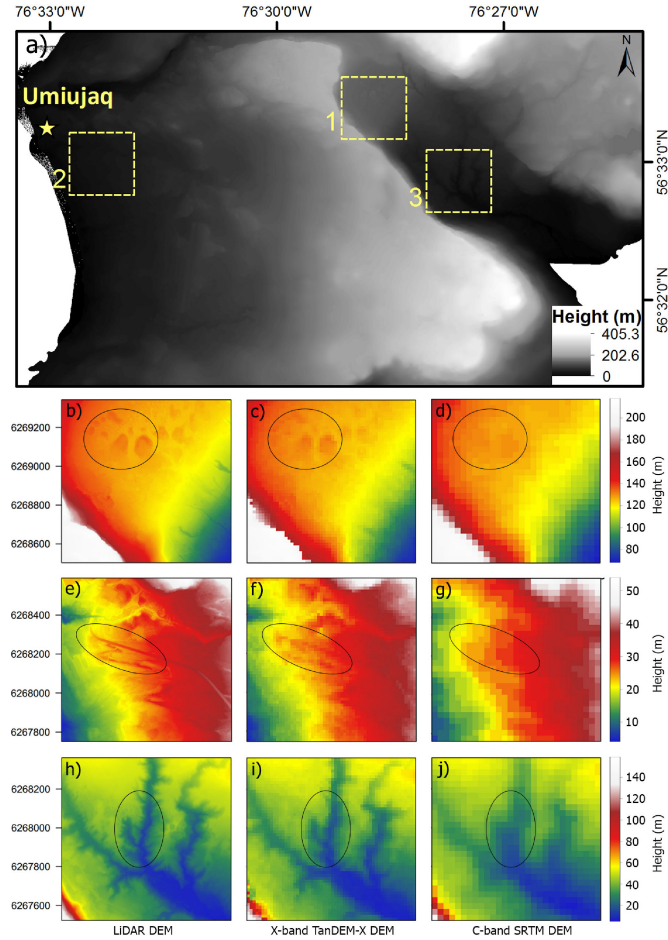


Fig. 3. Topography and DEM tile comparison. (a) Topography in the study area shown by the LiDAR DEM (1 m \times 1 m grid). (b)–(d) Topography features at sector 1 by the LiDAR DEM, TanDEM-X DEM, and SRTM DEM. The label in the last line marks the DEM source for each column. (e)–(g) Topography features at sector 2 by the LiDAR DEM, TanDEM-X DEM, and SRTM DEM. (h)–(j) Topography features at sector 3 by the LiDAR DEM, TanDEM-X DEM, and SRTM DEM.

outlined in Fig. 3 show that the geomorphology of permafrost mounds in sector 1, the road and micro-relief in sector 2, and the elevated valleys in sector 3 are clearly visible in the LiDAR DEM, detectable in the TanDEM-X DEM but far less detectable in the SRTM DEM.

To compare the similarities and differences of the three different DEMs, the TanDEM-X DEM was selected as the reference DEM and the differences between this DEM and the C-band SRTM DEM and LiDAR DEM were subsequently assessed. In addition, two statistics were calculated (see Fig. 4). First, all DEMs were projected and resampled to the coordinate system “WGS_1984_UTM_Zone_18N” with a 1 m resolution and then the DEM height were compared directly on each pixel of the delineated ROIs (see Fig. 1). The results are shown in Fig. 4(a). Second, to avoid errors introduced during the reprojection and resampling process for such heterogeneous topography, statistics are calculated on the DEMs in their original states with the geographic coordinate system. On each rectangular ROI record, the averaged DEM values are first calculated for each DEM and

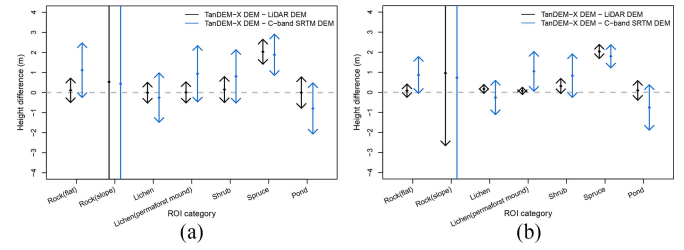


Fig. 4. Height difference among the three DEMs over different land covers. The mean ± 1 standard deviation is shown by the solid circles and arrows. (a) Pixel-based statistics (b) ROI record-based statistics

the subsequent comparison is based on the mean values of the ROI records. The results are shown in Fig. 4(b).

In general, two statistics capture similar features. The difference between the TanDEM-X DEM and LiDAR DEM is much smaller than the difference between the TanDEM-X DEM and C-band SRTM DEM. For the latter, the difference value is farther from 0 and shows a larger standard deviation.

In the category of rock (flat), a systematic offset appears between the TanDEM-X DEM and C-band SRTM DEM, with the C-band SRTM DEM 1 m lower than the TanDEM-X DEM and LiDAR DEM.

Elevation differences vary with vegetation cover category due to variations in penetration depth of the different sensors. For the most developed and tallest vegetation category (spruce), the TanDEM-X DEM is 2.0 m higher than the LiDAR DEM and 1.8 m higher than the C-band SRTM DEM if their systematic offset is not considered (0.8 m higher when the systematic offset is subtracted). For the other three vegetation categories (lichen, lichen over permafrost mound, and shrubs), the TanDEM-X DEM and LiDAR DEM do not show distinct differences, although statistics based on averaged ROI values suggest that the TanDEM-X DEM is 0.3 m higher than the LiDAR DEM. In the category of shrub and lichen over permafrost mounds, the TanDEM-X DEM and C-band SRTM DEM behave similarly, and for the differences found in the lichen category, the TanDEM-X DEM is 0.3 m lower than the C-band SRTM DEM (1.3 m when the systematic offset is considered). Obtaining elevation difference information between the InSAR-sensed DEM and the “bare-earth” DTM can be valuable for estimating the vegetation canopy height [50], [52].

For the pond/water category, the SRTM DEM has the highest elevation, which is primarily because the thermokarst ponds are too small to be depicted by the rough resolution of SRTM DEM data.

C. Processing of SAR Data

SAR image processing was conducted using GAMMA software [33], [56], [57]. The DInSAR processing workflow is shown in Fig. 5. Two-pass differential interferometry with phase unwrapping of the complex differential interferogram was adopted because the resulting differential interferogram is more robust [56]. In rugged terrain, the unwrapping of the differential phase (after subtracting the topographic phase) might be a much easier task than directly unwrapping the phase, which considers both the topographic and displacement phase terms [56].

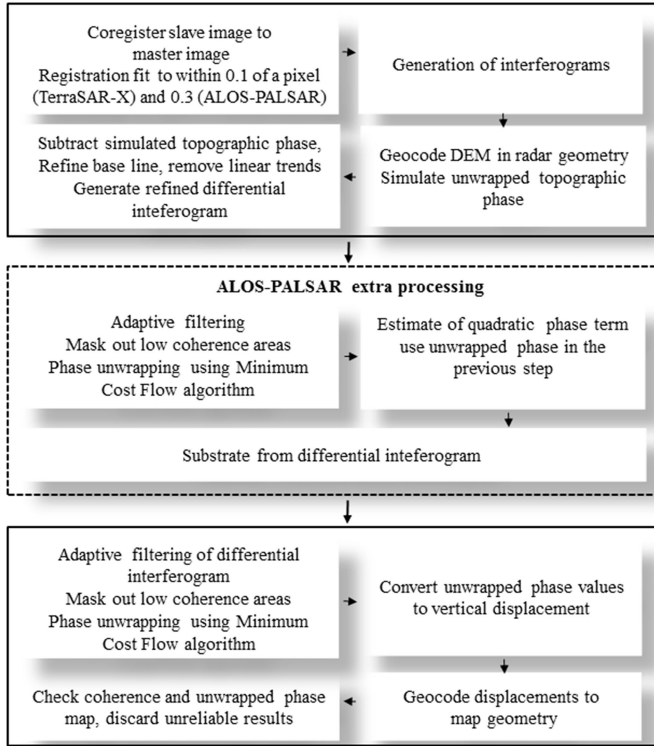


Fig. 5. DInSAR processing workflow.

Multilooking was applied when forming an interferogram. We used multilook factors (range \times azimuth) that allow for the retrieval of an image with roughly square pixels. For TerraSAR-X, three multilook factors were tested: $2 \text{ (range)} \times 1 \text{ (azimuth)}$ geocoded to a 3 m resolution, 4×2 geocoded to a 5 m resolution, and 11×6 geocoded to a 15 m resolution. For the ALOS PALSAR data, only a small multilook factor of 1×5 is applied because of the coarse resolution, and the final displacement output is geocoded to a map with a 15 m resolution. To mitigate the phase noise and facilitate phase unwrapping, both X-band and L-band interferograms were filtered using an adaptive filter [58] with a 32×32 window prior to phase unwrapping. The filtering program applies a nonlinear filter based on the power spectrum to the data. For phase unwrapping, an estimate of the local fringe quality after filtering is used. Because the degree of the filtering varies over the image, the filtering program also estimates the local phase standard deviation after filtering and converts this information into an effective correlation [57]. We used this effective correlation to create an unwrapping validity mask as a guide for the unwrapping process. Pixels with an effective correlation below 0.3 were not considered in the phase unwrapping. The phase unwrapping of differential interferograms was performed using the minimum cost flow-phase unwrapping algorithm [59], [60] because it optimizes the unwrapping of disconnected coherence areas [60] and delivers the most reasonable results among all the methods provided in GAMMA Software [46].

A point on the outcropping metamorphic bedrock assumed to be stable was selected as a phase reference point (set phase to 0), and all phase unwrapping started from this point. After

the unwrapping process, we also examined the displacement on the metamorphic bedrock, subtracted the offset from the entire displacement map.

The wrapped phase of a differential interferogram can be written as follows:

$$\psi = W\{\Delta\varphi_{\text{topo}} + \varphi_{\text{disp}} + \varphi_{\text{atm}} + \varphi_n\} \quad (1)$$

where $\Delta\varphi_{\text{topo}}$ represents the residual topographic component after removing the topographic phase. Orbit inaccuracies and DEM errors lead to incorrect topographic phase simulations and leave more significant topographic residues. φ_{disp} represents the ground displacement, which is the thawing settlement and frost heave caused by permafrost activities in this study, φ_{atm} is the difference in atmospheric delay between passes [27], [61], φ_n is the noise [13]–[16], and $W\{\cdot\}$ is the wrapping operator indicating that the phases are wrapped using modulo 2π , which leads to cycle ambiguities. The φ_{atm} and φ_n terms can be separated by time-series InSAR techniques, i.e., PSI and SBAS; however, separating them in a single interferogram is not easy.

In most cases, the unwrapped phase is assumed to be primarily composed of the displacement component. The displacement phase φ_{disp} can be easily converted to a relative displacement d in the line of sight direction and the vertical displacement d_v using the following equations:

$$\varphi_{\text{disp}} = \frac{4\pi}{\lambda}d \quad (2)$$

$$d_v = \frac{\varphi_{\text{disp}}}{\cos\theta} \quad (3)$$

where λ is the SAR wavelength and θ is the SAR incidence angle. Inaccurate orbit data and incorrect baseline estimates leave large-term trends on the differential interferograms, especially when processing ALOS PALSAR data because the ALOS satellite state vector is not accurately determined. Thus, extra steps are necessary to remove the residual phase trends. This process was accomplished in an iterative manner as shown in Fig. 4. First, phase unwrapping was applied to the baseline-refined differential interferogram. Second, the estimated quadratic phase term was subtracted from the differential interferogram. Finally, unwrapping was applied again to the second time-refined differential interferogram.

D. Comparison Analysis

The differential interferometric phase responds to the scattering center height change. The scattering center height is dependent on the target and the sensor characteristics. Kellndorfer *et al.* describe the influence factors on the single-pass scattering phase center [50]. In this paper, we adapted the concept and modified it for the DInSAR phase measurements. The DInSAR phase can be described as follows:

$$\varphi_{\text{disp}} = f_{\text{target}}(v_s, \Delta v_m, s_r, \Delta s_m) \circ f_{\text{sensor}}(\lambda, b, p, \theta)$$

where v_s represents the vegetation structure, Δv_m represents the vegetation water content change during two acquisitions, s_r represents the soil roughness, Δs_m represents the soil moisture change, \circ represents the concatenation operator, λ represents the

SAR wavelength, b represents the baseline length, p represents the polarization, and θ represents the SAR incidence angle. In our study, θ was assumed to be the same for two sensors and λ and p were different. The difference of λ and p changes the influence weight of each term in the target bracket.

The influence factors and application conditions for each sensor were analyzed based on the statistics from a large number of interferograms. In all, 45 interferograms for TerraSAR-X data and 55 for ALOS PALSAR data (27 from orbit 127 and 28 from orbit 128) were included in the analysis. The spatial perpendicular baseline of the TerraSAR-X pairs varied from 3.7 to 287.9 m, and the temporal baseline varied from 11 days to 451 days. Because of the highly accurate orbit of TerraSAR-X, the spatial baseline is short and the coregistration step can easily achieve notably good results. The mean error statistics of all coregistration steps were on the order of 0.01–0.02 times the SLC pixel spacing. The spatial perpendicular baseline of the ALOS PALSAR pairs varied from 55.3 to 4817.5 m, and the temporal baseline varied from 46 days to 1242 days. The mean error statistics of all coregistration steps were typically on the order of 0.04–0.08 times the SLC pixel spacing because of the larger baseline of the ALOS satellite.

For the comparison analysis, the differences between the retrieved displacements values were first examined when using the three DEMs. Subsequently, the differential interferometric phase quality with variations in timespan and vegetation cover was analyzed for the TerraSAR-X and ALOS PALSAR data individually, and then the displacement velocity of the X-band and L-band in the overlapped period was compared. Finally, the intra-annual displacement velocity on the permafrost-affected ROIs is presented for the TerraSAR-X and ALOS PALSAR data, and the interannual displacement is presented for the ALOS PALSAR data. The values were also compared with the *in situ* thaw tube measurements.

IV. RESULTS

A. DEM Influences

In this study, three DEMs (LiDAR DEM, X-band TanDEM-X DEM, and C-band SRTM DEM) were used to simulate the topographic phase. The resolution, systematic offset, and penetration-related measuring surface of these DEMs are different; thus, their influence on the final displacement outputs were investigated under the assumption that the influence would vary for different categories of ROIs. In categories 1 and 2 of rock outcrops, the terrain is stable, but certain topographic residues remain when the DEM is not sufficient. For all vegetation categories, the topography is gentle; thus, the differences are primarily caused by the resolution and elevation differences between the DEMs.

In the geocoding step, the SRTM DEM delivered error statistics that were several times larger than those of the LiDAR-based DEM and WorldDEM, thereby introducing more errors into the final displacement results.

1) *DEM Influences on TerraSAR-X Dataset*: Fig. 6 shows the displacement outputs for five categories of ROIs from the top to bottom: rock outcrop with flat terrain, rock outcrop with

sloped terrain, lichen-dominant terrain, shrub-dominant terrain, and spruce-dominant terrain. Categories 5 and 6 are highly dense and developed vegetation-covered regions, which means that they are less affected by permafrost. The displacement is introduced by the interaction of the SAR signals with the vegetation layer and the other phase residue terms rather than ground movement.

For the category of rock outcrop with flat terrain, the displacement lies completely within ± 0.5 cm using the three DEMs. Although the C-band SRTM DEM is systematically 1 m lower than the TanDEM-X DEM and LiDAR-based DEM, it does not bring out differences in displacement values within a perpendicular baseline of 300 m. Compared with the category of rock outcrop with sloped terrain, the difference is clear, especially when the perpendicular spatial baseline is greater than 200 m. The displacement caused by the residual topographic phase is largest when using the SRTM DEM as a reference. For the vegetation cover category, in certain interferogram pairs, the displacement is positively biased when the SRTM DEM is used compared with the displacement when the other two DEMs are used.

2) *DEM Influences on the ALOS PALSAR Dataset*: Fig. 7 shows the displacement values of the same five categories of ROIs as in Fig. 6. The remarkable baseline effects and large differences obtained using the different DEMs are displayed, especially in the interferograms of large spatial baselines.

For the category of rock outcrop with flat terrain, both the LiDAR DEM and SRTM DEM show augmented topographic residues when the spatial baseline is greater than 2000 m, and this tendency is aggravated in sloped terrain. For the category rock outcrop on flat terrain, the X-band TanDEM DEM shows the best results, and the left topographic phase is smaller than 1 cm. For the category rock outcrop in sloped terrain, the results for the TanDEM among the three DEMs are good, although the residue topographic phase can reach 4 cm. For the vegetation cover category, an offset is not observed among the displacement outputs using the three DEMs.

In conclusion, the TanDEM-X DEM displayed superior results and was adopted as the external DEM for the analysis in the next step. Because the ALOS PALSAR baselines can be quite large, an accurate DEM must be used to remove the topographic phase.

B. TerraSAR-X Interferometric Phase Quality

1) *Coherence*: The interferometric correlation indicates the quality of the DInSAR results. One of the main limitations of applying DInSAR is the signal loss caused by insufficient interferometric correlations. Noise, temporal decorrelations, geometric baselines, and volume decorrelations all contribute to a reduction in the signal coherence between two datasets [62]. Temporal decorrelations represent an important factor that describes changes in the scene microstructure and permittivity between two time-separated image acquisitions. For example, temporal decorrelations might be caused by small mutual shifts between the elementary scatterers. Other important decorrelation sources are geometric baselines and volume decorrelations. In the vegetated terrain, the coherence magnitude

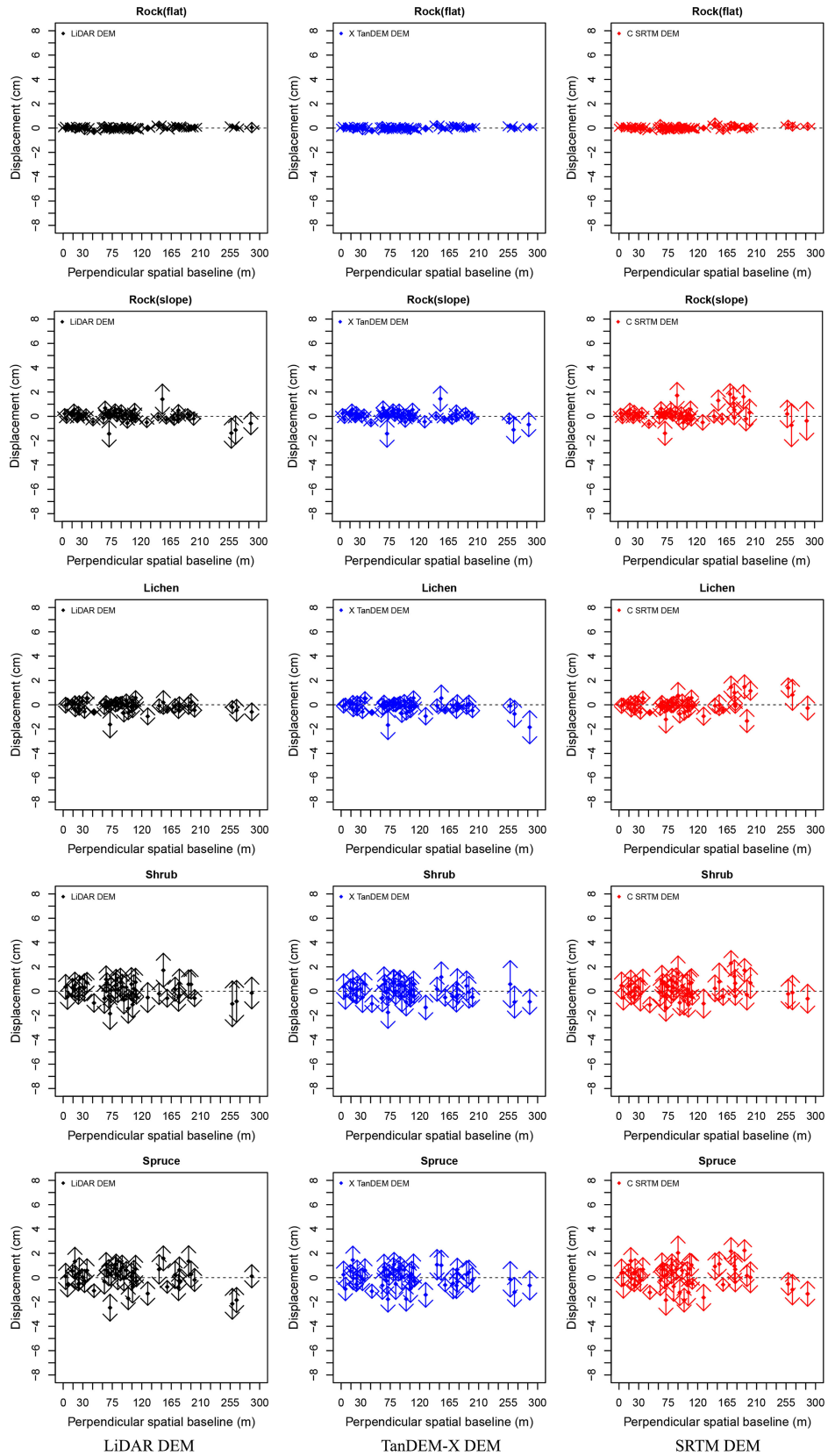


Fig. 6. TerraSAR-X displacement outputs with the application of the three DEMs with increasing spatial baseline. From the left column to the right column, the figure illustrates the LiDAR DEM results, TanDEM-X DEM results, and SRTM DEM results. The mean ± 1 standard deviation is shown with solid circle and arrows. Displacements are extracted for the five categories of ROIs. From the top to bottom: rock outcrop with flat terrain, rock outcrop with sloped terrain, lichen-dominant terrain, shrub-dominant terrain, and spruce-dominant terrain.

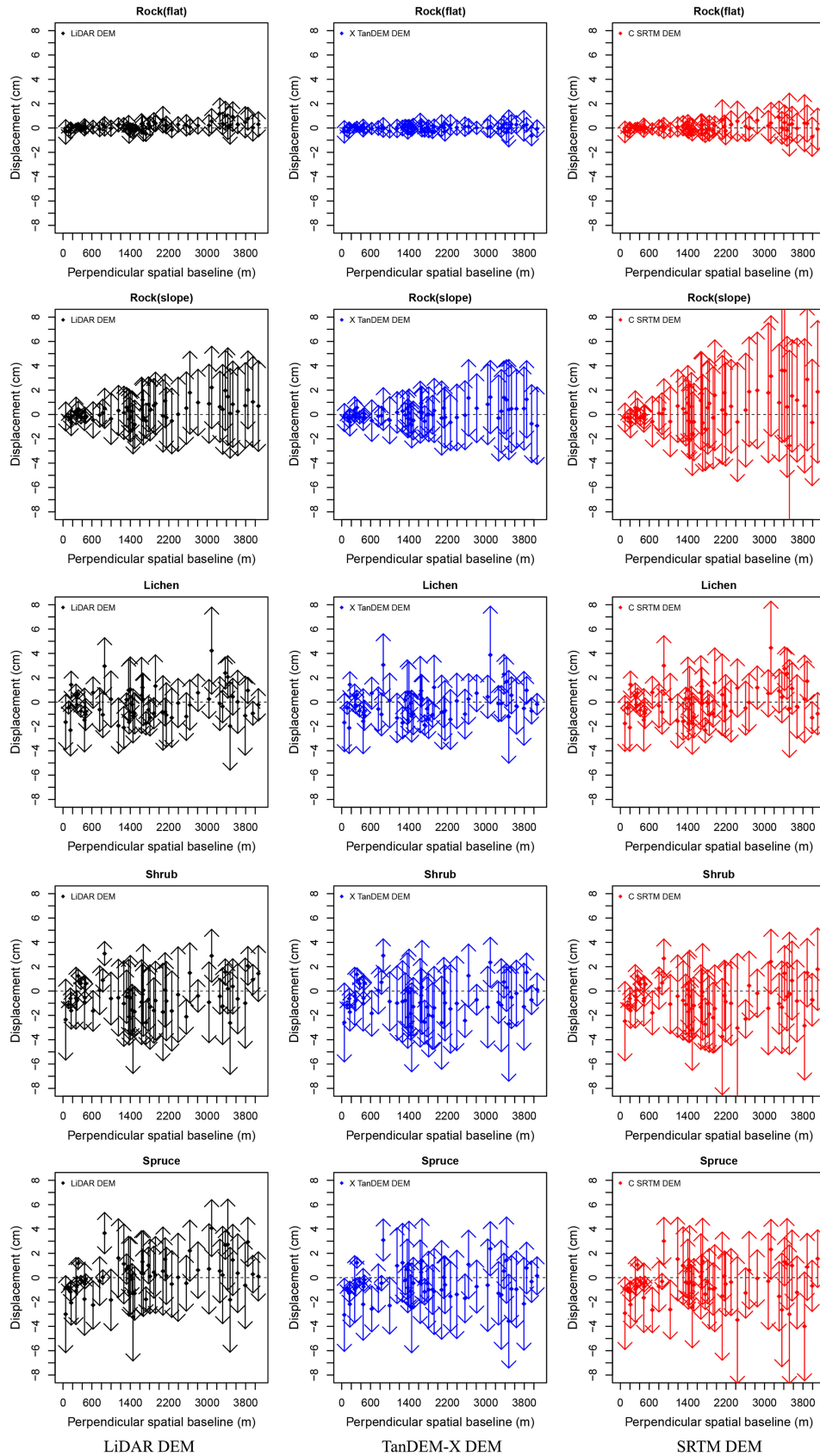


Fig. 7. ALOS PALSAR displacement outputs for the three DEMs with increasing spatial baselines. From the left column to the right column, the figure illustrates the LiDAR DEM results, TanDEM-X DEM results, and SRTM DEM results. The mean ± 1 standard deviation is shown with solid circles and arrows. Displacements are extracted for the five categories of ROIs. From the top to bottom: rock outcrop with flat terrain, rock outcrop with sloped terrain, lichen-dominant terrain, shrub-dominant terrain, and spruce-dominant terrain.

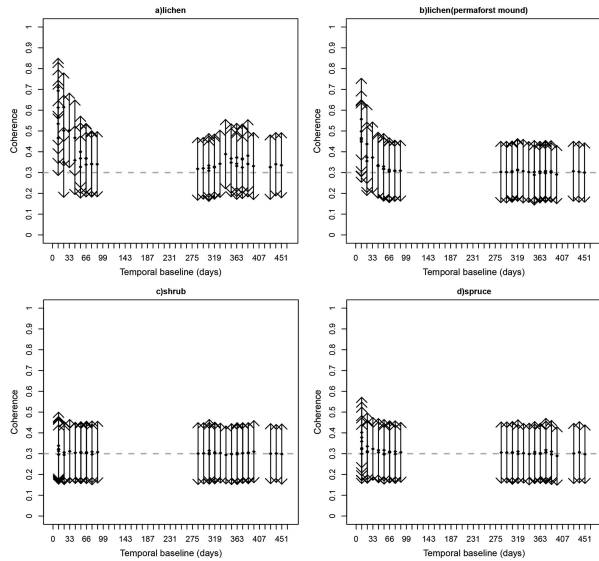


Fig. 8. Interferometric coherence with temporal spans using the TerraSAR-X dataset over four vegetation categories: (a) lichen, (b) lichen over permafrost mounds, (c) shrub, and (d) spruce. The mean ± 1 standard deviation is shown with solid circles and arrows.

and decorrelation speed are correlated with vegetation properties, such as coverage, height structure, growth/decline, and time span. The decorrelation primarily consists of volumetric decorrelations because of volume scattering within the vegetation and temporal decorrelations caused by the dislocation of scatterers [27], [63]. Such dislocations can be caused by wind on a very short timescale. In forested areas, wind is considered the main source of temporal decorrelation [64], [65], and rapid decorrelation can occur even at low wind speeds [64]. This effect is obvious when using high-frequency SAR systems (X- and C-band), for which a large proportion of scattering originates within the first few meters of the canopy, where temporally unstable scatterers are located (twigs, needles, small branches) [66]. Other sources of decorrelation are related to variations in the environmental conditions, such as precipitation events [63]. The vegetation phenology (greening and drying cycle of herbaceous and shrub vegetation) and soil moisture variations also contribute to decorrelations [67], [68]. In this paper, we used differential interferometric coherence to assess the quality of displacement outputs from TerraSAR-X and ALOS PALSAR.

Fig. 8 shows the TerraSAR-X 1×2 multilook differential interferogram coherence with increasing temporal baselines. Coherence was presented using the interferogram with the smallest multilook factors because a fine resolution is desired in most cases.

Fig. 8 shows that the interferogram quality is heavily dependent on the temporal spans. The coherence of the 11-day span is remarkably higher than that of longer temporal spans. When the temporal span reaches a threshold (greater than 33 days or 44 days), the coherence remains low. Considering the coherence of an 11-day span, tall dense vegetation [shrubs in Fig. 8(c) and spruce in Fig. 8(d)] leads to a larger decorrelation than low sparse vegetation [lichen dominated in Fig. 8(a) and Fig. 8(b)]. For dense vegetation [see Fig. 8(c) and (d)], co-

herence decreases rapidly when the temporal baseline exceeds 11 days. The ROI category of shrub is more susceptible to decorrelation than the spruce category when comparing the coherence of a 22-day span. Shrub is a main component of the discontinuous permafrost landscape, and shrubification is the major trend that occurs under permafrost degradation [43], [44].

As shown in Fig. 8(b), for our monitoring target, i.e., the ROI category of the permafrost-affected region, when the temporal baseline is within 22 days, the majority of the coherence remains above 0.3; however, when the temporal baseline increases to 44 days, the coherence is low. Therefore, when applying X-band DInSAR data to detect ground movements in the discontinuous permafrost zone, the temporal baseline should be limited to within 22 days.

Fig. 8 illustrates that the main constraint of applying DInSAR using X-band data originates from the volumetric decorrelation of developed vegetation (shrub and spruce). The developed vegetation cover (also vegetation phenology) strongly decorrelates the stability of the phase signal. The disconnection of coherent frozen ground (scattered permafrost pattern) is more likely to introduce errors in the unwrapping process because of the strong decorrelation from tall shrubs growing in gullies between such frozen grounds. Volumetric scattering for herbaceous plants/grasses is also similar to that observed in woody vegetation [69]. Thus, for herbaceous vegetation cover, the volumetric decorrelation is also high. The scattered thermokarst ponds also contribute to the insufficient interferometric correlation.

The strong temporal and volume decorrelation in woody vegetation terrain prevents ground movement monitoring; however, the decorrelation information is valuable for land cover classification [70]–[72] and forest/crop parameter retrieval [73]–[77].

2) *Multilook and Polarization Effect*: The statistics for TerraSAR-X are calculated using VV polarization, and the statistics for ALOS PALSAR data are calculated using HH polarization because of the data acquisition scheme. However, to compare the TerraSAR-X results with the ALOS PALSAR results, the difference in the polarization and resolution of the two sensors should be considered. Thus, the polarization and resolution effect on the coherence and displacement output was also analyzed using three TerraSAR-X acquisitions for which both VV and HH polarized signals are available. The scenes were acquired on 2010-08-01, 2010-08-12, and 2010-08-23.

Vertical and horizontal polarization signals interact differently with vertically oriented surface structures. This effect is obvious with vertically oriented plants and to a certain extent in vertically oriented rubble. Vertically polarized signals interact strongly with vertical scattering elements and produce relatively high backscatter in the VV polarization. However, the interaction of horizontally polarized signals with vertical structures is weaker than that with underlying surfaces [78]. Information on the canopy is usually embedded in the VV radar backscatter, whereas information on the underlying soil (e.g., soil moisture studies) can be retrieved from the HH backscatter. This feature is also noted that the backscatter in VV is considerably higher than the backscatter in HH over the rough ocean surface [78] because HH is less sensitive to water roughness or small-scale roughness than VV polarization.

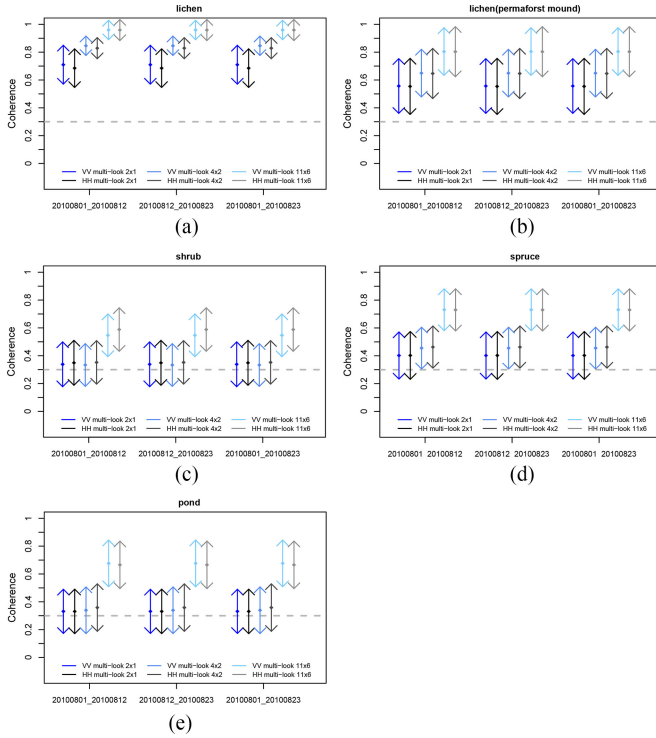


Fig. 9. Coherence with different multilook factors and polarizations over five categories of ROIs: (a) lichen, (b) lichen over permafrost mound, (c) shrub, (d) spruce, and (e) pond. The mean ± 1 standard deviation is shown with solid circle and arrows.

Fig. 9 shows the coherence for the five categories of ROIs when applying different multilook factors to the VV and HH polarized signals, and Fig. 10 shows their displacement outputs. Data voids are displayed in white on the map. These voids were introduced by masking out effective correlations below 0.3.

Figs. 9 and 10 indicate that a distinct difference is not observed between the two polarizations of X-band data. The coherence is in the same range, and the displacement velocity map shows a similar character. In the outlined permafrost-affected region, the movement pattern is not obvious or consistent in most places except in the left bottom corner of sector 2 inside the outlined permafrost-affected area, where a strong subsidence pattern was identified for two interferogram pairs at both polarizations. Several reasons can explain this random displacement pattern. First, the temporal span may not have been sufficiently long to detect strong thawing settlement. However, when the temporal span is too large, signal loss is introduced as indicated in the 22-day span interferogram 20100801_20100823. Second, in the X-band, the small terrain movement signal is usually mixed with or buried by the distortions of the vegetation layer and noise terms. The shortwave X-band signal interacts with various scatterers associated with leaves, branches, and stems over vegetated terrain; thus, the majority of the signal represents an interaction with the vegetation canopy layer rather than ground movement. This effect is also illustrated by a higher elevation generated by the TanDEM-X mission over developed vegetation cover in the section detailing the DEM height comparison. Thus, the phase change is not linked with topography movement but rather with interactions in the vegetation layers.

When applying larger multilook factors, the coherence increased significantly in both polarizations as shown in Fig. 9. Additionally, phase noise was reduced and displacement was smoothed as shown in the displacement map of Fig. 10. However, this phase estimation improvement was obtained by sacrificing spatial resolution and detail. Fig. 10 illustrates that a large multilook factor weakens the displacement signals by minimizing the displacement range, especially when applying notably large multilook factors, such as 11×6 factors. In the 11-day span interferogram for 20100801_20100812 and 20100812_20100823, at sector 2 in the left bottom corner of outlined permafrost affected area, a strong subsidence signal was detected in the displacement results for small multilook factors; however, a weak subsidence signal was detected in the displacement results for the large 11×6 multilook factor.

For the following analysis, TerraSAR-X output with a 4×2 multilook factor was used because it represents a compromise between a reduction in phase noise and maintenance of the displacement signal.

C. ALOS PALSAR Interferometric Phase Quality

1) *Coherence*: L-band is less sensitive to small deformation incidents but also less sensitive to temporal decorrelations induced by the vegetation canopy compared to C- and X-band. It allows for the preservation of higher coherence under unfavorable conditions, such as dense vegetation and wet surface.

Similar to the analysis of TerraSAR-X data, changes in coherence using the ALOS PALSAR dataset with increasing temporal spans were examined (see Fig. 11). Only the category permafrost-affected lichen showed a remarkable decorrelation tendency, which indicates permafrost terrain movement. The coherence was well maintained within a one-year span. For ROIs of lichen-dominated terrain, the coherence maintained a high level even over a 3-year time span. For the shrub category, a decorrelation trend was observed when the temporal baseline exceeded two years. With respect to the spruce category, the decorrelation trend was not as strong as that for the shrub category.

Given the longer wavelength, ALOS PALSAR data show considerable potential for forestry applications because of the deep penetration of the electromagnetic waves into the forest canopy and the higher backscatter saturation level [34], [51], [79]. Coherence information is beneficial for above-ground biomass estimation [80].

D. Comparison of TerraSAR-X and ALOS PALSAR Results in the Overlapped Period

The vertical displacement from TerraSAR-X and that from ALOS PALSAR were compared in the overlapped period from the beginning of August to the beginning of November in 2010. Table II lists the interferogram information used in the comparisons. Fig. 12 shows the displacement map acquired from two sensors in the overlapped period. For ease of comparison, the displacement values were normalized in terms of displacement velocity (mm/day).

Fig. 12 shows that a low number of void pixels is observed in the outputs of the L-band ALOS PALSAR in the

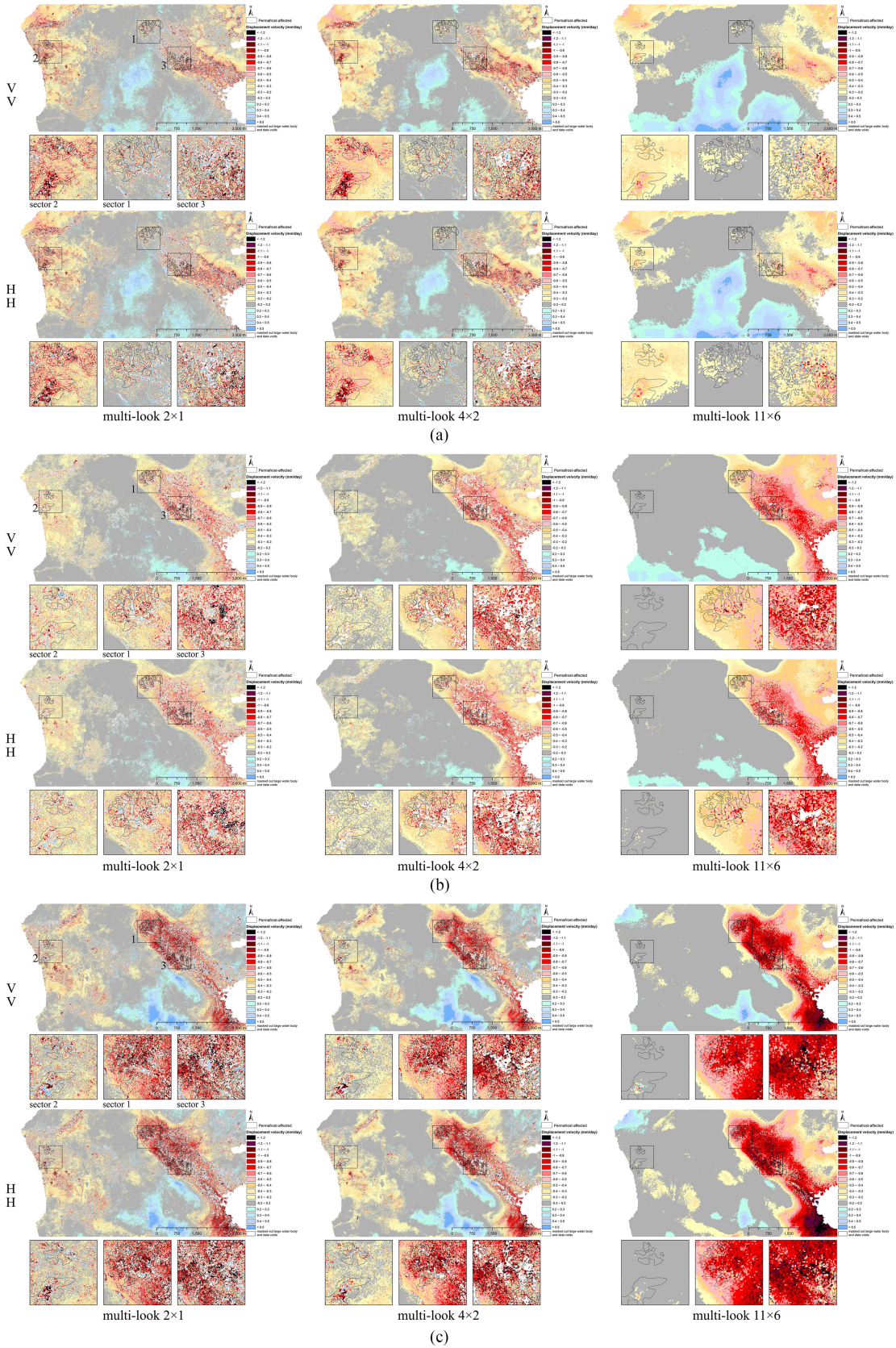


Fig. 10. Influence of different multilook factors and polarizations on three TerraSAR-X DInSAR pairs: (a) 20100801_20100812, (b) 20100812_20100823, and (c) 20100801_20100823. Negative (subsidence) displacement velocities (mm/day) are shown in yellow to red colors, and positive (uplift) displacement velocities are shown in blue colors. Data voids are displayed in white. For each subfigure, the first line always displays the VV result and the second line shows the HH results. Multilook factor information is indicated at the bottom of each panel, and the multilook factor increases from left to right.

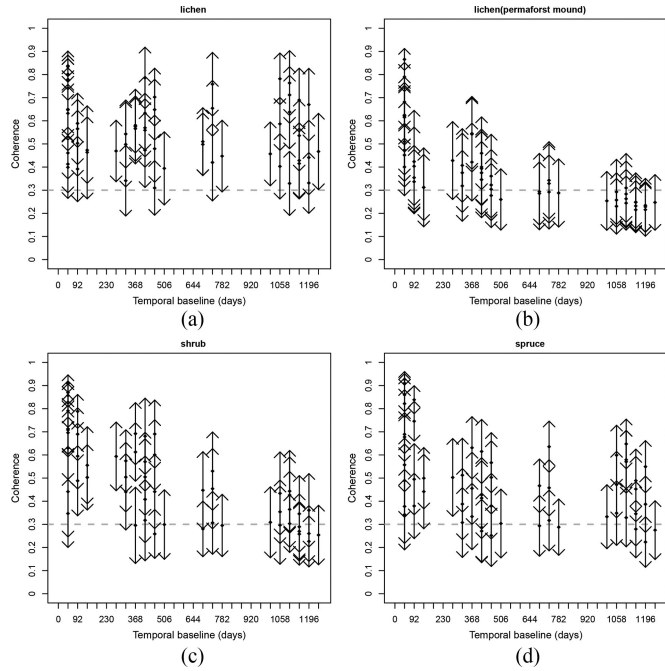


Fig. 11. Interferometric coherence with temporal spans using the ALOS PALSAR dataset over four vegetation categories: (a) lichen, (b) lichen over permafrost mounds, (c) shrub, and (d) spruce. The mean ± 1 standard deviation is shown with solid circles and arrows.

TABLE II
INTERFEROGRAM PAIR INFORMATION USED TO COMPARE THE TWO SENSORS

	Perpendicular Spatial Baseline (m)	Temporal Baseline (days)	Coherence of ROIs in Permafrost-affected Area
TerraSAR-X			
20100801_20100823	47.03	22	0.48
20100823_20101028	36.39	66	0.24
20100801_20101028	83.43	88	0.24
ALOSPALSAR Orbit 127			
20100716_20100831	455.21	46	0.79
20100831_20101016	372.95	46	0.62
20100716_20101016	828.03	92	0.34
ALOSPALSAR Orbit 128			
20100802_20100917	155.69	46	0.47
20100917_20101102	315.91	46	0.68
20100802_20101102	471.56	92	0.40

longer time span, e.g., interferogram pair 20100831_20101016 of the ALOS PALSAR orbit 127 (46 days temporal span) and 20100823_20101028 of TerraSAR-X (66 days) and interferogram pair 20100802_20101102 of the ALOS PALSAR orbit 128 (92 days temporal span) and 20100801_20101028 of TerraSAR-X (88 days). The L-band provided more reasonable results than the X-band because the large subsidence places in the L-band outputs are well confined in the outlined permafrost-affected areas and present obvious and consistent movement patterns across all of the interferogram pairs. In addition, the

two ALOS PALSAR orbits generated consistent and comparable movement patterns for the permafrost-affected area. The interferogram pairs 20100716_20100831, 20100831_20101016, 20100716_20101016, and 20100802_20101102 all clearly showed thawing subsidence in the same region. For the three sectors shown below the full frame, large subsidence values are confined inside the outlined permafrost affected areas. The good results of L-band data are related to the deeper penetration depth through the canopy layer and the advantage of coherence maintenance over time and space.

The exceptions are the two pairs 20100802_20100917 and 20100917_20101102, which shared an acquisition on 2010-09-17. For pair 20100802_20100917, and large areas excluding rock outcrop terrain manifest unrealistic negative movement. The influence of permafrost can still be detected because the permafrost-affected area shows larger movement values than those of other nonpermafrost affected places. For pair 20100917_20101102, the movement trend is opposite to pair 20100802_20100917 that large areas besides rock outcrop manifest “fake” uplift movement. In permafrost-affected regions, the uplift value is quite small and certain points show subsidence signals. However, when subtracting a “bias” from the entire displacement map, the large subsidence values in the permafrost-affected area are revealed. The potential cause of these two opposite patterns for the two pairs which share an acquisition on 2010-09-17 is assumed to be soil moisture changes [67], [81], [82], and the supporting information is addressed in the “Discussion” section.

The results obtained from X-band TerraSAR-X data are more dynamic and present many data voids, such as the large area of data voids shown in the interferograms 20100823_20101028 and 20100801_20101028. The displacements generated from the 11-day temporal span shown in Fig. 10 align better with the ALOS PALSAR output. In the left bottom corner of sector 2 inside the delineated permafrost region, the 11-day TerraSAR-X results also indicate strong subsidence at the same location shown on the ALOS PALSAR results. However, the TerraSAR-X outputs generated by longer temporal spans (shown in Fig. 12) are not comparable with the ALOS PALSAR results. As previously stated, the X-band signal can be largely attributed to volume scattering from within the upper canopy rather than the underlying ground surface, and the differential phase patterns presented in this paper are not related to topography or geomorphology but rather to changes in the scattering center height of the vegetation canopy layer. The findings were verified by a previous backscatter signal investigation for the same site, which demonstrates that the effect of soil characteristics was weak at X band, whereas the volume scattering from vegetation (and snow in winter) tends to dominate at this frequency [83].

E. Displacement Values From Two Sensors and Comparison With Thaw Tube Measurements

Displacements on permafrost mound ROIs (distribution is shown in Fig. 1) were extracted from promising interferograms pairs, which were selected by setting a data void threshold

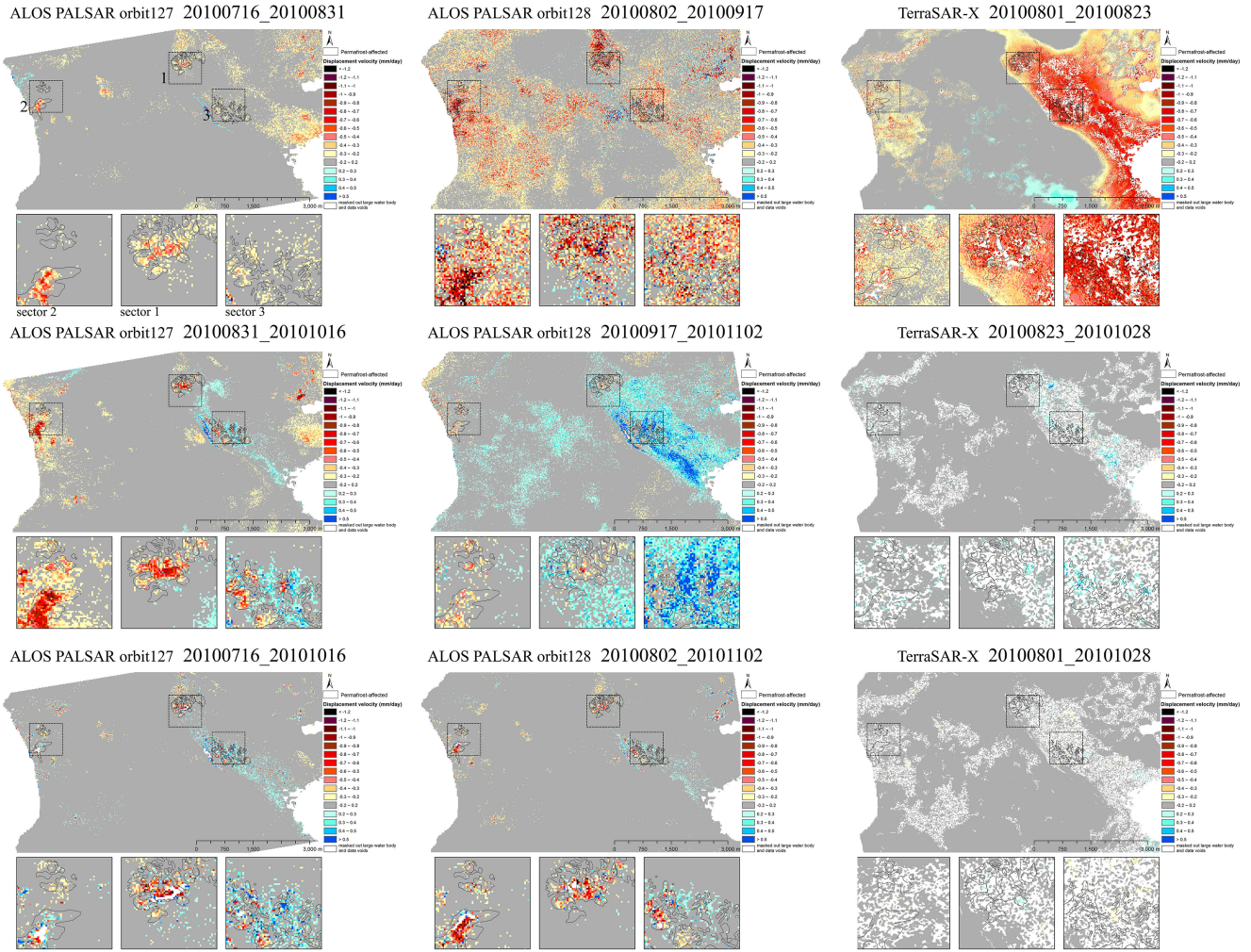


Fig. 12. Comparison of the displacement velocity of X-band and L-band outputs in the overlapped period. The left and middle columns show the results from the ALOS PALSAR orbits 127 and 128, and the right column shows the results from TerraSAR-X. The tag of the interferogram pair is shown on the top of each displacement velocity map. Yellow to red colors indicate negative (subsidence) displacement velocities (mm/day), and blue colors indicate positive (uplift) movement. Data voids are displayed in white.

of 5% for the ROI category of permafrost mounds. The displacement and coherence of the TerraSAR-X results and ALOS PALSAR results are shown in Figs. 13 and 14. For the intra-annual DInSAR pair, movement information is shown in terms of displacement velocity (mm/day). For the interannual DInSAR pair, because the uplift and subsidence occurs in a cycle accompanied by a freeze-thaw process, movement information is clearly demonstrated using centimeter.

Figs. 13 and 14 show that the standard deviation of displacement is closely related to coherence. High and convergent coherence normally leads to small standard deviations of displacement. Both the X-band and L-band intra-annual interferogram pairs show displacement velocity in the near range and are comparable to a certain degree. However, as previously stated, the X-band differential phase patterns presented in this paper are heavily influenced by scattering center height changes in the vegetation canopy layer. Interannual ground subsidence can also be identified from the ALOS PALSAR data, such as interferogram pair 20090713_20100716, for which the max subsidence reaches 8.6 cm and the mean value is 1.3 cm.

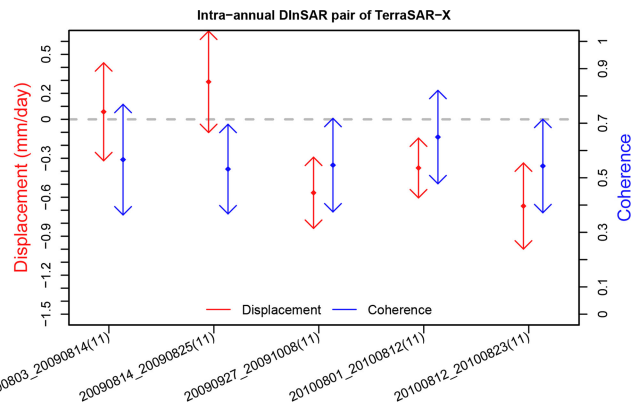


Fig. 13. Intra-annual displacement and coherence information from TerraSAR-X data. The mean ± 1 standard deviation is shown with solid circles and arrows. Numbers in parentheses following the interferogram pair tag indicate the temporal baseline.

The DInSAR results were also compared with the *in situ* displacements from two thaw tube measurements. The thaw/frost

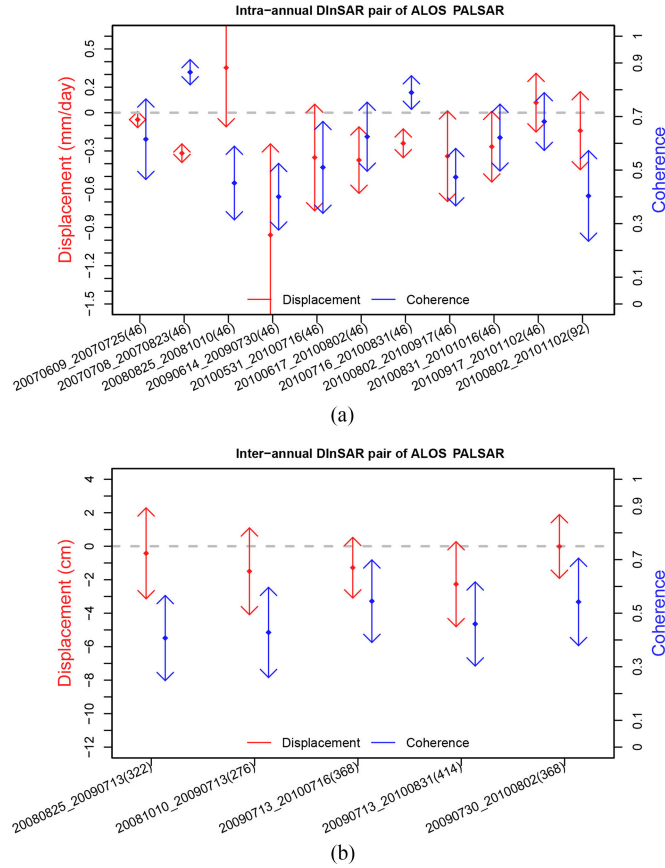


Fig. 14. Displacement and coherence information from the ALOS PALSAR data. (a) Intra-annual DInSAR pair in which movement information is shown as displacement velocities (mm/day); and (b) interannual DInSAR pair in which movement information is shown as displacement values (cm). The mean value ± 1 standard deviation is shown with solid circle and arrows. Numbers in parentheses following the interferogram pair tag indicate the temporal baseline.

tube is a classical method used to record thaw settlement and frost heave in permafrost terrain. In our study area, two thaw tubes were installed in June 2014, and their positions are shown in Fig. 1. Thaw tube 1 is located inside sector 1 on a large permafrost mound with surface sandy deposits and an ice-rich core below a depth of 120 cm. Thaw tube 2 is located inside sector 2 on a small permafrost mound with surface deposits characterized by coastal sands and a deep layer composed of marine clay below 200 cm. Although thaw/frost tube data are not acquired synchronously with DInSAR data, the values could help to identify whether the DInSAR-retrieved displacements are in the correct range.

At the thaw tube sites, the displacement values from seven intra-annual ALOS PALSAR DInSAR pairs in the 2010 [listed in Fig. 14(a)] are used to obtain the time series deformation through an SBAS inversion. The time series of deformation from ALOS PALSAR in 2010, the accumulated deformation from two pairs of TerraSAR-X in 2010 (listed in Fig. 13), and thaw tube measurements for 2014–2015 are shown in Fig. 15. For TerraSAR-X data, the displacement values were extracted at the thaw tube locations marked as “TerraSAR-X (point)” in Fig. 15. For the ALOS PALSAR data, we also extracted the mean displacement value for the entire permafrost mound where the

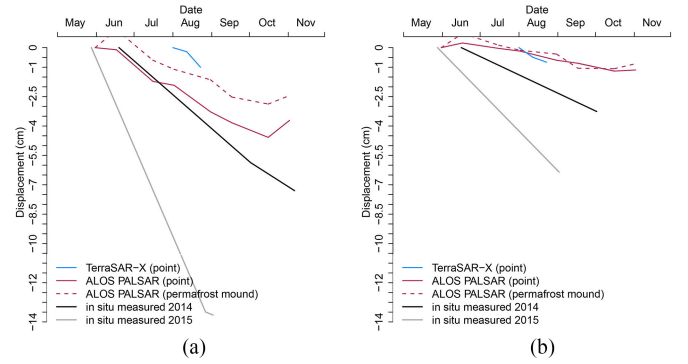


Fig. 15. Comparison of the DInSAR-retrieved displacements with the *in situ* measurements at the two thaw tube locations. (a) Thaw tube 1. (b) Thaw tube 2.

thaw tube was installed, which is marked as “ALOS PALSAR (permafrost mound).” According to Fig. 15(a) and (b), the ALOS PALSAR point-based time series of deformation or ALOS PALSAR permafrost mound-based time series of deformation share the same patterns. The *in situ* ground subsidence in 2015 and 2014 showed that thawing settlements are temporally varied. The displacement in 2015 is much larger than in 2014, which might have been related to the deepening of the active layer or (more likely) to the thawing of the bottom table of permafrost [84]. The distinction of *in situ* displacement at thaw tube 1 and thaw tube 2 demonstrates that the thawing settlements are spatially varied. The DInSAR-derived deformation from the ALOS PALSAR data show that the site of thaw tube 2 undergoes much smaller displacement than the site of thaw tube 1. At thaw tube 2, the DInSAR-derived displacement is less than the *in situ* measurements. This observation is assumed to be related to the small-sized permafrost mound on which thaw tube 2 was located (see Fig. 1). The permafrost mound where thaw tube 2 is located occupies only 5 pixels in the ALOS PALSAR geocoded image, which is small compared with the adaptive window size; thus, these pixels are easily filtered smoothly when a large portion of the surrounding area is stable. The ALOS PALSAR displacement velocity maps displayed in Fig. 12 also show that displacements are not easy to measure on small-sized permafrost mounds.

We cannot confidently state whether the TerraSAR-X results capture the ground movement pattern because only two interferogram results are listed. Additionally, when referring to the X-band displacement velocity map of Fig. 10, the permafrost-related signal is not strong.

V. DISCUSSION

A. Soil Moisture Influence

As shown in the section “Comparison of TerraSAR-X and ALOS PALSAR Results in the Overlapped Period,” the opposite displacement patterns in the large nonpermafrost affected area are assumed to be caused by soil moisture changes [30], [67], [82]. Moreover, Fig. 14(a) shows that pairs 20080825_20081010 and 20090614_20090730 have much larger displacements than the other pairs, especially pair 20080825_20081010, which shows strong uplift displacements.

TABLE III
PRECIPITATION VARIATIONS AND MEAN DISPLACEMENT VELOCITIES FOR 11
INTRA-ANNUAL ALOS PALSAR INTERFEROGRAM PAIRS

	Precipitation amount variation (mm)	Mean displacement velocity (mm/day)	Mean coherence
20070609_20070725	4.1	-0.4	0.62
20070708_20070823	1.2	-0.3	0.87
20080825_20081010	-4.8	0.4	0.45
20090614_20090730	12.0	-1.0	0.40
20100531_20100716	-0.3	-0.4	0.51
20100617_20100802	-0.1	-0.4	0.62
20100716_20100831	1.8	-0.2	0.79
20100802_20100917	5.0	-0.3	0.47
20100831_20101016	-0.6	-0.3	0.62
20100917_20101102	-4.6	0.1	0.68
20100802_20101102	0.4	-0.1	0.40

Studies have been conducted on the soil moisture influence in the DInSAR phase [30], [67], [81], [82]. Soil moisture is not available in our study area; thus, the variation in precipitation near the SAR acquisition date serves as an approximation of the soil moisture changes. For each SAR acquisition date, the precipitation value on the same day of the SAR data acquisition, the value one day before acquisition, and the value two days before acquisition are summed and assigned weights of 50%, 25%, and 25%, respectively. The summed precipitation amount is compared at the two dates of the interferogram pair, and the variation precipitation is calculated. Table III lists the precipitation variations and mean displacement velocity for the 11 intra-annual ALOS PALSAR interferogram pairs shown in Fig. 14(a). The mean displacement velocity and mean coherence are calculated for the ROI category permafrost mounds.

Table III shows that the precipitation variations are closely correlated with the mean displacement velocity for the permafrost mound category. Because the interferogram pairs are all generated in the thawing season (air temperature above 0 degrees), the displacement velocities should always be negative, which indicates thawing subsidence. However, two pairs (20080825_20081010 and 20100917_20101102) show an abnormal uplift trend (for pair 20100917_20101102, the displacement map is shown in Fig. 12). Correlating with the precipitation variations shows that the precipitation amount decreases more severely (drier soil) in the second pass of these two interferogram pairs. Pair 20080825_20081010, which presents a massive reduction of precipitation in the second pass (drier soil), shows high positive (uplift) values. For another two pairs (20090614_20090730 and 20100802_20100917), subsidence is observed over a large area besides permafrost-affected region, and both receive more precipitation in the second pass (wetter soil). Especially for pair 20090614_20090730, which shows a significant increase in precipitation in the second pass (wetter soil), shows the largest negative (subsidence) values.

These findings are consistent with those reported in the study by Zwieback *et al.* with two L-band airborne datasets of HH polarization [67], which showed that the phase dependence on soil moisture was significant and the sign corresponded to an

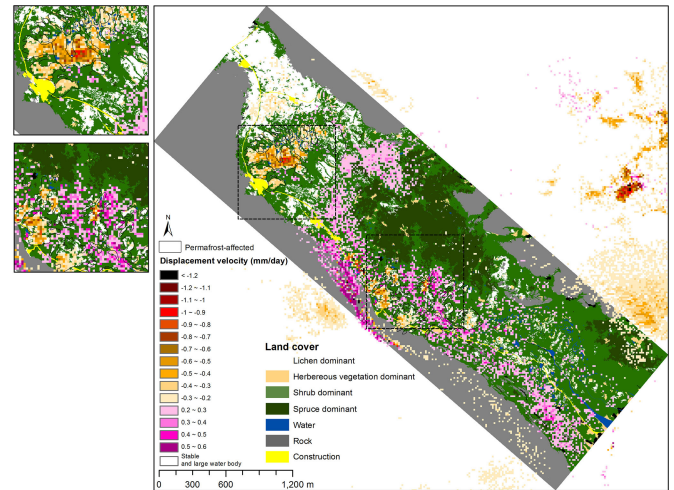


Fig. 16. Displacement velocity map of pair 20100831_20101016 for the late fall period overlain on the vegetation map in the Tasiapik Valley.



Fig. 17. Dryness of shrubs and herbaceous vegetation. Photo (a) was taken on 2014-09-01. Photo (b) was taken on 2014-10-24 [85].

increase in the optical path upon wetting. Furthermore, the magnitude of the associated deformation commonly exceeds 2 cm when the soil moisture changes by 20%.

Our study confirms that large soil moisture variations have an effect on the accuracy of displacement retrievals. Thus, the influence of soil moisture should not be neglected for applications in the permafrost region.

B. Vegetation Phenology Influence

Differential phase dependencies on changes in the vegetation water content/phenology in the L-band data are also detected in our study. The influence of variations in vegetation water content is the same as that of soil moisture because the dielectric properties of both are known to depend on the moisture content [47].

When the displacement velocity map of the ALOS PALSAR orbit 127 pair 20100831_20101016 is inspected (see Fig. 12) and overlain on the vegetation map [44] in the Tasiapik Valley region (see Fig. 16), the borders of the displacements patterns align well with the vegetation cover species. The shrubby region shows different leveled uplift values, whereas the spruce-covered area is stable. Two photos of a spruce-shrub-mixed stand at the BGR site [85], which is located 14 km northeast of the study area, are shown (see Fig. 17) to illustrate the phenology changes for the shrub and spruce species. One photo was taken on 2014-09-01, and the other was taken on 2014-10-24. In the two photos, the shrub canopies and branches are dry in the autumn season, whereas the spruces remain green.

The influence of soil moisture changes can be excluded in this pair based on the precipitation variations (see Table III) and the displacement velocity map shown in Fig. 12. According to Table III, a minimal amount of precipitation change (-0.6 mm) occurs during the two passes of the ALOS PALSAR sensor. From the displacement velocity map shown in Fig. 12, only permafrost-affected areas show large subsidence, and the other large area is quite stable. Thus, soil moisture distortion can be excluded.

The drying process of shrubs in the autumn season causes uplift displacements in the corresponding region. Over the surface permafrost-affected terrain, only low shrubs are scattered, however shrubification is the major trend accompanied by permafrost degradation in the discontinuous permafrost environment; thus, when applying DInSAR applications in such a permafrost environment, the increased difficulty caused by shrubification should be considered.

VI. CONCLUSION

The application of DInSAR to monitor the thermal states of discontinuous permafrost is limited by several features of this heterogeneous yet unique landscape, in which numerous scattered permafrost grounds alternate with developed shrub cover and thermokarst ponds. Nevertheless, this study is the first to quantitatively compare and analyze the ability of two sensors, TerraSAR-X and ALOS PALSAR, to monitor permafrost-induced ground movements in a discontinuous permafrost environment. The TanDEM-X DEM is used as an external DEM to remove the topographic phase and geocode the displacement products, and its performance is examined and compared with that of the C-band SRTM DEM and LiDAR DEM in the DInSAR application. The results show that the TanDEM-X DEM is superior to the other DEMs, especially for interferograms of large baselines.

Based on the analysis of a large number of interferogram pairs, the influencing factors and application conditions for different sensors in this special environment can be summarized as follows. In the discontinuous permafrost region, preserving reliable phase measurements is more challenging because of the strong decorrelations. Vegetation cover, vegetation phenology, and thermokarst ponds strongly decorrelate the phase signal and deteriorate the displacement height analysis. The disconnection of coherent frozen grounds (scattered permafrost pattern) is more likely to introduce errors in the unwrapping process because of the strong decorrelation from tall shrubs growing in gullies between such frozen grounds. With respect to X-band data, the main constraint originates from the temporal decorrelation and strong volume decorrelation caused by developed vegetation. When working in comparable permafrost landscapes, we suggested using SBAS with a temporal baseline of less than 22 days. However, in terrain with more developed vegetation (e.g., shrub and spruce), the differential phase change is not strongly linked to terrain topography, but rather to processes in the canopy layer. With respect to L-band data, displacement patterns related to thawing are obvious and

consistent in the permafrost-affected area, and the good results are related to the deeper penetration depth through the canopy layer and the strong advantages of maintaining coherence over time and space. Analyses of both intra-annual and interannual interferograms demonstrate the ability to monitor the permafrost state. Reliable displacement can be achieved using interferograms with a one-year span, and a longer temporal baseline is not advised. In conclusion, DInSAR performed on L-band data is more suitable in the large discontinuous permafrost environment of northern Quebec. By examining the displacement velocity maps and referring to the *in situ* measured ground displacements, it shows that the ALOS PALSAR results capture the permafrost-induced terrain movement characteristics and values in the correct range. The analyses confirm that the L-band has strong advantages over the X-band for monitoring discontinuous permafrost environments.

L-band electromagnetic waves penetrate deeper into the ground, and changes in the soil moisture conditions affect the DInSAR phase. The influence of soil moisture is detected in several interferogram pairs in our study. A distortion from changes in vegetation water content is also observed in the L-band data, and an uplift displacement error occurs under drier fall conditions. The distortion is the largest for shrub vegetation because of the considerable drying of shrub canopies and branches in the fall. Despite these distortions, permafrost-induced ground movement can still be detected by the distinct differences from the surrounding areas of none permafrost. In the current state, permafrost-affected areas can be characterized by minimal or short vegetation. Shrubby areas are considered to be the major trend accompanied with permafrost degradation in the discontinuous permafrost landscape. Therefore, this influence should be considered when quantitatively mapping permafrost movement in shrub-dominated terrain.

The study shows that for regional-scale permafrost monitoring, a high-resolution image is more suitable for detecting and describing highly scattered, differently sized permafrost patches in this heterogeneous landscape. The results obtained from the ALOS PALSAR data exhibit spatiotemporal thawing settlement variations that indicate the nonuniform internal thermal characteristics of permafrost ground, even within a small area. However, the sampling space and data acquisition scheme of the ALOS PALSAR FBD mode limits the ability to provide a detailed displacement process description for such permafrost environments. The relatively coarse resolution impedes the provision of displacements over and within small permafrost mounds. Multilooking and adaptive filtering are necessary to improve coherence, however they deteriorate the resolution even further. Currently, details on the heterogeneity of permafrost thermal characteristics are insufficiently obtained using L-band ALOS PALSAR data. In addition, the long spatial baseline leaves more topographic phase residues in the displacement output. Consequently, an L-band sensor with frequent repetition, high orbital stability, finer resolution, and short spatial baselines would be ideal for displacement studies of heterogeneously vegetated discontinuous permafrost landscapes.

ACKNOWLEDGMENT

The authors would like to thank the German Aerospace Centre (DLR) for supplying the TerraSAR-X data, the Alaska Satellite Facility Distributed Active Archive Centers (ASF DAAC) for providing access to the ALOS PALSAR data, and Airbus Defence and Space for providing the WorldDEM product. Displacement measurements from thaw tube data were kindly supplied by J. Roger (CEN) and J. Eppler (MDA). The authors also thank Prof. M. Allard (CEN) and D. Sarrazin (CEN) for supporting this research and Y. Chen and C. Touati for providing valuable assistance during the field work. The authors are grateful to CEN for providing helicopter time and logistical support.

REFERENCES

- [1] R. J. E. Brown and W. O. Kupsch, *Permafrost Terminology: National Research Council of Canada Associate Committee on Geotechnical Research*, Ottawa, ON, Canada, 1974.
- [2] C. Burn, "The active layer: Two contrasting definitions," *Permafrost Periglacial Processes*, vol. 9, pp. 411–416, 1998.
- [3] T. Stocker *et al.*, "IPCC, 2013: Climate change 2013: The physical science basis. Contribution of working group I to the fifth assessment report of the intergovernmental panel on climate change," Cambridge University Press, Cambridge, United Kingdom and New York, NY, USA, 2013.
- [4] V. E. Romanovsky, S. L. Smith, and H. H. Christiansen, "Permafrost thermal state in the polar Northern Hemisphere during the international polar year 2007–2009: A synthesis," *Permafrost Periglacial Processes*, vol. 21, pp. 106–116, 2010.
- [5] S. Payette, "Accelerated thawing of subarctic peatland permafrost over the last 50 years," *Geophys. Res. Lett.*, vol. 31, L18208, 2004.
- [6] M. Jolivel and M. Allard, "Thermokarst and export of sediment and organic carbon in the sheldrake river watershed, nunavik, canada," *J. Geophys. Res., Earth Surface*, vol. 118, pp. 1729–1745, 2013.
- [7] M. Allard and M. Lemay, "Nunavik and Nunatsiavut: From science to policy. An Integrated Regional Impact Study (IRIS) of climate change and modernization," *ArcticNet Inc.*, Quebec City, Canada, pp.171–197, 2012.
- [8] D. Massonnet, P. Briole, and A. Arnaud, "Deflation of Mount Etna monitored by spaceborne radar interferometry," *Nature*, vol. 375, pp. 567–570, 1995.
- [9] D. L. Galloway and J. Hoffmann, "The application of satellite differential SAR interferometry-derived ground displacements in hydrogeology," *Hydrogeol. J.*, vol. 15, pp. 133–154, 2007.
- [10] A. K. Gabriel, R. M. Goldstein, and H. A. Zebker, "Mapping small elevation changes over large areas: Differential radar interferometry," *J. Geophys. Res.*, vol. 94, pp. 9183–9191, 1989.
- [11] D. Massonnet *et al.*, "The displacement field of the Landers earthquake mapped by radar interferometry," *Nature*, vol. 364, pp. 138–142, 1993.
- [12] M. Tesauro, P. Berardino, R. Lanari, E. Sansosti, G. Fornaro, and G. Franceschetti, "Urban subsidence inside the city of Napoli (Italy) observed by satellite radar interferometry," *Geophys. Res. Lett.*, vol. 27, pp. 1961–1964, 2000.
- [13] A. Ferretti, C. Prati, and F. Rocca, "Permanent scatterers in SAR interferometry," *IEEE Trans. Geosci. Remote Sens.*, vol. 39, no. 1, pp. 8–20, Jan. 2001.
- [14] S. Usai, "A least squares database approach for SAR interferometric data," *IEEE Trans. Geosci. Remote Sens.*, vol. 41, no. 4, pp. 753–760, Apr. 2003.
- [15] P. Berardino, G. Fornaro, R. Lanari, and E. Sansosti, "A new algorithm for surface deformation monitoring based on small baseline differential SAR interferograms," *IEEE Trans. Geosci. Remote Sens.*, vol. 40, no. 11, pp. 2375–2383, Nov. 2002.
- [16] A. Hooper, "A multi-temporal InSAR method incorporating both persistent scatterer and small baseline approaches," *Geophys. Res. Lett.*, vol. 35, L16302, 2008.
- [17] A. Moreira, P. Prats-Iraola, M. Younis, G. Krieger, I. Hajnsek, and K. P. Papathanassiou, "A tutorial on synthetic aperture radar," *IEEE Geosci. Remote Sens. Mag.*, vol. 1, pp. 6–43, 2013.
- [18] N. Short, B. Brisco, N. Couture, W. Pollard, K. Murnaghan, and P. Budkewitsch, "A comparison of TerraSAR-X, RADARSAT-2 and ALOS-PALSAR interferometry for monitoring permafrost environments, case study from Herschel Island, Canada," *Remote Sens. Environ.*, vol. 115, pp. 3491–3506, 2011.
- [19] F. Calmels, M. Allard, and G. Delisle, "Development and decay of a lithals in Northern Québec: A geomorphological history," *Geomorphology*, vol. 97, pp. 287–299, 2008.
- [20] N. Short, B. Brisco, P. Budkewitsch, and K. Murnaghan, "ALOS-PALSAR interferometry for permafrost monitoring in Canada," in *Proc. 3rd Annu. ALOS Joint PI Symp.*, HI, USA, Hawaii, 2009.
- [21] N. Short, A.-M. LeBlanc, W. Sladen, G. Oldenborger, V. Mathon-Dufour, and B. Brisco, "RADARSAT-2 D-InSAR for ground displacement in permafrost terrain, validation from Iqaluit Airport, Baffin Island, Canada," *Remote Sens. Environ.*, vol. 141, pp. 40–51, 2014.
- [22] F. Chen, H. Lin, W. Zhou, T. Hong, and G. Wang, "Surface deformation detected by ALOS PALSAR small baseline SAR interferometry over permafrost environment of Beiluhe section, Tibet Plateau, China," *Remote Sens. Environ.*, vol. 138, pp. 10–18, 2013.
- [23] Z. Wang and S. Li, "Detection of winter frost heaving of the active layer of Arctic permafrost using SAR differential interferograms," in *Proc. IEEE Int. Geosci. Remote Sens. Symp.*, 1999, pp. 1946–1948.
- [24] Z. Wang and S. Li, "Thaw deformation of permafrost active layer near Toolik Lake, Alaska, imaged by DINSAR technique during summer time," *Trans. Amer. Geophys. Union*, Nov. 16, 1999, Fall Meeting Supplement (H41A-37), vol. 80, 1999.
- [25] L. Liu, T. Zhang, and J. Wahr, "InSAR measurements of surface deformation over permafrost on the North Slope of Alaska," *J. Geophys. Res., Earth Surface*, vol. 115, F03023, 2010.
- [26] T. Strozzi, U. Wegmüller, C. Werner, and A. Kos, "TerraSAR-X interferometry for surface deformation monitoring on periglacial area," in *Proc. IEEE Int. Geosci. Remote Sens. Symp.*, 2012, pp. 5214–5217.
- [27] H. Zebker and J. Villasenor, "Decorrelation in interferometric radar echoes," *IEEE Trans. Geosci. Remote Sens.*, vol. 30, no. 5, pp. 950–959, Sep. 1992.
- [28] J. R. Mackay, "A frost tube for the determination of freezing in the active layer above permafrost," *Can. Geotech. J.*, vol. 10, pp. 392–396, 1973.
- [29] C. Butterworth, *Measuring Seasonal Permafrost Deformation With Differential Interferometric Synthetic Aperture Radar*. Calgary, AB, Canada: Univ. Calgary, 2008.
- [30] B. Rabus, H. Wehn, and M. Nolan, "The importance of soil moisture and soil structure for InSAR phase and backscatter, as determined by FDTD modeling," *IEEE Trans. Geosci. Remote Sens.*, vol. 48, no. 5, pp. 2421–2429, May 2010.
- [31] I. Beck, R. Ludwig, M. Bernier, T. Strozzi, and J. Boike, "Vertical movements of frost mounds in subarctic permafrost regions analyzed using geodetic survey and satellite interferometry," *Earth Surface Dyn.*, vol. 3, pp. 409–421, 2015.
- [32] S. A. Wolfe, N. H. Short, P. D. Morse, S. H. Schwarz, and C. W. Stevens, "Evaluation of RADARSAT-2 DInSAR seasonal surface displacement in discontinuous permafrost terrain, Yellowknife, Northwest Territories, Canada," *Can. J. Remote Sens.*, vol. 40, pp. 406–422, 2014.
- [33] GAMMA RemoteSensing AG, "SAR, InSAR and DInSAR processing with GAMMA software: An example for ERS-ENVISAT cross-interferometry, Version 1.0," ed. Gümligen, Switzerland, 2008.
- [34] P. Zhao *et al.*, "Forest aboveground biomass estimation in Zhejiang Province using the integration of Landsat TM and ALOS PALSAR data," *Int. J. Appl. Earth Observation Geoinf.*, vol. 53, pp. 1–15, 2016.
- [35] M. Allard and M. K. Seguin, "Le pergélisol au Québec nordique: Bilan et perspectives," *Géographie Physique et Quaternaire*, vol. 41, pp. 141–152, 1987.
- [36] EnvironmentCanada. Canadian Climate Normals or Averages. 2017. [Online]. http://climate.weather.gc.ca/climate_normals/index_e.html
- [37] CEN 2017. Climate station data from the Umiujaq region in Nunavik, Quebec, Canada, v. 1.4 (1997–2016). Nordicana D9, doi: 10.5885/45120SL-067305A53E914AF0.
- [38] M. Pelletier, "Geomorphological, ecological and thermal time phase of permafrost degradation, Tasiapiik, Nunavik (Québec, Canada)," *Maîtrise en Sciences Géographiques*, Univ. Laval, QC, Canada, 2015.
- [39] F. Calmels and M. Allard, "Segregated ice structures in various heaved permafrost landforms through CT Scan," *Earth Surface Processes Landforms*, vol. 33, pp. 209–225, 2008.
- [40] A. Pissart, "Palsas, lithalsas and remnants of these periglacial mounds. A progress report," *Progress Physical Geography*, vol. 26, pp. 605–621, 2002.
- [41] C. Nolette, R. Lévesque, M. Allard, and M. K. Séguin, *Le pergélisol dans les formations quaternaires de la région des rivières Nastapoca et Sheldrake*, Québec nordique: Centre d'études Nordiques, Université Laval, 1988.

- [42] G. Delisle, M. Allard, R. Fortier, F. Calmels, and É. Larrivière, "Umiujaq, northern Québec: Innovative techniques to monitor the decay of a lithalsa in response to climate change," *Permafrost Periglacial Processes*, vol. 14, pp. 375–385, 2003.
- [43] I. Beck, R. Ludwig, M. Bernier, E. Lévesque, and J. Boike, "Assessing Permafrost Degradation and Land Cover Changes (1986-2009) using Remote Sensing Data over Umiujaq, Sub-Arctic Québec," *Permafrost Periglacial Processes*, vol. 26, pp. 129–141, 2015.
- [44] L. Provencher-Nolet, "Détection de changement à court terme de la toundra arbustive à partir de photographies aériennes, région d'Umiujaq, Nunavik (Québec, Canada)," Université du Québec, QC, Canada, 2014.
- [45] S.-H. Hong, S. Wdowinski, and S.-W. Kim, "Evaluation of TerraSAR-X observations for wetland InSAR application," *IEEE Trans. Geosci. Remote Sens.*, vol. 48, no. 2, pp. 864–873, Feb. 2010.
- [46] I. May, "Using in-field and remote sensing data to monitor permafrost dynamics in Northern Québec," Ph.D. dissertation, Ludwig-Maximilians-Universität München, Munich, Germany, 2011.
- [47] L. Tsang, J. A. Kong, and K.-H. Ding, *Scattering of Electromagnetic Waves, Theories and Applications*, vol. 27, Hoboken, NJ, USA: Wiley, 2000.
- [48] J. Hoffmann and D. Walter, "How complementary are SRTM-X and-C band digital elevation models?," *Photogrammetric Eng. Remote Sens.*, vol. 72, pp. 261–268, 2006.
- [49] R. Bamler, "The SRTM mission: A world-wide 30 m resolution DEM from SAR interferometry in 11 days," in *Photogrammetric Week*, 1999, pp. 145–154.
- [50] J. Kellndorfer *et al.*, "Vegetation height estimation from shuttle radar topography mission and national elevation datasets," *Remote Sens. Environ.*, vol. 93, pp. 339–358, 2004.
- [51] A. Peregon and Y. Yamagata, "The use of ALOS/PALSAR backscatter to estimate above-ground forest biomass: A case study in Western Siberia," *Remote Sens. Environ.*, vol. 137, pp. 139–146, 2013.
- [52] A. Shortridge and J. Messina, "Spatial structure and landscape associations of SRTM error," *Remote Sens. Environ.*, vol. 115, pp. 1576–1587, 2011.
- [53] WorldDEM, "WorldDEM Technical Product Specification," [Online]. Available: <http://www.geo-airbusds.com/worlddem/>, 2015
- [54] G. Riegler, S. D. Hennig, and M. Weber, "WorldDEM — A novel global foundation layer," *Int. Archives Photogrammetry, Remote Sens. Spatial Inf. Sci.*, vol. XL-3/W2, pp. 183–187, 2015.
- [55] N. R. Canada(NRCan). CanVec, Elevation in 2e5a, 2016 [Online]. <http://geogratis.gc.ca/api/en/nrcan-mcan/ess-sst/7e2e5007-c827-4ed6-b01f-706dbada7779.html>
- [56] GAMMARemoteSensingAG, "Differential Interferometry and Geocoding Software—DIFF&GEO, Version 1.3," ed, 2011.
- [57] GAMMARemoteSensingAG, "Interferometric SAR Processor - ISP, Version 1.6," ed. Gümligen, Switzerland, 2011.
- [58] R. M. Goldstein and C. L. Werner, "Radar interferogram filtering for geophysical applications," *Geophys. Res. Lett.*, vol. 25, pp. 4035–4038, 1998.
- [59] M. Costantini, "A novel phase unwrapping method based on network programming," *IEEE Trans. Geosci. Remote Sens.*, vol. 36, no. 3, pp. 813–821, May 1998.
- [60] C. L. W. Urs Wegmüller, T. Strozzi, and A. Wiesmann, "Phase Unwrapping with GAMMA ISP Technical Report, 13-May-2002," Gamma Remote Sens., Bern, Switzerland, 2002.
- [61] H. A. Zebker, P. A. Rosen, and S. Hensley, "Atmospheric effects in interferometric synthetic aperture radar surface deformation and topographic maps," *J. Geophys. Res., Solid Earth (1978–2012)*, vol. 102, pp. 7547–7563, 1997.
- [62] E. Rodriguez and J. Martin, "Theory and design of interferometric synthetic aperture radars," *IEE Proc. F Radar Signal Process.*, 1992, pp. 147–159.
- [63] S. Antonova, A. Kääh, B. Heim, M. Langer, and J. Boike, "Spatio-temporal variability of X-band radar backscatter and coherence over the Lena River Delta, Siberia," *Remote Sens. Environ.*, vol. 182, pp. 169–191, 2016.
- [64] J. Askne, M. Santoro, G. Smith, and J. E. Fransson, "Multitemporal repeat-pass SAR interferometry of boreal forests," *IEEE Trans. Geosci. Remote Sens.*, vol. 41, no. 7, pp. 1540–1550, Jul. 2003.
- [65] T. Castel, J.-M. Martinez, A. Beaudoin, U. Wegmüller, and T. Strozzi, "ERS INSAR data for remote sensing hilly forested areas," *Remote Sens. Environ.*, vol. 73, pp. 73–86, 2000.
- [66] M. A. Tanase, M. Santoro, U. Wegmüller, J. De La Riva, and F. Pérez-Cabello, "Properties of X-, C- and L-band repeat-pass interferometric SAR coherence in Mediterranean pine forests affected by fires," *Remote Sens. Environ.*, vol. 114, pp. 2182–2194, 2010.
- [67] S. Zwieback, S. Hensley, and I. Hajnsek, "Assessment of soil moisture effects on L-band radar interferometry," *Remote Sens. Environ.*, vol. 164, pp. 77–89, 2015.
- [68] X. Luo, J. Askne, G. Smith, and P. Dammert, "Coherence characteristics of radar signals from rough soil," *Progress Electromagn. Res.*, vol. 31, pp. 69–88, 2001.
- [69] L. F. de Almeida Furtado, T. S. F. Silva, and E. M. L. de Moraes Novo, "Dual-season and full-polarimetric C band SAR assessment for vegetation mapping in the Amazon várzea wetlands," *Remote Sens. Environ.*, vol. 174, pp. 212–222, 2016.
- [70] R. F. Hopkinson, D. W. McKenney, E. J. Milewska, M. F. Hutchinson, P. Papadopol, and L. A. Vincent, "Impact of aligning climatological day on gridding daily maximum—minimum temperature and precipitation over Canada," *J. Appl. Meteorol. Climatol.*, vol. 50, pp. 1654–1665, 2011.
- [71] D. Weydahl, "Analysis of ERS SAR coherence images acquired over vegetated areas and urban features," *Int. J. Remote Sens.*, vol. 22, pp. 2811–2830, 2001.
- [72] L. Bruzzone, M. Marconcini, U. Wegmüller, and A. Wiesmann, "An advanced system for the automatic classification of multitemporal SAR images," *IEEE Trans. Geosci. Remote Sens.*, vol. 42, no. 6, pp. 1321–1334, Jun. 2004.
- [73] U. Wegmüller and C. Werner, "Retrieval of vegetation parameters with SAR interferometry," *IEEE Trans. Geosci. Remote Sens.*, vol. 35, no. 1, pp. 18–24, Jan. 1997.
- [74] M. E. Engdahl, M. Borgeaud, and M. Rast, "The use of ERS-1/2 tandem interferometric coherence in the estimation of agricultural crop heights," *IEEE Trans. Geosci. Remote Sens.*, vol. 39, no. 8, pp. 1799–1806, Aug. 2001.
- [75] X. Blaes and P. Defourny, "Retrieving crop parameters based on tandem ERS 1/2 interferometric coherence images," *Remote Sens. Environ.*, vol. 88, pp. 374–385, 2003.
- [76] M. Santoro, J. Askne, G. Smith, and J. E. Fransson, "Stem volume retrieval in boreal forests from ERS-1/2 interferometry," *Remote Sens. Environ.*, vol. 81, pp. 19–35, 2002.
- [77] J. I. Askne and M. Santoro, "Automatic model-based estimation of boreal forest stem volume from repeat pass C-band InSAR coherence," *IEEE Trans. Geosci. Remote Sens.*, vol. 47, no. 2, pp. 513–516, Feb. 2009.
- [78] M. Shokr and N. Sinha, *Sea Ice: Physics and Remote Sensing*. Hoboken, NJ, USA: Wiley, 2015.
- [79] J. M. Carreiras, M. J. Vasconcelos, and R. M. Lucas, "Understanding the relationship between aboveground biomass and ALOS PALSAR data in the forests of Guinea-Bissau (West Africa)," *Remote Sens. Environ.*, vol. 121, pp. 426–442, 2012.
- [80] C. Thiel and C. Schmullius, "The potential of ALOS PALSAR backscatter and InSAR coherence for forest growing stock volume estimation in Central Siberia," *Remote Sens. Environ.*, vol. 173, pp. 258–273, 2016.
- [81] F. De Zan, A. Parizzi, P. Prats-Iraola, and P. López-Dekker, "A SAR interferometric model for soil moisture," *IEEE Trans. Geosci. Remote Sens.*, vol. 52, no. 1, pp. 418–425, Jan. 2014.
- [82] I. Hajnsek and P. Prats, "Soil moisture estimation in time with D-InSAR," in *Proc. IEEE Int. Geosci. Remote Sens. Symp.*, 2008, pp. III-546–III-549.
- [83] Y. Duguay, M. Bernier, E. Lévesque, and B. Tremblay, "Potential of C and X Band SAR for shrub growth monitoring in sub-arctic environments," *Remote Sens.*, vol. 7, pp. 9410–9430, 2015.
- [84] S. Buteau, R. Fortier, G. Delisle, and M. Allard, "Numerical simulation of the impacts of climate warming on a permafrost mound," *Permafrost Periglacial Processes*, vol. 15, pp. 41–57, 2004.
- [85] Pienitz, R., Bouchard, F., Narancic, B., Vincent, W. F., Sarrazin, D. 2017. Seasonal ice cover and catchment changes at northern thermokarst ponds in Nunavik: Observations from automated time-lapse cameras, v. 1.1 (2014–2016). Nordicana D24, doi: 10.5885/45418AD-AF6A8064C702444B.



Lingxiao Wang received the B.S. degree in geographical information system from South China Normal University, Guangzhou, China, in 2009, and the M.S. degree in cartography and geographical information system from Nanjing University, Nanjing, China, in 2012. She is currently working toward the Ph.D. degree in physical geography and remote sensing at the Ludwig-Maximilians-Universität München, Munich, Germany.

Her research interests include remote sensing of landscape and ground surface deformation, and environment modeling.



Philip Marzahn (M'09) received the Diploma degree from the Christian-Albrechts University of Kiel, Kiel, Germany, where he studied geography, soil science, hydrology, and landscape ecology, from 2001 to 2007. He received the Ph.D. degree from the Faculty of Geoscience, Ludwig-Maximilians-Universität München (LMU), Munich, Germany, in 2013.

He is currently working at the Department of Geography, LMU, as an Assistant Professor in the fields of remote sensing. His research interests include the monitoring of bio- and geophysical parameters from multidimensional SAR and optical data as well as the uncertainty assessment of such variables. He also focuses on the retrieval of parameters from remote sensing data across scales using space-, airborne as well as drone data in conjunction with wireless sensor networks. He participated in several ESA and national funded remote sensing campaigns and projects. He is a frequent reviewer of international remote sensing journals.



Monique Bernier (M'94–SM'06) received the B.S. and M.S. degrees in physical geography from the University of Sherbrooke, Sherbrooke, Canada, in 1978 and 1980, respectively. She received the Diploma in Business Administration from the University of Ottawa, Ottawa, ON, Canada, in 1987 and the Ph.D. degree in water science in 1991 from the Institut National de la Recherche Scientifique (INRS), QC, Canada.

In 1981, she began her career in remote sensing as an Environmental Scientist at the Canada Centre for Remote Sensing in Ottawa. She has been a Professor at INRS since 1993, where her research is mainly oriented toward the development of applications for SAR sensors in northern environments (snow, river ice, coastal ice, wetlands, frost ground monitoring) and the studies of the potential use of SAR data for monitoring soil moisture and estimating wind energy in coastal environments. She has more than 80 papers in refereed journals and has presented more than 325 conferences in Canadian and international symposia and workshops. She was appointed Co-Director of the Centre for Northern Studies (CEN) from 2008 to 2012. She is currently involved in the management of the CEN as the Deputy Director.

Prof. Bernier is involved on the Board of the Association of Canadian Universities for Northern Studies (ACUNS) since 2007 and was elected the ACUNS President in November 2015 for two years. In February 2016, she was appointed member of the Earth Science Advisory Committee (ESAC) for the ESA Earth Observation Program for the coming four years. She is an active member of the Canadian Remote Sensing Society (CRSS), being on the Board of Directors in the eighties and from 2002 to 2016, being the CRSS President from June 2009 to July 2014. She is the Technical Chair of the EO-Summit 2017, June 19–22, 2017. She was also the Vice-President and then the President of the Québec Association of Remote Sensing. In 2011, she was awarded the Ferdinand-Bonn Prize by AQT for her career achievements in the development of EO applications and training of high qualified persons in Canada. She hosted as the General Chair the joint IGARSS 2014/35th Canadian Symposium on Remote Sensing in Québec City. She has been an Associate Editor for the IEEE JOURNAL OF SELECTED TOPICS IN EARTH OBSERVATIONS AND REMOTE SENSING (J STARS) from 2008 (1st volume) to December 2015. She was a JSTARS Guest Editor for the Special Issue of IGARSS 2014/35th CSRS vol. 8 no. 7. She was also a member of the 2015 and 2016 GRSS Publications Awards Committee. She has been regularly invited to co-chair sessions at IGARSS and has been a member of the IGARSS Technical Program Committee in 2002, 2012, 2013, 2014, 2015, and 2016.



Andres Jacome received the B.S. degree in agricultural engineering from the Central University of Venezuela, Caracas, Venezuela, in 1990 and the Ph.D. degree in water science from the AgroParisTech Research Institute, Montpellier, France, in 2009.

He completed a postdoctoral internship at the Institut Nationale pour la Recherche Scientifique, Laboratoire Eau Terre Environnement (INRS-ETE, Québec University) and later worked as an Associate Researcher. He is currently working at FADQDI as a terrain coordinator in an international cooperation program in agricultural insurance. He has long experience in hydrological simulation for watershed management and soil erosion, land evaluation, and environmental impact. He is also expert in land survey (soil, land use and land cover, relief) with the help of Geomatics techniques: optical, radar, and LiDAR remote sensing, digital photogrammetric, GIS, and DGPS.



Jimmy Poulin received the B.S. degree in geometrics engineering from Laval University, QC, Canada, in 2004, and the M.S. degree in earth sciences from INRS, Centre Eau Terre Environnement, QC, Canada, in 2007 on CT images processing.

Since 2008, he has been a geomatics specialist with the remote sensing and hydrology lab led by professors M. Bernier and K. Chokmani. Responsible for geospatial data and geographic information systems, he develops, among other things, GIS tools for river ice monitoring, the morphological characterization of river channels, flood mapping, and stream flow estimation. He is also responsible for field equipments, including GPS systems and UAV. He is among those authorized to pilot them. He also developed an expertise in instrumentation for environmental studies.



Ralf Ludwig studied physical geography, geology, geophysics, and remote sensing and received the Diploma degree in 1993 and the Ph.D. degree from the Ludwig-Maximilians-Universität München, Munich, Germany, in 1999.

He is the Dean of the Faculty of Geosciences and a Professor in Applied Physical Geography and Environmental Modeling at LMU's Department of Geography. His research is focused on process-based and spatially distributed hydrological modeling at the catchment scale, data assimilation and model integration for water resources, land use and climate change impact assessment from Mediterranean to subarctic environments, and the energy-environment interface.

Prof. Ludwig is an Adjunct Professor at Université Laval, QC, Canada, the Co-Chair of the Collaborative Program "Changes in the Hydrological Cycle" of the European Climate Research Alliance, steering committee member of the Helmholtz research school MICMoR ("Mechanisms and Interactions of Climate Change in Mountain Regions"), and Spokesperson of the Albertan-Bavarian Energy-Environment research network ABBY-Net. He is the member of the European Geosciences Union, German Society for Photogrammetry, Remote Sensing und Geoinformation, and German Society for Canadian Studies.

3 High temporal resolution deformation monitoring over discontinuous permafrost terrain using Sentinel-1 time series

High temporal resolution deformation monitoring over discontinuous permafrost terrain using Sentinel-1 time series

Lingxiao Wang ^{a,c}, Philip Marzahn ^a, Monique Bernier ^{b,c}, Ralf Ludwig ^{a,c}

^a *Department of Geography, Ludwig-Maximilians-Universität München, Munich, Germany*

^b *Centre Eau, Terre & Environnement, Institut National de la Recherche Scientifique, Québec, Canada*

^c *Northern Research Center/Centre d'études nordiques (CEN), Québec City, Canada*

A B S T R A C T

Differential synthetic aperture radar interferometry (D-InSAR) has been applied in the permafrost environment to detect ground motion caused by permafrost activities. Discontinuous permafrost is more vulnerable to climate change because its temperature is precariously close to above freezing. Sub-Arctic discontinuous permafrost terrain shares some features with an Arctic continuous permafrost environment, but the sub-Arctic unique landscape increases the difficulty of applying D-InSAR. In this study, we explore the abilities and limitations of applying Sentinel-1 time series for monitoring surface deformation over discontinuous permafrost terrain. First, interferometric coherence and backscatter time series from September 2016 to April 2018 were analyzed over ten typical landscapes. A displacement time series is derived from the small baseline subset (SBAS) InSAR technique without any presupposition about the deformation characteristics, e.g., a commonly used sinusoidal model. The cumulative displacement is also compared with the L-band ALOS PALSAR results. The results indicate that the Sentinel-1 time series with a 6-day or 12-day span works well over discontinuous permafrost terrain below the tree line during the thawed season. Seasonal thaw subsidence in the summer of 2017 was in the range of 15 mm - 80 mm in the study area. Samples also illustrate that wet regions and drier areas tend to exhibit different seasonal thaw subsidence patterns. The wet region has a larger thaw subsidence and reaches the maximum subsidence in October before the ground freezes; the drier region has a smaller thaw subsidence and reaches maximum subsidence in August when the surface air temperature reaches its maximum.

Keywords: Permafrost, Surface deformation, Displacement curve, Sentinel-1, Interferometric coherence, SBAS-InSAR, Sub-Arctic

1. Introduction

The differential synthetic aperture radar interferometry (D-InSAR) technique has been widely used in mapping ground surface deformation, e.g., volcanology (Massonnet et al. 1995), tectonics (Massonnet et al. 1993), and in the analysis of urban and infrastructure deformation (Lanari et al. 2004). By differencing radar phases of two synthetic aperture radar (SAR) images acquired at different times, ground surface deformation occurring during two acquisitions in the line-of-sight (LOS) direction are obtained.

In permafrost areas, the seasonal freeze-thaw cycle in the active layer causes seasonal upward and downward ground motion; under the circumstance of regional warming in the northern high latitudes, thawing of the permafrost causes long-term subsidence. Several studies have demonstrated the ability of the D-InSAR technique to detect this freeze/thaw-related ground motion over permafrost regions of the Arctic (Antonova et al. 2018; Liu et al. 2014a; Liu et al. 2015; Liu et al. 2014b; Liu et al. 2012; Liu et al. 2010; Rudy et al. 2018; Rykhus and Lu 2008; Short et al. 2011; Short et al. 2014), sub-Arctic (Beck et al. 2015; Wang et al. 2017; Wolfe et al. 2014) and Qinghai-Tibet Plateau (Chang and Hanssen 2015; Chen et al. 2012; Chen et al. 2013; Daout et al. 2017; Li et al. 2015; Zhao et al. 2016). Among these studies, some have reported difficulties and challenges in continuously monitoring ground deformation over some permafrost terrain. Except for the common challenges faced by the D-InSAR technique, e.g., atmospheric disturbances (Zebker et al. 1997) and temporal decorrelation over long periods, applying D-InSAR in permafrost environments is more difficult because of severe temporal decorrelation (Antonova et al. 2018; Beck et al. 2015; Wang et al. 2017) and nonlinear motion trends caused by seasonal changes (Chen et al. 2012). InSAR accuracy and effectiveness in mapping ground surface deformation are determined by the interferometric coherence. Over permafrost terrain, winter snow cover and ground freeze-thaw cycles cause severe decorrelation. Snow cover influences the radar signal; seasonal freeze-thaw cycles alter the ground backscattering properties. Thus, decorrelation is strong in those interferograms generated by images from different seasons. In discontinuous permafrost terrain, vegetation is more developed than that in continuous permafrost areas, and the landscape is more heterogeneous. Both factors cause severe decorrelation, especially when using SAR datasets with short wavelengths (Wang et al. 2017; Wolfe et al. 2014).

With the increasing availability of datasets, several improvements have been introduced in interferometric processing to overcome the limitations of decorrelation and noise contamination, e.g., small baseline subsets (SBAS) strategy (Berardino et al. 2002; Usai 2003), persistent scatterer interferometry (PSI) (Ferretti et al. 2001), and synergistic use of SBAS and persistent scatterer (PS),

which is multi-temporal InSAR (MT-InSAR) (Hooper 2008). The SBAS strategy uses high-quality interferograms with small temporal and spatial baselines; PS uses coherent radar scatterers with high phase stability during the entire observation period; MT-InSAR increases the spatial density of coherent radar scatterers in nonurban areas.

Permafrost terrain applications normally use SBAS-InSAR and a given deformation model, usually sinusoidal (Li et al. 2015; Zhao et al. 2016) or consecutive displacement maps for one season are summarized to obtain one cumulative displacement map (Antonova et al. 2018; Rudy et al. 2018; Short et al. 2014). However, the sinusoidal model cannot fully capture the temporal variations in deformation because the surface deformation over permafrost is a complex physical process and is affected by many factors, such as precipitation, temperature, water content, heat flow, and so on, which may not vary in accordance with the sinusoidal model (Li et al. 2015; Zhao et al. 2016). The stacking method only uses the limited number of interferograms composed of acquisitions in a chronological sequence. A single seasonal cumulative displacement map is obtained from summarizing the time-sequent interferograms, but the temporal variations within the season are neglected.

The recent launch of Sentinel-1A/B has a shorter revisit time (6 days combining Sentinel-1A and 1B). The shorter revisit cycle can minimize the adverse effects of temporal decorrelation and also contributes to a detailed deformation curve description. In this study, we investigated the potential of the Sentinel-1 time series in monitoring ground surface deformation in a discontinuous permafrost environment of sub-Arctic areas. The discontinuous permafrost environment shares some landscape properties with Arctic continuous permafrost environments, e.g., tundra environment, but the discontinuous permafrost environment has a more heterogeneous landscape with scattered frozen ground and more developed vegetation cover (tall shrubs and coniferous stands) (Wang et al. 2017; Wolfe et al. 2014). The unique landscape results in more complicating factors for D-InSAR applications.

As far as we know, there is no published research analyzing potential improvements in permafrost monitoring using this high temporal resolution C-band dataset. For this study, 64 Sentinel-1 images of interferometric wide (IW) mode with VV polarization acquired from June 2014 to August 2016 were utilized. First, a time series of interferometric coherence and backscatter were analyzed. Then, the SBAS-InSAR method was implemented to calculate the deformation time series without presupposing a deformation model. Seasonal ground movements were mapped and compared with L-band ALOS PALSAR dataset. Finally, the abilities and limitations of permafrost environment

monitoring using Sentinel-1 time series were discussed.

2. Study area

The study area is located on the eastern shore of Hudson Bay in northern Québec, Canada, in the vicinity of the Inuit community of Umiujaq (56°32' N, 76°31' W) (Fig. 1 (a)). It is in a typical discontinuous permafrost region, in a transitional area between an isolated and sporadic permafrost zone (2-50% permafrost cover) and a widespread discontinuous permafrost zone (50-90% permafrost cover) (Allard and Seguin 1987), including a range of permafrost degradation states. Under a warming climate, the region changes from a widespread discontinuous permafrost zone to a sporadic and isolated permafrost zone, and this transition is currently in progress (Allard and Seguin 1987; Jolivel and Allard 2013).

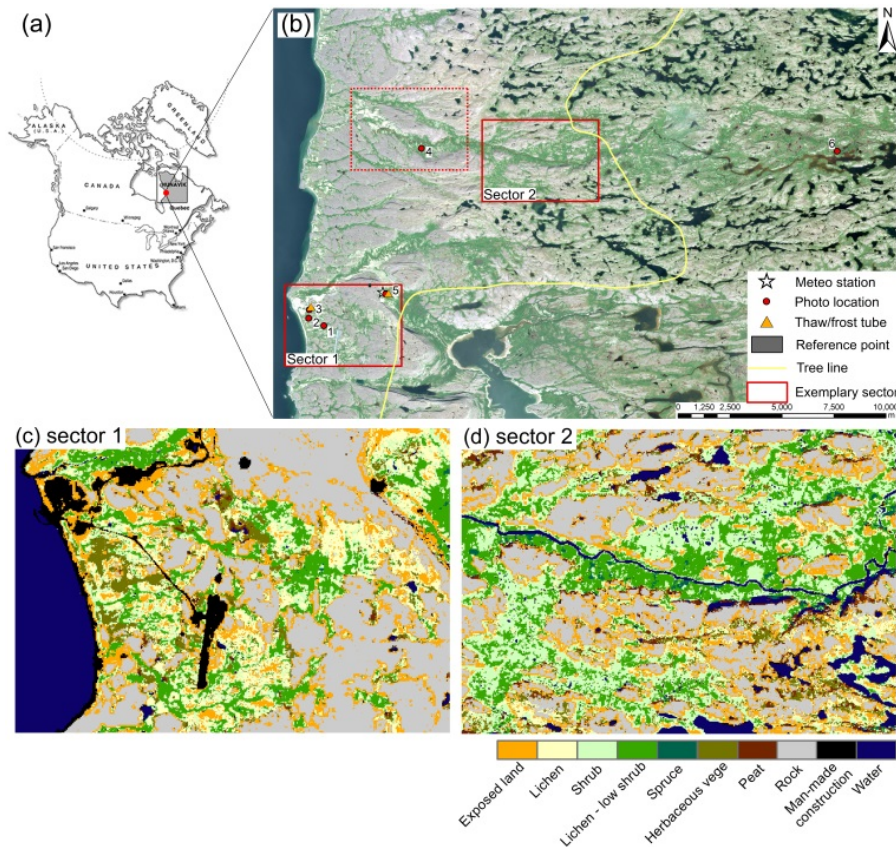


Fig. 1 (a): Location of the study area. (b): The base map is a Sentinel-2 image acquired on 2017-07-29 (RGB 4-3-2). Red rectangles indicate two exemplary sectors where maps of seasonal displacement and coherence are shown. (c) and (d) are land cover maps of the two sectors, which are interpreted using Sentinel-2 optical images.

The climate is sub-Arctic, with a mean annual air temperature (MAAT) of approximately -3 °C, the

winters are cold (-24 °C in January), and the summers are cool (10 °C in August) (EnvironmentCanada 2010). The MAAT remained stable in the 1960s-1990s; then, there was strong warming that occurred in the 1990s-2010s (MAAT increasing by two degrees). After peaking in 2010, the MAAT continuously dropped from 2010 to 2015, with the most recent two years (2016-2017) again exhibiting warming.

The cooling impact of Hudson Bay generates a west-east climate gradient from the shoreline inward; as a result, the tree line approximately 15 km inland is parallel to the coastline (Payette 1983; Payette and Gagnon 1979). In contrast to the continuous permafrost zone, the discontinuous permafrost zone is characterized by a heterogeneous landscape with numerous scattered frozen grounds of the deeper active layer, thermokarst ponds, and a more developed vegetative cover (i.e., tall shrubs and coniferous stands). The narrow coastal plain along the eastern shore of Hudson Bay is covered by a range of tundra plant communities dominated by herbaceous species, prostrate dwarf shrubs, lichens and mosses. The inland shrub-tundra landscape is dominated by lichens and erect shrubs. Black spruce patches can also be found in the shrub-tundra environment, although within small, isolated tree islands. The landscape of the forest-tundra environment 15 km inland is composed of clusters of black spruces, tundra plants, peatland and fen/bog vegetation. Permafrost is patchier and decays more rapidly in the forest-tundra environment than in the shrub-tundra environment (Jolivel and Allard 2013).

Lithalsas (mineral permafrost mounds), permafrost plateaus (elongated and wide mineral permafrost landforms), palsas (permafrost mounds with a peat cover), and peat plateaus (elongated and wide peaty permafrost landforms) are the dominant permafrost landforms in the study area (Jolivel and Allard 2013). Permafrost-affected areas are covered by either low vegetation (e.g., lichen and mosses with prostrate dwarf shrubs, herbaceous vegetation with prostrate dwarf shrubs) or by peat deposits (Wang et al. 2018). Photos of typical permafrost landforms and their vegetation cover are shown in Appendix Fig. A1, the locations of which are marked in Fig. 1 (b).

Two thaw/frost tubes within the study area provide seasonal thaw subsidence for 2014 and 2015. These thaw tubes are located over permafrost mounds of different sizes and soil textures. One thaw tube is located on a large permafrost mound deposited as a mixture of sand and silt in the active layer. Another thaw tube is located on a small permafrost mound deposited as sand in the active layer, where the soil is much coarser and drier than the first mound. The seasonal thaw subsidence measurements at the first thaw tube are 7.3 cm and 13.7 cm for 2014 and 2015, respectively. The seasonal thaw subsidence measurements at the second thaw tube are 3.3 cm and 6.4 cm for 2014

and 2015, respectively.

Two sectors (marked in Fig. 1 (b)) are selected to illustrate the seasonal displacement and coherence maps. Sector 1 is a coastal wetland located in the widespread discontinuous permafrost zone. The surface of sector 1 is modified by seasonal freeze-thaw actions, including the development of permafrost mounds and frost blisters (Fraser et al. 2005). Sector 2 is 10 km northeast to sector 1 in the sporadic permafrost zone. Permafrost mounds and small thermokarst ponds are abundant in sector 2. Sector 2 is near the tree line between the forest-tundra and shrub-tundra environments and has high shrubs in the gullies between scattered permafrost mounds.

3. Dataset and data processing

3.1. Sentinel-1

The Sentinel-1 sensor frequency is 5.4 GHz, which corresponds to a wavelength of approximately 5.6 cm. The repetition time is 12 days with Sentinel-1A or 1B alone and 6 days by combining Sentinel-1A and 1B. For this study, 64 Sentinel-1 SLC products in interferometric wide swath (IW) mode at VV polarization, acquired between 2016-09-14 and 2017-04-25, were analyzed. All scenes were acquired in ascending orbit, with an acquisition time of 18:55 local time (22:55 UTC). The incidence angles were approximately 43.5° - 45.5°. The majority of the time spans between successive acquisitions were 6 or 12 days, with two exceptions of 24 days and one exception of 18 days.

3.2 In situ data

A meteorological station (location marked in Fig. 1(b)) provided daily air temperatures (maximum, minimum, and mean values), precipitation (including rainfall and snowfall components) and snow depth information (Fig. 2). The meteorological records on the Sentinel-1 acquisition date and during the five-day period prior to image acquisition are listed in Appendix Table 1.

In the fall of 2016, snow appears on the ground for the first time on 2016-10-11, but the steady accumulation starts on 2016-10-27. The snow depth record is missing after 2017-02-25. In the fall of 2017, precipitation records are missing from 2017-12-20 to 2018-02-12. Snow appears on the ground on 2017-10-14, but the steady accumulation starts on 2017-10-29 and reaches 87 cm deep by the end of April.

The ground temperature and soil moisture content were also continuously measured at eight sites between September 2016 and September 2017. Plots of these variables can be found in Appendix Fig. A2. Dates of ground freeze-up and thaw depend on the vegetation cover, soil texture, micro-topography and snow cover conditions. Generally, peatland and high vegetation cover grounds take longer to thaw and freeze-up due to the strong insulation provided by the thick peat and dense vegetation cover.

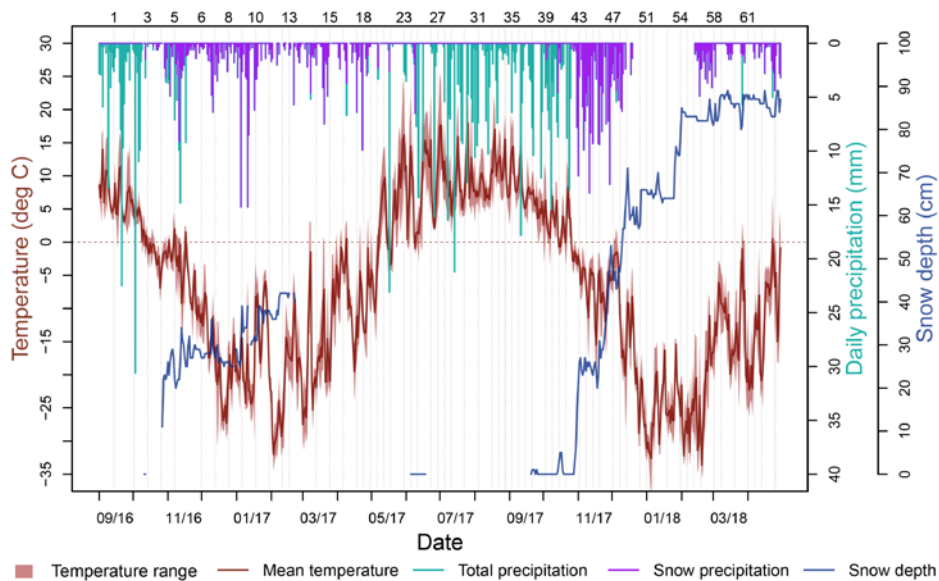


Fig. 2 Meteorological conditions from September 2016 to April 2018, including the daily air temperature (maximum, minimum, and mean values), accumulated precipitation (rainfall and snowfall components) and snow depth information. Dashed lines mark Sentinel-1 acquisitions.

3.3 Auxiliary data

A digital elevation model (DEM) was employed to simulate the topographic phase and geocode displacement results. SRTM 1-arc-second-resolution DEM (~30 m) was used in this study.

The land cover map is used to interpret the spatial distribution pattern of the derived displacements. The land cover map is generated through a maximum likelihood supervised classification based on three Sentinel-2 images acquired on 2017-07-29, 2017-08-23 and 2017-10-02. First, classification is individually applied to three Sentinel-2 images. Then, the majority of the three classification results are taken to guarantee a higher accuracy (overall accuracy is 94.8%).

L-band ALOS PALSAR-1 datasets are also utilized for comparison with the displacement results generated using Sentinel-1 datasets.

4. Methods

The SBAS-InSAR approach was selected to overcome the aforementioned strong temporal decorrelation over permafrost terrain and to calculate the surface deformation time series. The fundamental procedures of the SBAS-InSAR method are briefly introduced below; more detailed descriptions can be found in Berardino et al. (2002). In SBAS-InSAR, only the interferograms with small temporal-spatial baselines are processed and considered for deformation calculation.

Considering that $N+1$ SAR images are acquired in the chronological sequence of t_0, t_1, \dots, t_n covering the same area and each image could serve as a master image and produce at least one interferogram with other acquisitions, total M interferograms are generated according to certain temporal baseline and spatial baseline thresholds. M interferometric pairs are processed by two-pass D-InSAR and unwrapped with the same reference point. Assuming that the deformation information of the j -th interferogram $D_j(x, r)$ is obtained by comparing two acquisitions at times of t_A and t_B , this can be described as follows:

$$D_j(x, r) = d(t_B, x, r) - d(t_A, x, r) + d(\text{distortion}, x, r) \quad (1)$$

where x and r denote the pixel coordinates and $d(t_B, x, r)$ and $d(t_A, x, r)$ denote the cumulative deformation at times t_A and t_B , respectively, which relates to the value of $d(t_0, x, r)=0$. $d(\text{distortion}, x, r)$ represents the distortion terms, including the residual topographic phase, atmospheric phase and other noise. Equation (1) can be simplified as follows by only considering $d(t_B, x, r)$ and $d(t_A, x, r)$:

$$D_j(x, r) \approx d(t_B, x, r) - d(t_A, x, r) \quad (2)$$

Then, an index-like matrix A with a size of $M \times N$ is built, which indicates the two image acquisitions for each interferogram (Berardino et al. 2002). Every row in matrix A presents one interferogram combination, with number "1" indicating the master image and "-1" indicating the slave image.

$$AC = D \quad (3)$$

C is a vector of length N , loading the cumulative deformation in the chronological sequence of t_1, \dots, t_n .

The deformation time series of vector C can be obtained by solving equation (3). A simple solution for inverting the system in (3) is provided by the singular-value decomposition (SVD) method. The pseudoinverse of matrix A is calculated, and the minimum-norm LS solution of the system of (3) is obtained.

The processing workflow is shown in Fig. 3. Interferograms were generated by every image acquisition interfering with each of its three temporally neighboring acquisitions.

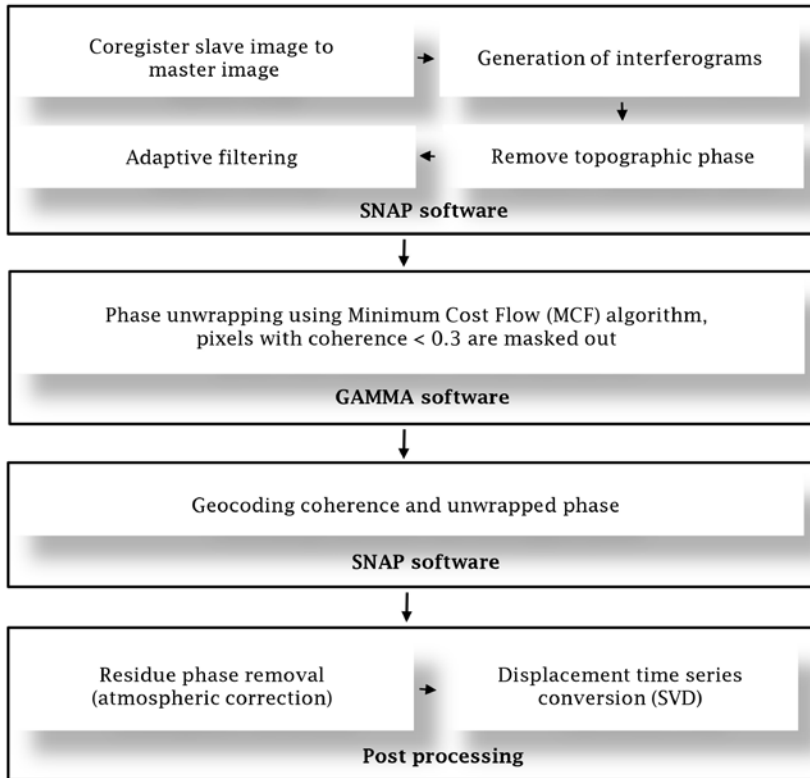


Fig. 3 Flowchart of data processing.

Interferogram processing was conducted using the Sentinel Application Platform (SNAP) software. After removal of the flat earth and topographic phase components in the generated interferogram, the differential interferogram was obtained. Then, the differential interferogram was filtered with an adaptive filter (Goldstein-Werner filter) with the settings of filtering FFT window size 32. Usually, the multi-looking operation could improve the interferogram and suppress the phase noise. However, considering the landscape heterogeneity of the discontinuous permafrost terrain, multi-looking is not applied in this study, and a small window size is used in the adaptive filtering. The phase unwrapping step is conducted using GAMMA software with a minimum cost flow algorithm (GAMMARemoteSensingAG 2011). Pixels with interferometric coherence below 0.3 were masked out and were not part of the phase unwrapping. Then, the unwrapped differential phase was geocoded to WGS 1984 UTM Zone 18N with a pixel spacing of 10 m by using a lookup table between the radar and map geometry. A small box on stable exposed bedrock was selected as a reference (see Fig. 1(b)) and the phase was set to zero. The entire displacement map was corrected to this point by subtracting the phase value at this reference point. Finally, the unwrapped phase in the radar line-of-sight (LOS) direction was converted to displacement in the vertical direction.

The atmospheric distortion influence is evident in the resulting displacement maps. The atmospheric phase delays could be identified by patterns that vary smoothly and are uncorrelated in time. The atmospheric phase delays could also be identified by the fact that they appear at the same location on the interferograms which are composed of the same contaminated acquisition. Rock outcrops are densely distributed in the study area, which provides an ideal condition to perform atmospheric phase correction in a simplified way. We assume that the displacement values on the rocky outcrops are caused by atmospheric distortions and that the nearby regions are similarly affected. To remove the atmospheric term, we first extract the residue phase on the rocky outcrop and then use an interpolator with an adaptive window size to fill the gaps.

The interferometric coherence describes the degree of correlation between two SAR observations, which indicates the quality of the D-InSAR results (Moreira et al. 2013). Accurate InSAR measurements require high coherence. In our study, coherence is estimated on the filtered differential interferogram with a 3×3 window size. A total of 169 interferograms are formed to analyze the interferometric coherence temporal variation over different landscape features in discontinuous permafrost environments. Interferograms of high-quality with short temporal baselines were selected to calculate the deformation time series using SVD conversion. These interferograms were selected to avoid the effects of wet snow, ground freezing/thawing events by virtue of metrological information and coherence information. Interferograms with obvious unwrapping errors were excluded. Finally, 44 interferogram pairs were adopted for summer 2017 and 25 pairs were adopted for winter 2017-2018. The spatial-temporal baselines of interferograms used to calculate the deformation time series are shown in Appendix Fig. A3. The spatial perpendicular baseline varied from 0.5 m to 133.8 m with a mean of 58.4 m and a standard deviation of 40.2 m, and the temporal baseline varied from 6 days to 24 days.

The mean displacement velocity is also calculated to supplement and compare with cumulative deformation by SVD convention. In the mean displacement velocity results, the noise term was somehow suppressed because the noise term was temporally uncorrelated (Hooper et al. 2007). The mean displacement velocity map and cumulative deformation map should agree with each other in the distribution pattern if good results are achieved in both calculations.

5. Results

5.1 Coherence and backscattering intensity time series

The interferometric coherence time series, along with the backscatter intensity, are shown in Fig. 5

over ten typical landscape features in the discontinuous permafrost terrain: (1) construction, (2) rocky outcrop, (3) exposed land, (4) lichen, (5) lichen - low shrub, (6) shrub, (7) spruce, (8) wetland low vegetation, and (9) peatland. For each landscape, 70 polygons of the same size (30 m long and 30 m wide) were selected on the land cover map to study the coherence and displacement properties. In the water body, coherence is completely lost for the entire time series and thus is not displayed here.

The coherence time series shown in Fig. 4 represents the mean coherence for the selected samples:

- The blue line represents the coherence calculated from the interferogram combinations of SAR images in the chronological sequence of t_i and t_{i+1} , starting with the image acquisition t_0 .
- The green line represents the coherence calculated from the interferogram combinations in the chronological sequence of t_i and t_{i+2} , starting with the image acquisition t_0 .
- The brown line represents the coherence calculated from the interferogram combinations in the chronological sequence of t_i and t_{i+2} , starting with the image acquisition t_1 .

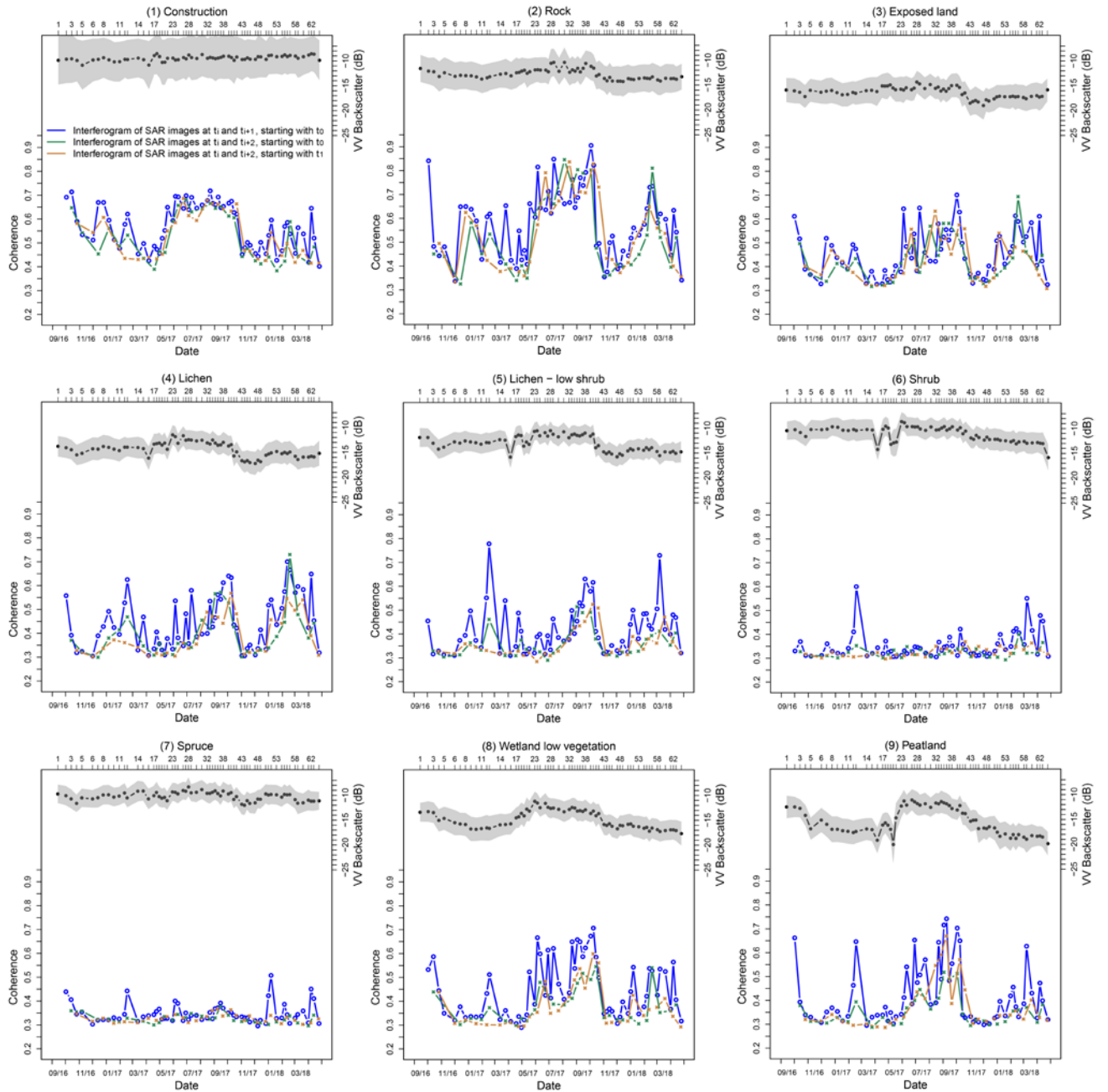


Fig. 4 Coherence and backscatter time series during the period of 2016-09-14 to 2018-04-25. The blue line represents the coherence calculated from the interferogram combinations of SAR images in the chronological sequence of t_i and t_{i+1} , starting with image acquisition t_0 ; the green line represents the coherence calculated in the chronological sequence of t_i and t_{i+2} , starting with image acquisition t_0 ; and the brown line represents the coherence calculated in the chronological sequence of t_i and t_{i+2} , starting with image acquisition t_i . The shaded area shows the mean \pm one standard deviation of the VV polarized backscatter.

Generally, landscapes from high interferometric coherence to low coherence are ordered as follows:

rock, man-made construction, exposed land, wetland low vegetation, lichen, peatland, lichen - low shrub, shrub, spruce, and water. Interferometric coherence decreases with increasing vegetation coverage and vegetation height. Temporal decorrelation is not strong over non-vegetated terrain, i.e., (1) man-made construction, (2) rocky outcrop, and (3) exposed land. Over moderately vegetated terrain, i.e., (4) lichen, (5) lichen - low shrub, (8) wetland low vegetation, and (9) peatland, the coherence of interferogram combinations in the chronological sequence of t_i and t_{i+1} (normally a time span of 6 or 12 days) is higher than in the chronological sequence of t_i and t_{i+2} (normally a time span of 12 or 18 days). Over developed vegetation, i.e., (6) shrub and (7) spruce, temporal decorrelation is already very severe with a minimum time span of 6 days.

The coherence time series shows distinctive seasonal patterns, except for (6) shrub and (7) spruce. Affected by snow metamorphism (especially wetness) and the land surface freeze/thaw cycle, the interferograms at the beginning of winter and beginning of spring are of low quality. Higher coherence occurs during the thaw season and some certain periods during winter. Over the two types with the highest coherence, i.e., (1) construction and (2) rock, the influence of snow cover accumulation and melt is especially visible since the effect of the land surface freeze/thaw cycle is negligible over these two types. During winter stable snow conditions, the moderately vegetated terrain, i.e., (4) lichen, (5) lichen - low shrub, (8) wetland low vegetation, and (9) peatland, can have higher coherence than during the summer season because the volume scattering in the canopy layer is weak during winter.

The influence of the ground freeze/thaw cycle is not distinctive in the coherence time series, which is mainly because the timing of the ground freeze/thaw transition coincides with the timing of snow accumulation and ablation; the two influences are not easily separated. Previous studies also indicate less sensitivity of coherence to moisture variations or soil freeze/thaw events compared to the backscatter sensitivity (Barrett et al. 2012).

5.2 Map of displacement and coherence

Maps of displacement and coherence are shown for one thawing season and one frozen season both in sector 1 and sector 2. SBAS-InSAR-derived cumulative deformation at the end of the season and the average deformation velocity from all interferograms used are both shown. Pixels with averaged coherences lower than 0.35 are masked out in the final displacement map to guarantee the displacement result reliability. Water bodies are also masked out.

5.2.1 Thawing season (2017-05-30 to 2017-10-21)

Fig. 5 shows the displacement map and mean coherence map derived from 44 interferograms during the thawing season of 2017. Significant seasonal thaw subsidence is evident on all displacement related maps in Fig. 5; these features are shown in the same locations both on the mean displacement velocity map and SVD converted cumulative displacement map.

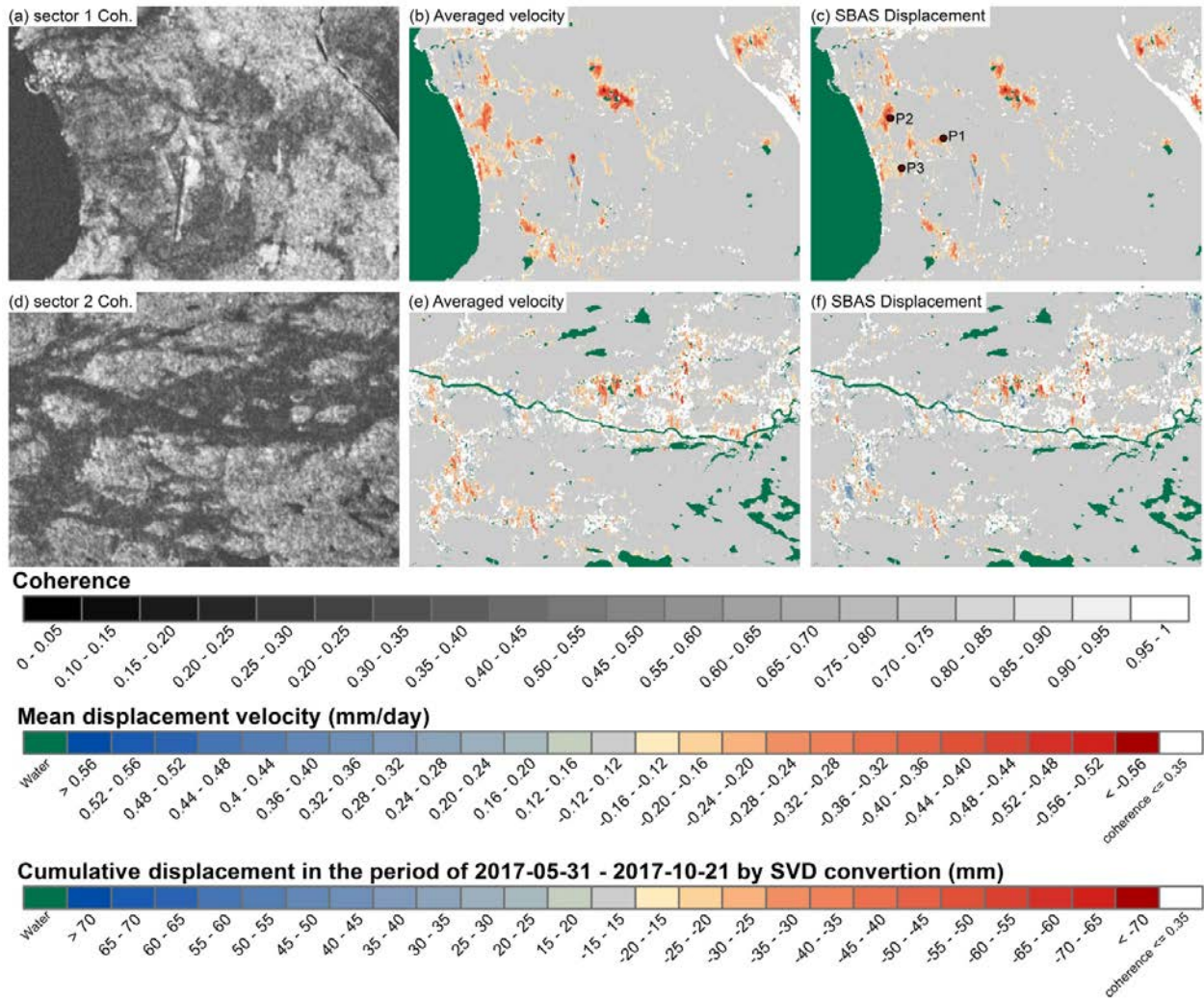


Fig. 5 Map of the vertical displacement and coherence during the period from 2017-05-31 to 2017-10-21. The first row shows the results in sector 1, and the second row shows the results in sector 2. (a) and (d) are the mean coherence values for all interferograms; (b) and (e) are the mean displacement velocities for all interferograms; (c) and (f) are the cumulative displacements derived from the SVD convention. A positive value represents surface uplift, and a negative value indicates surface settlement. The white color indicates data voids that are masked out because of decorrelation. Water bodies are masked out and displayed in green. Points “P1”, “P2” and “P3” in (c) indicate the three field photo locations shown in Fig. 6.

The coastal wetland (sector 1, first row of Fig. 5) has a higher coherence than the shrub-tundra area (sector 2, second row of Fig. 5). Another potential cause of lower coherence in the shrub-tundra area is the limited spatial resolution. The shrub-tundra landscape area is very heterogeneous: the permafrost mound is on the order of 1000 m² size, tall and dense shrubs or spruce colonize the gullies between these mounds, and small thermokarst ponds are distributed on these mounds. Phase decorrelation also arises from multiple scatterers with variable phase contributions within a resolution cell.

Large spatial variations of thaw subsidence are also observed on the displacement maps. Sectors 1 and 2 have thaw subsidence velocities in the range of 0.12 mm/day to 0.65 mm/day and cumulative subsidence rates in the range of 15 mm to 80 mm from 2017-05-30 to 2017-10-21. Apart from the permafrost-affected area, sector 1 (Fig. 5 (b) (c)) is generally stable, except for some sites in the Umiujaq village and near the airport, where a distinct uplift of up to 55 mm appears. The uplift signal is caused by new civil infrastructures. For sector 2, some slight uplift signals (50 mm) appear in the valley, which may be caused by volume scattering in the highly vegetated area.

The displacement maps were also verified with field investigations conducted in August 2015. Three field photos are shown in Fig. 6, and their locations are marked in Fig. 5 (c).



Fig. 6 Field photos of thermokarst activities. (a) P1: The road to the airport shows evidence of thaw settlement. (b) and (c) are two thermokarst ponds indicating an active thermokarst process. All photos were taken in August 2015. © Lingxiao Wang

“P1” depicts thaw subsidence of a road leading to the Umiujaq Airport. Reportedly, 15 years after the 1991 road construction, the thaw subsidence reached 0.63 m due to the thawing of underlying permafrost. Based on a field GPR survey (Fortier and Bolduc 2008), the first deposit layer is a 4.2-m-thick deltaic sand layer, and below that layer is a marine clay unit. The thawing front is already approximately 7 m in July 2007. With the increase in air temperature over the last decade, thaw settlement is in process. Seasonal thaw subsidence is clearly visible in the east and west directions from the road in displacement map Fig. 5 (b) and (c). “P2” and “P3” depict the thermokarst

ponds left by the thawing of ice-rich permafrost, which already appears in 2015 during the field campaign.

5.2.2 Freezing season (2017-12-26 to 2018-04-13)

The displacement map and mean coherence map are derived from 25 interferograms during the winter of 2017 - 2018, as shown in Fig. 7. The coherence in the frozen season is much lower than the summer thaw time because of the snow influence. Coherence is approximately 0.58 on the rocky outcrop and approximately 0.53 on top of the permafrost mounds. These two exposed features maintain higher coherence values than the other terrains because snow is swept off these exposed features by strong wind during winter.

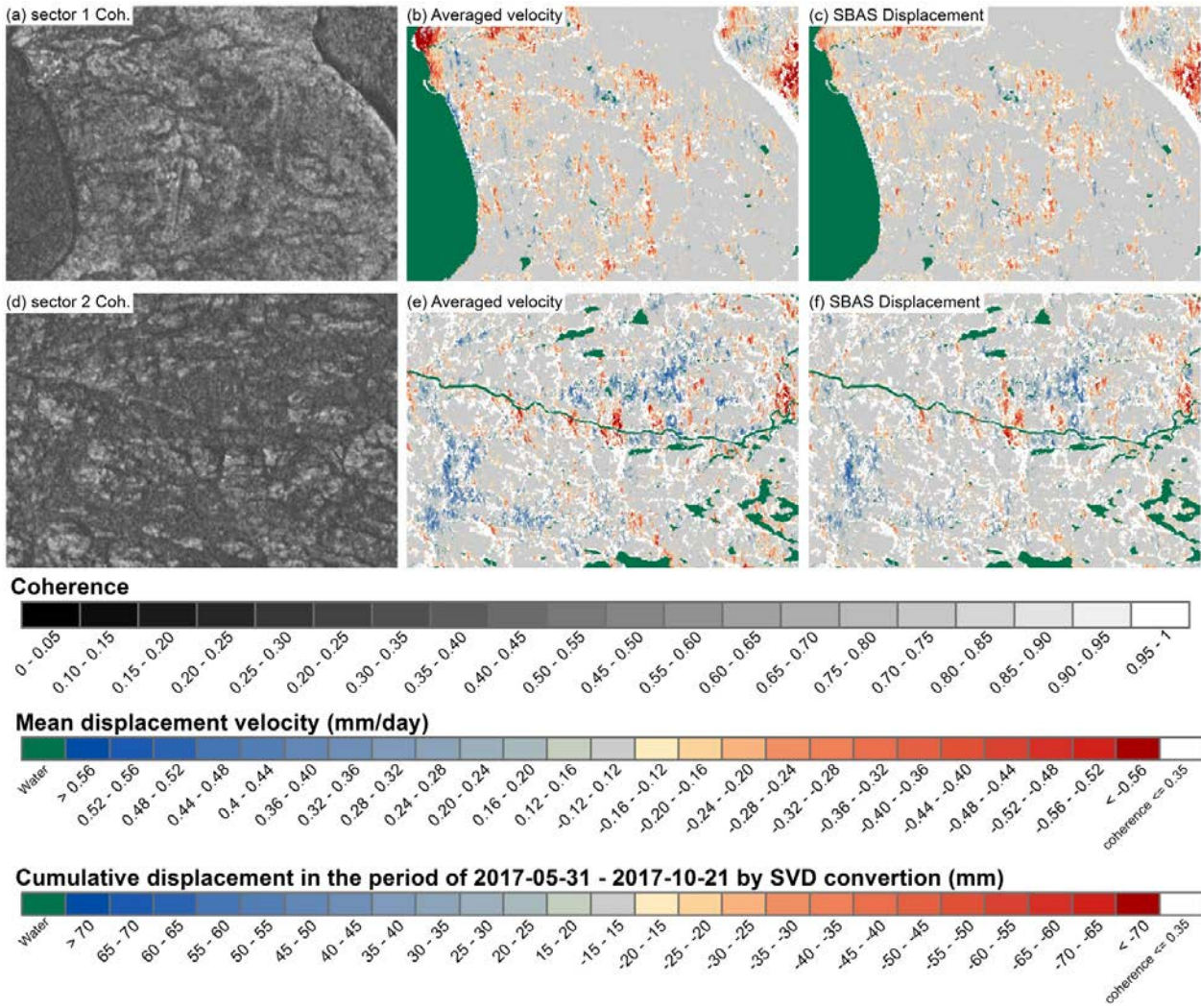


Fig. 7 Map of the vertical displacement and coherence during the winter (2017-12-26 to 2018-04-13). The first row shows results in sector 1, and the second row shows results in sector 2. (a) and (d) are the mean coherence values of all interferograms; (b) and (e) are the mean displacement velocities of all interferograms; (c) and (f) are

cumulative displacements derived from the SVD convention.

The displacement signal is related to the changes in snow water equivalent (Rott et al. 2003), more than the real ground movement. In addition, the displacement value is relative to the rocky outcrops, which means the displacement value is the difference in the changes in snow accumulation or snow water equivalent on different landscapes compared to the changes on the rocky outcrops. For example, the majority of locations exhibiting seasonal thaw subsidence (Fig. 5) do not exhibit frost heaving (Fig. 7). In sector 2, the majority of the valley shows an uplift of approximately 60 mm. The areas with high shrubs and spruces show a “subsidence” signal, most likely due to the decorrelation caused by snow accumulation.

5.2.3 Inter-annual interferogram

The interferometric coherence was also tested in the inter-annual interferogram pairs to study the ability of inter-annual monitoring.

Five interferogram pairs of autumn-autumn combinations were generated: 20160914_20170903, 20160914_20170909, 20160914_20170915, 20160914_20170921, and 20160914_20171003. The average coherence map from these five interferograms is shown in Fig. 8 (a) and (c). Image acquisitions during autumn (late August to the beginning of October, before the snow falls and ground freezes) are used because the coherence is higher than during the summer time, June and July, based on the coherence time series shown in section 5.1. Fig. 8 (a) and (c) show that only rocky outcrop and civil infrastructures maintain high coherence, and the vegetated area is completely decorrelated. Volume scattering within the vegetation layer contributes to this decorrelation.

Another five interferogram pairs of winter-winter combinations are generated: 20170130_20180131, 20170211_20180131, 20170211_20180206, 20170418_20180407, and 20170418_20180413. These image acquisitions are selected because they are not affected by wet snow and atmospheric phase delay. The average coherence map from these five interferograms is shown in Fig. 8 (b) and (d). The correlation is below 0.3 for the entire landscape, except for the Umiujaq village buildings, where moderate coherence is maintained. On the image acquisition dates, the snow is dry, inferred by the very high coherence shown in the coherence time series in Fig. 4; however, the changing snow parameters during different winters leads to decorrelation over the entire landscape. Previously, the frost mounds and rocky outcrops were assumed to have the potential to maintain moderate coherence during winter because snow is usually quickly removed from these exposed features by

the wind (Beck et al. 2015). However, the difference in snow parameters during different winters prohibits inter-annual D-InSAR monitoring using winter-winter combinations.

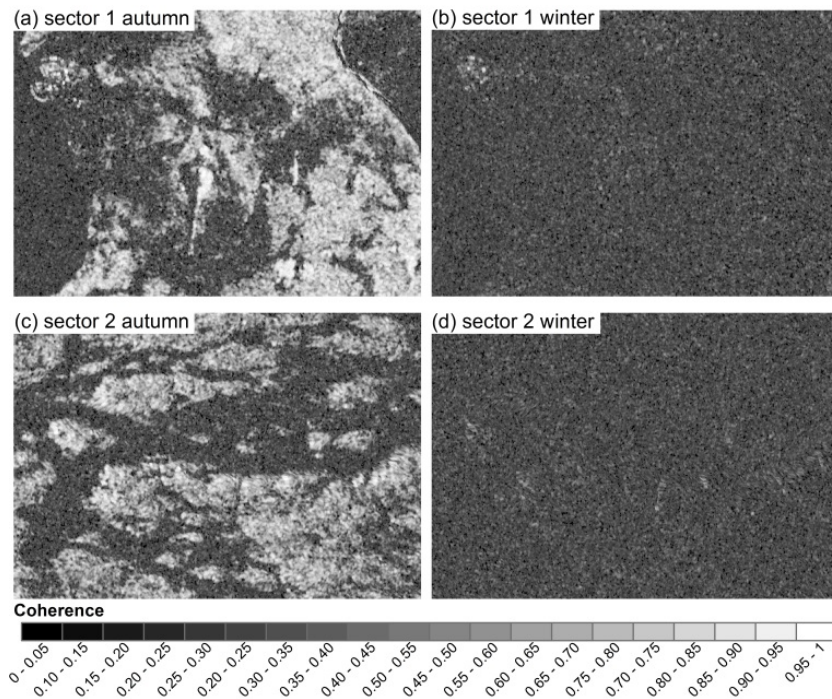


Fig. 8 The average coherence map from five inter-annual interferogram pairs in sector 1 and sector 2, (a) and (c) are derived from autumn-autumn combinations, and (b) and (d) are derived from winter-winter combinations.

5.3 Comparison with deformation maps derived from ALOS PALSAR data

Our previous study using X-band TerraSAR-X and L-band ALOS PALSAR in the same study area illustrates that the L-band result is close to the results of the ground measured displacement (Wang et al. 2017). The X-band differential phase, however, is linked to the canopy rather than the topography, and the derived ground displacement is largely underestimated due to volume scattering within the vegetation layer at our study site. Thus, result from ALOS PALSAR datasets is used as a reference to compare and validate Sentinel-1 result. The characteristics of two datasets are summarized in Table 1.

Fig. 9 shows the comparison of results between different datasets in sector 1 and sector 2. The interferogram processing procedure for ALOS PALSAR datasets is the same as the Sentinel-1 datasets, but the displacement map is obtained from a cumulative stack of consecutive interferograms and not by SVD conversion. Although the acquisition date and processing method are different for the two datasets, the location and magnitude order of the displacements should be comparable.

Table 1. List of Sentinel -1 and ALOS PALSAR-1 dataset parameters for comparison.

	Sentinel -1	ALOS PALSAR-1	
Frequency (GHz), Wavelength (cm)	5.4 GHz, 5.6cm	1.27 GHz, 23.6 cm	
Mode	Interferometric Wide swath (IW)	Fine Beam, Dual mode	
Orbit	Ascending	Ascending	
Polarization used	VV	HH	
Pixel spacing	Range: 2 m, azimuth: 14 m; Geocoded to 10 m	Range: 9.4 m, Azimuth: 3.1 m; Geocoded to 15 m	
		Orbit 127	Orbit 128
Incidence angle (°)	~44.5	~38.8	~38.7
Acquisition time	22:55 UTC, 18:55 Local	03:17 UTC, 23:17 Local	03:19 UTC, 23:19 Local
Acquisition date	2017-05-30 to 2017-10-21 19 acquisitions	2010-05-31, 2010-07-16, 2010-08-31, 2010-10-16, 4 acquisitions	2010-06-17, 2010-08-02, 2010-09-17, 2010-11-02, 4 acquisitions

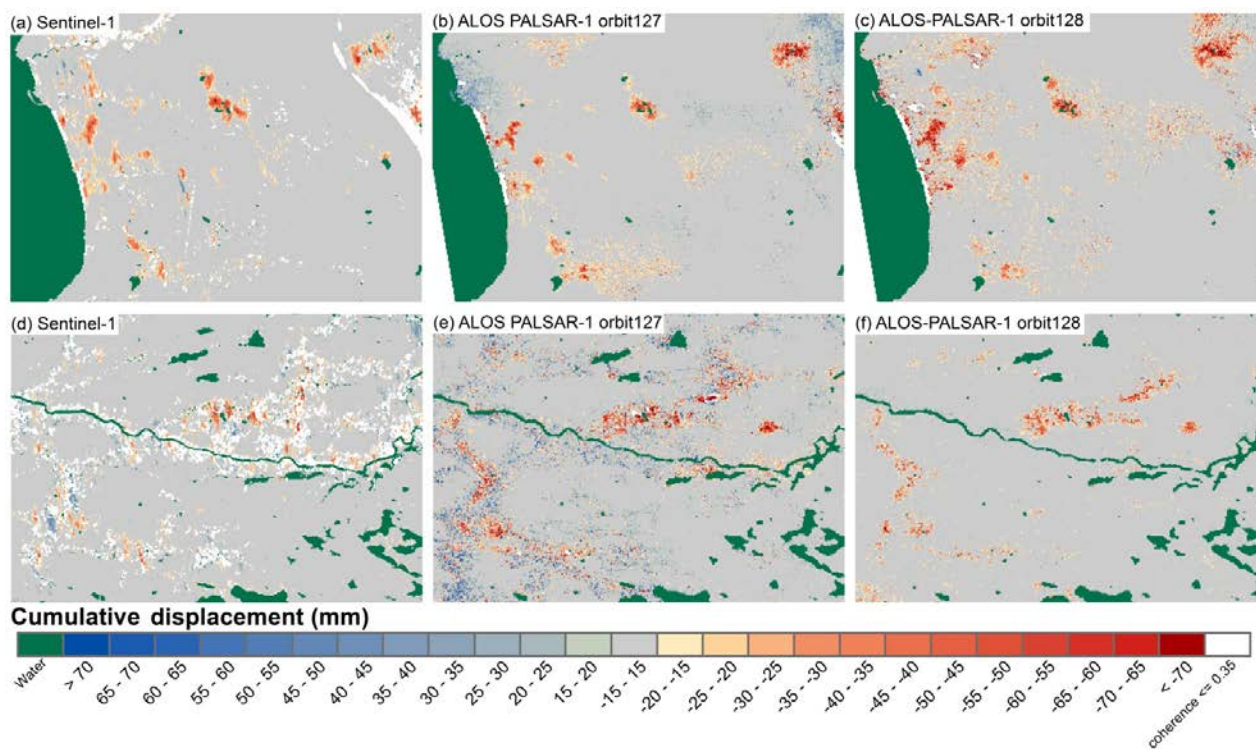


Fig. 9 Comparison of the vertical deformation map acquired using (a, d) Sentinel-1, (b, e) ALOS PALSAR orbit 127, and (c, f) ALOS PALSAR orbit 128 datasets. The first row shows a comparison in sector 1, and the second row shows a comparison in sector 2. The pixels with averaged coherence of less than 0.35 are masked out and displayed in white.

There is much more noise left in the ALOS PALSAR result because 1) only three interferograms are used to derive the cumulative displacement map and 2) the influences of soil moisture and vegetation phenology are strong considering the deeper penetration of the L-band sensor (Wang et al.

2017).

Data voids introduced by masking out the averaged coherence below 0.35 are displayed in white on the map. The results obtained from Sentinel-1 present more data voids due to decorrelation at shorter C-band wavelengths. The decorrelation phenomenon is especially clear in sector 2 near the tree line with developed vegetation cover.

In sector 1, the locations that underwent seasonal thaw subsidence perfectly matched in all the results irrespective of data voids and noise. Regarding the subsidence magnitude, the thaw subsidence derived from Sentinel-1 is approximately 10 mm smaller than that derived from ALOS PALSAR. For sector 2, near the tree line in the shrub-tundra environment, the locations that underwent seasonal subsidence do not match in the two datasets. A large amount of subsidence is visible over several permafrost mounds, according to the ALOS PALSAR results; however, the subsidence signal pattern is not distinctive in the Sentinel-1 results. In conclusion, there is good agreement over the sparsely vegetated terrain between both datasets, but considerable disagreement appears in the developed vegetation terrain. The difference comes from the volume scattering in the vegetation layer. These results also suggest that C-band Sentinel-1 could obtain good results in sub-Arctic tundra environments, but for shrub-tundra and forest-tundra environments covered by developed vegetation, the results and accuracy are not promising. We also provide another comparison result in the region marked with a red dashed box in Fig. 1(b) shown in Appendix Fig. A4. The vegetation condition of this sector is between sector 1 and sector 2, which also supports the previous findings.

5.4 Representative displacement curves

Fig. 10 shows the deformation time series from 2017-05-30 to 2017-10-21 for 70 samples from two vegetated landscapes: one is herbaceous vegetation growing on relatively wet terrain, and the other is lichen cover with prostrate shrubs growing on drier terrain.

Thawing degree days (TDD), which is an accumulation of daily air temperature above 0 °C, is indicated with a red line in Fig. 10. The ground may already begin to subside before 2017-05-30 (the date our SBAS-InSAR analysis starts) because TDD has already reached 140.4 °C on 2017-05-30, and *in situ* soil moisture and temperature measurements indicate that the ground surface starts to thaw on 2017-05-09 at some sites. However, due to snow melting and diurnal temperature oscillation in May, the decorrelation is severe before 2017-05-30. In September 2017, the air temperature starts to decrease. On 2017-10-15, the mean air temperature drops below 0 °C, and there is 3 cm of snow on

the ground (see Fig. 2 and Appendix Table 1). Interferograms with the 2017-10-15 SAR image are of low quality due to decorrelation caused by ground freezing and are thus excluded from the calculation.

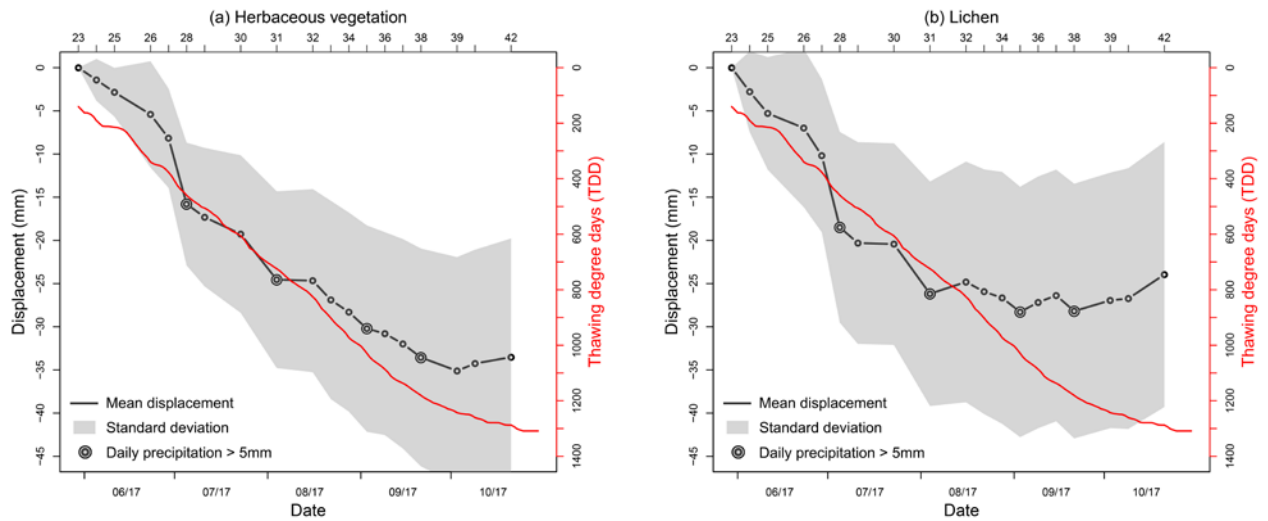


Fig. 10. SBAS-InSAR-derived displacement time series over (a) herbaceous vegetated and (b) lichen-dominated terrain. Shaded areas show the mean \pm one standard deviation.

Terrain dominated by herbaceous vegetation has a larger displacement magnitude, reaching 33.5 ± 13.7 cm from 2017-05-30 to 2017-10-21, while the displacement is 24.0 ± 15.3 cm for lichen-covered terrain.

For herbaceous vegetation-covered terrain, the cumulative subsidence from 2017-05-30 to 2017-10-03 is 33.6 ± 13.2 cm. The subsidence is gradual, and the subsidence curve is in line with the TDD curve. Normally, soil under herbaceous vegetation has a thin layer of peat cover, which may contribute to maintaining this gradual subsidence speed.

Over terrain covered by lichen and prostrate shrubs, the cumulative subsidence from 2017-05-30 to 2017-10-03 is 28.2 ± 14.8 cm. The subsidence reaches its maximum in August (Fig. 10 (b)). Subsidence velocity is large during June to July; after August, the subsidence signal is unclear.

On 2017-10-21, the slight heave in both Fig. 10(a) and (b) may be induced by superficial ground freezing, inferred from the mean air temperature dropping below zero degrees (Fig. 2). The drier terrain has a larger heave magnitude on 2017-10-21 than the wetter terrain, probably because the higher soil moisture slows the freeze-up speed considering the latent heat. The different ground freezing speeds with different soil moisture are notable in the *in situ* measurements of soil temperature and moisture each year (see Fig. A2).

The image acquisition dates with precipitation greater than 5 mm are marked with double circles in Fig. 10. The variation brought by precipitation is especially distinctive on the displacement curve of the drier terrain (Fig. 10 (b) lichen).

6. Discussion

6.1 Displacement characteristics

On a local scale with the same climate forcing, seasonal thaw subsidence/frost heave is mainly determined by the soil water content in the active layer and the active layer thickness; the secular surface subsidence is mainly determined by the excess ground ice in the permafrost beneath the active layer (Chen et al. 2013; Daout et al. 2017; Liu et al. 2010).

In our case study, the wet terrain covered by herbaceous vegetation tended to have a greater seasonal thaw subsidence than the drier terrain covered by lichen. This phenomenon agrees with previous studies. One study in the Lena River Delta of Siberia using D-InSAR monitoring with TerraSAR-X data also stated that the subsidence spatial pattern corresponded well with the relative surface wetness, as the wetter grounds showed prominent subsidence (Antonova et al. 2018). Another study in the Tibetan Plateau using an SBAS-InSAR analysis with Envisat data found that smaller seasonal ground movements occur on slopes where less water is available in the soil (Daout et al. 2017).

Ground measurements indicate a similar phenomenon that the wetter grounds showed prominent subsidence. *In situ* thaw tubes at Baffin Island, Canada (Short et al. 2014) recorded a summer settlement of 1.4 cm at a well-drained site and 8.5 cm in the low-lying wet area in 2012. Two ground-based leveling measurements over the Tibetan Plateau also show that sites with dry soil and sparse vegetation have less seasonal movement than sites with high soil water content and high vegetation coverage (Wu et al. 2018). Within our study area, the same observations are made based on measurements from two thaw tubes. One thaw tube is located in a mixture of sand and silt in the active layer; the other tube is located in sand. According to the thaw tube records, the active layer thickness is approximately 160 cm in the former and 200 cm in the latter during the same year. However, the first site has twice the seasonal thawing subsidence of the second site. The large subsidence difference is caused by the difference in soil water content, primarily determined by the soil texture on a local scale.

Regarding the timing of maximum thaw subsidence during summer, studies in the Qinghai-Tibet Plateau by (Daout et al. 2017; Li et al. 2015) indicated that the time lags between the maximum thawing settlement and highest air temperature were 1 - 3 months. The air temperature reached its maximum in mid-July, and the thawing depth reached its maximum between the beginning of September and middle of October.

In our study area, in July and August 2017, the air temperature does not show a significant difference, and the air temperature begins to drop in September (Fig. 2). According to the deformation time series curve (Fig. 10), the thawing settlement already reached its maximum in August over the lichen-dominated terrain; however, the thawing settlement reached its maximum in the first half of October over the herbaceous vegetated terrain. This phenomenon is suspected to be related with the transient zone at the bottom of the active layer and above the permafrost table. There is normally abundant of ice in the transient zone; an increase in the energy budget is required to thaw such amounts of ice, which may explain why there is no distinctive subsidence between August and the beginning of October over the lichen-dominated terrain. In our case study, herbaceous and lichen vegetation are used as simplified indicators of surficial soil water content; the discrimination of displacement characteristics over wet and dry terrain is clear, as shown in Fig. 10. However, a quantitative correlation between displacement and soil water content could not be obtained in our study, and the relation is not always true because the soil texture is substantially different in the active layer vertical profile in the study area (Lévesque et al. 1988).

6.2 Abilities and limitations of using Sentinel-1 time series with SBAS-InSAR analysis to monitor deformation over permafrost terrain

6.2.1 InSAR accuracy and effectiveness

InSAR application in deformation monitoring over permafrost terrain is limited by fast decorrelation, which is especially severe over discontinuous permafrost terrain. This decorrelation increases with a shorter radar wavelength (such as the X-band), with increasing time span, and in terrain covered by developed vegetation (Wang et al. 2017).

A previous study using a RADARSAT-2 time series with a temporal baseline of more than 24 days shows the C-band data limitation in the wet areas (Short et al. 2014). A comparison of D-InSAR result with thaw tube ground measurements suggests that D-InSAR can reasonably capture ground settlement in well-drained areas, but in wet areas subject to saturation and flooded vegetation, the D-InSAR stack significantly underestimates the actual settlement. The underestimation is due to

coherence loss and probably phase unwrapping errors (phase aliasing) caused by a high phase gradient (Short et al. 2014). A study using a 24-day-span Sentinel-1 time series also indicated that displacement is undervalued by SBAS-InSAR analysis in some regions with high vegetation coverage and high soil water content. In contrast, in regions with dry soils and sparse vegetation, the derived surface deformation is more representative of the ground movement (Wu et al. 2018). The C-band interferogram with a 24-day span is not adequate to monitor ground motion over soil with a high moisture content.

Benefiting from the short revisit cycles of Sentinel-1A/B datasets, with temporal spans of 6 or 12 days in our study area, we did not find a clear decorrelation or unwrapping error in the coastal wetland (Fig. 5, sector 1) The displacement magnitude (15 mm to 80 mm) agrees well with the ALOS PALSAR results (Fig. 9).

In the frozen winter season, the decorrelation of interferograms with 6-day or 12-day spans is caused by state changes in snow, such as changes in snow depth, snow surface roughness or hardness after a storm, and especially the liquid water content during spring. In the winter season of 2017-2018, sector 1 had a higher interferometric coherence than sector 2 (Fig. 7), which indicates snow effect. Sector 1 is located in the coastal plain, and strong winds from Hudson Bay swept the snow off the ground. Sector 2 is located inland and has a thicker snow cover because the windblown snow is captured by the abundance of shrubs and forest stands.

Previous research in the Arctic tundra regions using C-band ERS data shows the potential for maintaining coherence for individual seasons and even for several years (Liu et al. 2010). However, in the sub-Arctic shrub-tundra region of discontinuous permafrost terrain, our study illustrates that the C-band coherence cannot persist over one year after analyzing the autumn - autumn combinations and winter - winter combinations. However, benefiting from the very short revisit cycle of Sentinel-1A/B, images are acquired densely on the time scale, and a comparison of the displacement curves during snow-free periods each year is an alternative option for long-term monitoring over discontinuous permafrost terrain.

6.2.2 Distortion terms

The influence of precipitation events is seen in the displacement curve (Fig. 10). Phase dependencies on the changes of soil dielectric properties have been studied by (De Zan et al. 2014; Zwieback et al. 2015; Zwieback et al. 2016). Soil wetting acts as the increasing in the optical path between the satellite sensor and ground scatter. The influence of soil moisture increases with longer

radar wavelengths (such as the L-band) because of the deeper penetration depth (Wang et al. 2017; Zwieback et al. 2015). In our previous study using ALOS PALSAR-1 data in the same study area, the influence of vegetation phenology is also visible when shrubs turn brown/yellow in the autumn (decrease in the water content of the vegetation layer). The influence of variations in vegetation water content is the same as that of soil moisture because the dielectric properties of both depend on the water content (Tsang et al. 2000). The influence of vegetation phenology change is not detected in this study because the regions with high shrub cover are generally decorrelated in the interferogram and masked out in the final displacement map. It is possible that the slight uplift signal in the displacement curve over the terrain dominated by lichen - prostrate shrub (Fig. 10 (b)) from September to the beginning of October before ground freezing is related to vegetation yellowing. However, the displacement magnitude is too small to be treated as a real signal rather than noise.

If we assume the soil moisture has a close relationship with cumulative precipitation several days prior to the image acquisition date, the variation in precipitation near the SAR acquisition date can serve as an approximation of the soil moisture changes. The cumulative precipitation five days prior to the image acquisition date is summarized in Appendix Table A1. The three dates that have the largest cumulative precipitation variation compared to the former date are 2017-07-11 (scene number: 29), 2017-09-15 (scene number: 37), and 2017-06-29 (scene number: 27); however, the displacement curve variation is not as distinctive as a precipitation event. The strong precipitation event on the image acquisition date has a more direct and profound effect on the displacement variation than the cumulative precipitation several days prior to the image acquisition date.

The atmospheric phase delay is also visible in the generated interferogram. The atmospheric phase delay could result in a noticeable displacement error. In MT-InSAR processing, a phase due to atmospheric delay and orbit errors was estimated and removed by spatiotemporal filtering, taking the properties of deformation signals correlated in time, and atmospheric effects correlated in space but not in time (Hooper 2008; Hooper et al. 2007). Some methods and models have been proposed to estimate atmospheric delays on a single interferogram. The phase delay due to the stratified atmosphere is estimated using weather reanalysis datasets (e.g., ECMWF ERA-Interim, NARR, MERRA) or GPS estimated tropospheric zenith total delay data (Jolivet et al. 2014; Jolivet et al. 2011; Yu et al. 2018; Yu et al. 2017). The ionospheric effect is due to the propagation velocity changes of microwaves, which are caused by the high density of free electrons in the ionosphere. Low-frequency (L or P-band) radars are more severely affected than higher frequency (C or X-band) systems. Ionospheric effects on Sentinel-1 interferograms have also been reported to be strong in

recent studies (Gomba et al. 2017). The range split-spectrum method has been developed to estimate the differential ionospheric path delay (Gomba et al. 2017; Gomba et al. 2015). In our study, atmospheric correction was first attempted by using the method provided by Yu et al. (2018). However, the phase residues caused by ionospheric influence were still visible. Thus, an alternative method was tested, which makes use of the residual phase left on the stable rocky outcrops. The residual phase on the stable rocky outcrops is assumed to be mainly caused by atmospheric distortion; the atmospheric phase in the nearby region is estimated through the interpolation of residue phases on the rocky outcrops and subtracted from the displacement map. This method provides a spatial estimation of atmospheric phase residue and performs well in our case study.

6.2.3 Spatial resolution and validation difficulty

The causes of surface deformation over permafrost terrain are complicated. Surface deformation is controlled by the active layer thickness and water/ice content stored in the active layer and the underlying permafrost (Daout et al. 2017). Substrate properties and water content can be largely different, even over small distances (Nelson et al. 1999; Burgess et al. 2000; Walker et al. 2004). A non-uniform distribution of the thermal state and water content in the ground leads to heterogeneous uplift/subsidence within the sensor resolution cell (Antonova et al. 2018).

The spatial resolution is approximately 20 m for the Sentinel -1 IW mode datasets. Phase decorrelation can arise from multiple scatterers with variable phase contributions within a resolution cell (Hooper et al. 2007; Zwieback et al. 2016). This can result in phase decorrelation and systematic errors influencing the accuracy. The spatial resolution is an especially limiting factor over discontinuous permafrost terrain. Strong decorrelation over discontinuous permafrost terrain can arise from the high spatial variability of the landscape within the resolution cell and developed vegetation cover (Wang et al. 2017; Wolfe et al. 2014), and some permafrost mounds are even smaller than 20 m across.

In situ ground measurements of displacements over permafrost terrain are obtained from thaw tubes (Antonova et al. 2018; Short et al. 2014; Wang et al. 2017), linear variable differential transformers displacement transducers (LVDTs) (Harris et al. 2007), dGPS (Beck et al. 2015; Little et al. 2003; Shiklomanov et al. 2013; Streletskiy et al. 2017) and ground leveling measurements (Chen et al. 2013; Wu et al. 2018). The inadequate resolution also makes it difficult to compare the pointwise *in situ* ground measurements with the D-InSAR results. In addition, due to the limited points of ground-truth measurements, it is difficult to quantitatively evaluate the accuracy of the

D-InSAR results using statistical methods.

7. Conclusions

In this study, we explored the abilities and limitations of applying Sentinel-1 time series for monitoring ground deformation over discontinuous permafrost terrain. Interferometric coherence and backscatter time series from September 2016 to April 2018 were analyzed over ten typical landscapes. A displacement time series was derived using the SBAS-InSAR technique without any presupposition about the deformation characteristics, e.g., sinusoidal model. The cumulative displacement is also compared with the L-band ALOS PALSAR result. The following conclusions are obtained:

1) The Sentinel-1 time series with a 6-day or 12-day span can work well over some regions of discontinuous permafrost terrain during the thawed season. Good results could be obtained in the sub-Arctic tundra environment below the tree line (tundra, tundra wetlands and less developed shrub-tundra environment), but the results and accuracy are not promising over developed shrub-tundra and especially forest-tundra environments.

Deformation mapping during the winter season is difficult in our study area due to snow effect, and the uplift signal during the winter period is more likely related to the change in the snow metamorphic state (depth, hardness, wetness) rather than frost heaving in the active layer of permafrost. Affected by snow metamorphism (especially wetness) and the land surface freeze/thaw cycle, the interferogram in the beginning of winter and beginning of spring is low quality.

In contrast to the Arctic tundra, C-band interferometric coherence could not persist over the year in this sub-Arctic shrub-tundra environment after analyzing the inter-annual autumn - autumn combination or winter - winter combination.

2) The SBAS-InSAR analysis without any presupposition about the deformation characteristics works well with high temporal resolution Sentinel-1 time series, and the displacement curve can be depicted in detail.

Seasonal thaw subsidence during the summer of 2017 was estimated to be in the range of 15 mm - 80 mm. Wetter soils tend to have greater seasonal thaw subsidence. The thaw subsidence also exhibits different patterns over different land covers. The coastal wetland has a gradual subsidence

from early June to early October. Over the drier terrain dominated by lichen and prostrate shrubs, subsidence reaches its maximum in August when the surface air temperature reaches its maximum; after August, the subsidence signal is unclear. This phenomenon is suspected to be related with the transient zone at the bottom of the active layer and above permafrost table.

3) The spatial resolution is a limiting factor over discontinuous permafrost terrain. The decorrelation caused by the landscape heterogeneity and developed vegetation is especially clear in the shrub-tundra environment near the tree line.

In the study area, the inter-annual D-InSAR monitoring is difficult to apply due to decorrelation using C-band data. However, benefiting from the very short revisit cycle of the Sentinel-1A/B, SAR images are acquired densely on the time scale. Then, an annual comparison of the displacement curve during the snow-free period could be used as an alternative option for long-term monitoring over discontinuous permafrost terrain.

Acknowledgments

The authors acknowledge the European Commission and European Space Agency (ESA) for providing access to the Sentinel-1 data, and the Alaska Satellite Facility Distributed Active Archive Centers (ASF DAAC) for providing access to the ALOS PALSAR data. This project is supported by grants and contributions from the Bavarian Research Alliance (BayFOR), the Canadian Space Agency (CSA, grant number: 14SUSMAPIN), the Helmholtz Research School of Mechanisms and Interactions of Climate Change in Mountain Regions (MICMoR) and the Québec Research Funds (FRQ) - Northern Research Center (CEN). Displacement measurements from thaw tubes were kindly supplied by Jonathan Roger (CEN) and Jayson Eppler (MDA). The authors also thank Prof. Michel Allard (CEN) for his expert advice and Denis Sarrazin (CEN) for his technical and logistical assistance as well as Jimmy Poulin (INRS), Andres Jacome (INRS), Chaima Touati (INRS) and Yueli Chen (LMU) for providing valuable assistance during field work and field data analysis. The authors are grateful to the CEN for providing helicopter use and logistical support. We are also grateful to the Inuit community of Umiujaq for their generous hospitality.

Appendix

Table A1 Meteorological conditions on the date of Sentinel-1 image acquisition and the five-day period prior to image acquisition.

Scene No.	Date of Sentinel-1 Acquisition	Maximum Temperature (°C)		Mean Temperature (°C)		Minimum Temperature (°C)		Rain Precipitation (mm)		Snow Precipitation (mm)		Total Precipitation (mm)		Snow Depth (cm)	
		Over pass Day	Five days prior	Over pass Day	Five days prior	Over pass Day	Accu. Five days prior	Over pass Day	Accu. Five days prior	Over pass Day	Accu. Five days prior	Over pass Day	Five days prior	Over pass Day	Five days prior
23	2017-05-30	22.5	19.5	16.2	12.5	9.9	5.3	2.6	2.6	0.0	0.0	2.6	2.6	NA	NA
24	2017-06-05	22.6	13.6	14.5	7.9	6.3	2.2	0.0	3.5	0.0	0.0	0.0	3.5	0	NA
25	2017-06-11	2.9	4.8	1.5	2.5	0.0	0.3	0.0	9.2	0.0	7.8	0.0	17.0	0	0
26	2017-06-23	22.3	19.0	15.4	13.1	8.4	7.1	0.3	0.3	0.0	0.0	0.3	0.3	NA	NA
27	2017-06-29	17.6	9.5	11.2	6.1	4.7	2.7	0.0	19.5	0.0	0.0	0.0	19.5	NA	NA
28	2017-07-05	17.8	19.0	12.2	13.9	6.6	8.8	5.4	5.7	0.0	0.0	5.4	5.7	NA	NA
29	2017-07-11	6.8	10.8	4.0	7.3	1.2	3.8	1.4	31.4	0.0	0.0	1.4	31.4	NA	NA
30	2017-07-23	10.1	9.2	7.1	6.7	4.0	4.2	0.0	22.8	0.0	0.0	0.0	22.8	NA	NA
31	2017-08-04	7.4	9.6	6.9	7.4	6.4	5.2	7.4	28.5	0.0	0.0	7.4	28.5	NA	NA
32	2017-08-16	13.7	10.5	10.9	8.2	8.0	5.9	0.6	15.6	0.0	0.0	0.6	15.6	NA	NA
33	2017-08-22	15.5	16.6	12.1	13.1	8.7	9.7	0.6	11.4	0.0	0.0	0.6	11.4	NA	NA
34	2017-08-28	18.9	15.3	15.5	11.5	12.1	7.7	0.9	4.4	0.0	0.0	0.9	4.4	NA	NA
35	2017-09-03	17.0	13.0	13.8	9.4	10.5	5.7	6.4	9.4	0.0	0.0	6.4	9.4	NA	NA
36	2017-09-09	12.5	10.6	9.5	8.7	6.5	6.6	0.0	5.2	0.0	0.0	0.0	5.2	NA	NA
37	2017-09-15	6.6	10.3	5.1	7.9	3.5	5.5	0.0	26.1	0.0	0.0	0.0	26.1	NA	NA
38	2017-09-21	10.4	9.9	7.3	7.6	4.1	5.2	7.8	16.6	0.0	0.0	7.8	16.6	1	NA
39	2017-10-03	9.9	8.2	6.3	4.8	2.7	1.2	4.1	23.8	0.0	0.0	4.1	23.8	0	0
40	2017-10-09	8.1	5.2	6.9	2.9	5.7	0.7	3.5	32.8	0.0	0.3	3.5	33.1	0	0
41	2017-10-15	0.6	5.0	-0.7	2.8	-1.9	0.5	0.0	14.0	0.4	5.0	0.4	19.0	3	0.8
42	2017-10-21	3.4	4.2	-0.1	1.7	-3.6	-0.7	0.0	6.4	0.0	0.0	0.0	6.4	0	1.2

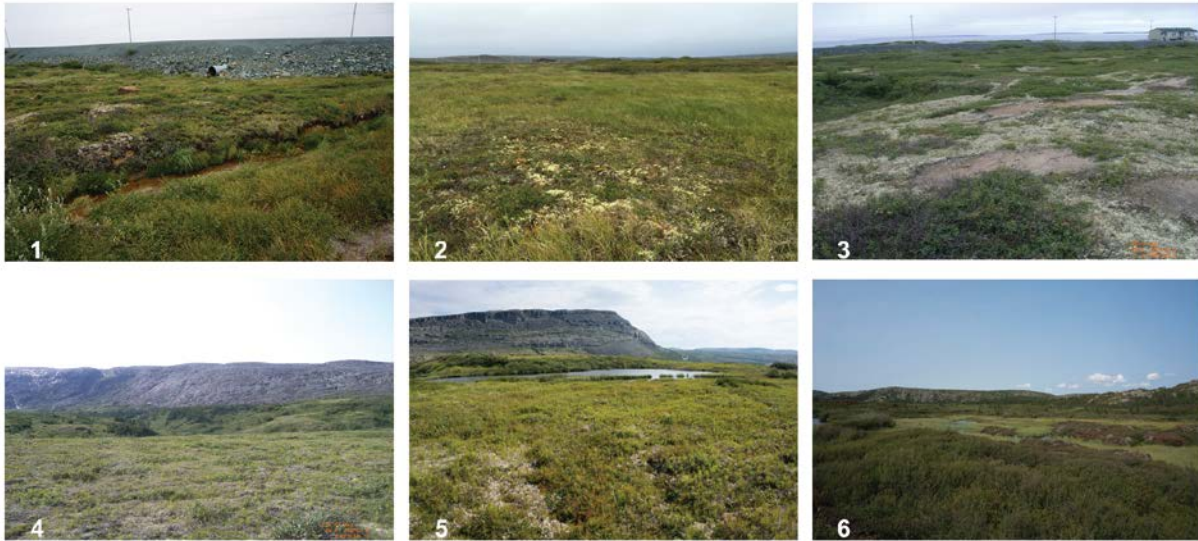


Fig. A1 Field photos of vegetation on typical permafrost landforms, the locations of which are marked in Fig. 1 (b). (1) and (2) are located on the coastal wetland dominated by herbaceous vegetation and prostrate/very low shrubs (~20 cm). (3) is located on a permafrost mound covered by a mixture of lichen and prostrate shrubs (<20 cm). (4) and (5) are located on the large permafrost mound or permafrost plateau covered by a mixture of lichen, moss and low shrubs (~25 cm). (6) is located on an elongated peaty permafrost mound with peat exposure, shrubs (~30 cm) and small cracks spread over the surface.

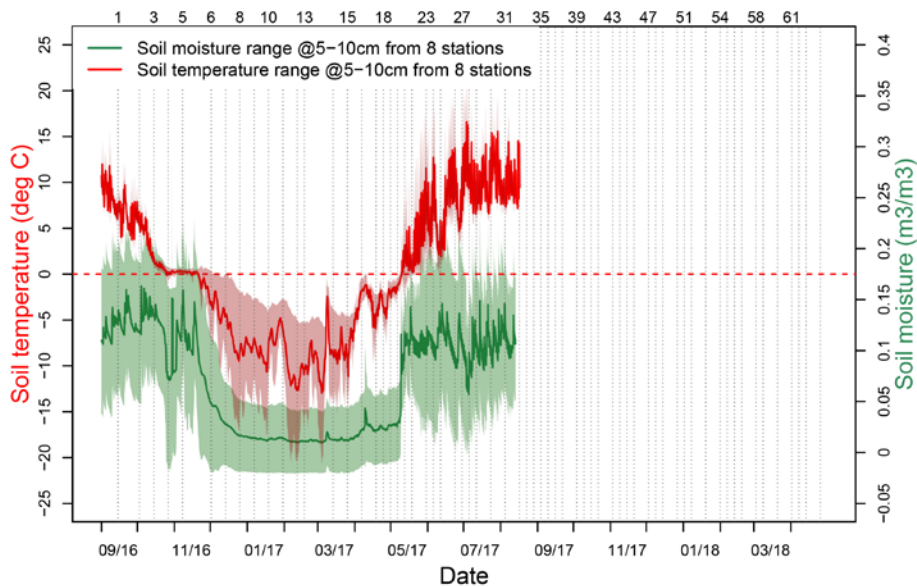


Fig. A2 *In situ* measurements of soil temperature (red) and soil water content (green) at 5 cm and 10 cm depth from eight sites within the study area. The solid lines indicate the averaged values from all measurements on a given date, and the light colored areas show the mean \pm one standard deviation. The dashed lines mark Sentinel-1 acquisitions.

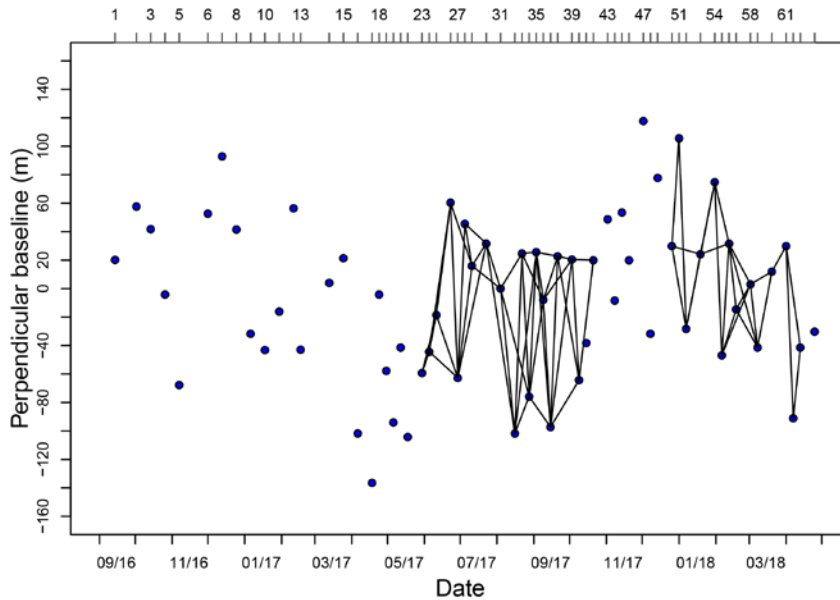


Fig. A3 The spatial-temporal baselines of interferograms used to calculate the deformation time series. The blue circles represent the Sentinel-1 acquisitions, and the gray lines represent the interferogram combinations.

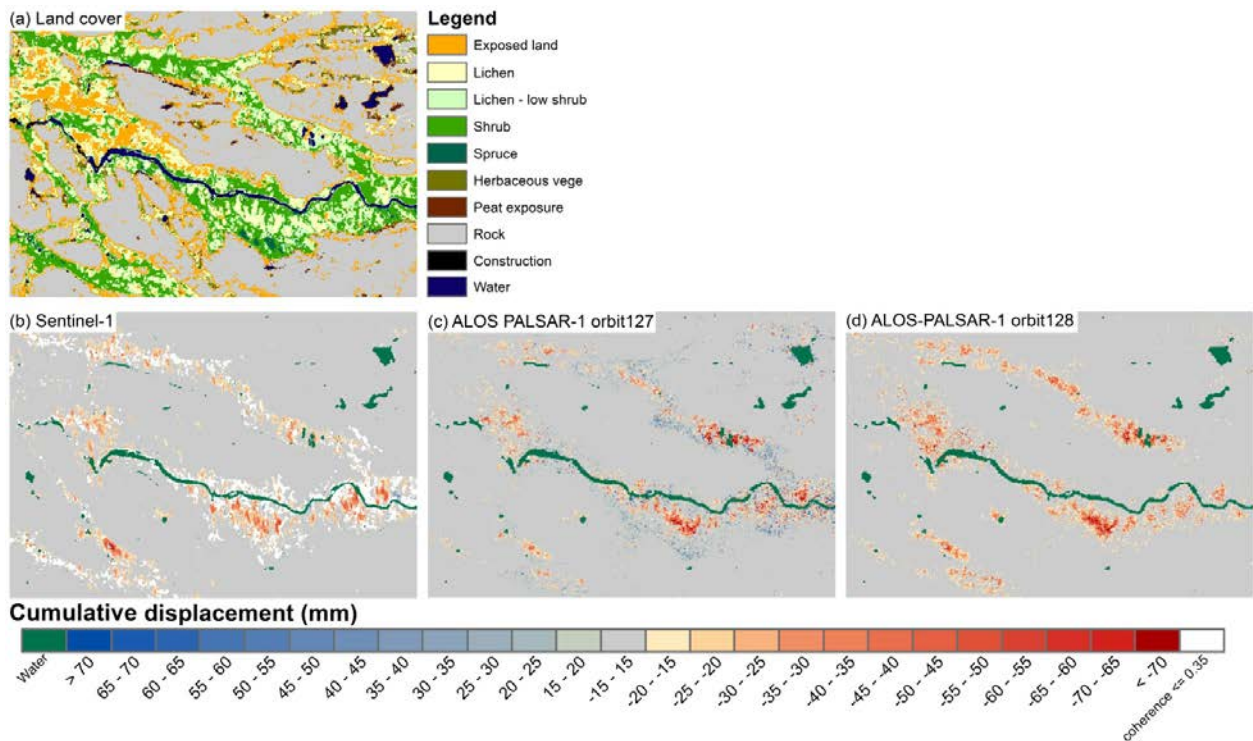


Fig. A4 Comparison of the vertical deformation map in the region marked with a red dashed box in Fig. 1(b). (a) Land cover map of this region; (b) results acquired by Sentinel-1 datasets, (c) ALOS PALSAR -1 orbit 127 datasets, and (d) ALOS PALSAR -2 orbit 128 datasets. Pixels with an average coherence of less than 0.35 are masked out and displayed in white. The spatial displacement pattern agrees well with the Sentinel-1 and ALOS PALSAR results. Regarding the displacement magnitude, the Sentinel-1 result also slightly underestimates the displacement compared to the ALOS PALSAR result.

References

- Allard, M., & Seguin, M.K. (1987). Le pergélisol au Québec nordique: bilan et perspectives. *Géographie physique et Quaternaire*, 41, 141-152
- Antonova, S., Sudhaus, H., Strozzi, T., Zwieback, S., Kääb, A., Heim, B., Langer, M., Bornemann, N., & Boike, J. (2018). Thaw Subsidence of a Yedoma Landscape in Northern Siberia, Measured In Situ and Estimated from TerraSAR-X Interferometry. *Remote Sensing*, 10, 494
- Barrett, B., Whelan, P., & Dwyer, E. (2012). The use of C-and L-band repeat-pass interferometric SAR coherence for soil moisture change detection in vegetated areas. *Open Remote Sensing Journal*, 5, 37-53
- Beck, I., Ludwig, R., Bernier, M., Strozzi, T., & Boike, J. (2015). Vertical movements of frost mounds in subarctic permafrost regions analyzed using geodetic survey and satellite interferometry. *Earth Surface Dynamics*, 3, 409-421
- Berardino, P., Fornaro, G., Lanari, R., & Sansosti, E. (2002). A new algorithm for surface deformation monitoring based on small baseline differential SAR interferograms. *Geoscience and Remote Sensing, IEEE Transactions on*, 40, 2375-2383
- Chang, L., & Hanssen, R.F. (2015). Detection of permafrost sensitivity of the Qinghai–Tibet railway using satellite radar interferometry. *International Journal of Remote Sensing*, 36, 691-700
- Chen, F., Lin, H., Li, Z., Chen, Q., & Zhou, J. (2012). Interaction between permafrost and infrastructure along the Qinghai–Tibet Railway detected via jointly analysis of C-and L-band small baseline SAR interferometry. *Remote Sensing of Environment*, 123, 532-540
- Chen, F., Lin, H., Zhou, W., Hong, T., & Wang, G. (2013). Surface deformation detected by ALOS PALSAR small baseline SAR interferometry over permafrost environment of Beiluhe section, Tibet Plateau, China. *Remote Sensing of Environment*, 138, 10-18
- Daout, S., Doin, M.P., Peltzer, G., Socquet, A., & Lasserre, C. (2017). Large - scale InSAR monitoring of permafrost freeze - thaw cycles on the Tibetan Plateau. *Geophysical Research Letters*, 44, 901-909
- De Zan, F., Parizzi, A., Prats-Iraola, P., & López-Dekker, P. (2014). A SAR interferometric model for soil moisture. *IEEE Transactions on Geoscience and Remote Sensing*, 52, 418-425
- EnvironmentCanada (2010). Canadian Climate Normals or Averages. In. http://climate.weather.gc.ca/climate_normals/results_1981_2010_e.html?stnID=6083&autofwd=1
- Ferretti, A., Prati, C., & Rocca, F. (2001). Permanent scatterers in SAR interferometry. *Geoscience and Remote Sensing, IEEE Transactions on*, 39, 8-20
- Fortier, R., & Bolduc, M. (2008). Thaw settlement of degrading permafrost: A geohazard affecting the performance of man-made infrastructures at Umiujaq in Nunavik (Québec). In, *J. Locat, D. Perret, D. Turmel, D. Demers and Leroueil, S. 2008. Proceedings of the 4th Canadian Conference on Geohazards: From Causes to Management. Presse de l'Université Laval, Québec* (pp. 279-286)
- Fraser, C., Hill, P.R., & Allard, M. (2005). Morphology and facies architecture of a falling sea level strandplain, Umiujaq, Hudson Bay, Canada. *Sedimentology*, 52, 141-160
- GAMMARemoteSensingAG (2011). Interferometric SAR Processor - ISP, Version 1.6. In. Gümligen, Switzerland
- Gomba, G., González, F.R., & De Zan, F. (2017). Ionospheric phase screen compensation for the Sentinel-1 TOPS and ALOS-2 ScanSAR modes. *IEEE Transactions on Geoscience and Remote Sensing*, 55, 223-235
- Gomba, G., Parizzi, A., De Zan, F., Eineder, M., & Bamler, R. (2015). Toward operational compensation of ionospheric effects in SAR interferograms: The split-spectrum method. *IEEE Transactions on Geoscience and Remote Sensing*, 54, 1446-1461
- Harris, C., Luetschg, M., Davies, M.C., Smith, F., Christiansen, H.H., & Isaksen, K. (2007). Field instrumentation for real - time monitoring of periglacial solifluction. *Permafrost and Periglacial Processes*, 18, 105-114
- Hooper, A. (2008). A multi-temporal InSAR method incorporating both persistent scatterer and small baseline approaches. *Geophysical Research Letters*, 35

- Hooper, A., Segall, P., & Zebker, H. (2007). Persistent scatterer interferometric synthetic aperture radar for crustal deformation analysis, with application to Volcán Alcedo, Galápagos. *Journal of Geophysical Research: Solid Earth* (1978–2012), 112
- Jolivel, M., & Allard, M. (2013). Thermokarst and export of sediment and organic carbon in the Sheldrake River watershed, Nunavik, Canada. *Journal of Geophysical Research: Earth Surface*, 118, 1729-1745
- Jolivet, R., Agram, P.S., Lin, N.Y., Simons, M., Doin, M.P., Peltzer, G., & Li, Z. (2014). Improving InSAR geodesy using global atmospheric models. *Journal of Geophysical Research: Solid Earth*, 119, 2324-2341
- Jolivet, R., Grandin, R., Lasserre, C., Doin, M.P., & Peltzer, G. (2011). Systematic InSAR tropospheric phase delay corrections from global meteorological reanalysis data. *Geophysical Research Letters*, 38
- Lanari, R., Lundgren, P., Manzo, M., & Casu, F. (2004). Satellite radar interferometry time series analysis of surface deformation for Los Angeles, California. *Geophysical Research Letters*, 31
- Lévesque, R., Allard, M., & Séguin, M.K. (1988). *Le pergélisol dans les formations quaternaires de la région des rivières Nastapoca et Sheldrake, Québec nordique*. Centre d'études nordiques, Université Laval
- Li, Z., Zhao, R., Hu, J., Wen, L., Feng, G., Zhang, Z., & Wang, Q. (2015). InSAR analysis of surface deformation over permafrost to estimate active layer thickness based on one-dimensional heat transfer model of soils. *Scientific reports*, 5
- Little, J.D., Sandall, H., Walegur, M.T., & Nelson, F.E. (2003). Application of differential global positioning systems to monitor frost heave and thaw settlement in tundra environments. *Permafrost and Periglacial Processes*, 14, 349-357
- Liu, L., Jafarov, E.E., Schaefer, K.M., Jones, B.M., Zebker, H.A., Williams, C.A., Rogan, J., & Zhang, T. (2014a). InSAR detects increase in surface subsidence caused by an Arctic tundra fire. *Geophysical Research Letters*, 41, 3906-3913
- Liu, L., Schaefer, K., Chen, A., Gusmeroli, A., Zebker, H., & Zhang, T. (2015). Remote sensing measurements of thermokarst subsidence using InSAR. *Journal of Geophysical Research: Earth Surface*, 120, 1935-1948
- Liu, L., Schaefer, K., Gusmeroli, A., Grosse, G., Jones, B.M., Zhang, T., Parsekian, A.D., & Zebker, H.A. (2014b). Seasonal thaw settlement at drained thermokarst lake basins, Arctic Alaska. *Atmospheric Chemistry and Physics*, 8, 815
- Liu, L., Schaefer, K., Zhang, T., & Wahr, J. (2012). Estimating 1992–2000 average active layer thickness on the Alaskan North Slope from remotely sensed surface subsidence. *Journal of Geophysical Research: Earth Surface*, 117
- Liu, L., Zhang, T., & Wahr, J. (2010). InSAR measurements of surface deformation over permafrost on the North Slope of Alaska. *Journal of Geophysical Research: Earth Surface*, 115
- Massonnet, D., Briole, P., & Arnaud, A. (1995). Deflation of Mount Etna monitored by spaceborne radar interferometry. *Nature*, 375, 567
- Massonnet, D., Rossi, M., Carmona, C., Adragna, F., Peltzer, G., Feigl, K., & Rabaute, T. (1993). The displacement field of the Landers earthquake mapped by radar interferometry. *Nature*, 364, 138
- Moreira, A., Prats-Iraola, P., Younis, M., Krieger, G., Hajnsek, I., & Papathanassiou, K.P. (2013). A tutorial on synthetic aperture radar. *Geoscience and Remote Sensing Magazine, IEEE*, 1, 6-43
- NordicanaD (2014). Environmental data from the Umiujaq region in Nunavik, Quebec, Canada. In. <http://www.cen.ulaval.ca/nordicanad/dpage.aspx?doi=45291SL-34F28A9491014AFD>
- Rott, H., Nagler, T., & Scheiber, R. (2003). Snow mass retrieval by means of SAR interferometry. In, *3rd FRINGE Workshop, European Space Agency, Earth Observation* (pp. 1-6): Citeseer
- Rudy, A.C., Lamoureux, S.F., Treitz, P., Short, N., & Brisco, B. (2018). Seasonal and multi-year surface displacements measured by DInSAR in a High Arctic permafrost environment. *International Journal of Applied Earth Observation and Geoinformation*, 64, 51-61
- Rykhus, R.P., & Lu, Z. (2008). InSAR detects possible thaw settlement in the Alaskan Arctic Coastal Plain. *Canadian Journal of Remote Sensing*, 34, 100-112
- Shiklomanov, N.I., Streletskiy, D.A., Little, J.D., & Nelson, F.E. (2013). Isotropic thaw subsidence in undisturbed permafrost landscapes. *Geophysical Research Letters*, 40, 6356-6361

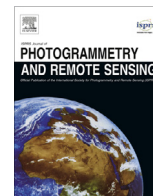
- Short, N., Brisco, B., Couture, N., Pollard, W., Murnaghan, K., & Budkewitsch, P. (2011). A comparison of TerraSAR-X, RADARSAT-2 and ALOS-PALSAR interferometry for monitoring permafrost environments, case study from Herschel Island, Canada. *Remote Sensing of Environment*, *115*, 3491-3506
- Short, N., LeBlanc, A.-M., Sladen, W., Oldenborger, G., Mathon-Dufour, V., & Brisco, B. (2014). RADARSAT-2 D-InSAR for ground displacement in permafrost terrain, validation from Iqaluit Airport, Baffin Island, Canada. *Remote Sensing of Environment*, *141*, 40-51
- Streletskiy, D.A., Shiklomanov, N.I., Little, J.D., Nelson, F.E., Brown, J., Nyland, K.E., & Klene, A.E. (2017). Thaw subsidence in undisturbed tundra landscapes, Barrow, Alaska, 1962–2015. *Permafrost and Periglacial Processes*, *28*, 566-572
- Tsang, L., Kong, J.A., & Ding, K.-H. (2000). *Scattering of Electromagnetic Waves, Theories and Applications*. John Wiley & Sons
- Usai, S. (2003). A least squares database approach for SAR interferometric data. *Geoscience and Remote Sensing, IEEE Transactions on*, *41*, 753-760
- Wang, L., Marzahn, P., Bernier, M., Jacome, A., Poulin, J., & Ludwig, R. (2017). Comparison of TerraSAR-X and ALOS PALSAR Differential Interferometry With Multisource DEMs for Monitoring Ground Displacement in a Discontinuous Permafrost Region. *IEEE Journal of Selected Topics in Applied Earth Observations and Remote Sensing*
- Wang, L., Marzahn, P., Bernier, M., & Ludwig, R. (2018). Mapping permafrost landscape features using object-based image classification of multi-temporal SAR images. *ISPRS Journal of Photogrammetry and Remote Sensing*, *141*, 10-29
- Wolfe, S.A., Short, N.H., Morse, P.D., Schwarz, S.H., & Stevens, C.W. (2014). Evaluation of RADARSAT-2 DInSAR seasonal surface displacement in discontinuous permafrost terrain, Yellowknife, Northwest Territories, Canada. *Canadian Journal of Remote Sensing*, *40*, 406-422
- Wu, Z., Zhao, L., Liu, L., Zhu, R., Gao, Z., Qiao, Y., Tian, L., Zhou, H., & Xie, M. (2018). Surface-deformation monitoring in the permafrost regions over the Tibetan Plateau, using Sentinel-1 data. *Sciences in Cold and Arid Regions*, *10*, 114-125
- Yu, C., Li, Z., & Penna, N.T. (2018). Interferometric synthetic aperture radar atmospheric correction using a GPS-based iterative tropospheric decomposition model. *Remote Sensing of Environment*, *204*, 109-121
- Yu, C., Penna, N.T., & Li, Z. (2017). Generation of real - time mode high - resolution water vapor fields from GPS observations. *Journal of Geophysical Research: Atmospheres*, *122*, 2008-2025
- Zebker, H.A., Rosen, P.A., & Hensley, S. (1997). Atmospheric effects in interferometric synthetic aperture radar surface deformation and topographic maps. *Journal of Geophysical Research: Solid Earth (1978–2012)*, *102*, 7547-7563
- Zhao, R., Li, Z.-w., Feng, G.-c., Wang, Q.-j., & Hu, J. (2016). Monitoring surface deformation over permafrost with an improved SBAS-InSAR algorithm: With emphasis on climatic factors modeling. *Remote Sensing of Environment*, *184*, 276-287
- Zwieback, S., Hensley, S., & Hajnsek, I. (2015). Assessment of soil moisture effects on L-band radar interferometry. *Remote Sensing of Environment*, *164*, 77-89
- Zwieback, S., Liu, X., Antonova, S., Heim, B., Bartsch, A., Boike, J., & Hajnsek, I. (2016). A statistical test of phase closure to detect influences on DInSAR deformation estimates besides displacements and decorrelation noise: Two case studies in high-latitude regions. *IEEE Transactions on Geoscience and Remote Sensing*, *54*, 5588-5601

4 Mapping permafrost landscape features using object-based image classification of multi-temporal SAR images



Contents lists available at ScienceDirect

ISPRS Journal of Photogrammetry and Remote Sensing

journal homepage: www.elsevier.com/locate/isprsjprs

Mapping permafrost landscape features using object-based image classification of multi-temporal SAR images

Lingxiao Wang^{a,c,*}, Philip Marzahn^a, Monique Bernier^{b,c}, Ralf Ludwig^{a,c}^a Department of Geography, Ludwig-Maximilians-Universität München, Munich, Germany^b Centre Eau, Terre & Environnement, Institut National de la Recherche Scientifique, Québec, Canada^c Northern Research Center/Centre d'études nordiques (CEN), Québec, Canada

ARTICLE INFO

Article history:

Received 2 August 2017

Received in revised form 5 March 2018

Accepted 27 March 2018

Available online 17 April 2018

Keywords:

SAR

TerraSAR-X

Backscatter intensity

Interferometric coherence

OBIA classification

CART

Sub-arctic

Multi-temporal analysis

Heterogeneous environment

ABSTRACT

Microwave imagery has a distinct advantage over optical imagery in high-latitude areas because it allows data to be acquired independently of cloud cover and solar illumination. Synthetic aperture radar (SAR)-based monitoring has become increasingly important for understanding the state and dynamics of permafrost landscapes at the regional scale. This study presents a permafrost landscape mapping method that uses multi-temporal TerraSAR-X backscatter intensity and interferometric coherence information. The proposed method can classify permafrost landscape features and map the two most important features in sub-arctic permafrost environments: permafrost-affected areas and thermokarst ponds. First, a land cover map is generated through the combined use of object-based image analysis (OBIA) and classification and regression tree (CART) analysis. An overall accuracy of 98% is achieved when classifying rock and water bodies, and an accuracy of 79% is achieved when discriminating between different vegetation types with one year of single-polarized acquisitions. Second, the distributions of the permafrost-affected areas and thermokarst ponds are derived from the classified landscapes. Permafrost-affected areas are inferred from the relationship between vegetation cover and the existence of permafrost, and thermokarst pond distributions are directly inherited from the land cover map. The two mapped features exhibit good agreement with manually delineated references. The proposed method can produce permafrost landscape maps in complex sub-arctic environments and improve our understanding of the effects of climate change on permafrost landscapes. This classification strategy can be transferred to other time-series SAR datasets, e.g., Sentinel-1, and other heterogeneous environments.

© 2018 International Society for Photogrammetry and Remote Sensing, Inc. (ISPRS). Published by Elsevier B.V. All rights reserved.

1. Introduction

Permafrost is one of the primary components of the cryosphere in northern regions because it influences hydrological processes, energy exchanges, natural hazards, and carbon budgets. The degradation of permafrost (i.e., a decrease in the thickness and/or areal extent of permafrost) is inevitable because of the effects of climate change (Stocker et al., 2013). Permafrost degradation adversely affects resources that are traditionally available for residents in the north by significantly altering vegetation, water bodies, and soil drainage (Allard et al., 2012) and has become problematic for the integrity of some transportation infrastructures. In recent

years, widespread permafrost degradation has been reported across North America, Russia, Northern Europe, and the Tibetan Plateau (Romanovsky et al., 2010; Stocker et al., 2013), which accelerates thermokarst processes and thus significantly changes the landscape. The rate of degradation is extremely high within the discontinuous permafrost zone (Jolivel and Allard, 2013; Payette et al., 2004).

The state of the permafrost environment in arctic and sub-arctic regions is of great concern to researchers (Schaefer et al., 2015). According to Hugelius et al. (2014), permafrost soils in the northern hemisphere contain a total of approximately thirteen hundred petagrams (1.3E15 kg) of organic carbon. Rapid permafrost thawing is directly linked to the carbon budget and is expected to play a major role in the dynamics of the future climate. Permafrost degradation processes can act as either a carbon source due to greenhouse gas (GHG) emissions that originate from the thawing

* Corresponding author at: Department of Geography, Ludwig-Maximilians-Universität München, Munich, Germany.

E-mail address: l.wang@iggf.geo.uni-muenchen.de (L. Wang).

of permafrost (Laurion et al., 2010; Schuur et al., 2008; Walter et al., 2006) or a carbon sink through rapid terrestrialization because of fen/bog vegetation growth and peat accumulation (Payette et al., 2004).

However, permafrost degradation processes have yet to be fully understood and quantified at different temporal and spatial scales. Direct in situ observations are sporadic and intermittent because of the harsh conditions and limited access to these regions. Satellite-based monitoring strategies are becoming increasingly important to understand the state and dynamics of permafrost landscapes at the regional scale.

Optical satellite data have been used to classify land covers and assess their changes over time in northern high-latitude permafrost regions, from the small-scale application through high-resolution aerial photograph, GeoEye, and RapidEye images (Provencher-Nolet, 2014), to the regional scale through moderate-resolution Landsat and SPOT data (Beck et al., 2015), to the circumpolar scale through AVHRR and MODIS data (Cihlar et al., 1996; Sulla-Menashe et al., 2011; Walker et al., 2002). The notable heterogeneity of the landscape, particularly for sub-arctic permafrost environments, requires the use of high-spatial-resolution data to capture and interpret subtle changes (Frost et al., 2014). A high spatial resolution is also crucial to map thermokarst lakes and ponds (Bartsch et al., 2008; Muster et al., 2012), because newly formed lakes are often small, with a mean area of ~60–140 m² (Sannel and Kuhry, 2011).

Microwave imagery has a distinct advantage over optical imagery in high-latitude areas because it allows data to be acquired independently of cloud cover and solar illumination. This characteristic is very useful when working in arctic and sub-arctic regions. Recent studies have exemplified the value of Synthetic Aperture Radar (SAR) data in tundra regions (Duguay et al., 2016; Ullmann et al., 2014). Modern spaceborne platforms, including TerraSAR-X (X-band), Radarsat-2 (C-band), Sentinel-1 (C-band), and ALOS-PALSAR-2 (L-band), provide single-, dual-, or quad-polarized images with high spatial resolutions that are suitable for heterogeneous landscape monitoring and can provide information on the vertical structure of the vegetation.

1.1. Land cover mapping in high-latitude permafrost environments with SAR imagery

Several attempts have been made to use SAR imagery to classify and map land cover types in arctic and sub-arctic permafrost environments. Banks et al. (2013) assessed the potential of dual polarimetric TerraSAR-X data for land cover mapping with backscatter coefficients, while Banks et al. (2014) classified quad-pol Radarsat-2 imagery by using Kennaugh matrix elements. Duguay et al. (2016) also evaluated the performance of full-polarimetric Radarsat-2C-band images on the classification of land cover types by using a support vector machine (SVM) method. Ullmann et al. (2014), Ullmann et al. (2016) analyzed the characteristics and correlation of land cover scattering with PolSAR features from Radarsat-2 (quad-pol) and TerraSAR-X (HH/VV) data in Canada's Mackenzie Delta.

Time-series high-resolution SAR data have become freely available with the launch of the Sentinel-1 satellites. Methods to apply multi-temporal/time-series SAR images for permafrost environment classification and monitoring have yet to be developed.

1.2. Permafrost landscape features

In contrast to the continuous permafrost zone, the discontinuous permafrost zone is characterized by a heterogeneous land-

Table 1

Main permafrost landforms in the discontinuous permafrost zone after Allard and Seguin (1987), Jolivel and Allard (2013), and Pissart (2002).

Permafrost landform	Description
Lithalsa	Mineral permafrost mound
Permafrost plateau	Elongated and wide mineral permafrost landform
Palsa	Peaty permafrost mound or permafrost mound with a peat cover
Peat plateau	Elongated and wide peaty permafrost landforms

scape with numerous scattered frozen grounds of deeper active layer, thermokarst ponds, and a more developed vegetative cover (i.e., tall shrubs and coniferous stands). Table 1 lists the four main permafrost landforms. For simplicity, as suggested by Jolivel and Allard (2013), the term “lithalsa” is used in our study to include permafrost plateaus, and the term “palsa” encompasses peaty plateaus. All these upheaved landforms stand above the surrounding terrain by several meters (generally 3–5 m) because of the development of ice segregation lenses formed by the cryosuction of soil water in freezing, fine-grained, frost-susceptible soils (Pissart, 2002). Their volumetric ice contents vary between 50 and 80% (Calmels and Allard, 2004, 2008; Calmels et al., 2008).

In the discontinuous permafrost zone, the permafrost thermal regime is closely related to the vegetation structure through the interactions and dynamic processes between the vegetation and snow cover (Allard and Seguin, 1987; Goodrich, 1982; Nicholson, 1979, 1976; Pelletier, 2015; Schimel et al., 2004; Widhalm et al., 2017; Zhang, 2005). For instance, tall shrubs capture wind-drifted snow, and the snow cover retains relatively warmer soil temperatures during winter, which creates positive feedback by providing enhanced conditions for shrub growth (Schimel et al., 2004; Sturm et al., 2001a, 2005). Vegetation species and vegetation structures are indicators of the presence or absence of surficial permafrost and associated thermal regimes (Allard and Seguin, 1987; Pelletier, 2015; Thom, 1969; Widhalm et al., 2017).

Changes in the natural environment accompany permafrost degradation. The expansion of shrub vegetation in arctic and sub-arctic environments, which is also known as arctic greening, has received much attention over the past few decades (Elmendorf et al., 2012; Fraser et al., 2011; Jia et al., 2009; Macias-Fauria et al., 2012; Myers-Smith et al., 2011; Sturm et al., 2001b, 2005). This process is driven by an increase in tall vegetation, namely, spruce and tall shrubs, at the expense of low-lying vegetation such as lichens, prostrate shrubs, and wetland low vegetation (Beck et al., 2015; Cornelissen et al., 2001; Fraser et al., 2014; Myers-Smith et al., 2011; Provencher-Nolet, 2014; Sturm et al., 2001b; Tremblay et al., 2012). Meanwhile, rising air and ground temperatures have accelerated thermokarst processes, thereby creating features such as thaw lakes (Jones et al., 2011; Kokelj and Jorgenson, 2013), which are the result of the thawing of ice-rich permafrost or the melting of massive ice (Serreze et al., 2000). Studies have reported that the expansion and drainage of thermokarst lakes and ponds occur simultaneously in the continuous permafrost zone (Marsh et al., 2009; Smith et al., 2005), whereas new thermokarst ponds form and older ponds shrink in sporadic and discontinuous permafrost zones (Beck et al., 2015; Payette et al., 2004; Provencher-Nolet, 2014; Yoshikawa and Hinzman, 2003). The surface areas of permafrost mounds have substantially decreased in the discontinuous permafrost zone of northern Quebec. However, this change was not compensated by a corresponding increase in the total surface area of thermokarst ponds but by a remarkable three-fold increase in vegetation cover (Bouchard et al., 2014).

1.3. Objectives

The main objective of this study is to map permafrost landscape features and extract the distributions of permafrost-affected areas and thermokarst ponds, which are the two most important features in sub-arctic permafrost environments. We propose a classification method that fully explores the features derived from time-series TerraSAR-X backscatter intensity and interferometric data through multi-temporal analysis. The following questions should be answered through the development of the proposed method. (1) How to classify heterogeneous discontinuous permafrost environments by using the multi-temporal features of SAR images? (2) What are the most efficient features for classification with multi-temporal SAR images?

Following this introduction, this paper describes the study area and dataset in Sections 2 and 3, respectively. The proposed permafrost landscape mapping method is stated in Section 4. Section 5 illustrates the classification accuracy and mapping results of the method, and Section 6 compares the classification accuracies when using HH and VV polarizations with acquisitions either throughout the year or only during the summer. The conclusions of the study are presented in Section 7.

2. Study area

The study area is situated near the Inuit community of Umiujaq (56°32' N, 76°31' W) on the eastern shore of Hudson Bay (northern Quebec, Canada; see Fig. 1).

The climate is sub-arctic with a mean annual air temperature (MAAT) of approximately -3°C , cold winters (-24°C in January), and cool summers (10°C in August) (EnvironmentCanada, 2010). However, the region is currently experiencing climate warming: the MAATs have increased by two degrees over the past two decades (EnvironmentCanada, 2010). The testing site is entirely within the discontinuous permafrost zone and is currently transitioning into a zone of sporadic permafrost (Allard and Seguin, 1987; Jolivel and Allard, 2013).

The cooling effect of Hudson Bay generates a west–east climate gradient from the shoreline inland, resulting in a tree line that is parallel to the coastline approximately 15 km inland (Payette, 1983). A forest tundra environment is located to the east of the tree line with a shrub tundra environment to the west. The degradation rate of permafrost in the forest tundra area has been much faster than that in the shrub tundra area (Jolivel and Allard, 2013). The dominant tree species in the region is black spruce, which grows as krummholz (Beck et al., 2015). To the west of the tree line, very small patches of trees are restricted to sites that are sheltered from the wind; to the east of the tree line, larger spruce stands are found.

A sub-arctic heterogeneous landscape can be categorized according to the types of features in Table 2. Field photos are shown in Fig. 2. This classification system is consistent with those of previous studies in the same study area (Beck et al., 2015; Duguay et al., 2016; Provencher-Nolet, 2014). Five example sectors (marked in Fig. 1) are selected to illustrate the proposed method. These sectors are distributed throughout the Sheldrake catchment

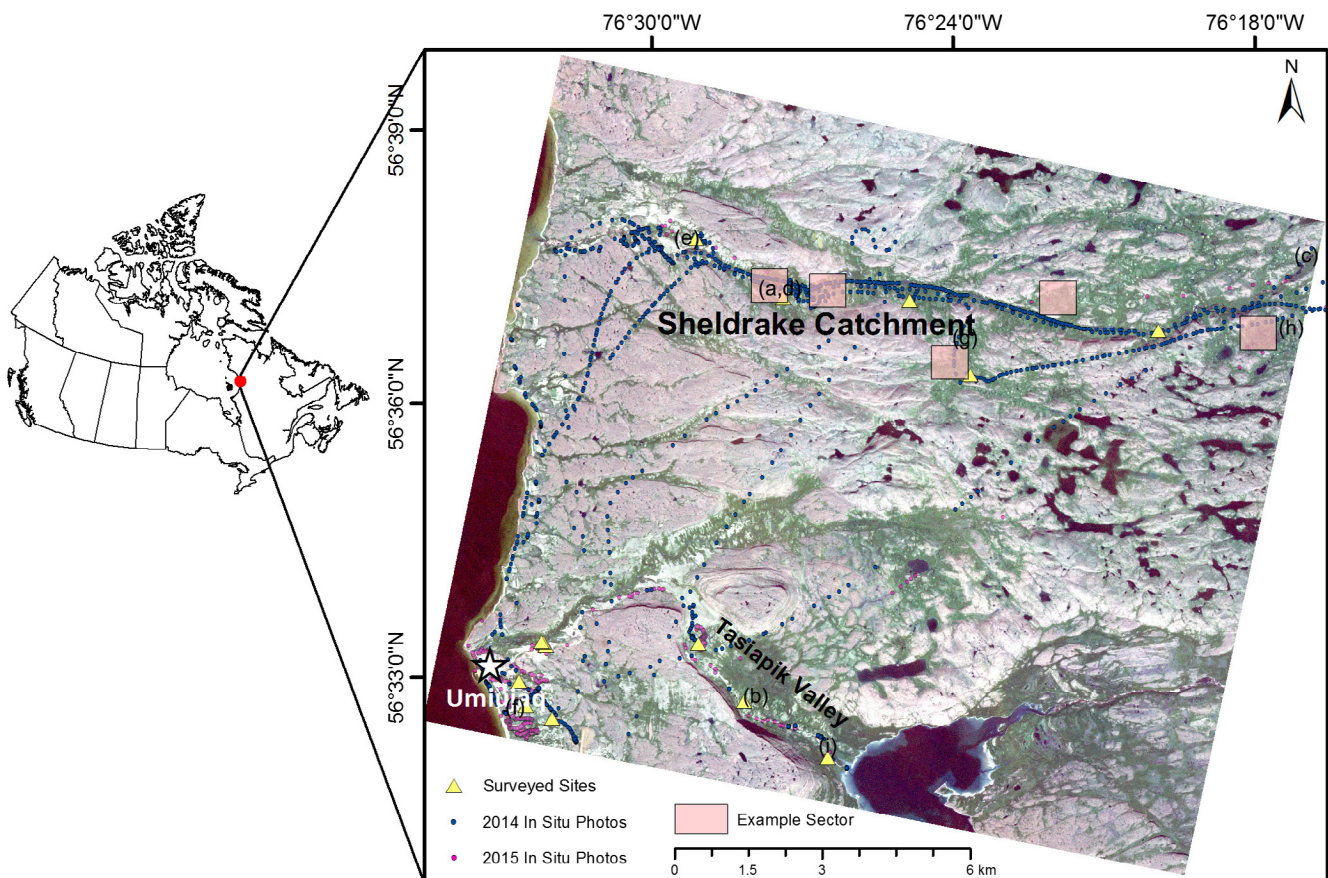


Fig. 1. Study area, including the Umiujaq village region, Tasiapik Valley and Sheldrake catchment. The base map is a RapidEye image from August 13, 2010 (R: red channel; G: green channel; B: blue channel). The marked squares with black outlines and a light red infill demarcate the classification maps in Fig. 4. Sites with detailed vegetation surveys are marked with yellow triangles. In situ photo points are shown with small dots. (For interpretation of the references to colour in this figure legend, the reader is referred to the web version of this article.)

Table 2

Description of landscape features (after Beck et al., 2015; Duguay et al., 2016; Provencher-Nolet, 2014) in the discontinuous permafrost zone with permafrost indicators (after Allard and Seguin, 1987; Beck et al., 2015; Pelletier, 2015) for each landscape.

Landscape	Description	Permafrost indicator
Large water body	Large lake, sea	None
Rock	Exposed bedrock, block fields or rubble	Permafrost or none
Exposed land	Bare sandy soil, no or very limited vegetation cover	Permafrost table is deep
Lichen	Covered with at least 50% lichens mixed with scattered low shrubs (<30 cm) and herbaceous vegetation	High possibility of surface permafrost
Shrub	Covered with at least 50% shrubs, where the average shrub height is greater than or equal to 50 cm	Very low possibility of permafrost or the permafrost table is very deep
Spruce	Coniferous trees comprise 75% or more of the stands	Very low possibility of permafrost or the permafrost table is very deep
Wetland low vegetation	Coastal plain wetland covered by herbs, moss and prostrate shrubs, or by peatlands with some herbs and prostrate shrubs	High possibility of surface permafrost
Saturated wetland	Mixture of sedge/grass and moss, surface is saturated	Absence of permafrost
Thermokarst pond	Pond	Absence of permafrost or the thawing of permafrost beneath

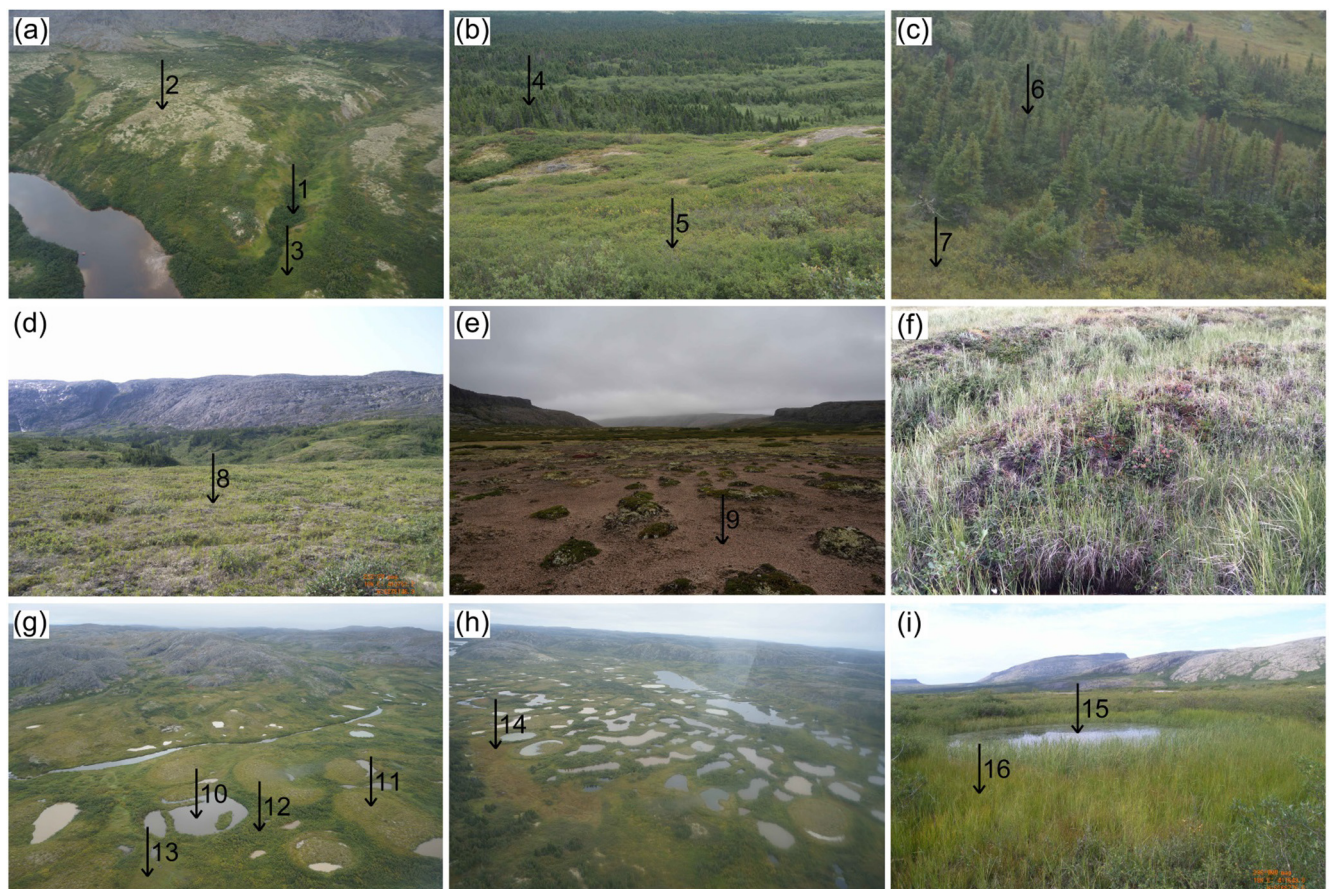


Fig. 2. Field photos, the locations of which are marked in Fig. 1. (a) Permafrost plateau downstream of the Sheldrake catchment; Arrow 1 shows spruce stands; Arrow 2 indicates the top of the permafrost plateau, which is covered by lichens that are mixed with scattered low shrubs and herbaceous vegetation; Arrow 3 shows tall shrubs that are growing in the gullies. (b) Tasiapik Valley; Arrow 4 shows localized forest patches; Arrow 5 shows shrub cover. (c) Spruce-shrub mixed stand upstream of the Sheldrake catchment; Arrow 6 points to a spruce patch; Arrow 7 points to shrubs. (d) Same permafrost plateau as panel (a), where the vegetation is a mix of lichens, scattered low shrubs, and herbaceous vegetation. (e) Arrow 9 indicates exposed land. (f) Coastal plain wetland with a mixture of herbs, moss and prostrate shrubs. (g) Degraded permafrost landscape upstream of the Sheldrake catchment; Arrow 10 shows a thermokarst pond; Arrow 11 shows a mix of lichens with low shrub cover on a permafrost mound; Arrow 12 shows shrubs along the ridges of a thermokarst pond; Arrow 13 notes saturated wetland. (h) Degraded permafrost landscape similar to that in panel (g) upstream of the Sheldrake catchment; Arrow 14 indicates saturated wetland. (i) Degraded permafrost mound; Arrow 15 shows a thermokarst pond in the middle of the surrounding sedge (Arrow 16).

from the shoreline inward, including a range from a shrub tundra environment to a forest tundra environment, which represent different permafrost conditions.

Permafrost-affected areas in the study area are predominantly covered by a mixture of lichens and other low vegetation and are generally surrounded by dense shrubs or spruces, as shown in

Fig. 2(a), (d), (g), and (h). Tall shrubs and spruces retain thick snow cover during winter and are thus typically indicative of an absence of permafrost or a very deep permafrost table. The wetland low vegetation class generally represents a coastal plain wetland environment that is covered by a mixture of herbs, moss and prostrate shrubs or by peatlands with some herbs and prostrate shrubs, which indicates the high possibility of the existence of permafrost. The saturated wetland class represents poorly drained wetlands, covered with hydrophytic plants, and is usually permafrost free (Thom, 1969). Herbaceous plant communities that are dominated by palustrine grasses suggest saturated conditions. The two wetland landscapes have different vegetation species and different freeze/thaw cycles. Saturation conditions in the “saturated wetland” landscape cause soil to have very high heat capacity and resist freezing during winter. Thus, permafrost is usually absent in “saturated wetland”. The landscape features and related permafrost indicators are summarized in Table 2. The rocks in the study area are not our research interest and thus are not accounted for in the permafrost landscape descriptions in this study.

3. Dataset and data processing

3.1. TerraSAR-X time series

Time-series dual-co-polarized HH-VV TerraSAR-X images were acquired between August 2013 and September 2014 in Single-Look Slant-Range complex (SSC) format in descending, right-looking passes. The incidence angles were between 38.8° and 38.9°. The images were acquired in StripMap mode with pixel spacings of 0.9 m and 2.3 m along the range and azimuth directions, respectively. The acquisition time was 07:27 am locally (11:27 UTC). Images that were acquired during snow precipitation (snow storms) and snow melt events were discarded. In total, 28 SAR images were used for the analysis, which covered a time range of one year. Fourteen of the images were absent of snow cover on the ground (summer acquisition). The other 14 images were considered as winter acquisitions (at least 10 cm of snow on the ground). With one exception of 33 days, the time span between each TerraSAR-X acquisition was 11 days.

3.2. Digital elevation model

A digital elevation model (DEM) was used to compensate for topography-induced effects and mask out regions with strong lay-over and foreshortening effects. Backscatter in SAR imagery is strongly affected by the topography (more precisely, the local inci-

dence angle), so regions with local incidence angles below 16.3° and above 66.4° were masked before classification because they would have been subject to strong geometric distortions. The WorldDEMcore digital surface model (DSM) product (Riegler et al., 2015; WorldDEM, 2015), which is a TanDEM-X-based DEM that was generated from interferometric radar data (Krieger et al., 2007), was used in this study. This product is an unedited DSM distributed by Airbus Defence and Space. The latitudinal grid spacing is 0.4 arc seconds, which equals approximately 12 m (WorldDEM, 2015). The longitudinal pixel spacing depends on the latitude; in our study area, this value is 0.6 arc seconds. The absolute vertical accuracy is less than 4 m (90% linear error), and the absolute horizontal accuracy is less than 6 m (90% circular error) (WorldDEM, 2015).

3.3. In situ survey and reference data

In situ ground truth data of the land cover were recorded during two field campaigns in the summers of 2014 and 2015. Fig. 1 shows the locations of the detailed survey sites and GPS tracking data (including helicopter tracks and ground routines) during the two field campaigns. The vegetation parameters at each detailed survey site, including the type, height, and coverage, were recorded. The GPS tracking data were recorded by using a handheld GPS device (Garmin GPSMAP). The GPS data were imported into ArcGIS and subsequently used for correlation with the in situ photographs according to the time attribute (ArcGIS). The in situ photos were geotagged on the map accordingly.

A very-high-resolution (VHR) GeoEye-1 multispectral image of the study area was acquired in the summer of 2009, and VHR aerial photographs were acquired during the summer of 2010. Additionally, high-resolution (HR) multispectral RapidEye images are available for August 2010 and August 2015. The VHR images provide highly detailed information regarding the vegetation type and distribution but only cover the southern portion of the testing site (i.e., the Umiujaq region and Tasiapik Valley). The northern portion is complemented by Google Earth™ online VHR imagery and RapidEye images. Table 3 lists the parameters of these sensors together with the acquisition dates. Geotagged photos, vegetation records and HR images served as references for the interpretation of the SAR imagery and the selection of the training and validation samples for the classification.

Air temperature, precipitation, and snow depth data were acquired from a meteorological station in the northern Tasiapik Valley. The ground temperature and soil moisture content were also continuously measured between August 2013 and September

Table 3
Parameters of the datasets used in this study.

	TerraSAR-X	RapidEye	GeoEye-1	Aerial photography
Wavelength mode polarization	3.1 cm (9.6 GHz) StripMap HH-VV dual-pol			
Spectral bands		440–510 nm (blue) 520–590 nm (green) 630–685 nm (red) 690–730 nm (redEdge) 760–850 (NIR)	450–510 nm (blue) 510–580 nm (green) 655–690 nm (red) 780–920 (NIR)	blue green red
Pixel spacing	Range: 0.9 m; azimuth: 2.3 m; geocoded to 3 m	5 m	0.5 m (pansharpened)	0.15 m
Acquisition date	2013-08-29–2014-09-29 every 11 days	2010-08-13 and 2015-08-31	2009-09-24	2010-08-12
Product level	Level 1B (single-look slant-range complex (SSC))	Level 3A		
Coverage	Entire test site	Entire test site	Umiujaq region and Tasiapik Valley	Umiujaq region and Tasiapik Valley

2014. Plots of these variables can be found in the Appendix (Fig. A1). Meteorological variables were used to exclude TerraSAR-X scenes acquired during snow storms and snow melt events, which can affect SAR signals (Mätzler and Schanda, 1984; Stiles and Ulaby, 1980; Ulaby et al., 1977). A total of nine sensor stations provided ground surface temperature measurements at depths of 5 cm and 10 cm, six of which provided soil moisture measurements at three different depths (5 cm, 10 cm, and 20 cm). One of these stations is located in the coastal region, six are located in the Tasiapik Valley, and the other two are situated in the Sheldrake catchment. The ground conditions can be interpreted in the context of the soil temperature and moisture conditions.

Maps of the permafrost mound and thermokarst pond distributions in the Sheldrake catchment are available for year 2009 (Jolivel and Allard, 2013) and served as validation sources when mapping the permafrost features. Each permafrost mound and thermokarst pond was manually delineated on the 2009 GeoEye satellite image (0.6 m resolution).

3.4. Data processing

The TerraSAR-X multi-temporal scenes were processed using the GAMMA radar software (GAMMARemoteSensingAG, 2009, 2011a, 2011b; Werner et al., 2000) according to the following processing steps.

(1) Image co-registration

All the complex-valued Single Look Complex (SLC) scenes were co-registered to one scene with a common geometry in range-Doppler. A subpixel accuracy greater than 0.1 SLC pixels was achieved (Oliver and Quegan, 2004; Werner et al., 2000).

(2) Multi-looking

The co-registered SLC data were multi-looked by 2 looks and 1 look in the range and azimuth directions, respectively, resulting in an approximately 3×3 m ground-range spatial resolution.

(3) Coherence calculation

The interferometric coherence, which is defined as the absolute value of the normalized complex correlation coefficient, is calculated by

$$|\gamma| = \left| \frac{\langle s_2 \cdot s_1^* \rangle}{\sqrt{\langle s_1 \cdot s_1^* \rangle \cdot \langle s_2 \cdot s_2^* \rangle}} \right|, \quad (1)$$

where s_1 and s_2 denote the first and second complex SAR images, respectively, and $*$ denotes the complex conjugation. The brackets $\langle \rangle$ represent the ensemble average, which is estimated by spatial averaging, for which an adaptive window size varying between 3×3 and 9×9 pixels is used. The coherence value varies from 0 (decorrelated signals) to 1 (perfectly correlated signals).

Coherence images were generated for every two same-polarization images for time spans of 11 days, 22 days and 33 days. The X-band is more likely to be susceptible to temporal decorrelation because of its high signal frequency (9.6 GHz) (Zebker and Villasenor, 1992). Based on our previous study (Wang et al., 2017), coherence images with time spans greater than 33 days contain very limited information over vegetated area compared to those with shorter time spans.

(4) Radiometric calibration and terrain correction for backscatter intensity

Intensity images were first calibrated to sigma nought (σ_{dB}^0 , expressed in dB) by using the following equation (Airbus, 2014):

$$\sigma_{dB}^0 = 10 \log_{10}(k_s \times |DN|^2 \times \sin \theta_{loc}) \quad (2)$$

where k_s is the calibration and processor scaling factor (calFactor) given in the TerraSAR-X data annotation file; $|DN|^2$ is the intensity value computed from the SLC data; and θ_{loc} is the local incidence angle, which can be calculated from the DEM.

Then, the value of sigma nought σ_{dB}^0 is corrected to the gamma nought (γ_{dB}^0) by considering topographic effects through the following equation (GAMMARemoteSensingAG, 2009; Ulander, 1996):

$$\gamma_{dB}^0 = \sigma_{dB}^0 \times \frac{A_{flat}}{A_{slope}} \times \left(\frac{\cos \theta_{ref}}{\cos \theta_{loc}} \right)^n \quad (3)$$

where θ_{loc} and θ_{ref} represent the local incidence angle and reference angle (e.g., the incidence angle at mid-swath) for the normalization of the backscatter, respectively; A_{slope} and A_{flat} represent the true pixel area and the local pixel area for a theoretically flat terrain, respectively. The factor n is related to the opacity of the scattering media. It is assumed that $n=1$ provides an overall acceptable solution. The detailed calculation procedure can be reviewed in the literature (GAMMARemoteSensingAG, 2009). The gamma nought γ_{dB}^0 (expressed in dB) used in this study is referenced when the backscatter intensity is mentioned.

(5) Spatio-temporal filtering

To increase the signal-to-noise ratio (SNR) of the SAR imagery, a temporal and spatial filtering algorithm with a 3×3 kernel (Bruzzone et al., 2004; Frost et al., 1982; Quegan et al., 2000; Quegan and Yu, 2001) was utilized to reduce the effects of speckle. Such a temporal approach provides a major advantage compared to conventional spatial filters in that it can remove noise without sacrificing the spatial resolution.

(6) Geocoding

The processed images were geocoded to WGS 1984 UTM Zone 18N by using a lookup table between the radar and map geometry. An image cross-correlation algorithm between the SAR imagery and simulated backscattered intensity from the WorldDEMcore product was used to build the lookup table (GAMMARemoteSensingAG, 2011a; Wegmuller, 1999). The geocoding accuracy was less than one-half of a pixel.

4. Landscape classification approach

Bruzzone et al. (2004) proposed a system for the automatic land cover classification of multi-temporal SAR images that jointly employs the temporal variability of backscattering and long-term coherence values to discriminate between several land cover classes. Interferometric coherence describes the degree of correlation between two radar images and is defined by both the amplitude and phase components of the SAR signal; thus, it is potentially more sensitive to changes in the land surface than using amplitude variations alone (Antonova et al., 2016b). Bruzzone et al. (2004) demonstrated that multi-temporal SAR images contain sufficient information to differentiate among land cover types. Antonova et al. (2016b) explored time-series TerraSAR-X backscatter intensity and interferometric coherence data across a variety of tundra environments within the Lena River Delta in Siberia and assessed their potential to detect major seasonal changes on the land surface. Other investigations have used

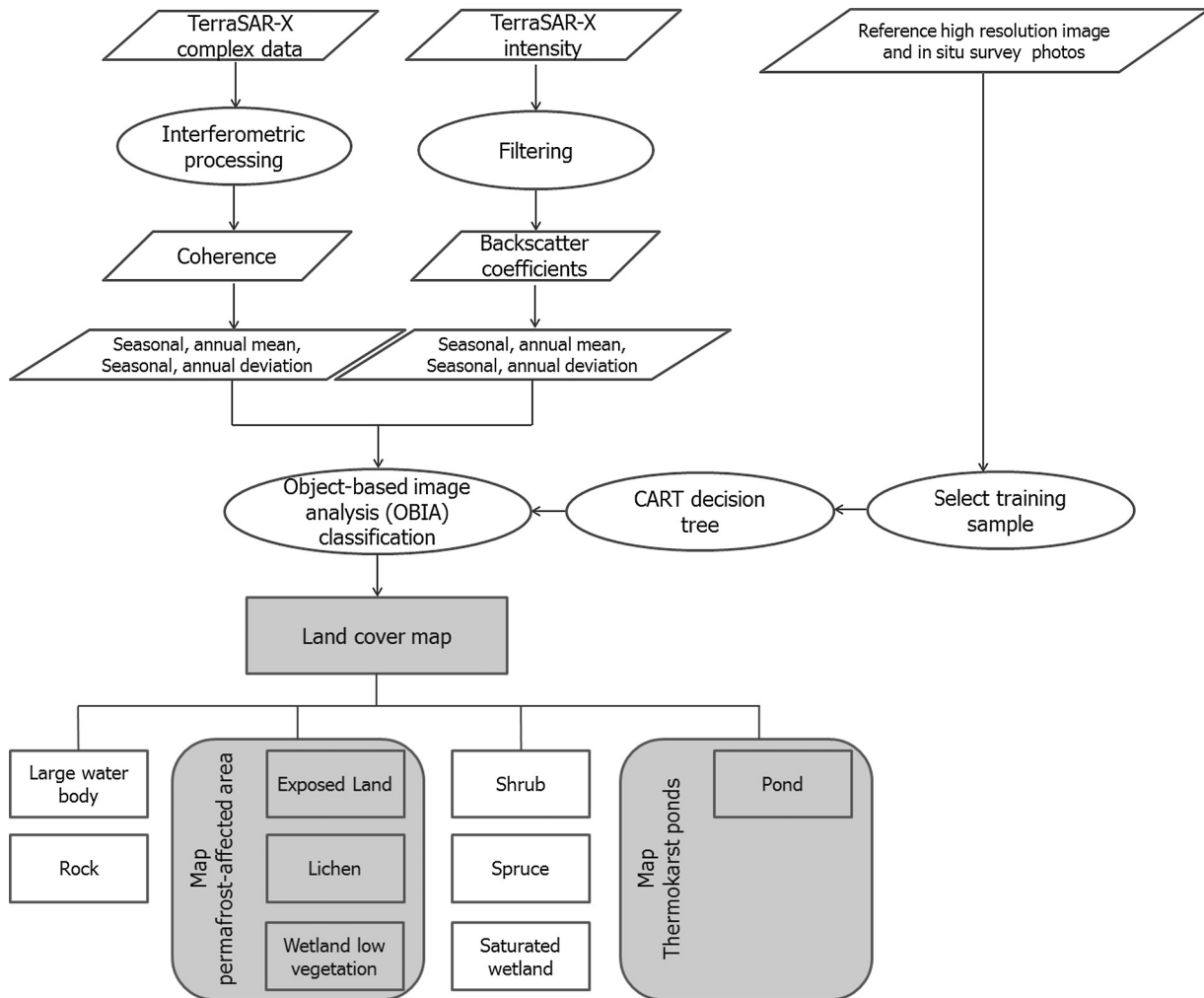


Fig. 3. Flowchart of permafrost landscape mapping using coherence and backscattering coefficients of multi-temporal SAR.

interferometric coherence to classify land cover types (Hall-Atkinson and Smith, 2001; Meyer et al., 2011; Wegmüller and Werner, 1997). However, the use of coherence has been rarely utilized compared to changes in backscatter. In this study, we investigate the potential of using features that are derived from time-series SAR backscatter intensity and interferometric coherence data to characterize permafrost landscape features.

Fig. 3 illustrates the workflow of the proposed approach. The first step is to perform a classification to acquire the land cover map. Object-based image analysis (OBIA) is frequently applied when working with HR imagery or performing a combined analysis of data from various sources (de Almeida Furtado et al., 2016; Evans and Costa, 2013; Hellesen and Matikainen, 2013; Robson et al., 2015; Sasaki et al., 2012). An OBIA approach is especially advantageous for classifications that use SAR imagery because of the nature of the original radiometric signal, e.g., speckles introduce noise into the classification results. Objects that are created by a segmentation process provide a more intuitive representation of ground features than pixels that are influenced by speckle noise. Some studies have successfully utilized an OBIA approach with a combination of SAR and optical imagery or with different sources of SAR imagery to map land cover types (Durieux et al., 2007; Evans and Costa, 2013; Robson et al., 2015; Walker et al., 2010). When performing OBIA classification, the stacked data are first segmented using a segmentation algorithm, after which the class attributes are assigned to the segmented objects. A thermokarst pond map can be directly inherited from the pond class based on

the classification results, and permafrost-affected areas can be inferred according to the relationship between the vegetation cover and the existence of permafrost (as shown in Table 2).

4.1. Multi-resolution segmentation

The multi-resolution segmentation algorithm (Baatz and Schäpe, 2000) from Trimble eCognition was used in this study. The region-merging algorithm begins with a single pixel and a pairwise comparison of its neighbors with the goal of minimizing the resulting summed heterogeneity (Evans and Costa, 2013). The multi-resolution segmentation algorithm in eCognition is controlled by three user-defined parameters: scale, shape, and compactness. The scale parameter determines the maximum allowable heterogeneity of the image objects and varies the sizes of the resulting image objects; for example, larger values produce larger objects. The shape parameter determines the degree of influence of the radiometry versus the object shape during the delineation of the image objects; the input values range between 0 and 1, wherein smaller values result in objects that are optimized for radiometric homogeneity, and higher values generate objects that are optimized for shape homogeneity (Esch et al., 2008). The compactness also varies between 0 and 1 and determines the degree of smoothing of the object's borders. In our study, different sets of parameters were tested, and the optimal values were subsequently selected. The segmentation is based on the feature layer "Temporal mean backscatter intensity of the summer

Table 4

Overview of the selected features that were used in the CART analyses; the abbreviations of the features are shown in the right two columns.

Features	Mean value of an object, which ends in “_m”	Standard deviation of an object, which ends in “_sd”
Temporal mean backscatter intensity of the summer acquisitions	M_su_m (HH)	M_su_sd (HH)
Temporal standard deviation of the backscatter intensity of the summer acquisitions	SD_su_m (HH)	SD_su_sd (HH)
Temporal mean backscatter intensity of the winter acquisitions	M_wi_m (HH)	M_wi_sd (HH)
Temporal standard deviation of the backscatter intensity of the winter acquisitions	SD_wi_m (HH)	SD_wi_sd (HH)
Temporal mean backscatter intensity of acquisitions throughout the year	M_a_m (HH)	M_a_sd (HH)
Temporal standard deviation of the backscatter intensity of acquisitions throughout the year	SD_a_m (HH)	SD_a_sd (HH)
Mean coherence of 11-day-span interferograms in the summer	M_CC11_su_m (HH)	SD_CC11_su_sd (HH)
Mean coherence of 11-day-span interferograms in the winter	M_CC11_wi_m (HH)	SD_CC11_wi_sd (HH)
Mean coherence of 11-day-span interferograms throughout the year	M_CC11_a_m (HH)	SD_CC11_a_sd (HH)
Mean coherence of 22-day-span interferograms in the summer	M_CC22_su_m (HH)	SD_CC22_su_sd (HH)
Mean coherence of 22-day-span interferograms in the winter	M_CC22_wi_m (HH)	SD_CC22_wi_sd (HH)
Mean coherence of 22-day-span interferograms throughout the year	M_CC22_a_m (HH)	SD_CC22_a_sd (HH)
Mean coherence of 33-day-span interferograms in the summer	M_CC33_su_m (HH)	SD_CC33_su_sd (HH)
Mean coherence of 33-day-span interferograms in the winter	M_CC33_wi_m (HH)	SD_CC33_wi_sd (HH)
Mean coherence of 33-day-span interferograms throughout the year	M_CC33_a_m (HH)	SD_CC33_a_sd (HH)

acquisitions”, which is labeled M_su_m (HH) in Table 4, because this layer has the sharpest contours, with the strongest contrast between the different types of land cover and thus facilitates the segmentation procedure.

After segmentation, the mean and standard deviation values for each of the descriptor features in each object were calculated and combined within the classification input sets. Although geometric information, i.e., the extent (e.g., area and length) and shape (e.g., the asymmetry, elliptical fit, and rectangular fit), might help improve the classification accuracy, the goal of this study is to evaluate the use of multi-temporal SAR features (backscatter intensity and coherence) in the classification process. Consequently, geometric information was not considered.

4.2. Candidate features and classification and regression tree (CART) analysis

Many features were derived from the time-series TerraSAR-X images through analyses of the multi-temporal backscatter intensity and interferometric data. These features are listed in Table 4. The multi-temporal SAR features that were used in this study were the temporal mean and standard deviation values of the SAR backscatter intensity and interferometric coherence. For simplicity, we first used only features derived from the HH single polarization, the results of which are described in Section 5. Then, in Section 6, we compare the accuracies of the classifications when using the HH- and VV-polarized acquisitions both throughout the year and only during the summer.

CART analysis was applied because of the large quantity of candidate features. The CART approach is a data mining method that can test a large number of features in a short amount of time to derive the most effective features for the classification. CART analysis does not require assumptions regarding the distribution of the data and has become increasingly popular because of its high degree of automation, flexibility, and capacity to handle large quantities of input attributes. CART analysis can be used to automatically create classification rules given training samples with a broad relevant candidate features (Friedl and Brodley, 1997; Hellesén and Matikainen, 2013; Lawrence and Wright, 2001; Matikainen and Karila, 2011). CART analysis was adopted in this study because this approach can effectively find the most suitable features and threshold values for the classification. The classification rules are derived from the training samples, which were selected based on the HR optical imagery, field surveys, and geo-tagged photos.

CART analysis was implemented using the SPM Salford Predictive Modeler software. The rules of tree-growth cessation

depended on the sample size: (1) the node was not split if the sample size was less than 20, and (2) a terminal node was not created if the sample size was smaller than 10.

4.3. Two-level classification procedure

A two-level OBIA classification scheme was applied to improve the classification efficiency. This procedure is demonstrated in Fig. 4 for five example sectors (their locations are shown in Fig. 1). The Level 1 classification results are shown in the 3rd column of Fig. 4, and the Level 2 classification results are shown in the 4th column. In the Level 1 classification, some large thermokarst ponds were classified as “large water bodies” because of their intrinsic water characteristics; their class attributes were manually corrected to “target environment” for participation in the Level 2 classification. The segmentation parameters were defined based on our knowledge of the landscape and the visual interpretation of the segmentation results. The functions of each classification level and segmentation parameter are listed in Table 5.

Figs. 5 and 6 show the two decision trees that were used for the two-level classification scheme. Very few tree nodes were needed for the Level 1 classification (Fig. 5). High classification accuracy could be achieved with three nodes, while any performance improvement with a higher number of nodes was very limited. The two features that were used during the classification with HH polarization were the temporal standard deviation of the backscatter intensity of acquisitions throughout the year (SD_a_m (HH)) and the mean coherence of 33-day-span interferograms in the summer (M_CC33_su_m (HH)).

We selected the best tree with fewer than 20 nodes for the Level 2 classification; when the number of tree nodes approached this quantity, the tree reached a comparatively steady state, and the performance improved negligibly thereafter. The eight features that were used in the classification with HH polarization were the temporal mean of the backscatter intensity of acquisitions throughout the year (M_a_m (HH)), the temporal mean of the backscatter intensity of the winter acquisitions (M_wi_m (HH)), the temporal mean of the backscatter intensity of the summer acquisitions (M_su_m (HH), M_su_sd (HH)), the mean coherence of 11-day-span interferograms in the winter (M_CC11_wi_m (HH)), the mean coherence of 11-day-span interferograms in the summer (M_CC11_su_m (HH)), the temporal standard deviation of the backscatter intensity of the summer acquisitions (SD_su_m (HH)), the temporal standard deviation of the backscatter intensity of the winter acquisitions (SD_wi_m (HH)), and the temporal standard deviation of the backscatter intensity of acquisitions throughout the year (SD_a_m (HH)). A detailed assessment of the accuracy

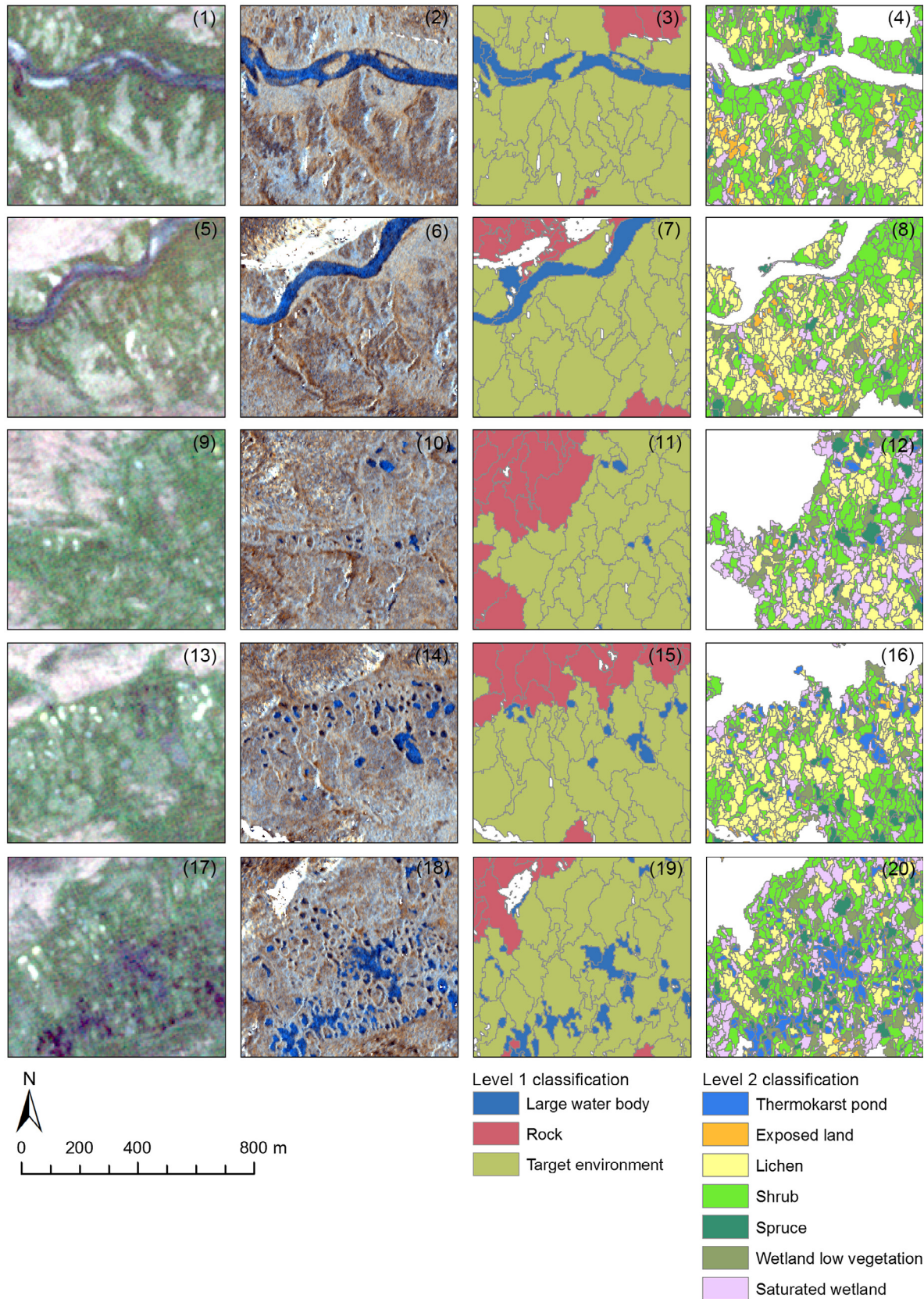


Fig. 4. Classification procedure and distribution map of permafrost-affected areas and thermokarst ponds. Five example sectors are illustrated from top to bottom. From left to right, the columns show RapidEye satellite images (R: red channel, G: green channel, B: blue channel), TerraSAR-X images (R: M_{su_m}, G: M_{a_m}, B: M_{wi_m}), the results of the Level 1 classification, and the results of the Level 2 classification. (For interpretation of the references to colour in this figure legend, the reader is referred to the web version of this article.)

Table 5
Two-level OBIA classification and segmentation parameters.

	Function	Segmentation parameters
Level 1 classification	Separate the research target of interest from the background environment by using large-scale segmentation. This process initially roughly classifies the region into “rock”, “large water body” (i.e., large lakes and sea), and “target environment”	Scale = 20 Shape = 0.1 Compactness = 0.5 A large scale value was used to decrease the number of segmented objects and save computation time.
Level 2 classification	Refine the “target environment” class into (1) spruces, (2) tall shrubs (>50 cm), (3) lichens mixed with scattered low shrubs, (4) wetland low vegetation (a mixture of sedge, moss, and prostrate shrubs), (5) saturated wetland (a mixture of sedge/grass and moss wetland), (6) exposed land, and (7) thermokarst ponds	Scale = 5 Shape = 0.1 Compactness = 0.5 A small scale value was adopted to guarantee that small-sized land features, i.e., thermokarst ponds and spruce patches, can still be distinguished

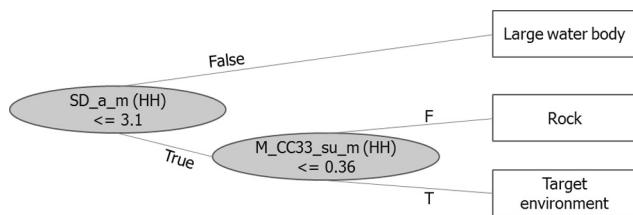


Fig. 5. Decision tree for the Level 1 classification.

of this approach is discussed in Sections 5 “Results” and 6 “Discussion”.

5. Results

5.1. Classification accuracy with HH-polarized acquisitions

The accuracies of the two levels of classifications were separately evaluated by using 1056 and 2244 manually interpreted object samples (Tables 6 and 7, respectively). For each class, the producer’s accuracy (PA) represents errors of exclusion or omission; the user’s accuracy (UA) represents errors of inclusion or commission. The overall accuracy (OA) is calculated from the ratio of the correctly classified pixels (along the diagonal) to the total number of pixels in the confusion matrix. According to recent studies (Olofsson et al., 2014), the OA is typically favored over other common accuracy measures, such as kappa coefficients.

The accuracy of the Level 1 classification when distinguishing among rock, water and vegetation targets was very high, with an OA of 97.9% (Table 6), because of the completely different scattering mechanisms for these land cover types. According to Fig. 4 of the CART decision tree, the coherence during the summer season and the temporal variability of the annual backscatter intensity (i.e., the standard deviation of the SAR backscatter throughout the year) are very effective for discriminating among these three types.

The OA of the Level 2 classification was 79.3% when distinguishing between the different vegetation cover types and thermokarst ponds (Table 7), wherein the classification of thermokarst ponds exhibited the highest accuracy (94.4% PA and 94.4% UA).

The statistics in Table 7 show good discrimination between short-vegetation (i.e., exposed land, lichen, and wetland low vegetation) and high-vegetation areas (shrubs and spruces). Meanwhile, large confusion was observed within the short-vegetation and high-vegetation categories. Within the low-vegetation category, 6% of the lichen validation data were misclassified as exposed land, and 8.6% were misclassified as wetland low vegetation (omission errors). For wetland low vegetation, 10.0% of the validation data were misclassified as lichens. Within the high-vegetation category, 29.2% of the shrub validation data were misclassified as

spruces, and 16.0% of the spruces were misclassified as shrubs. The classification results using the RADARSAT-2 quad-pol imagery also showed that shrubs and spruces are more prone to being misclassified as one another (Duguay et al., 2016). Both X-band (9.6 GHz) and C-band (5.4 GHz) signals can easily reach a backscatter saturation level because of the high signal frequencies and shallow penetration depths of electromagnetic waves through forest or shrub canopies.

The saturated wetland class exhibited the lowest accuracies (PA: 70.3%; UA: 60.6%). This class was incorrectly labeled as exposed land (11.6%), wetland low vegetation (11.0%), and even lichens (4.5%).

5.2. Permafrost-affected areas and thermokarst ponds mapping

Based on the relationship between vegetation and the existence of permafrost (Table 2), the areas that were occupied by low-vegetation classes (i.e., exposed land, lichen, and wetland low vegetation) exhibit a high possibility for the existence of permafrost (see the flowchart in Fig. 3). Consequently, a map of permafrost-affected areas can be obtained.

Fig. 7 shows the inferred permafrost-affected areas for five example sectors. These findings were compared to a reference of the same areas through manual delineations on VHR optical imagery (Jolivel and Allard, 2013). A good consistency was found between the permafrost-affected areas based on the classification results and these reference maps. The reference created by manual delineation comprehensively considered the vegetation species, topographies and human expertise of the local environment, whereas the permafrost mapping in this study was based only on vegetation cover. The difference between the two mapping results was especially clear in the area with high heterogeneity. Over some areas of permafrost mounds, small patches of shrubs and spruces resided. These highly vegetated areas were considered to be absent of permafrost or otherwise have a low possibility of permafrost and thus were not mapped as permafrost-affected areas. However, in the manually delineated reference, these highly vegetated areas were embraced in the permafrost outlines if they only occupied a small portion and their topographic conditions remained consistent with their surroundings. In other areas, lichen-covered or sparsely vegetated rocks were classified as short vegetation and were consequently mapped as permafrost-affected areas. This type of error was more pronounced when permafrost was located near a rock outcrop, as shown in Fig. 7 (4), the lichen-covered rock in the bottom-left corner of the sector was recognized as a permafrost-affected area.

Fig. 7 also compares the classified thermokarst ponds with the manual delineation reference (blue lines). The classification results show good agreement with the reference outlines; only very small thermokarst ponds could not be classified, because they are smaller than the resolution of the TerraSAR-X data. The abundance of

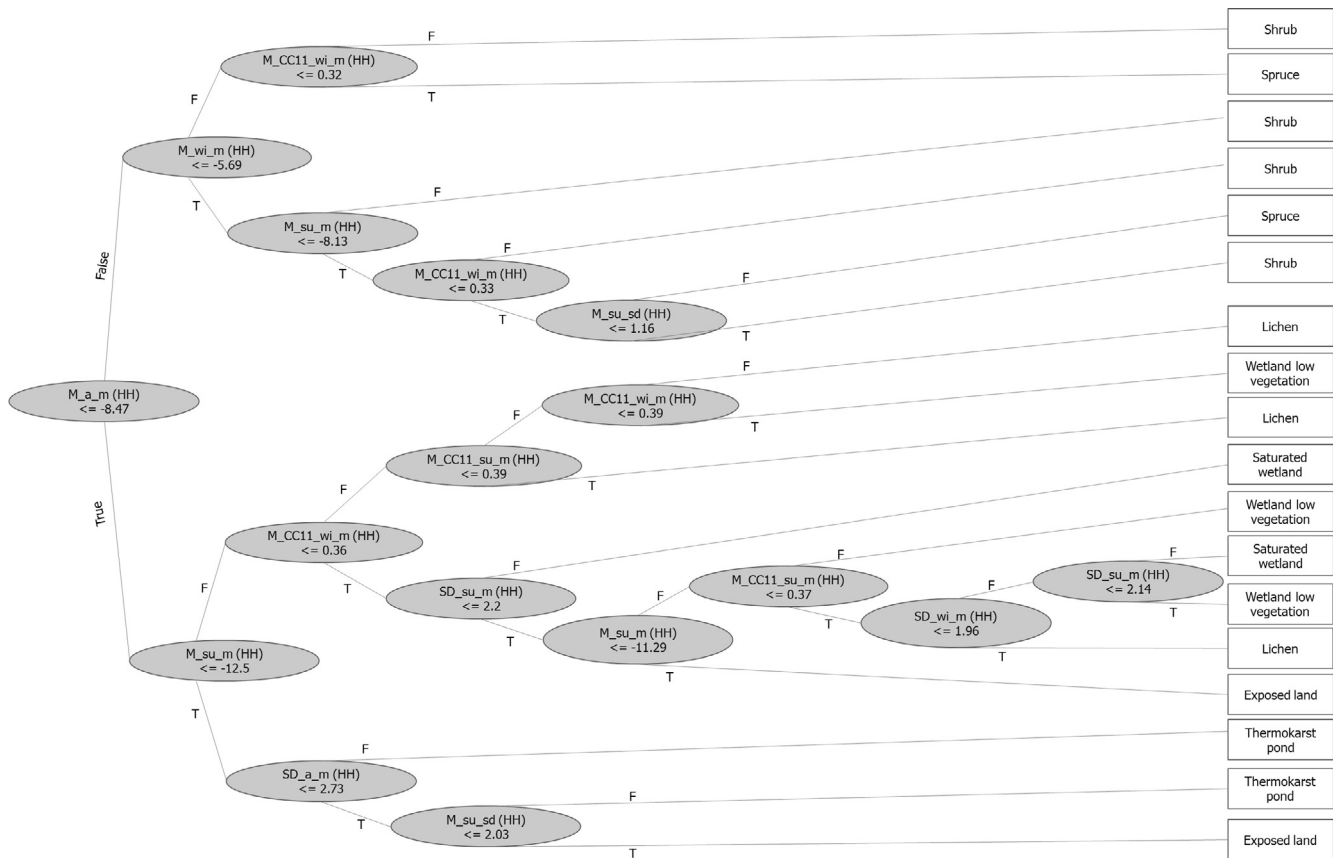


Fig. 6. Decision tree for the Level 2 classification.

Table 6

Accuracy assessment for the Level 1 classification with the confusion matrix, producer's accuracy (PA) and user's accuracy (UA) for each class and the overall accuracy (OA) of the image.

Ref. \ Predicted	Large water body	Rock	Target environment	Total	Accuracy	
					PA (%)	UA
Large water body	274	0	1	275	99.6	98.9
Rock	2	435	7	444	98.0	97.1
Target environment	1	13	323	337	95.8	97.6
Total	277	448	331	1056	OA (%): 97.9	

thermokarst ponds increases from the left sector (near the Hudson Bay coastline) to the right sector (inland of the catchment), illustrating that the number of thermokarst ponds increases inland from the coastal zone.

6. Discussion

6.1. Classification accuracy comparisons with other research studies

Sub-arctic terrains within the ecotone between forest tundra and shrub tundra environments exhibit high spatial heterogeneity with respect to their vegetation cover and ground properties, which creates a complex mixture of scattering mechanisms.

The tests showed an OA of 79% when using a single year of single-polarized data. In terms of the classification accuracy, our results are comparable with those of two previous studies in the same study area, which used VHR (0.15 m) aerial photographs with an OBIA classification scheme (Provencher-Nolet 2014) (OA ≈ 84%) and RADARSAT-2 fine quad-pol images (8 m) with an SVM classifi-

cation scheme (OA ≈ 75% with one quad-pol image; OA ≈ 85% after adding a second image with a different date or incidence angle) (Duguay et al., 2016).

6.2. Classification accuracies when using different polarizations and periods

In the previous section, we illustrated the classification approach proposed herein and reported the classification accuracies when using HH-polarized acquisitions throughout the year. It is worthwhile, then, to compare the classification accuracies when employing VV and HH polarizations with acquisitions throughout the year versus only during the summer. Tables 8 and 9 show the PA and UA for each class for the classifications when using HH-polarized acquisitions throughout the year, HH-polarized acquisitions only during the summer, VV-polarized acquisitions throughout the year, and VV-polarized acquisitions only during the summer.

Table 7

Accuracy assessment for the Level 2 classification with the confusion matrix, producer's accuracy (PA) and user's accuracy (UA) for each class and the overall accuracy (OA) of the image.

Ref. \ Predicted	Thermo-pond	Exposed land	Lichen	Shrub	Spruce	Wetland low vegetation	Saturated wetland	Total	Accuracy	
									PA (%)	UA (%)
Thermo-pond	390	9	3	0	0	2	9	413	94.4	94.4
Exposed land	13	217	17	0	0	8	11	266	81.6	79.2
Lichen	5	26	329	0	0	37	33	430	76.5	85.2
Shrub	0	0	4	287	122	4	1	418	68.7	82.7
Spruce	0	0	4	55	282	2	0	343	82.2	69.1
Wetland low vegetation	2	4	22	5	3	166	17	219	75.8	70.3
Saturated wetland	3	18	7	0	1	17	109	155	70.3	60.6
Total	413	274	386	347	408	236	180	2,244	OA (%): 79.3%	

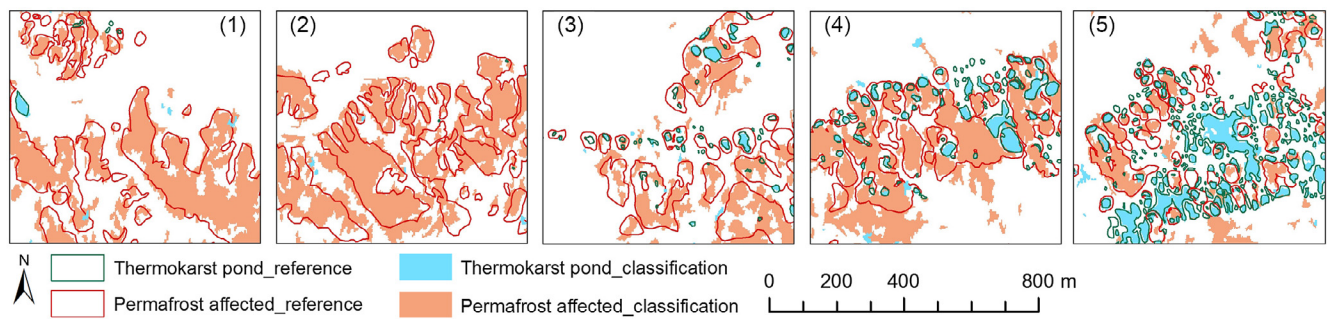


Fig. 7. Comparison of the classification-based permafrost-affected areas and thermokarst ponds with those by manual delineation on VHR image.

Table 8

Producer's and user's accuracies (PA and UA, respectively) for each class from the Level 1 classifications when using HH-polarized acquisitions throughout the year, HH-polarized acquisitions only during the summer, VV-polarized acquisitions throughout the year, and VV-polarized acquisitions only in summer.

Class	HH		VV		HH summer		VV summer	
	PA (%)	UA (%)	PA (%)	UA (%)	PA (%)	UA (%)	PA (%)	UA (%)
Large water body	99.6	98.9	99.6	99.6	97.8	99.6	96.7	99.6
Rock	98.0	97.1	96.6	98.8	98.2	97.1	96.6	98.8
Target environment	95.9	97.6	98.5	95.7	96.1	96.1	98.5	93.5
OA (%)	97.9		98.4		97.6		98.3	

Table 9

Producer's and user's accuracies (PA and UA, respectively) for each class from the Level 2 classifications when using HH-polarized acquisitions throughout the year, HH-polarized acquisitions only during the summer, VV-polarized acquisitions throughout the year, and VV-polarized acquisitions only during the summer.

Class	HH		VV		HH summer		VV summer	
	PA (%)	UA (%)	PA (%)	UA (%)	PA (%)	UA (%)	PA (%)	UA (%)
Thermokarst pond	94.4	94.4	95.9	99.0	94.4	94.2	96.4	96.1
Exposed land	81.6	79.2	72.6	74.0	68.8	84.3	69.2	76.0
Lichen	76.5	85.2	69.3	85.1	57.0	65.0	45.6	58.2
Shrub	68.7	82.7	78.0	82.0	55.0	73.0	57.9	72.2
Spruce	82.2	69.1	83.1	76.2	72.0	56.7	69.4	51.0
Wetland low vegetation	75.8	70.3	74.4	68.0	61.2	58.5	54.3	47.0
Wetland	70.3	60.6	79.4	56.1	74.2	44.9	70.3	55.6
OA (%)	79.3		79.5		68.8		66.2	

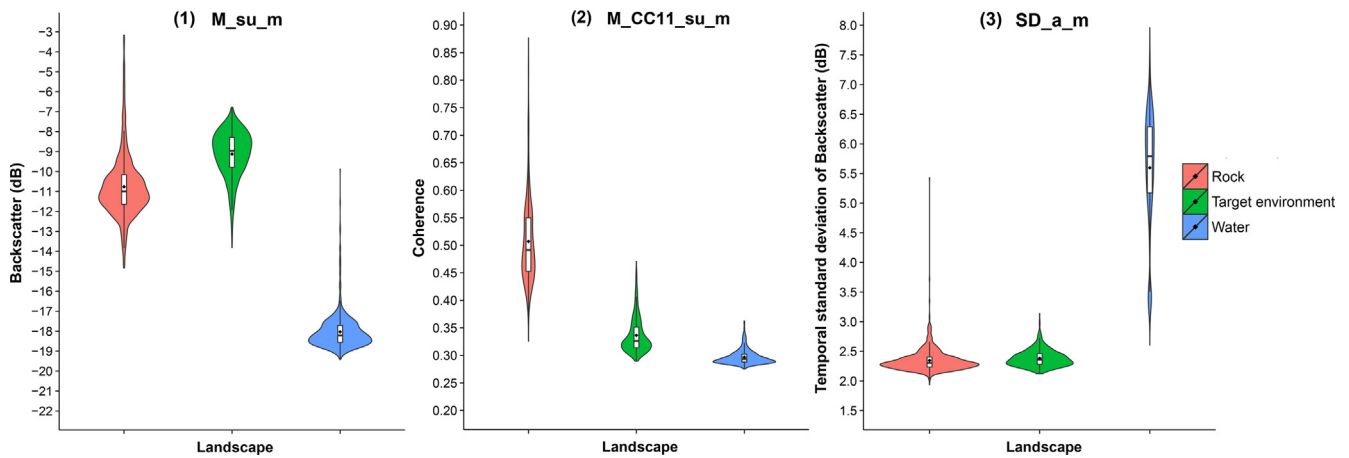


Fig. 10. Violin plots of the backscatter and coherences properties from 2156 training and validation samples of each Level 1 class. Each violin plot contains a box plot and a kernel density plot. A kernel density plot overlays each box plot. The black markers indicate the medians, and the boxes indicate the interquartile ranges of the values. The width of the violin in each subfigure is scaled by the number of samples.

It is consistent with the findings that strong decorrelation occurs over vegetated areas in the X-band data during the summer and that the coherence retains only a limited amount of information when the time span exceeds 22 days (Wang et al., 2017; Zhang et al., 2018).

6.4. Scattering mechanism of the permafrost landscapes at X-band

The sensitive features shown in Figs. 8 and 9 and the classification accuracies shown in Tables 6–9 were employed to explain the scattering mechanism of the permafrost landscapes at X-band.

Fig. 10 shows the highly ranked features in Fig. 8 and the features in Fig. 5 that were used for Level 1 classification with HH-polarized acquisitions. Rock was easily classified because of its high coherence (Fig. 10 (2)). Water was easily classified because of its low backscatter during the summer (Fig. 10 (1)) or its high temporal variability throughout the year (Fig. 10 (3)). When open water froze during the winter, the strong dielectric contrast between the ice and the water beneath created a strong reflectance in the radar signal from the ice–water interface (Antonova et al., 2016a; Engram et al., 2013), thus substantially increasing the backscatter during the winter. The special backscattering characteristics of water facilitate the classification of this feature with SAR images, which is also shown in the Level 2 classification, with thermokarst ponds manifesting the highest accuracy (Tables 7 and 9).

Fig. 11 shows the highly ranked features in Fig. 9 and the features in Fig. 6 that were used for Level 2 classification with HH-polarized acquisitions. Table 7 demonstrates that good discrimination existed between short-vegetation (i.e., exposed sand, lichen, and wetland low vegetation) and high-vegetation areas (shrubs and spruces). Fig. 11 (1), (2), and (3) show that high-vegetation areas manifest higher backscatter throughout the year. The feature “M_a_m ≤ -8.47 ” is employed to discriminate between short- and high-vegetation categories, as shown in the decision tree of Fig. 6.

A comparison between Fig. 11 (1) and Fig. 11 (2) revealed that short vegetation (i.e., exposed sand, lichen, and wetland low vegetation) manifest smaller backscatter increases during the winter than high vegetation. A previous study in the same study area showed that the presence of snow during the winter increased the total backscatter at X-band (Duguay et al., 2015). The X-band, with its short wavelength, is more sensitive to scattering from smaller particles, such as snow grains, consequently increasing the volume scattering generated by the snowpack. The differ-

ent magnitudes of the backscatter increases occur because strong winds can affect snow distribution during winter. Snow is swept off permafrost mounds and plateaus and caught in surrounding depressions with high vegetation (Allard and Seguin, 1987; Ménard et al., 1998; Pelletier, 2015). Field data in the study area has shown that higher shrubs will often retain more snow, thus creating a deeper snowpack in areas where shrubs are taller and more dense (Duguay et al., 2015).

Fig. 11 also explains the misclassification between spruces and shrubs. All the subfigures in Fig. 11 exhibit overlapping value ranges between spruces and shrubs in terms of both backscatter and coherence. Only features from the winter scenes (i.e., names that have “_wi_”) showed an ability to distinguish between the two classes. Spruces have higher backscatter and lower coherence during winter (Fig. 11(2) (5)). The elevated backscatter is higher in the spruce areas than in the shrubby areas, possibly because taller spruces retain deeper snow packs than shrubs. For this reason, tall shrubs are also easily misclassified as spruces. The decorrelation is stronger in the spruce stands because of the deeper snow pack. The decision tree in Fig. 6 employed the feature “M_CC11_wi_m” (Fig. 11 (5)) to discriminate between the two classes.

Among all the classes, exposed land and lichen had relatively higher coherence during winter, especially lichen, which had even higher coherence during winter (Fig. 11 (5)) than during summer (Fig. 11 (4)). Lichen was detected mainly on the permafrost mound/plateau terrain. Snow on the hummocks and elevated regions is swept off by strong wind during winter. Lichen cover had higher coherence during winter because it is less affected by snow and less affected by the volumetric decorrelation from the vegetation layer compared to the summer season. A study in the Qinghai-Tibet Plateau using X-band data also indicated that alpine meadow areas yield lower coherence values in the summer season than in the winter season because vegetation withers in winter and thus the volume scattering of the surface is weak (Zhang et al. 2018). Thus, “M_CC11_wi_m” was employed to separate the lichen class in the decision tree in Fig. 6.

The “wetland low vegetation” class was unique compared to the other short-vegetation classes. This class had higher coherence during summer and decreased backscatter during winter. One possible explanation is the strong double-bounce effect, in which the radar pulse is backscattered twice from wet soil and vegetation stems/branches. The conditions for “double-bouncing” do not exist during winter because the ground is frozen, which decreases the backscatter and coherence, as shown in Fig. 11 (1), (2), (4), and

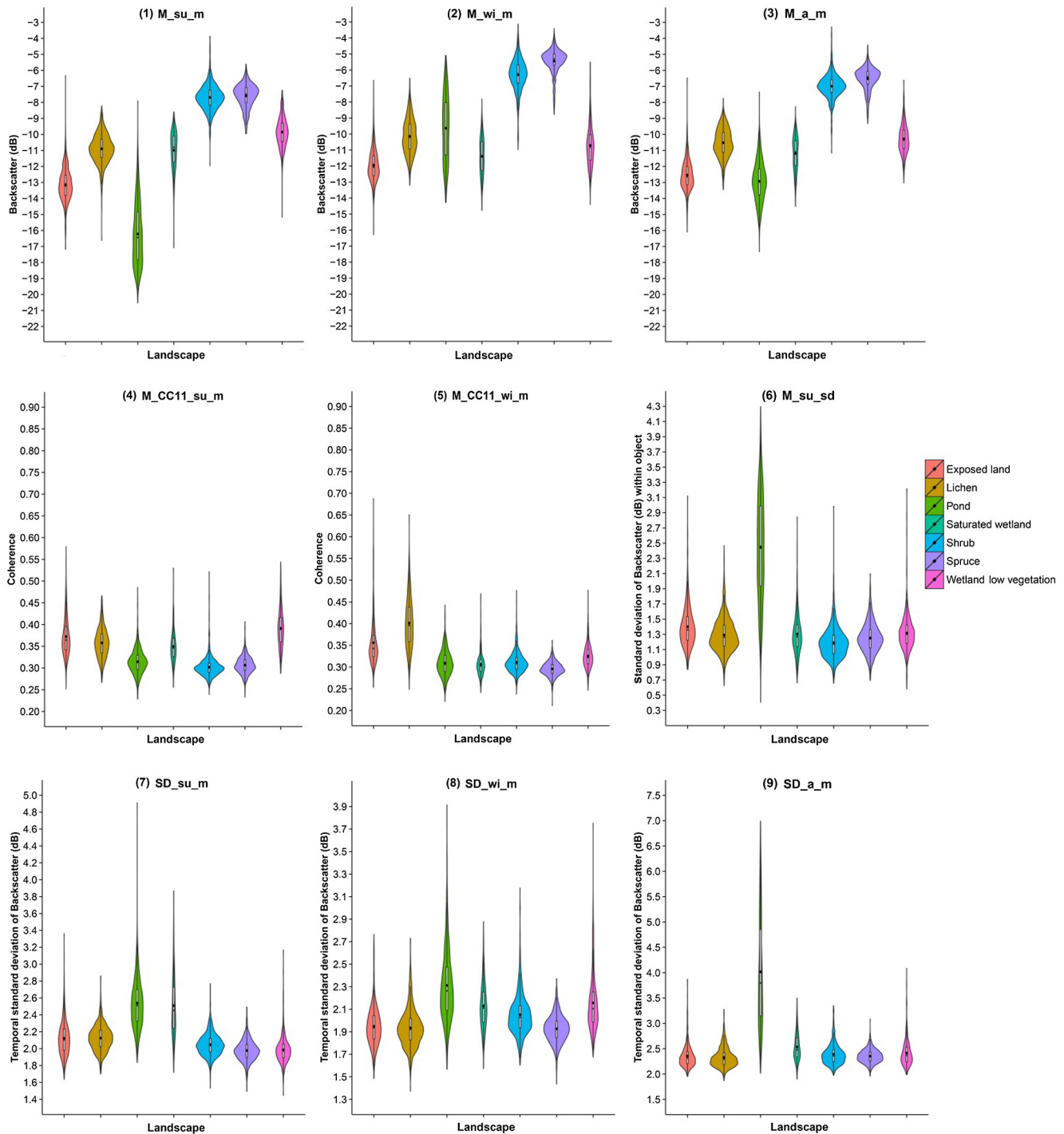


Fig. 11. Violin plots of the backscatter and coherences properties from 4607 training and validation samples of each Level 2 class. Each violin plot contains a box plot and a kernel density plot. A kernel density plot overlays each box plot. The black markers indicate the medians, and the boxes indicate the interquartile ranges of the values. The width of the violin in each subfigure is scaled by the number of samples.

(5). Another possible explanation for the backscatter decrease during winter could be the effect of soil freezing. The dielectric constant ϵ_r of liquid water and ice has a large contrast across the microwave spectrum. For pure ice, $\epsilon_r \approx 3.15 - j0.001$, independent of microwave frequencies; in contrast, liquid water has a remarkably high dielectric constant. Wetland low vegetation had very high soil- and vegetation-water contents during summer. When the soil and vegetation freeze during winter, the reduced real part of the dielectric constant substantially decreases the backscatter (Rignot and Way, 1994; Way et al., 1990; Zwieback et al., 2012).

The low vegetation allowed the radar signal to reach the ground, so the freezing effect of the vegetation layer and soil reduced the backscatter during winter.

Another wetland class “saturated wetland” was covered by a mixture of sedge/grass and moss (Fig. 2 and Table 2). The vegetation was more easily affected by wind, and the slanted vegetation reduced the double-bounce effect. Thus, the double-bounce scattering was weaker, and the coherence was lower in this class than the “wetland low vegetation” class during summer. Additionally, the soil was not always frozen during winter, producing different

scattering properties than the “wetland low vegetation” class. This class also exhibited a large temporal standard deviation for the backscatter intensity of the summer acquisitions (Fig. 11 (7)), which facilitated its separation from other classes.

Exposed land had low backscatter because of its smooth surface (Fig. 11 (1)). Thus, a distinct misclassification occurred between exposed land and thermokarst ponds. A previous study that used the C-band showed that sandy deserts can be misclassified as water because their temporal standard deviations and mean backscattering values were as low as calm water bodies (Santoro et al., 2015). In our study, all the subfigures in Fig. 11 show that exposed land had an overlapping value range with thermokarst ponds and lichen, which explains the misclassification in Table 7.

6.5. Method transferability

The proposed methodology can be easily transferred to other multi-temporal/time-series SAR datasets. Time-series high-resolution SAR data have become freely available with the launch of the Sentinel-1 satellites. The interferometric wide swath (IW) mode offers dual-polarized data over a 250-km swath width with approximately 10-m pixel spacing. The deeper penetration through the canopy layer, which is associated with the longer wavelength of C-band, and dual-polarized acquisitions make Sentinel-1 datasets have the advantage of better distinguishing among different vegetation types.

Given the shorter wavelength of X-band, TerraSAR-X signal has very limited penetration depth into the vegetation canopy, and it easily reaches a backscatter saturation level. Distinguishing between different vegetation covers is not easy. The longer wavelength of C-band can improve the situation in a certain way. At X-band, volume scattering from vegetation and snow tends to dominate in regions of dense and high vegetation cover, and the effects of soil characteristics are not obvious (Duguay et al., 2015). In contrast, at the C-band, ground scattering (e.g., the effects of soil freezing and thawing) holds a larger component of the total backscatter (Duguay et al., 2015). These characteristics are beneficial to achieve higher accuracy when distinguishing among different landscapes.

The information regarding splitters/features could be transferable to other studies of land cover classifications in high-latitude regions when using X-band datasets. Alternatively, when using datasets of different frequencies, CART analysis can be employed to effectively determine the most suitable features and threshold values for land cover classification from a variety of candidate features that are derived from multi-temporal/time-series backscatter intensity and interferometric images.

In this study, the geometric information of objects (e.g., area, border length, width, asymmetry, compactness, elliptic fit, roundness) was not used in the OBIA analysis because we wanted to test whether features that were derived from multi-temporal SAR images could adequately classify land cover types in heterogeneous discontinuous permafrost environments. Thus, the geometric information of objects and DEM information were not included in the analysis. Users can add the geometric information of object and DEM information into their analyses, which can improve the classification accuracy in some study areas.

Sigma nought was converted to gamma nought by using Eq. (3) in Section 3.4. In our study, sigma nought could also be used for the analysis because classification was applied on the segmented objects. Within each object, the variations in the topography and local incidence angle were very small because segmented objects were formed to minimize the resulting summed heterogeneity (Evans and Costa, 2013). Compensation

for topography-induced effects and incidence angle normalization is preferred to conduct when applying pixel-based classification over wide swaths.

We explored the potential of multi-temporal backscatter intensity and interferometric information for land cover classification in a discontinuous permafrost environment when using TerraSAR-X datasets. This multi-temporal analysis can also be applied to pixel-based classifications. Compared to pixel-based classifications, OBIA analysis raises the problem of image segmentation: choosing appropriate segmentation parameters is an issue. However, the benefits are also notable: (1) segmentation on the most sharply stacked mean backscatter intensity image reduced the noise in the classification results; (2) OBIA allows for easy fusion of the backscatter intensity and interferometric information; and (3) the standard deviation of the backscatter within each object can contribute to improve the classification accuracy. As shown in Figs. 8–11, these features, i.e., features whose names ended with “_sd”, had high predictor rankings (also known as variable importance) in some classification processes.

Regarding segmentation parameters, we used shape = 0.1 and compactness = 0.5 in this study because they provided an overall acceptable solution; these values are also the default settings in eCognition. The scale numbers 20 (Level 1 segmentation) and 5 (Level 2 segmentation) were defined based on our knowledge of the landscape and the visual interpretation of the segmentation results. The Estimate Scale Tool (ESP) could also help determine the optimal scale number (Drăguț et al., 2010).

7. Conclusions

Ecological changes in northern high-latitude regions and their interactions with permafrost degradation processes have drawn attention in recent years. Cloud cover and solar illumination issues largely limit the suitability of optical remote sensing data for regular monitoring purposes. Modern spaceborne platforms provide HR single-, dual- or quad-polarized images independent of the cloud cover and solar illumination, which is especially useful in heterogeneous sub-arctic environments. However, a permafrost landscape feature mapping strategy using SAR data is still under development.

In this study, a processing and classification method was developed to implement land cover classification in a heterogeneous environment with multi-temporal SAR backscatter and interferometric images. The proposed method included two main advantages. (1) The noise in the classification results brought by the speckle noise within the radar imagery was largely reduced without sacrificing the spatial resolution. This was achieved through two steps: first, the spatio-temporal filtering of time-series images diminished the speckle noise in the radar images; second, the segmentation step in the OBIA analysis was implemented on the stacked mean backscatter intensity image. The stacked mean backscatter intensity image provided the sharpest contrast between different landscapes, facilitated segmentation, and created accurate object boundaries for the classification. (2) Features that were derived from multi-temporal backscatter intensity and interferometric images were fully employed in the classification, which was achieved through the combined usage of OBIA and CART analysis. The OBIA analysis allows for easy fusion of the backscatter intensity and interferometric information. The CART analysis effectively determined the most suitable features and threshold values for land cover classification from a variety of candidate features that were derived from multi-temporal/time-series backscatter intensity and interferometric images.

The proposed methodology was applied in a discontinuous permafrost environment. The results showed that the proposed permafrost landscape mapping method can classify permafrost landscapes and describe the important features of a permafrost environment, e.g., the distribution of permafrost-affected areas and thermokarst ponds. In terms of the accuracy of the classification, our results were comparable with those of two previous studies in the same study area, which used VHR aerial photographs (Provencher-Nolet, 2014) and RADARSAT-2 quad-pol images with an SVM classification scheme (Duguay et al., 2016). The performance of this method was qualified when applied to the heterogeneous environment of our test site; we assume that the method will show improvement in a less heterogeneous environment.

These findings demonstrate the potential of using multi-temporal backscatter intensity and interferometric coherence features to classify land cover types in a complex sub-arctic environment. In addition, such a processing and classification strategy with multi-temporal SAR images could be transferred to other heterogeneous environments. In this study, we chose not to perform polarimetric analyses of the dual-polarized TerraSAR-X images. Polarimetric information can further improve the classification accuracy, so the inclusion of polarimetric information into a multi-temporal/time-series analysis is recommended for future applications.

Acknowledgments

The authors acknowledge the German Aerospace Centre (DLR) for supplying the TerraSAR-X data, Airbus Defence and Space for providing the WorldDEMcore product, Planet Labs for providing the RapidEye imagery through the RapidEye Science Archive (RESA) Initiative, and the Salford Systems company for providing the SPM Salford Predictive Modeler software for the CART analysis. This project is supported by grants and contributions from the Bavarian Research Alliance (BayFOR), the Canadian Space Agency (CSA, grant number: 14SUSMAPIN), the Helmholtz Research School of Mechanisms and Interactions of Climate Change in Mountain Regions (MICMoR) and the Centre d'Études Nordiques (CEN). The authors also thank Prof. Michel Allard (CEN) and Denis Sarrazin (CEN) for supporting this research. The authors also thank Jimmy Poulin, Andres Jacome, Yueli Chen, and Chaima Touati for providing valuable assistance during the fieldwork and Maxime Jolivel for providing the reference data. The authors are grateful to the CEN for providing helicopter time and logistical support. We are also grateful to the Inuit community of Umiujaq for their generous hospitality.

Appendix

See Figs. A1 and A2.

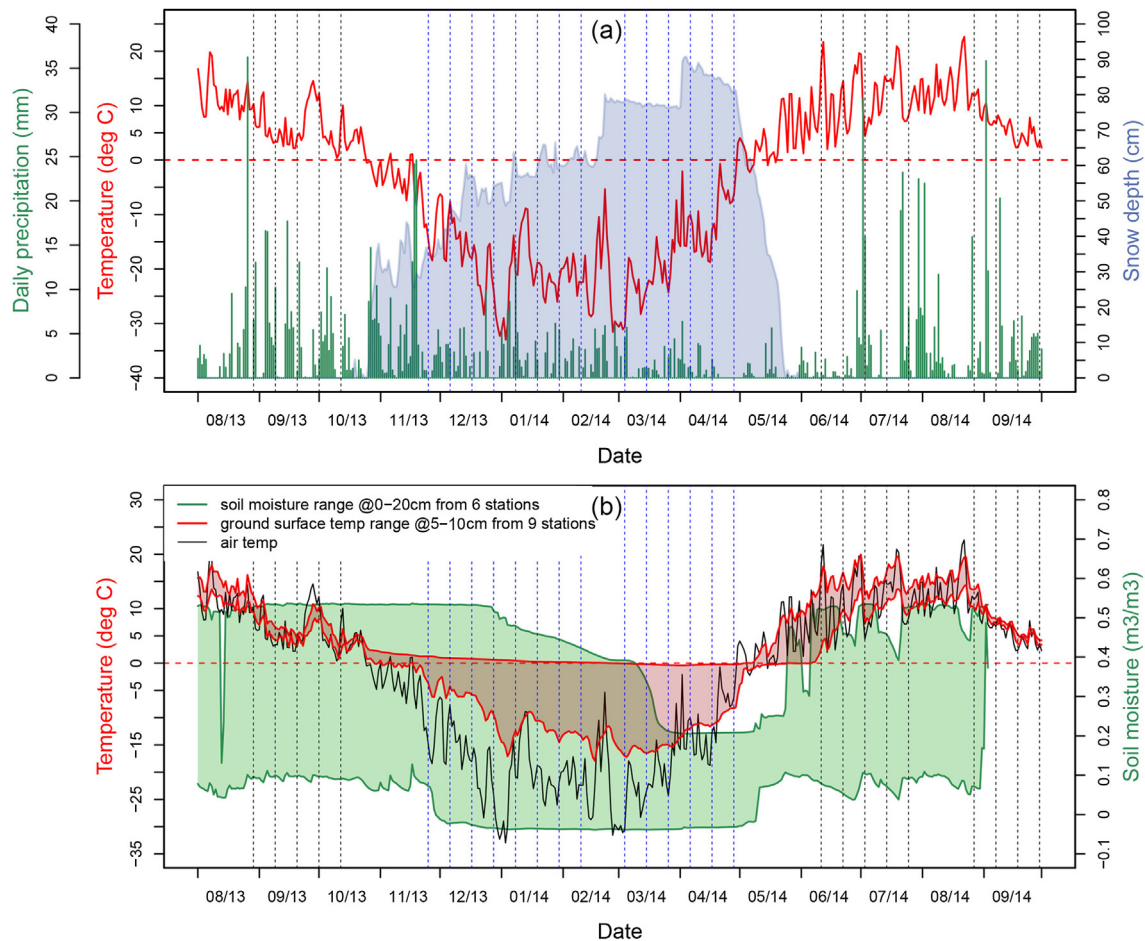
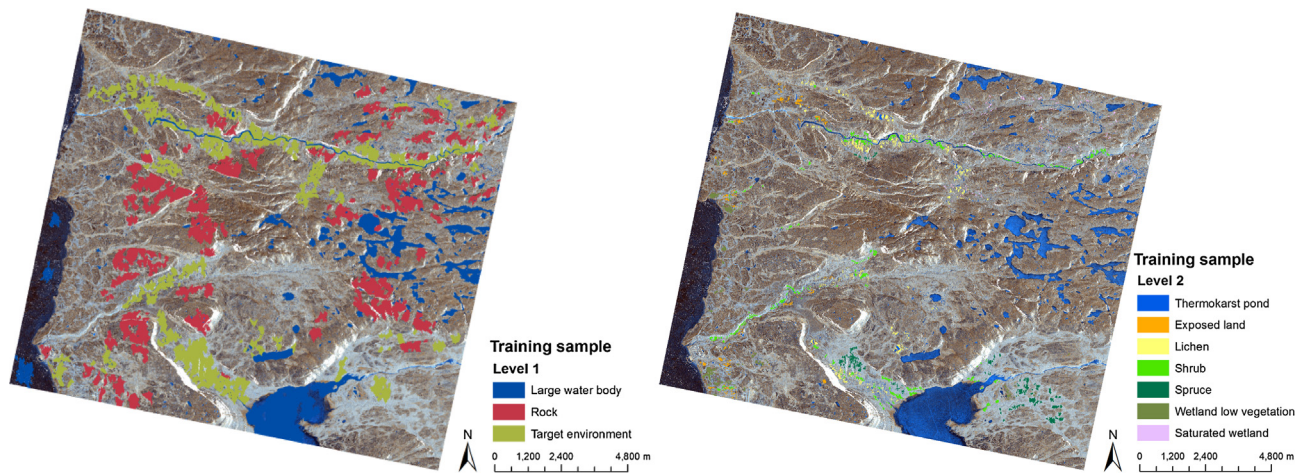


Fig. A1. (a) Air temperature, daily accumulated precipitation, and snow depth data from the meteorological station in the northern Tasiapik Valley for the period from August 2013 to September 2014. The dashed lines mark TerraSAR-X acquisitions; the black lines represent the summer; and the blue lines represent the winter. (b) Soil moisture (0–20 cm) and soil temperature (5 cm and 10 cm) conditions. Nine of the sites provided soil temperature measurements at depths of 5 cm and 10 cm, six of which provided soil moisture measurements at three different depths (5 cm, 10 cm, and 20 cm). One site is located in the coastal region, six are located in the Tasiapik Valley, and the other two are situated in the Sheldrake catchment. The ground conditions can be interpreted in the context of soil temperature and moisture conditions. (For interpretation of the references to colour in this figure legend, the reader is referred to the web version of this article.)



(a) Training and testing samples for the OBIA Level 1 classification. (b) Training and testing samples for the OBIA Level 2 classification.

Fig. A2. Training and testing samples for the two-level OBIA classification. Half of the samples served as training samples for the CART analysis, whereas the other half served as testing samples for the assessment of the classification accuracy. The base map is a composite TerraSAR-X image (R: M_su_m, G: M_a_m, B: M_wi_m).

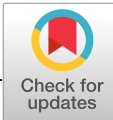
References

- Airbus, D., 2014. Space, "Radiometric Calibration of TerraSAR-X Data: Beta Naught and Sigma Naught Coefficient Calculation. In: TSXX-ITD-TN-0049.
- Allard, M., Lemay, M., Barrette, C., L'Hérault, E., Sarrazin, D., Bell, T., Doré, G., 2012. Permafrost and climate change in Nunavik and Nunatsiavut: Importance for municipal and transportation infrastructures.
- Allard, M., Seguin, M.K., 1987. The Holocene evolution of permafrost near the tree line, on the eastern coast of Hudson Bay (northwestern Quebec). *Can. J. Earth Sci.* 24, 2206–2222.
- Antonova, S., Duguay, C.R., Kääh, A., Heim, B., Langer, M., Westermann, S., Boike, J., 2016a. Monitoring bedfast ice and ice phenology in lakes of the Lena river delta using TerraSAR-X backscatter and coherence time series. *Remote Sens.* 8, 903.
- Antonova, S., Kääh, A., Heim, B., Langer, M., Boike, J., 2016b. Spatio-temporal variability of X-band radar backscatter and coherence over the Lena River Delta, Siberia. *Remote Sens. Environ.* 182, 169–191.
- ArcGIS. An overview of the Photos toolset. In: <<http://desktop.arcgis.com/en/arcmap/10.3/tools/data-management-toolbox/an-overview-of-the-photos-toolset.htm>>
- Baatz, M., Schäpe, A., 2000. Multiresolution segmentation: an optimization approach for high quality multi-scale image segmentation. *Angewandte geographische informationsverarbeitung XII* 58, 12–23.
- Banks, S., Ullmann, T., Roth, A., Schmitt, A., Dech, S., King, D., 2013. Classification of Arctic Coastal land covers with polarimetric SAR data. In: *Radar Conference (RADAR), 2013 IEEE, IEEE*, pp. 1–6.
- Banks, S.N., King, D.J., Merzouki, A., Duffe, J., 2014. Characterizing scattering behaviour and assessing potential for classification of arctic shore and near-shore land covers with fine quad-pol RADARSAT-2 data. *Can. J. Remote Sens.* 40, 291–314.
- Bartsch, A., Pathe, C., Wagner, W., Scipal, K., 2008. Detection of permanent open water surfaces in central Siberia with ENVISAT ASAR wide swath data with special emphasis on the estimation of methane fluxes from tundra wetlands. *Hydrol. Res.* 39, 89–100.
- Beck, I., Ludwig, R., Bernier, M., Lévesque, E., Boike, J., 2015. Assessing Permafrost Degradation and Land Cover Changes (1986–2009) using Remote Sensing Data over Umiujaq, Sub-Arctic Québec. *Permafrost and Periglacial Processes*.
- Bouchard, F., Francus, P., Pienitz, R., Laurion, I., Feyte, S., 2014. Subarctic thermokarst ponds: investigating recent landscape evolution and sediment dynamics in thawed permafrost of northern Québec (Canada). *Arctic, Antarctic, Alpine Res.* 46, 251–271.
- Bruzzone, L., Marconcini, M., Wegmuller, U., Wiesmann, A., 2004. An advanced system for the automatic classification of multitemporal SAR images. *IEEE Trans. Geosci. Remote Sens.* 42, 1321–1334.
- Calmels, F., Allard, M., 2004. Ice segregation and gas distribution in permafrost using tomodensitometric analysis. *Permafrost Periglacial Processes* 15, 367–378.
- Calmels, F., Allard, M., 2008. Segregated ice structures in various heaved permafrost landforms through CT Scan. *Earth Surf. Processes Landforms* 33, 209–225.
- Calmels, F., Allard, M., Delisle, G., 2008. Development and decay of a lithalsa in Northern Québec: a geomorphological history. *Geomorphology* 97, 287–299.
- Cihlar, J., Ly, H., Xiao, Q., 1996. Land cover classification with AVHRR multichannel composites in northern environments. *Remote Sens. Environ.* 58, 36–51.
- Cornelissen, J.H.C., Callaghan, T.V., Alatalo, J., Michelsen, A., Graglia, E., Hartley, A., Hik, D., Hobbie, S., Press, M., Robinson, C.H., 2001. Global change and arctic ecosystems: is lichen decline a function of increases in vascular plant biomass? *J. Ecol.* 89, 984–994.
- de Almeida Furtado, L.F., Silva, T.S.F., de Moraes Novo, E.M.L., 2016. Dual-season and full-polarimetric C band SAR assessment for vegetation mapping in the Amazon várzea wetlands. *Remote Sens. Environ.* 174, 212–222.
- Drăguț, L., Tiede, D., Levick, S.R., 2010. ESP: a tool to estimate scale parameter for multiresolution image segmentation of remotely sensed data. *Int. J. Geogr. Inf. Sci.* 24, 859–871.
- Duguay, Y., Bernier, M., Lévesque, E., Domine, F., 2016. Land cover classification in SubArctic regions using fully polarimetric RADARSAT-2 data. *Remote Sens.* 8, 697.
- Duguay, Y., Bernier, M., Lévesque, E., Tremblay, B., 2015. Potential of C and X band SAR for shrub growth monitoring in sub-arctic environments. *Remote Sens.* 7, 9410–9430.
- Durieux, L., Kropáček, J., De Grandi, G., Achard, F., 2007. Object-oriented and textural image classification of the Siberia GBFM radar mosaic combined with MERIS imagery for continental scale land cover mapping. *Int. J. Remote Sens.* 28, 4175–4182.
- Elmendorf, S.C., Henry, G.H., Hollister, R.D., Björk, R.G., Boulanger-Lapointe, N., Cooper, E.J., Cornelissen, J.H., Day, T.A., Dorrepaal, E., Elumeeva, T.G., 2012. Plot-scale evidence of tundra vegetation change and links to recent summer warming. *Nat. Climate Change* 2, 453–457.
- Engram, M., Anthony, K., Meyer, F., Grosse, G., 2013. Characterization of L-band synthetic aperture radar (SAR) backscatter from floating and grounded thermokarst lake ice in Arctic Alaska. *Cryosphere* 7, 1741–1752.
- EnvironmentCanada, 2010. Canadian Climate Normals or Averages. In: <http://climate.weather.gc.ca/climate_normals/results_1981_2010_e.html?stnID=6083&autofwd=1>.
- Esch, T., Thiel, M., Bock, M., Roth, A., Dech, S., 2008. Improvement of image segmentation accuracy based on multiscale optimization procedure. *IEEE Geosci. Remote Sens. Lett.* 5, 463–467.
- Evans, T.L., Costa, M., 2013. Landcover classification of the lower Nhecolândia subregion of the Brazilian Pantanal Wetlands using ALOS/PALSAR, RADARSAT-2 and ENVISAT/ASAR imagery. *Remote Sens. Environ.* 128, 118–137.
- Fraser, R., Olthof, I., Carrière, M., Deschamps, A., Pouliot, D., 2011. Detecting long-term changes to vegetation in northern Canada using the Landsat satellite image archive. *Environ. Res. Lett.* 6, 045502.
- Fraser, R.H., Lantz, T.C., Olthof, I., Kokelj, S.V., Sims, R.A., 2014. Warming-induced shrub expansion and lichen decline in the Western Canadian Arctic. *Ecosystems* 17, 1151–1168.
- Friedl, M.A., Brodley, C.E., 1997. Decision tree classification of land cover from remotely sensed data. *Remote Sens. Environ.* 61, 399–409.
- Frost, G.V., Epstein, H.E., Walker, D.A., 2014. Regional and landscape-scale variability of Landsat-observed vegetation dynamics in northwest Siberian tundra. *Environ. Res. Lett.* 9, 025004.
- Frost, V.S., Stiles, J.A., Shanmugan, K.S., Holtzman, J.C., 1982. A model for radar images and its application to adaptive digital filtering of multiplicative noise. *IEEE Trans. Pattern Anal. Mach. Intell.*, 157–166.
- GAMMARemoteSensingAG, 2009. Land Application Tools – LAT, Version 1.0. In: Gümligen, Switzerland.

- GAMMAREmoteSensingAG, 2011a. Differential Interferometry and Geocoding Software – DIFF&GEO, Version 1.3. In: Gümligen, Switzerland.
- GAMMAREmoteSensingAG (2011b). Interferometric SAR Processor - ISP, Version 1.6. In. Gümligen, Switzerland
- Goodrich, L., 1982. The influence of snow cover on the ground thermal regime. *Can. Geotech. J.* 19, 421–432.
- Hall-Atkinson, C., Smith, L.C., 2001. Delineation of delta ecozones using interferometric SAR phase coherence: Mackenzie River Delta, NWT, Canada. *Remote Sens. Environ.* 78, 229–238.
- Hellesen, T., Matikainen, L., 2013. An object-based approach for mapping shrub and tree cover on grassland habitats by use of LiDAR and CIR orthoimages. *Remote Sens.* 5, 558–583.
- Hugelius, G., Strauss, J., Zubrzycki, S., Harden, J.W., Schuur, E., Ping, C.-L., Schirmer, L., Grosse, G., Michaelson, G.J., Koven, C.D., 2014. Estimated stocks of circumpolar permafrost carbon with quantified uncertainty ranges and identified data gaps. *Biogeosciences* 11, 6573–6593.
- Jia, G.J., Epstein, H.E., Walker, D.A., 2009. Vegetation greening in the Canadian Arctic related to decadal warming. *J. Environ. Monitoring* 11, 2231–2238.
- Jolivel, M., Allard, M., 2013. Thermokarst and export of sediment and organic carbon in the Sheldrake River watershed, Nunavik, Canada. *J. Geophys. Res.: Earth Surf.* 118, 1729–1745.
- Jones, B.M., Grosse, G., Arp, C., Jones, M., Walter Anthony, K., Romanovsky, V., 2011. Modern thermokarst lake dynamics in the continuous permafrost zone, northern Seward Peninsula, Alaska. *J. Geophys. Res.: Biogeosci.* 116.
- Kokelj, S.V., Jorgenson, M., 2013. Advances in thermokarst research. *Permafrost Periglacial Processes* 24, 108–119.
- Krieger, G., Moreira, A., Fiedler, H., Hajnsek, I., Werner, M., Younis, M., Zink, M., 2007. TanDEM-X: a satellite formation for high-resolution SAR interferometry. *IEEE Trans. Geosci. Remote Sens.* 45, 3317–3341.
- Laurion, I., Vincent, W.F., MacIntyre, S., Retamal, L., Dupont, C., Francus, P., Pienitz, R., 2010. Variability in greenhouse gas emissions from permafrost thaw ponds. *Limnol. Oceanogr.* 55, 115–133.
- Lawrence, R.L., Wright, A., 2001. Rule-based classification systems using classification and regression tree (CART) analysis. *Photogrammetric Eng. Remote Sens.* 67, 1137–1142.
- Macias-Fauria, M., Forbes, B.C., Zetterberg, P., Kumpula, T., 2012. Eurasian Arctic greening reveals teleconnections and the potential for structurally novel ecosystems. *Nat. Climate Change* 2, 613–618.
- Marsh, P., Russell, M., Pohl, S., Haywood, H., Onclin, C., 2009. Changes in thaw lake drainage in the Western Canadian Arctic from 1950 to 2000. *Hydrol. Processes* 23, 145–158.
- Matikainen, L., Karila, K., 2011. Segment-based land cover mapping of a suburban area—comparison of high-resolution remotely sensed datasets using classification trees and test field points. *Remote Sens.* 3, 1777–1804.
- Mätzler, C., Schanda, E., 1984. Snow mapping with active microwave sensors. *Remote Sens.* 5, 409–422.
- Ménard, É., Allard, M., Michaud, Y., 1998. Monitoring of ground surface temperatures in various biophysical micro-environments near Umiujaq, eastern Hudson Bay, Canada. In: *Proceedings of the 7th International Conference on Permafrost*. Yellowknife, Canada, pp. 723–729.
- Meyer, F.J., Mahoney, A.R., Eicken, H., Denny, C.L., Druckenmiller, H.C., Hendricks, S., 2011. Mapping arctic landfast ice extent using L-band synthetic aperture radar interferometry. *Remote Sens. Environ.* 115, 3029–3043.
- Muster, S., Langer, M., Heim, B., Westermann, S., Boike, J., 2012. Subpixel heterogeneity of ice-wedge polygonal tundra: a multi-scale analysis of land cover and evapotranspiration in the Lena River Delta, Siberia. *Tellus B*, 64.
- Myers-Smith, I.H., Forbes, B.C., Wilms, M., Hallinger, M., Lantz, T., Blok, D., Tape, K.D., Macias-Fauria, M., Sass-Klaassen, U., Lévesque, E., 2011. Shrub expansion in tundra ecosystems: dynamics, impacts and research priorities. *Environ. Res. Lett.* 6, 045509.
- Nicholson, F., 1979. Permafrost spatial and temporal variations near Schefferville, Nouveau-Québec. *Géographie physique et Quaternaire* 33, 265–277.
- Nicholson, F.H., 1976. Permafrost thermal amelioration tests near Schefferville, Québec. *Can. J. Earth Sci.* 13, 1694–1705.
- Oliver, C., Quegan, S., 2004. *Understanding Synthetic Aperture Radar Images*. SciTech Publishing.
- Olofsson, P., Foody, G.M., Herold, M., Stehman, S.V., Woodcock, C.E., Wulder, M.A., 2014. Good practices for estimating area and assessing accuracy of land change. *Remote Sens. Environ.* 148, 42–57.
- Payette, S., 1983. The forest tundra and present tree-lines of the northern Québec-Labrador peninsula. *Nordicana* 47, 3–23.
- Payette, S., Delwaide, A., Caccianiga, M., Beauchemin, M., 2004. Accelerated thawing of subarctic peatland permafrost over the last 50 years. *Geophys. Res. Lett.* 31.
- Pelletier, M., 2015. Geomorphological, ecological and thermal time phase of permafrost degradation, Tasiapik, Nunavik (Québec, Canada). In: *Géographiques*. University of Laval, Québec, Canada.
- Pissart, A., 2002. Palsas, lithalsas and remnants of these periglacial mounds. A progress report. *Progr. Phys. Geogr.* 26, 605–621.
- Provencher-Nolet, L., 2014. Détection de changement à court terme de la toundra arbustive à partir de photographies aériennes, région d'Umiujaq, Nunavik (Québec, Canada). In: *Université du Québec*.
- Quegan, S., Le Toan, T., Yu, J.J., Ribbes, F., Floury, N., 2000. Multitemporal ERS SAR analysis applied to forest mapping. *IEEE Trans. Geosci. Remote Sens.* 38, 741–753.
- Quegan, S., Yu, J.J., 2001. Filtering of multichannel SAR images. *IEEE Trans. Geosci. Remote Sens.* 39, 2373–2379.
- Riegler, G., Hennig, S.D., Weber, M., 2015. WorldDEM – a novel global foundation layer. *ISPRS – Int. Arch. Photogrammetry XL-3/W2 Remote Sens. Spatial Inf. Sci.* 183–187.
- Rignot, E., Way, J.B., 1994. Monitoring freeze–thaw cycles along North–South Alaskan transects using ERS-1 SAR. *Remote Sens. Environ.* 49, 131–137.
- Robson, B.A., Nuth, C., Dahl, S.O., Hölbling, D., Strozzi, T., Nielsen, P.R., 2015. Automated classification of debris-covered glaciers combining optical, SAR and topographic data in an object-based environment. *Remote Sens. Environ.* 170, 372–387.
- Romanovsky, V.E., Smith, S.L., Christiansen, H.H., 2010. Permafrost thermal state in the polar Northern Hemisphere during the international polar year 2007–2009: a synthesis. *Permafrost Periglacial Processes* 21, 106–116.
- Sannel, A., Kuhry, P., 2011. Warming-induced destabilization of peat plateau/thermokarst lake complexes. *J. Geophys. Res.: Biogeosci.* 116.
- Santorio, M., Wegmüller, U., Lamarche, C., Bontemps, S., Defourny, P., Arino, O., 2015. Strengths and weaknesses of multi-year Envisat ASAR backscatter measurements to map permanent open water bodies at global scale. *Remote Sens. Environ.* 171, 185–201.
- Sasaki, T., Imanishi, J., Ioki, K., Morimoto, Y., Kitada, K., 2012. Object-based classification of land cover and tree species by integrating airborne LiDAR and high spatial resolution imagery data. *Landscape Ecol. Eng.* 8, 157–171.
- Schaefer, K., Liu, L., Parsekian, A., Jafarov, E., Chen, A., Zhang, T., Gusmeroli, A., Panda, S., Zebker, H.A., Schaefer, T., 2015. Remotely sensed active layer thickness (ReSALT) at Barrow, Alaska using interferometric synthetic aperture radar. *Remote Sens.* 7, 3735–3759.
- Schimel, J.P., Bilbrough, C., Welker, J.M., 2004. Increased snow depth affects microbial activity and nitrogen mineralization in two Arctic tundra communities. *Soil Biol. Biochem.* 36, 217–227.
- Schuur, E.A., Bockheim, J., Canadell, J.G., Euskirchen, E., Field, C.B., Goryachkin, S.V., Hagemann, S., Kuhry, P., Laflaur, P.M., Lee, H., 2008. Vulnerability of permafrost carbon to climate change: implications for the global carbon cycle. *Bioscience* 58, 701–714.
- Serreze, M., Walsh, J., Chapin, F.S., Osterkamp, T., Dyrugerov, M., Romanovsky, V., Oechel, W., Morison, J., Zhang, T., Barry, R., 2000. Observational evidence of recent change in the northern high-latitude environment. *Climatic Change* 46, 159–207.
- Smith, L.C., Sheng, Y., MacDonald, G., Hinzman, L., 2005. Disappearing arctic lakes. *Science* 308, 1429–1429.
- Stiles, W.H., Ulaby, F.T., 1980. The active and passive microwave response to snow parameters: 1. Wetness. *J. Geophys. Res.: Oceans* 85, 1037–1044.
- Stocker, T., Qin, D., Plattner, G., Tignor, M., Allen, S., Boschung, J., Nauels, A., Xia, Y., Bex, B., & Midgley, B., 2013. *IPCC, 2013: climate change 2013: the physical science basis. Contribution of working group I to the fifth assessment report of the intergovernmental panel on climate change*.
- Sturm, M., Holmgren, J., McFadden, J.P., Liston, G.E., Chapin III, F.S., Racine, C.H., 2001a. Snow–shrub interactions in Arctic tundra: a hypothesis with climatic implications. *J. Climate* 14, 336–344.
- Sturm, M., Racine, C., Tape, K., 2001b. Climate change: increasing shrub abundance in the Arctic. *Nature* 411, 546–547.
- Sturm, M., Schimel, J., Michaelson, G., Welker, J.M., Oberbauer, S.F., Liston, G.E., Fahnestock, J., Romanovsky, V.E., 2005. Winter biological processes could help convert arctic tundra to shrubland. *Bioscience* 55, 17–26.
- Sulla-Menashe, D., Friedl, M.A., Krankina, O.N., Baccini, A., Woodcock, C.E., Sibley, A., Sun, G., Kharuk, V., Elsakov, V., 2011. Hierarchical mapping of Northern Eurasian land cover using MODIS data. *Remote Sens. Environ.* 115, 392–403.
- Thom, B.G., 1969. *New permafrost investigations near Schefferville*. Presses de l'Université de Montréal, PQ.
- Tremblay, B., Lévesque, E., Boudreau, S., 2012. Recent expansion of erect shrubs in the Low Arctic: evidence from Eastern Nunavik. *Environ. Res. Lett.* 7, 035501.
- Ulaby, F.T., Stiles, W., Dellwig, L., Hanson, B., 1977. Experiments on the radar backscatter of snow. *IEEE Trans. Geosci. Electron.* 15, 185–189.
- Ulander, L.M., 1996. Radiometric slope correction of synthetic-aperture radar images. *IEEE Trans. Geosci. Remote Sens.* 34, 1115–1122.
- Ullmann, T., Schmitt, A., Jagdhuber, T., 2016. Two component decomposition of dual polarimetric HH/VV SAR data: case study for the tundra environment of the Mackenzie delta region, Canada. *Remote Sens.* 8, 1027.
- Ullmann, T., Schmitt, A., Roth, A., Duffe, J., Dech, S., Hubberten, H.-W., Baumhauer, R., 2014. Land cover characterization and classification of arctic tundra environments by means of polarized synthetic aperture X- and C-Band Radar (PolSAR) and Landsat 8 multispectral imagery—Richards Island, Canada. *Remote Sens.* 6, 8565–8593.
- Walker, D., Gould, W., Maier, H., Reynolds, M., 2002. The circumpolar arctic vegetation map: AVHRR-derived base maps, environmental controls, and integrated mapping procedures. *Int. J. Remote Sens.* 23, 4551–4570.
- Walker, W.S., Stickler, C.M., Kelldorfer, J.M., Kirsch, K.M., Nepstad, D.C., 2010. Large-area classification and mapping of forest and land cover in the Brazilian Amazon: a comparative analysis of ALOS/PALSAR and Landsat data sources. *IEEE J. Selected Topics Appl. Earth Observations Remote Sens.* 3, 594–604.
- Walter, K.M., Zimov, S., Chanton, J.P., Verbyla, D., Chapin, F.S., 2006. Methane bubbling from Siberian thaw lakes as a positive feedback to climate warming. *Nature* 443, 71–75.
- Wang, L., Marzahn, P., Bernier, M., Jacome, A., Poulin, J., Ludwig, R., 2017. Comparison of TerraSAR-X and ALOS PALSAR Differential Interferometry with multisource DEMs for monitoring ground displacement in a discontinuous permafrost region. *IEEE J. Selected Topics Appl. Earth Observations Remote Sens.*

- Way, J., Paris, J., Kasischke, E., Slaughter, C., Viereck, L., Christensen, N., Dobson, M.C., Ulaby, F., Richards, J., Milne, A., 1990. The effect of changing environmental conditions on microwave signatures of forest ecosystems: preliminary results of the March 1988 Alaskan aircraft SAR experiment. *Int. J. Remote Sens.* 11, 1119–1144.
- Wegmüller, U., 1999. Automated terrain corrected SAR geocoding. In: *Geoscience and Remote Sensing Symposium, 1999. IGARSS'99 Proceedings. IEEE 1999 International, IEEE*. pp. 1712–1714.
- Wegmüller, U., Werner, C., 1997. Land applications using ERS-1/2 tandem data. ESA SP.
- Werner, C., Wegmüller, U., Strozzi, T., Wiesmann, A. (2000). Gamma SAR and interferometric processing software. In: *Proceedings of the ERS-Envisat symposium, gothenburg, Sweden*. p. 1620.
- Widhalm, B., Bartsch, A., Leibman, M., Khomutov, A., 2017. Active-layer thickness estimation from X-band SAR backscatter intensity. *Cryosphere* 11, 483.
- WorldDEM, 2015. WorldDEM™ Technical Product Specification. In. <<http://www.geo-airbusds.com/worlddem/>>.
- Yoshikawa, K., Hinzman, L.D., 2003. Shrinking thermokarst ponds and groundwater dynamics in discontinuous permafrost near Council, Alaska. *Permafrost Periglacial Processes* 14, 151–160.
- Zebker, H., Villasenor, J., 1992. Decorrelation in interferometric radar echoes. *Geosci. Remote Sens., IEEE Trans.* 30, 950–959.
- Zhang, T., 2005. Influence of the seasonal snow cover on the ground thermal regime: an overview. *Rev. Geophys.* 43.
- Zhang, Z., Wang, C., Zhang, H., Tang, Y., Liu, X., 2018. Analysis of permafrost region coherence variation in the Qinghai-Tibet Plateau with a high-resolution TerraSAR-X image. *Remote Sens.* 10, 298.
- Zwieback, S., Bartsch, A., Melzer, T., Wagner, W., 2012. Probabilistic fusion of Ku and C band scatterometer data for determining the freeze/thaw state. *IEEE Trans. Geosci. Remote Sens.* 50, 2583–2594.

5 Thermokarst pond dynamics in subarctic environment monitoring with radar remote sensing



RESEARCH ARTICLE

WILEY

Thermokarst pond dynamics in subarctic environment monitoring with radar remote sensing

Lingxiao Wang^{1,4} | Maxime Jolivel^{2,4} | Philip Marzahn¹ | Monique Bernier^{3,4} | Ralf Ludwig^{1,4}

¹Department of Geography, Ludwig-Maximilians-Universität München, Munich, Germany

²Département de Géographie, Université Laval, Quebec, Canada

³Centre Eau, Terre and Environnement, Institut National de la Recherche Scientifique, Quebec, Canada

⁴Northern Research Center/Centre d'études nordiques (CEN), Quebec, Canada

Correspondence

Lingxiao Wang, Department of Geography, Ludwig-Maximilians-Universität München, Munich, Germany.

Email: l.wang@iggf.geo.uni-muenchen.de

Funding information

Canadian Space Agency, Grant/Award Number: 14SUSMAPIN

Abstract

Permafrost degradation can be monitored through changes in the surface area and depth of thermokarst ponds. Radar remote sensing allows for discrimination of thermokarst ponds of different depths across large areas because different water depths produce different ice regimes in winter. In this study, patterns in the spatial distribution of ice-cover regimes of thermokarst ponds in a typical discontinuous permafrost region are first revealed. Correlations of these ice-cover regimes with the permafrost degradation states and thermokarst pond development in two historical phases were analyzed and compared. The results indicate that the ice-cover regimes of thermokarst ponds are affected by soil texture, permafrost degradation stage and permafrost depth. Permafrost degradation is difficult to assess directly from the coverage area of floating-ice ponds and the percentage of all thermokarst ponds consisting of such floating-ice ponds in a single year. Therefore, continuous monitoring of ice-cover regimes and surface areas can help to elucidate the hydrological trajectory of the thermokarst process and permafrost state.

KEYWORDS

discontinuous permafrost, ice cover, pond dynamics, remote sensing, synthetic-aperture radar (SAR), thermokarst

1 | INTRODUCTION

Thermokarst ponds, which are closed depressions formed by ground subsidence following the thawing of ice-rich permafrost or ground ice,¹⁻⁴ are abundant in Arctic and subarctic permafrost lowlands. Thermokarst development thus indicates permafrost degradation. Many studies have monitored thermokarst/drainage development in Arctic and subarctic regions based on surface area changes in thermokarst ponds/lakes using optical remote sensing imagery.^{2,5-14} Once thermal erosion is initiated, the presence of a water body on permafrost serves as positive feedback to permafrost degradation. Depending on the excess ice content in permafrost, this positive feedback accelerates the growth of thermokarst ponds/lakes in both the lateral and the vertical direction.^{3,15,16} Over time, small, shallow water bodies can deepen, enlarge and coalesce to form medium-sized water bodies. The growth of thermokarst ponds facilitates the development of taliks (a thawed zone beneath a pond); large taliks can completely

penetrate the underlying permafrost. These taliks allow internal drainage throughout the year causing the ponds to shrink.⁹

Water depth is difficult to measure in Arctic and subarctic regions with limited access. However, due to different water depths, thermokarst ponds and lakes exhibit different ice regimes in winter. In winter, these ponds/lakes are shallower and can freeze completely to the bottom, and no liquid water remains when the seasonal ice thickness is at a maximum, resulting in grounded ice. If the ponds/lakes are deeper than the ice thickness, liquid water persists under the thick ice cover all winter, resulting in floating ice.^{17,18} Radar remote sensing permits detection of ice-cover regimes across large areas. The dielectric constant ϵ_v of liquid water and ice has a large contrast across the microwave spectrum. Liquid water has a remarkably high dielectric constant, whereas pure ice has a low value. Floating pond/lake ice has high backscatter intensity because liquid water beneath the ice cover provides a high dielectric contrast, causing most of the radar signal to reflect back. In contrast, in the case of grounded

lake ice, the microwaves pass through the snow and lake ice, and most of the radar signal is transmitted below the lake bed,¹⁸ resulting in low-intensity backscatter. Therefore, radar remote sensing can distinguish between these two ice-cover regimes due to the difference in the backscatter intensities between grounded and floating ice.¹⁷⁻²³ On radar images acquired during winter, ponds/lakes with floating ice exhibit high backscatter intensity, whereas those with grounded ice exhibit remarkable lower values.

Jeffries et al. (1996) used synthetic-aperture radar (SAR) imagery to determine thermokarst lake depth and water availability in the Barrow area, Alaska.¹⁹ Their results showed that 77% of the lakes in Barrow were completely frozen by the end of winter. In contrast, 100 km to the south, only 23% of the lakes froze completely. Studies have also explored the temporal balance between bedfast- and floating-ice regimes in thermokarst ponds/lakes. Arp et al. (2012) compared the ice-cover regime across the Arctic Coastal Plain of northern Alaska during the period 2003–2011 with the regime since 1980; 16% of the bedfast-ice lakes had shifted to the floating-ice regime.¹⁷ A shift from the bedfast-ice to the floating-ice regime can initiate talik development²⁴ and potentially release large stocks of carbon previously frozen in permafrost in the form of methane.^{10,25} By the end of the 21st century, near-surface permafrost area is projected

to decrease by between 37% (for the Representative Concentration Pathways (RCP) scenario 2.6) and 81% (for RCP scenario 8.5).²⁶ The shift of thermokarst ponds/lakes from grounded- to floating-ice regimes or vice versa due to water-level or ice-thickness changes is an indicator of climate variability and can be a result of lake drainage or lake expansion, thus indicating a permafrost state.^{17,27,28}

There is, to our knowledge, no research on ice-cover regime characteristics in the subarctic discontinuous permafrost zone. The distributions of ice-cover regimes and water depths of thermokarst ponds have yet to be elucidated. In the sporadic and discontinuous permafrost zones, thermokarst/drainage development is highly complex. A trend of pond shrinkage has been reported⁹; however, numerous small thermokarst ponds have also been observed forming in these regions.^{10,29} Time series of high-resolution SAR data have become freely available with the launch of the Sentinel-1 satellites. However, baseline information regarding the distribution and characteristics of ice-cover regimes of thermokarst ponds in the discontinuous permafrost region is lacking. In this study, we mapped the thermokarst pond distribution and winter ice-cover types in a typical discontinuous permafrost region using high-resolution TerraSAR-X radar imagery (3 m) acquired in 2013 and 2014. The relationships between ice-cover regime and thermokarst pond surface area, thermokarst pond

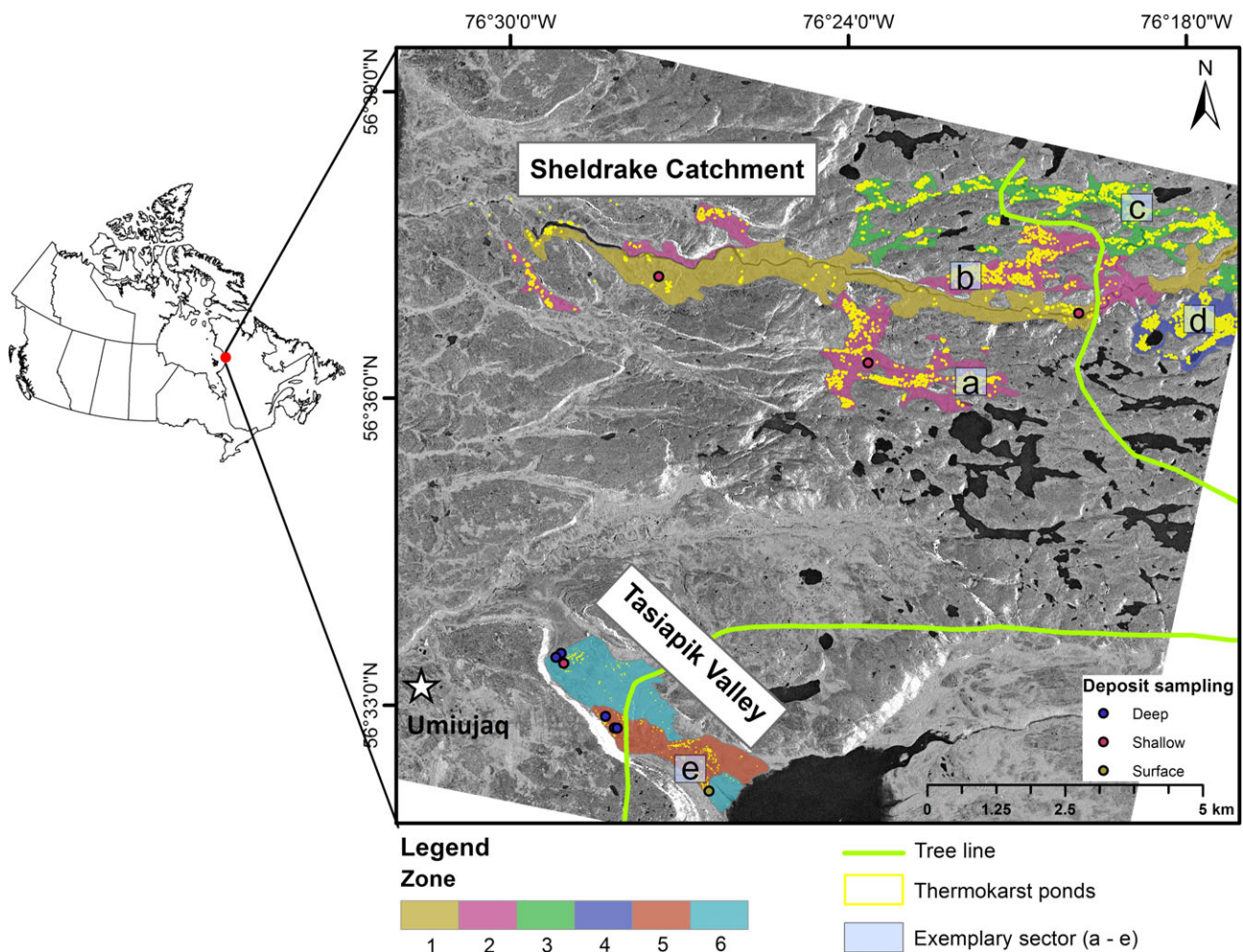


FIGURE 1 Study area within the Sheldrake River catchment. The base map is a TerraSAR-X image acquired in winter. The labeled squares delineate the maps shown in Figure 8. Soil texture sampling locations, and the tree line are overlain on the base map [Colour figure can be viewed at wileyonlinelibrary.com]

evolution and permafrost degradation states are thus explored for the first time. The method of processing the SAR images outlined in this study can be adopted by other researchers.

2 | STUDY AREA

The study area is located on the eastern shore of Hudson Bay in northern Quebec, Canada (56°32'N, 76°31'W), around the village of Umiujaq, and includes the Tasiapik Valley and Sheldrake River catchment (Figure 1). The study area is in a typical discontinuous permafrost region, in a transitional area between an isolated and sporadic permafrost zone (2–50% permafrost cover) and a widespread discontinuous permafrost zone (50–90% permafrost cover),³⁰ including a range of permafrost degradation states. The cooling impact of Hudson Bay generates a west–east climate gradient from the shoreline inward, resulting in the tree line being parallel to the coastline and approximately 15 km inland.^{31,32} The coastal zone is characterized by cooler summers due to frequent marine fog and high cloudiness, and by cold winters due to strong and dry winds traveling over the frozen bay. Inland, i.e., 15 km

or more from the coast, the landscape is forest-tundra, and the climate there is warmer and characterized by a thicker snow cover, particularly in forest stands. Consequently, the permafrost is patchier and decays more rapidly inland, east of the tree line, in the forest-tundra environment, than in the coastal shrub-tundra environment.²⁹ The variety of landscapes and permafrost degradation states within the study area makes it a good location to explore the relationship between ice-cover regimes and permafrost degradation states.

The climate is subarctic, with a mean annual air temperature (MAAT) of approximately -3°C ; the area experiences cold winters (-24°C in January) and cool summers (10°C in August).³³ However, the region is currently experiencing climate changes. Figure 2 shows the MAAT at three meteorological stations near the study area. Two stations (Kuujuarapik, 55°17'N, 77°45'W, 150 km south of the study area; and Inukjuak, 58°28'N, 78°05'W, 200 km north of the study area) have complete air temperature records from 1960 to 2017. The two stations reveal the same trend: MAAT remained stable in the 1960s–1990s; then, there was strong warming in the 1990s–2010s (with MAAT increasing by 2°C). After peaking in 2010, MAAT continuously dropped from 2010 to 2015, with the most recent two years (2016–2017) again exhibiting a warming. Although air temperature data from the Umiujaq station (10 km south of the study area) have been available only since 1997, these data agree with the observed trend in the data from the other two stations. Borehole temperature measurements collected within volcanic rock in the village of Umiujaq show strong ground warming over the previous decade. At a depth of 20 m, the ground temperature increased from -2.5°C in 1998 to 0.5°C in 2013.³⁴ Increases in air temperature trigger ground warming and widespread reduction in the extent of permafrost.

Lithalsas, permafrost plateaus, palsas and peat plateaus are the dominant permafrost landforms in the study area.²⁹ The volumetric ice contents of these landforms vary between 50 and 80%.^{35–37} Thermokarst ponds are abundant in the study area. Studies indicate that the thermokarst ponds at several locations on the eastern shore of Hudson Bay are generally round (10–30 m in diameter) and quite shallow (1–3.5 m deep).³⁸ In most cases, the 1–2-m-high peripheral ridges resulting from solifluction on the permafrost mounds are now covered by dense shrub and tree vegetation.³⁸ Figure 3 shows field photographs of thermokarst ponds in the study area.

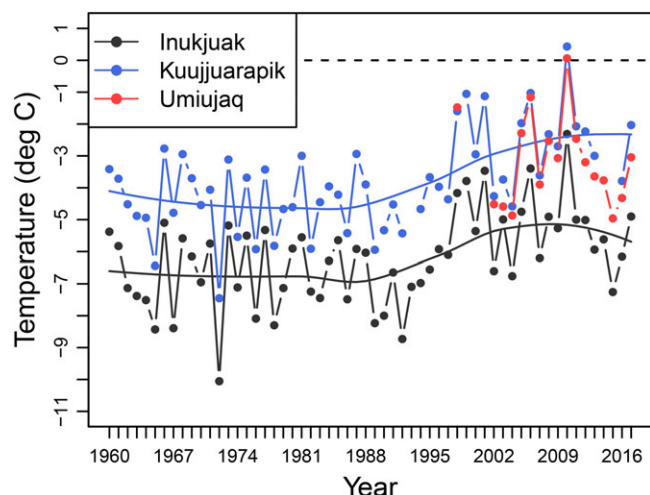


FIGURE 2 Mean annual air temperatures (MAATs) in the period 1960–2017 at three meteorological stations. The solid line is a non-parametric local regression applied on the original MAAT line curve of points [Colour figure can be viewed at wileyonlinelibrary.com]

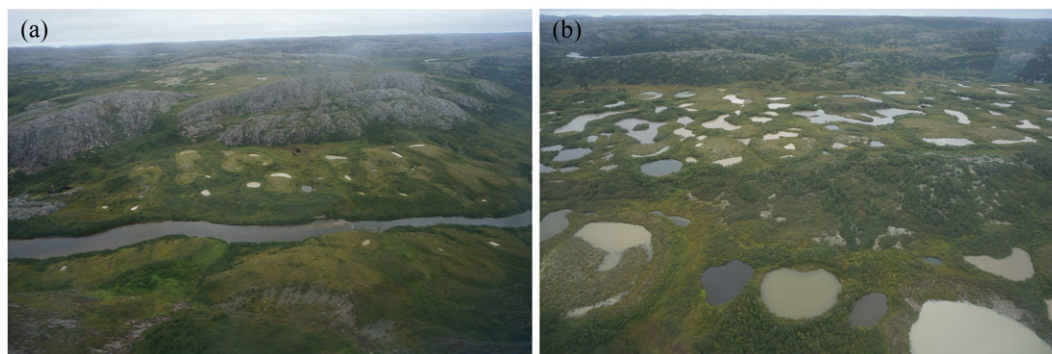


FIGURE 3 Field photographs of thermokarst ponds. (a) Small thermokarst ponds embedded in the permafrost mounds in the downstream of the catchment. (b) Many thermokarst ponds in degraded permafrost mounds upstream of the catchment [Colour figure can be viewed at wileyonlinelibrary.com]

Our analysis was conducted in six zones (Figure 1 and Table 1) representing different landscapes (shrub-tundra and forest-tundra), different permafrost degradation states and different soil textures, as listed in Table 1. Information regarding the local deposits was acquired from maps³⁹ and previous studies.^{29,36,40} The surficial deposits consist of glacial, glacio-fluvial, glacio-marine and marine sediments. Figure 1

shows the points where detailed soil texture information was available; information from four deep bore holes in the Tasiapik Valley is from previous studies,^{36,40} and shallow- (~1 m) and surface-soil sampling was conducted as part of our field campaign. In zones 1–4 in the Sheldrake catchment, the deposits consist of marine silty clay along the vertical profile with a texture that does not vary considerably.

TABLE 1 Information of six zones analyzed in this study

Zone	Location	Soil texture	Permafrost degradation state (%)	Area (km ²)	Thermokarst pond area fraction (%) of total area (2009–2010)
1	Sheldrake catchment	Silty clay	0–5	5.66	0.31
2	Sheldrake catchment	Silty clay	6–15	6.41	3.5
3	Sheldrake catchment	Silty clay	16–30	3.97	4.61
4	Sheldrake catchment	Silty clay	31–50	1.45	9.51
5	Tasiapik Valley	Silt loam	>50	1.75	2.06
6	Tasiapik Valley	Mainly sand, with a silty rich part	31–50	2.51	0.65

TABLE 2 Data used in this study

Historical data			Radar images
Region	Phase I	Phase II	2013–2014 28
Sheldrake catchment	1957	2009	TerraSAR-X images
	Aerial photograph (original scale of 1:40000, ~1-m resolution)	GeoEye satellite image (0.6-m resolution)	
	Thermokarst pond and permafrost feature map (via manual delineation)	Thermokarst pond and permafrost feature map (via manual delineation)	
Tasiapik Valley	1994	2010	
	Aerial photograph (0.15-m resolution)	Aerial photograph (0.15-m resolution)	
	Thermokarst pond and permafrost feature map (via classification)	Thermokarst pond and permafrost feature map (via classification)	

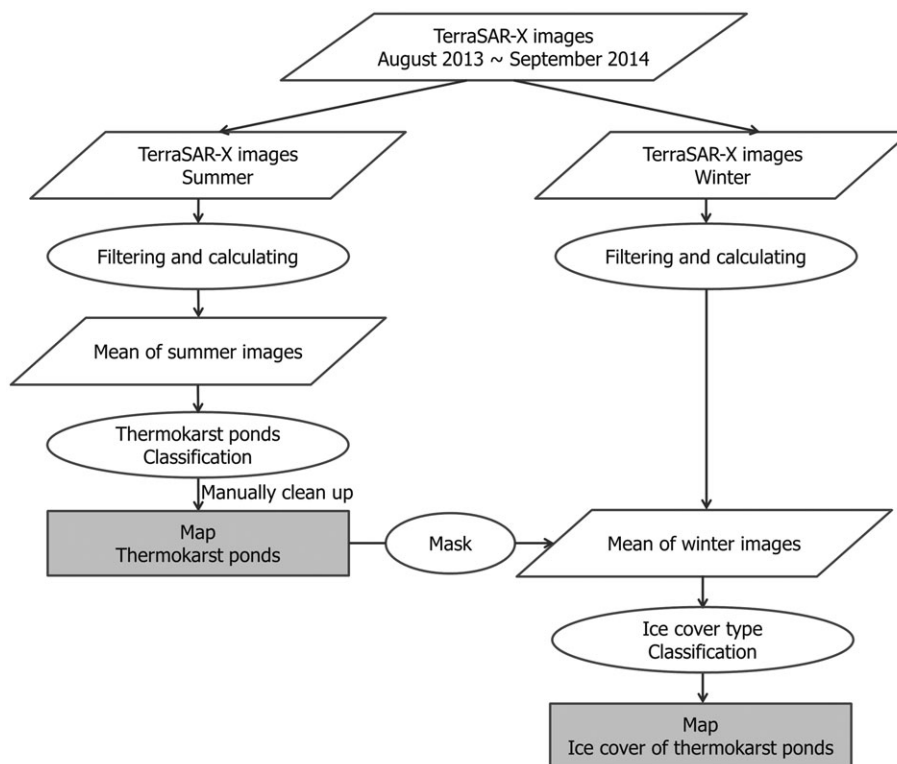


FIGURE 4 Workflow. First, the images were split into winter and summer acquisitions. The summer images were used to distinguish the thermokarst ponds from other land cover types, and the winter images were used to classify the ice-cover regimes of the thermokarst ponds

In zone 5, the deposits are a mixture of silt and sand, and the deposits in zone 6 are composed mainly of sand with a silty rich part along the profile. Table 1 lists the dominant textural components in the deposit profiles. Zone 2 is largest in area, followed by zones 1, 3, 6, 5 and 4. Five example sectors (marked in Figure 1) were selected to illustrate the thermokarst pond distribution and ice-cover regime mapping results in Figure 8 below.

3 | DATA

3.1 | Radar TerraSAR-X images

A time series of dual-co-polarized (HH, VV) TerraSAR-X images was collected between August 2013 and September 2014. The images were in StripMap mode with a pixel spacing of 0.9 and 2.3 m along the range and azimuth directions, respectively. Images that were affected by snow precipitation and snow melt events were discarded. In all, 28 SAR images were used for the analysis, which covered a time range of 1 year. Fourteen images that were free of ground snow cover were regarded as summer acquisitions. The other 14 images with snow cover were regarded as winter acquisitions.

3.2 | Historical data1

In both the Sheldkrake catchment and Tasiapik Valley, there were historical data in two phases, listed in Table 2. In the Sheldkrake catchment, permafrost features and thermokarst ponds were manually mapped on very high-resolution optical images (Phase I: 1957; Phase II: 2009). In the Tasiapik Valley, permafrost features and thermokarst ponds were mapped on very high-resolution optical images based on classification (Phase I: 1994; Phase II: 2010). Permafrost degradation states were determined by comparing the permafrost-affected areas in Phase I and Phase II. The degradation percentages are 0–5, 6–15, 16–30, 31–50, >50 and 31–50% in zones 1–6, respectively.

4 | METHODOLOGY

The TerraSAR-X intensity images were first converted to sigma nought (σ_{dB}^0 , expressed in dB) by using the following equation⁴¹:

$$\sigma_{dB}^0 = 10 \log_{10} \left(k_s \times |DN|^2 \times \sin \theta_{loc} \right),$$

where k_s is the calibration and processor scaling factor (calFactor) given in the TerraSAR-X data annotation file; $|DN|^2$ is the intensity

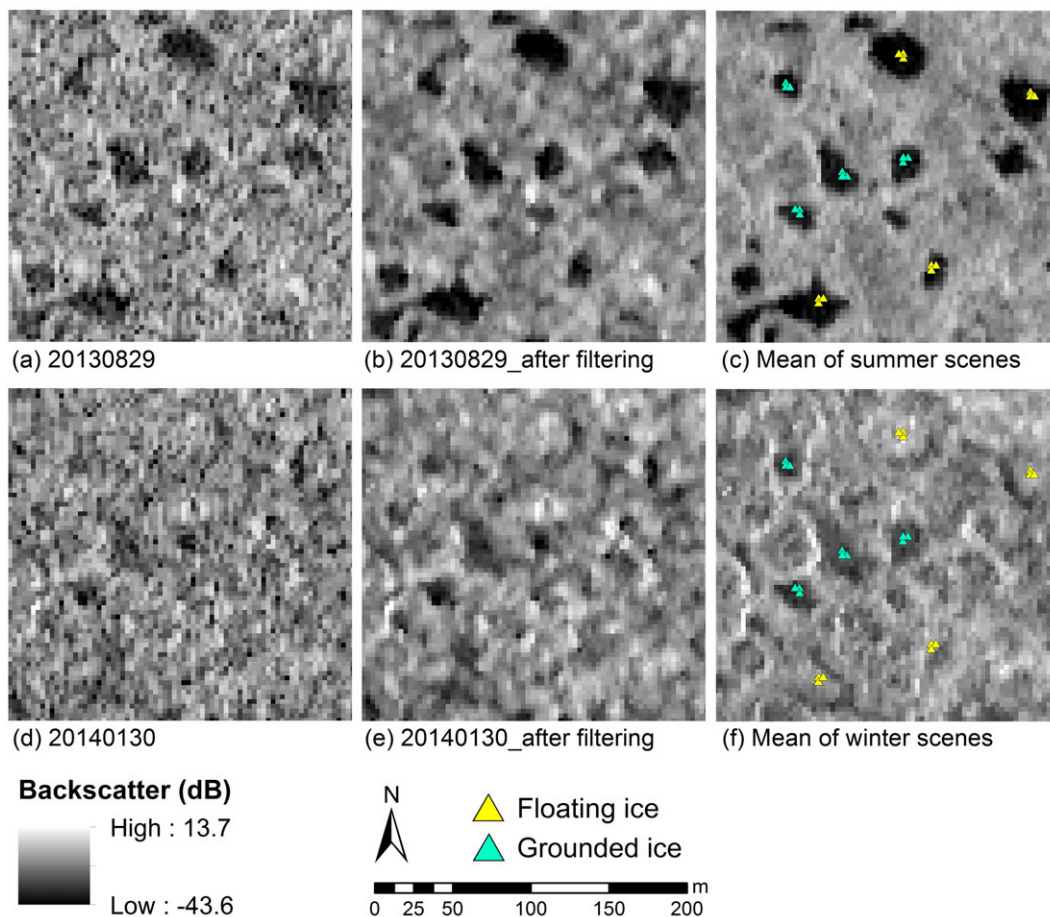


FIGURE 5 (a) TerraSAR-X backscatter intensity acquired on 08-29-2013 before filtering. (b) Backscatter intensity acquired on 08-29-2013 after filtering. (c) Mean backscatter intensity of summer acquisitions. (d) Backscatter intensity acquired on 01-30-2014 before filtering. (e) Backscatter intensity acquired on 01-30-2014 after filtering. (f) Mean backscatter intensity of winter acquisitions. The difference between backscatter intensities from the grounded and floating ice is clear in the winter image (f). Time series of backscatter intensities of the 12 pixels of floating ice (yellow) and 12 pixels of grounded ice (cyan) are shown in Figure 6 [Colour figure can be viewed at wileyonlinelibrary.com]

value computed from the Single Look Complex (SLC) data; and θ_{loc} is the local incidence angle, which can be calculated from the Digital Elevation Model (DEM).

A workflow for using TerraSAR-X images to map the thermokarst ponds and their ice-cover regimes is shown in Figure 4. The images were first split into two groups: summer acquisitions and winter acquisitions. Within each group, to increase the signal-to-noise ratio (SNR) of the SAR imagery, a temporal and spatial filtering algorithm with a 3×3 kernel⁴²⁻⁴⁵ was used to reduce the effects of speckle noise. Such a temporal approach provides a major advantage compared to conventional spatial filters in that it can remove noise without sacrificing the spatial resolution. Figure 5 shows two images before and after temporal and spatial filtering: the contrast between water bodies and land is substantially increased. Mean backscatter intensities for the summer and winter groups were then calculated. The advantage of calculating this seasonal mean backscatter intensity is that it further reduces the speckle noise in the radar images and increases the accuracy of the mapping, as shown in Figure 5. The

processed images were geocoded to WGS 1984 UTM Zone 18 N with a ground spacing of 3 m by using a lookup table correlating the radar and map geometries. An image cross-correlation algorithm between the SAR imagery and simulated backscattered intensity from the WorldDEMcore DEM product^{46,47} was used to build the lookup table.^{48,49}

The summer mean backscatter intensity image was used to distinguish the thermokarst ponds from other types of land cover. A supervised classification using the minimum distance classifier was applied. Because water bodies normally have lower backscatter intensities than land, high classification accuracy can be easily achieved (94% in our case study). However, bare ground is sometimes misclassified as water because the backscatter intensities from calm water bodies and bare ground are similarly low.⁵⁰ The classification results were further refined by performing the following post-processing steps. (1) The classified binary raster file of water and non-water types was converted to a vector file, and the polygons of rivers and natural lakes were removed from the vector file because the classification results

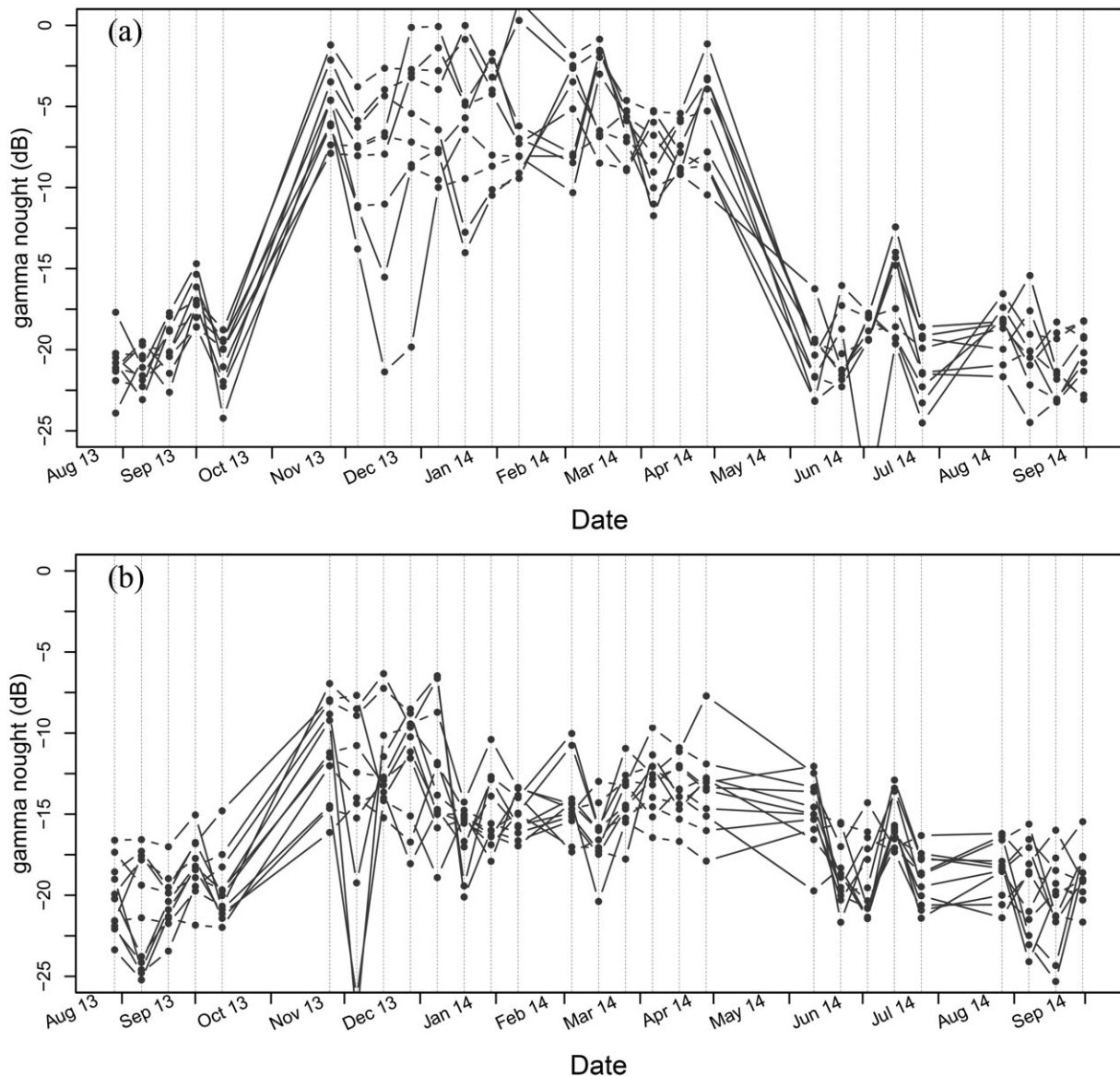


FIGURE 6 Time series of backscatter intensities from the pixels marked in Figure 5: (a) 12 pixels of floating ice and (b) 12 pixels of grounded ice

included not only the targeted thermokarst ponds but also other water bodies. (2) The classification results were visually compared with very high-resolution Google Earth images. Misclassifications were corrected so that the virtual error would be equal to zero. Despite the post-processing, some small thermokarst ponds (up to 36 m²) were still probably neglected due to the limited resolution of the TerraSAR-X StripMap mode data.

The winter mean backscatter intensity image was used to classify the ice-cover regimes of the thermokarst ponds. Because floating ice produces high backscatter intensity and grounded ice produces low backscatter intensity, the strong contrast allows these two ice-cover regimes to be easily differentiated. Figure 5 shows the distinction between these two regimes over the thermokarst ponds in the study area. Figures 5(c) and 5(f) show the summer and winter mean backscatter intensities, respectively. The difference between the backscatter intensities from the floating ice and grounded ice is apparent in the winter images and is confirmed by the time-series curves of backscatter intensity of the marked pixels from August 2013 to September 2014, as shown in Figure 6. Figures 6(a) and 6(b) illustrate the variations in backscatter intensity over 1 year in 12 marked pixels of floating ice and in 12 pixels of grounded ice, respectively.

We manually selected 1200 pixels with floating ice cover and 1200 pixels with grounded ice cover from the winter images. Half of these pixels were used as training samples, and the other half were used in the validation. The data analysis shows that using a threshold of -10.36 dB permitted discrimination between the two ice-cover regimes at an accuracy of more than 99%. Figure 7 shows a scatterplot of these 2400 pixels in the summer and winter images.

The peripheral ridge of each pond is generally classified as grounded ice cover in winter. Because we focused our research on the overall ice-cover regime of each thermokarst pond rather than

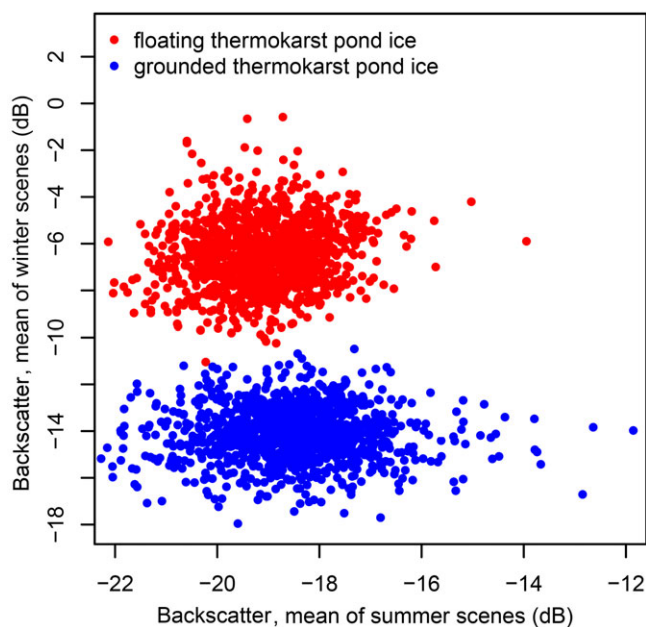


FIGURE 7 Scatterplot of backscatter intensities of the 2400 pond pixels in the summer and winter images; 1200 pixels correspond to floating ice cover, and another 1200 pixels correspond to grounded ice cover [Colour figure can be viewed at wileyonlinelibrary.com]

TABLE 3 Statistics of number and surface area of the thermokarst ponds in two historical phases

Zone	Number of thermokarst ponds				Mean surface area (m ²)				Surface area (m ²) (quantile 25–75%)							
	Phase 1	Phase 2	In both Phases I and II	Change	Phase 1	Phase 2	In both Phases I and II	Change	Phase 1	Phase 2	In both Phases I and II	Change				
	Only in Phase 1	Only in Phase 2	Only in Phase 1 and II	Only in Phase 1 and II	Only in Phase 1	Only in Phase 2	Only in Phase 1 and II	Only in Phase 1 and II	Only in Phase 1	Only in Phase 2	Only in Phase 1 and II	Only in Phase 1 and II				
1	55	112	23	57	186.5	156	32	-30.5	58.5	100.9	293.7	30–168.2	36.9–172.6	22.8–77.7	36.2–140.7	58.9–274.5
2	506	863	197	357	249.3	259.8	311	10.5	79.7	161.2	434.8	47.6–196.4	61.2–285.4	34.9–94.5	52.6–223.0	75.8–479.5
3	591	892	235	301	137.5	205.3	355	67.8	72.6	172	255.7	44.2–149.9	53.9–250.2	28.7–80.2	50.7–226.5	62–304.1
4	374	501	153	127	184.4	275.1	198	90.7	70.6	179.6	421.4	38–184.0	50.8–297.7	24.9–67.5	43.9–260.7	65–376.1
5	347	264	138	-83	127.7	136.5	202	8.8	50.6	49.2	163.3	25.6–117.1	34.2–135.8	18.2–53.0	24.5–64.5	41.9–161.9
6	171	155	63	-16	122.3	104.8	114	-17.5	44.1	36.5	129.3	27.2–119.7	26.6–106.6	19.6–49.3	19.8–38.4	31.5–130.1
All zones	2044	2787	743	809	168.0	189.6	1212	21.6	62.7	116.6	283.0					

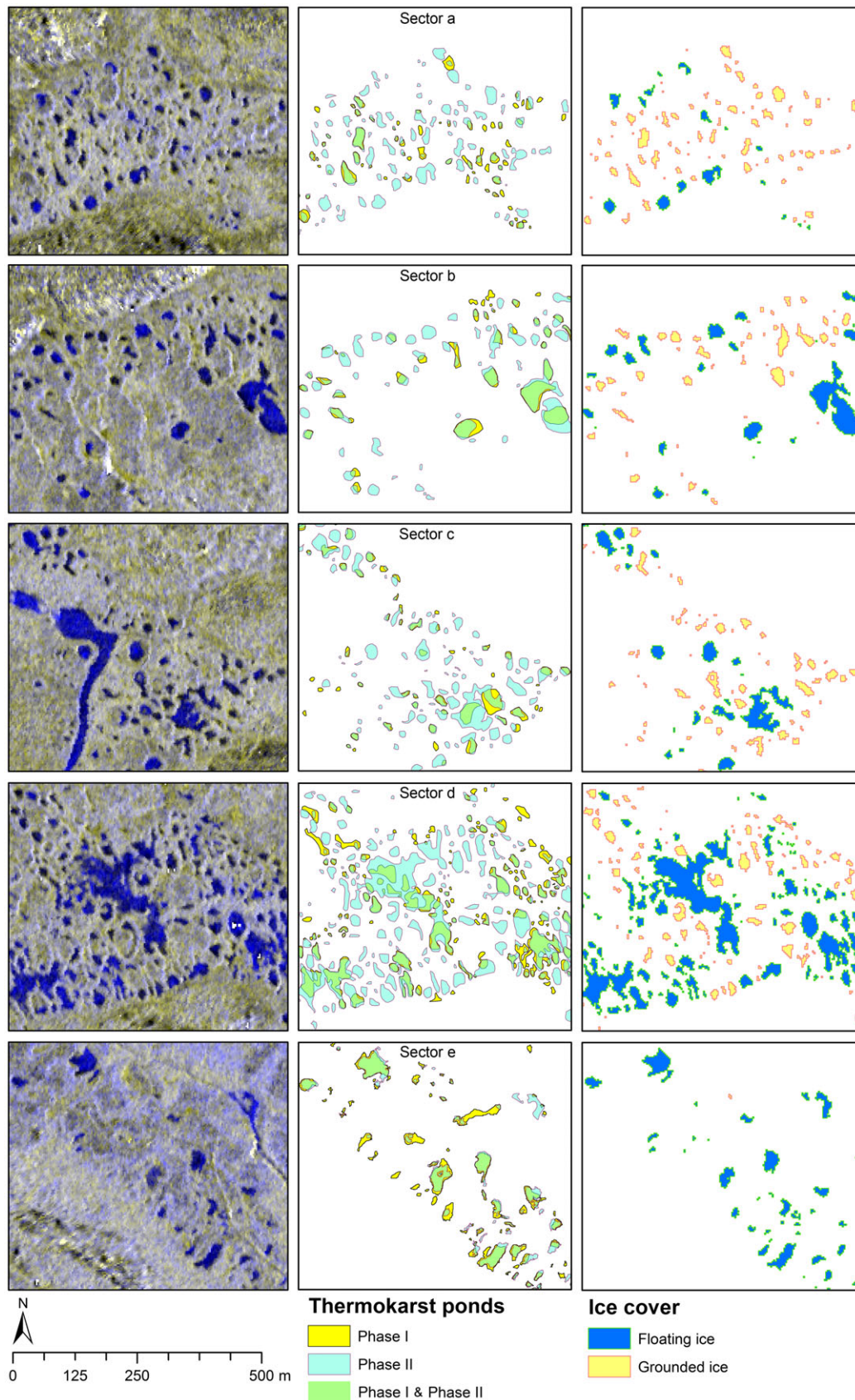


FIGURE 8 Mapping results of the thermokarst pond distribution and ice-cover regimes. Rows 1–5 show selected exemplary sectors 1–5, respectively. The left column shows the TerraSAR-X images (red: mean backscatter intensity of summer acquisitions; green: mean backscatter intensity of summer acquisitions; blue: mean backscatter intensity of winter acquisitions); in this color-composed image, bright blue denotes floating ice cover, and dark blue denotes grounded ice. The middle column shows maps of thermokarst ponds delineated on the very high-resolution optical images (yellow: Phase I; blue: Phase II; green: ponds present in both Phases I and II). The right column shows ponds and ice-cover regimes derived from the TerraSAR-X image (Figure 4) [Colour figure can be viewed at wileyonlinelibrary.com]

on every single pixel of the pond, we calculated statistics on the majority of ice-cover types within each thermokarst pond and used that information in the following analysis.

5 | RESULTS

5.1 | Evolution of thermokarst ponds between the two historical phases

Table 3 lists the characteristics of the thermokarst ponds in the six zones at two historical phases, interpreted from optical images. Between Phase I and Phase II, a greater number of thermokarst ponds appear in zones 1–4, whereas fewer thermokarst ponds exist in Phase II in zones 5 and 6. Between Phase I and Phase II, the thermokarst ponds expand in area in zones 1–5, whereas only in zone 6 does the surface area of thermokarst ponds shrink. The thermokarst ponds present in both Phase I and Phase II were much greater in surface area in Phase II.

5.2 | Thermokarst ponds and ice-cover regimes based on radar remote sensing

Figure 8 illustrates the thermokarst pond distribution and their winter ice-cover regimes in the five selected example sectors based on the radar remote sensing (locations shown in Figure 1). The middle column in Figure 8 shows maps of the thermokarst ponds delineated using the very high-resolution optical images. The third column shows the thermokarst pond distribution and ice-cover regime based on the radar remote sensing. The mapping based on the radar remote sensing (third column) agrees well with the reference outlines (second column in Figure 8). Table 4 lists statistics of the surface area and ice-cover regimes of thermokarst ponds in the six zones, based on the radar remote sensing.

The permafrost degradation percentages of the exemplary sectors from top to bottom in Figure 8 are 6–15, 6–15, 16–30, 31–50 and > 50%. The number of thermokarst ponds and the proportion of thermokarst ponds with floating ice cover in winter increases with increasing permafrost degradation. Table 4 lists the ratios of numbers and areas of the floating-ice-covered thermokarst ponds to those of all thermokarst ponds in each zone. Based on these statistics, there is no clear relationship between the percentages of the numbers and coverage areas of floating-ice ponds and permafrost degradation. However, in zones 4–6 (degradation percentages of 31–50, > 50 and 31–50%), when the percentage of permafrost degradation exceeds 30%, the percentages of the number and coverage area of the floating-ice ponds rise. Limited by the radar image resolution, very small ponds with surface areas of less than 36 m² were difficult to detect. Therefore, the number of thermokarst ponds in the grounded-ice regime should be greater, given that small ponds are more prone to be in the grounded-ice regime.

Table 4 indicates that ponds with floating ice have a larger surface area than ponds with grounded ice, which is also manifested in Figure 8, suggesting that the larger ponds are generally deeper. Figure 9 shows the probability density of surface areas of thermokarst pond having grounded ice and floating ice in each of the six zones,

TABLE 4 Surface area and ice cover regimes of thermokarst ponds in six zones

Zone	Number of thermokarst ponds (%)			Pond area (m ²) (%) calculated by pond			Mean surface area of thermokarst ponds (m ²)			Area (m ²) (%) calculated by pixel		
	Dominated by grounded ice	Dominated by floating ice	Sum	Dominated by grounded ice	Dominated by floating ice	Sum	Dominated by grounded ice	Dominated by floating ice	Average	Grounded ice	Floating ice	
1	66 (60.6%)	43 (39.4%)	109	5283 (43.7%)	6813 (56.3%)	12096	80	158.4	111	5652 (46.7%)	6444 (53.3%)	
2	614 (70.2%)	261 (29.8%)	875	72675 (45.1%)	88605 (54.9%)	161280	118.4	339.5	184.3	80595 (50%)	80685 (50%)	
3	546 (70.8%)	225 (29.2%)	771	56781 (47.8%)	61974 (52.2%)	118755	104	275.4	154	62865 (52.9%)	55890 (47.1%)	
4	247 (58.4%)	176 (41.6%)	423	34353 (33.9%)	66924 (66.1%)	101277	139.1	380.2	239.4	39402 (38.9%)	61875 (61.1%)	
5	53 (27.6%)	139 (72.4%)	192	2889 (11.1%)	23175 (88.9%)	26064	54.5	166.7	135.8	6093 (23.4%)	19971 (76.6%)	
6	38 (37.6%)	63 (62.4%)	101	2214 (21.7%)	7983 (78.3%)	10197	58.3	126.7	101	3249 (31.9%)	6948 (68.1%)	
All zones	1564(54.2%)	907(45.8%)	2471	174195 (40.5%)	255474 (59.5%)	429669	111.4	281.7	173.9	197559 (40.6%)	231606(59.4%)	

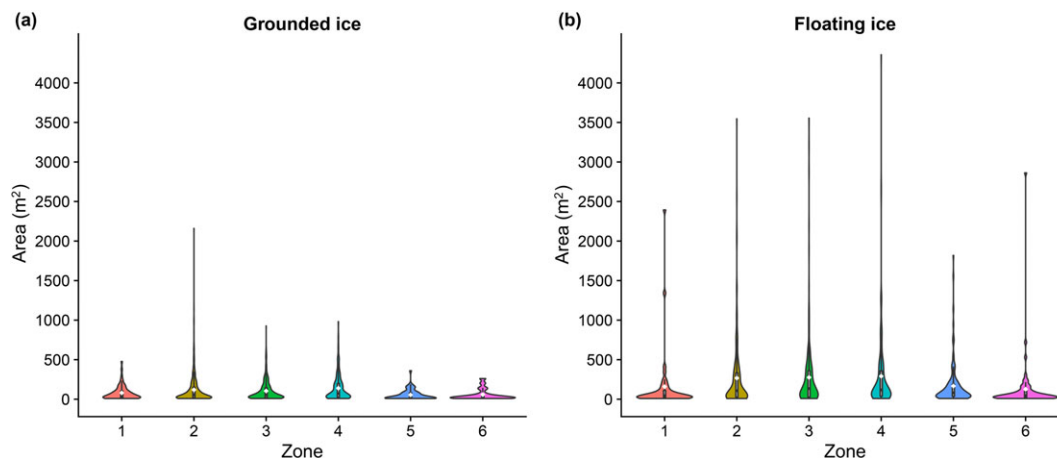


FIGURE 9 Violin plots of the surface areas of the thermokarst ponds in each of the six zones: grounded-ice ponds (a) and floating-ice ponds (b) [Colour figure can be viewed at wileyonlinelibrary.com]

which illustrates the surface area difference of thermokarst ponds having grounded ice and floating ice more clearly. The surface area influences the ice regimes (pond depths), but there is no clear surface-area threshold to differentiate the two ice-cover regimes.

In zones 2 and 3 (permafrost degradation percentages of 6–15 and 16–30%), the surface areas of ponds in the grounded-ice regime are concentrated at the bottom of the plot (Figure 9a), meaning that the majority of the ponds in the grounded-ice regime (Figure 9a) have very small surface areas. In contrast, the ponds in the floating-ice regime (Figure 9b) have larger surface areas in zones 2 and 3. In zone 1, where the percentage of permafrost degradation is lowest (0–5%), the surface areas of the thermokarst ponds with floating ice are also very small. In zones 5 and 6, because of the different deposit types, the thermokarst ponds are much smaller and the surface area difference between grounded-ice ponds and floating-ice ponds is not as distinctive as in zones 2–4.

Figure 9(a) also shows that the surface areas of the thermokarst ponds increase from zone 1 to zone 4 with the increase in percentage of permafrost degradation in the Sheldrake catchment, which is underlain by marine silty clay deposits. By contrast, the pattern of surface areas of the ponds with floating ice in Figure 9(b) does not change as much with the increase in permafrost degradation percentage from zones 1 to 4.

5.3 | Ice-cover regime and thermokarst pond evolution

The thermokarst ponds were assigned to two categories: ponds present in both Phases I and II and visible in the TerraSAR-X image (older ponds), and ponds present only in Phase II and visible in the TerraSAR-X image (younger ponds). The characteristics of ponds in these two categories for each ice-cover regime are listed in Table 5.

According to Table 5, the percentage of ponds in the floating-ice regime is not higher in the category of older ponds. In zones 1–4 (permafrost degradation < 30%), the size ratios of ponds in the floating-ice regime to ponds in the grounded-ice regime are larger among the older ponds than among the younger ones.

Figure 10 shows the changes in pond surface area from Phase I to Phase II among the ponds that were present in both Phases I and II and were visible in the TerraSAR-X images. In zones 2–4, the ponds in the grounded-ice regime display nearly equal probabilities to expand and shrink, whereas the ponds in the floating-ice regime were more likely to expand than to shrink. In zone 1, in the early permafrost degradation stage, which corresponds to the smallest permafrost degradation percentage, the ponds in both the grounded-ice regime and the floating-ice regime were more likely to expand. In zones 5 and 6, where the surface deposits are coarser and more permeable, the pond surface-area changes were much smaller in magnitude than in the other zones. In zones 5 and 6, the ponds in the floating-ice regime showed more dynamic surface-area changes from Phase I to Phase II than those in the grounded-ice regime but do not show a clear trend of shrinkage or expansion.

6 | DISCUSSION

6.1 | Thermokarst pond development and underlying soil texture

In zones 1–4, where the deposits consist of less-permeable marine silty clay, the dominant trends were increases in the numbers and surface areas of thermokarst ponds. Because the soil is impermeable below the ponds, the ponds remain even after the permafrost has completely disappeared, unless the vegetation recolonizes the system and the aquatic state recedes.⁵¹ However, in zone 6, where the deposits consist of more-permeable sand, the number and area of thermokarst ponds declined (Table 3). Meanwhile, the surface areas of thermokarst ponds in zones 5 and 6 are generally smaller than those in zones 1–4. The surface-area difference between the grounded-ice ponds and floating-ice ponds in zones 5 and 6 is not as distinct as that of the ponds over the silty clay deposits, in zones 1–4.

Drainage is slow through the marine silty clay but is rapid through the sandy deposits. A study conducted in a tundra terrain located in the discontinuous permafrost near Council, Alaska, showed that the

TABLE 5 Characteristics of thermokarst ponds in two categories

Zone	Ponds present in both Phases I and II and visible in TerraSAR-X image				Ponds present only in Phase II and visible in TerraSAR-X image			
	Number of ponds		Mean pond surface area (m ²)		Number of ponds		Mean pond surface area (m ²)	
	Dominated by grounded ice	Dominated by floating ice	Dominated by grounded ice	Dominated by floating ice	Dominated by grounded ice	Dominated by floating ice	Dominated by grounded ice	Dominated by floating ice
1	9	9	142	539	42	19	103.7	289.4
2	188	73	191.1	831.1	484	204	141.1	457.7
3	196	80	114.2	419.5	477	196	118.7	339
4	85	77	160.5	624.9	229	164	150.9	600.3
5	32	101	74.8	212.5	43	127	65.1	186
6	20	39	92.2	186.7	22	49	86.3	163.8
All zones	530	379	146.2	464.2	1297	759	129.9	389.2
							Percentage of ponds with floating ice	
							31.1	
							29.7	
							29.1	
							41.7	
							74.7	
							69.0	
							36.9	
							Size ratio	
							3.8	2.8
							4.3	3.2
							3.7	2.9
							3.9	4.0
							2.8	2.9
							2.0	1.9
							3.2	3.0

Percentage of ponds with floating ice: floating-ice-dominated thermokarst ponds to all thermokarst ponds.

Size ratio: ratio of mean size of floating-ice ponds to that of grounded-ice ponds.

ponds there are shrinking with the development of taliks.⁹ During thermokarst development, surface-water ponding precedes permafrost retreat. Once the permafrost thaws completely under a pond, an open talik forms, and the surface-water system connects directly to a sub- or intra-permafrost aquifer. These taliks allow internal drainage throughout the year; consequently, the pond starts to drain. This situation is present in zones 5 and 6. In zones 1–4, however, water stagnates at the soil surface because infiltration through the silty clay is very slow. In zones 1–4, therefore, ponds are more likely to remain and to merge with other ponds, whereas in zones 5 and 6, ponds are more likely to drain via internal drainage accompanied by the development of taliks. Notwithstanding the effects of the water balance between precipitation and evaporation, the soil texture has a large impact on the drainage speed of the thermokarst ponds and is a major factor driving thermokarst pond development.

6.2 | Thermokarst pond development and ice-cover regime

Figure 11 shows the development of a single thermokarst pond in zone 5 in 1994, 2010 and 2013 and the corresponding ice-cover regime in 2013–2014. The west side of the pond shrank from 1994 to 2013 as the surface area shrank, and the muddy pond bed was visible in 2010. Thermokarst development was occurring in the right bottom corner of the pond as the small permafrost mound visible in 1994 was replaced by water by 2013. The two sites are both in the grounded-ice regime, which reflects pond shrinkage and expansion.

Accelerated permafrost thawing can result in two alternative or parallel processes: (1) an increase in thermokarst, for example through the formation of new ponds or the expansion of existing ones, and (2) pond drainage with the development of a talik^{9,11,14} or strong evaporation. The ice-cover regimes of the thermokarst ponds are related to these thermokarst and drainage process.

Based on the results of our and other studies, one may conclude that if the thermokarst develops quickly, many small shallow ponds will form and freeze to their beds. As observed in zones 1–3, located in the Sheldrake catchment with a relatively low percentage of permafrost degradation, a large proportion of the ponds have grounded ice. For example, sectors a–c (Figure 8) also show an increasing number of small shallow ponds (grounded ice) forming in the early stage of thermokarst development. As all the ponds reach “maturity” (become fully developed), the average pond depth across the landscape increases, and the proportion of ponds with floating ice should also increase. If the underlying soil allows for good drainage, then the aging thermokarst ponds will shrink, and the ice-cover regime will then revert back to grounded ice. Permafrost degradation is not simply characterized by a larger proportion of water surface area covered by floating ice.

Pond age is not the factor controlling the ice-cover regime in our study area (Table 5). The ponds present in both Phases I and II (older ponds) are larger than those present only in Phase II (younger ones), but they are not always deeper. This finding differs from some studies that found older thermokarst ponds are generally deeper.¹⁰ This difference arises because the depths of the thermokarst ponds depend

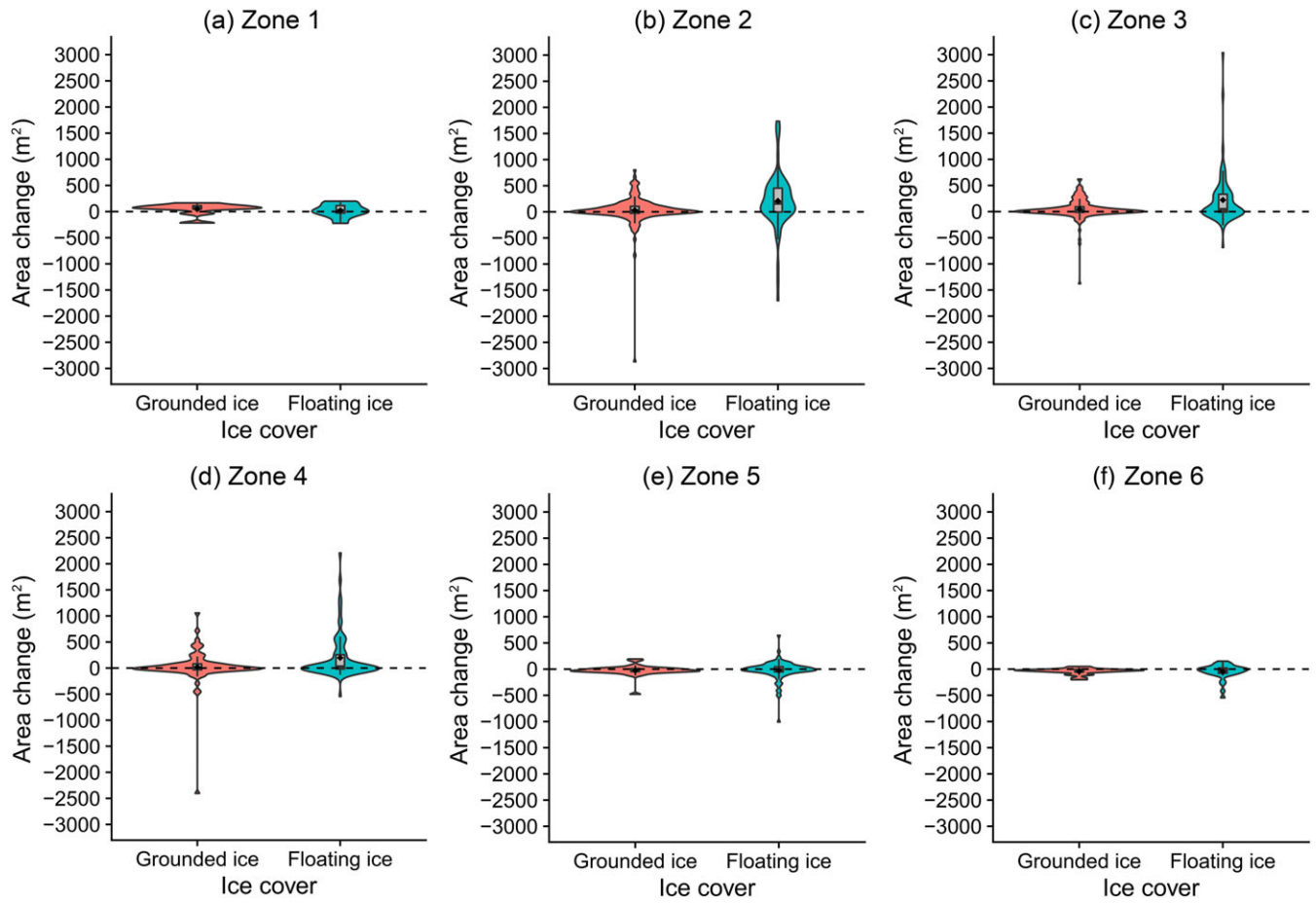


FIGURE 10 Surface-area changes from Phase I to Phase II among ponds present in both Phase I and Phase II and visible in the TerraSAR-X images (older ponds) in zones 1–6 (a–f), based on historical data [Colour figure can be viewed at wileyonlinelibrary.com]

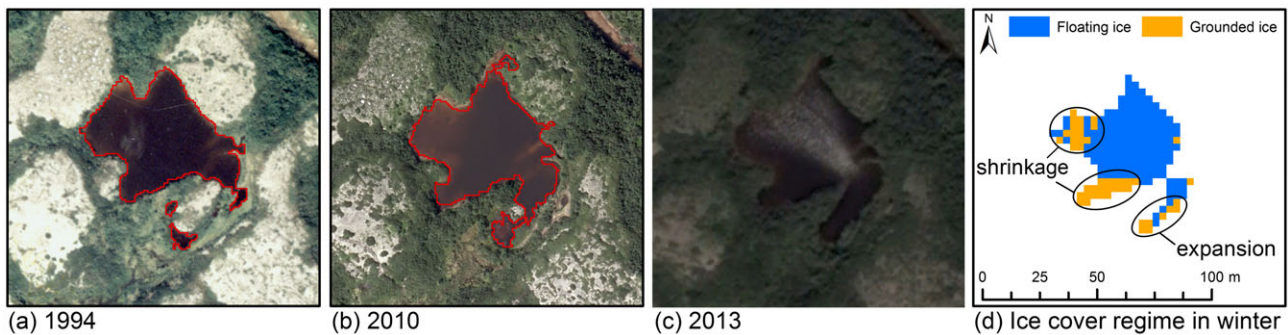


FIGURE 11 Development of a single thermokarst pond over a span of 19 years, and its ice cover regime. (a) Thermokarst pond outline and aerial photograph in 1994. (b) Thermokarst pond outline and aerial photograph in 2010. (c) Satellite image in 2013 from Google Earth. (d) Corresponding ice cover regime retrieved from the TerraSAR-X images [Colour figure can be viewed at wileyonlinelibrary.com]

largely on the segregation ice content and thawing depth of the permafrost. The permafrost in our study area is very shallow, less than 20 m.³⁹ After the underlying permafrost is thawed completely and permafrost meltwaters no longer provide an additional source of water, eventual drainage of the lakes will progress due to strong evaporation. Studies show that in highly degraded permafrost regions, the thermokarst ponds/lakes are potentially most vulnerable to become evaporation-dominated.^{52,53} Consequently, the older ponds (present in both Phase I and Phase II) are not always deeper in our study area.

This indicates that permafrost depth is also a factor influencing the ice-cover regimes of thermokarst ponds and lakes.

6.3 | Continuous monitoring of ice-cover regimes with Sentinel-1 time series

With the availability of free C-band SAR data from Sentinel-1 satellite since autumn 2014, monitoring large areas at high temporal

frequencies is now possible. The processing method used in this study can be adopted for processing Sentinel-1 time-series data: distinguish thermokarst ponds from other types of land cover using summer images and classify the ice-cover regimes of thermokarst ponds using winter images. Therefore, the surface areas and ice-cover regimes of thermokarst ponds could be obtained simultaneously.

Our results show that assessing permafrost degradation directly from the percentages of the number and coverage area of floating-ice ponds in a single year is difficult. In addition to the content of segregation ice and thawing depth of the permafrost, the winter ice regime of thermokarst ponds in a particular year is also affected by a pond's shape and climatic conditions.⁵⁴ Some shallow ponds can convert to fen/bog vegetation and then revert back to ponds^{10,54} due to temporal fluctuations in the water table. Continuous annual monitoring is recommended for recording the temporal dynamics of thermokarst pond surface extents and ice-cover regimes. More detailed water-depth information could be obtained from continuous time series of SAR images. Antonova et al. (2016) used time-series backscatter intensity data to derive the timing of ice grounding of thermokarst ponds/lakes with grounded ice.²³ The ice thickness (water depth) of thermokarst ponds/lakes with grounded ice can be retrieved by combining the timing of ice grounding and a model of ice growth.

7 | CONCLUSIONS

In this study, patterns of the spatial distribution of ice-cover regimes of thermokarst ponds in a typical discontinuous permafrost are first revealed. The correlations of these regimes with the permafrost degradation states and thermokarst pond development between two historical phases were analyzed. The following conclusions were developed:

1. The soil texture underlying a pond has a large impact on the drainage speed of the thermokarst ponds.
2. The ice-cover regime is controlled by the combined effects of soil texture, permafrost degradation stage and permafrost depth. In our study area, the first stage of the thermokarst process is the appearance of many small, shallow ponds with grounded-ice in winter. Then, as all the ponds reach "maturity" (become fully developed), the average pond depth across the landscape increases, as does the proportion of ponds with floating ice. The segregation ice content and thawing depth of the permafrost, rather than the thermokarst pond age, control the water level of the thermokarst pond. In our study area, the older ponds (those present in both Phases I and II) are greater in surface area than the younger ones (those present only in Phase II) but are not necessarily deeper (i.e., more ponds have the floating-ice regime). The underlying soil texture (hydraulic conductivity) influences the speed of thermokarst pond drainage. Over the impermeable deposits, floating-ice ponds generally have larger surface areas than the grounded-ice ponds.
3. It is difficult to assess permafrost degradation directly from the numbers and coverage areas of floating-ice ponds as percentages

of all thermokarst ponds in a single year; therefore, continuous monitoring is strongly recommended.

Starting with the freely available Sentinel-1 SAR imagery, the ice-cover regimes and surface extents of thermokarst ponds can be recorded continuously. The processing method used in this study can be adopted for Sentinel-1 datasets: distinguish thermokarst ponds from other types of land cover using summer images and classify the ice-cover regimes (monitor ice phenology) using winter images. Thermokarst pond development can be better described through the monitoring of thermokarst pond surface extents and ice cover regimes.

ACKNOWLEDGEMENTS

The authors acknowledge the German Aerospace Centre (DLR) for supplying the TerraSAR-X data. This project was supported by grants and contributions from the Bavarian Research Alliance (BayFOR), the Canadian Space Agency (CSA, grant number 14SUSMAPIN), the Helmholtz Research School of Mechanisms and Interactions of Climate Change in Mountain Regions (MICMoR) and the Centre d'Études Nordiques (CEN). The authors also thank Prof. Michel Allard (CEN) and Denis Sarrazin (CEN) for supporting this research. The authors thank Laurence Provencher-Nolet for providing classified maps in the Tasiapik Valley, and Jimmy Poulin, Andres Jacome, Yueli Chen and Chaima Touati for providing valuable fieldwork assistance. The authors are grateful to the CEN for allocating helicopter flight times and providing logistical support. We are also grateful to the Inuit community of Umiujaq for their generous hospitality.

ORCID

Lingxiao Wang  <http://orcid.org/0000-0003-2081-1022>

REFERENCES

1. Serreze M, Walsh J, Chapin FS, et al. Observational evidence of recent change in the northern high-latitude environment. *Clim Change*. 2000;46(1-2):159-207.
2. Jones BM, Grosse G, Arp C, Jones M, Walter Anthony K, Romanovsky V. Modern thermokarst lake dynamics in the continuous permafrost zone, northern Seward Peninsula, Alaska. *J Geophys Res Biogeosci*. 2011;116(G2):G00M03.
3. Kokelj SV, Jorgenson M. Advances in thermokarst research. *Permafrost Periglacial Process*. 2013;24(2):108-119.
4. Allard M, Seguin MK. The Holocene evolution of permafrost near the tree line, on the eastern coast of Hudson Bay (northern Quebec). *Can J Earth Sci*. 1987;24(11):2206-2222.
5. Hinkel KM, Jones BM, Eisner WR, Cuomo CJ, Beck RA, Frohn R. Methods to assess natural and anthropogenic thaw lake drainage on the western Arctic coastal plain of northern Alaska. *J Geophys Res Earth*. 2007;112(F2):F02S16.
6. Marsh P, Russell M, Pohl S, Haywood H, Onclin C. Changes in thaw lake drainage in the Western Canadian Arctic from 1950 to 2000. *Hydrological Processes*. 2009;23(1):145-158.
7. Roach JK, Griffith B, Verbyla D. Landscape influences on climate-related lake shrinkage at high latitudes. *Glob Chang Biol*. 2013;19(7):2276-2284.
8. Smith LC, Sheng Y, MacDonald G, Hinzman L. Disappearing arctic lakes. *Science*. 2005;308(5727):1429-1429.

9. Yoshikawa K, Hinzman LD. Shrinking thermokarst ponds and ground-water dynamics in discontinuous permafrost near Council, Alaska. *Permafrost Periglacial Process*. 2003;14(2):151-160.
10. Payette S, Delwaide A, Caccianiga M, Beauchemin M. Accelerated thawing of subarctic peatland permafrost over the last 50 years. *Geophys Res Lett*. 2004;31(18). <https://doi.org/10.1029/2004GL020358>
11. Sannel A, Kuhry P. Warming-induced destabilization of peat plateau/thermokarst lake complexes. *J Geophys Res Biogeo*. 2011;116(G3):G03035.
12. Beck I, Ludwig R, Bernier M, Lévesque E, Boike J. Assessing permafrost degradation and land cover changes (1986-2009) using remote sensing data over Umiujaq, Sub-Arctic Québec. *Permafrost Periglacial Process*. 2015;26(2):129-141.
13. Provencher-Nolet L. *Détection de changement à court terme de la toundra arbustive à partir de photographies aériennes, région d'Umiujaq*. Nunavik (Québec, Canada): Université du Québec; 2014.
14. Riordan B, Verbyla D, McGuire AD. Shrinking ponds in subarctic Alaska based on 1950-2002 remotely sensed images. *J Geophys Res Biogeo*. 2006;111:G44002.
15. Jorgenson MT, Shur Y. Evolution of lakes and basins in northern Alaska and discussion of the thaw lake cycle. *J Geophys Res Earth*. 2007;112:F0217.
16. Lindgren P, Grosse G, Anthony KW, Meyer F. Detection and spatiotemporal analysis of methane ebullition on thermokarst lake ice using high-resolution optical aerial imagery. *Biogeosciences*. 2016;13(1):27-44.
17. Arp CD, Jones BM, Lu Z, Whitman MS. Shifting balance of thermokarst lake ice regimes across the Arctic Coastal Plain of northern Alaska. *Geophys Res Lett*. 2012;39(16):L16503.
18. Ingram M, Anthony K, Meyer F, Grosse G. Characterization of L-band synthetic aperture radar (SAR) backscatter from floating and grounded thermokarst lake ice in Arctic Alaska. *The Cryosphere*. 2013;7(6):1741-1752.
19. Jeffries M, Morris K, Liston G. A method to determine lake depth and water availability on the North Slope of Alaska with spaceborne imaging radar and numerical ice growth modelling. *Arctic*. 1996;367-374.
20. Duguay C, Lafleur P. Determining depth and ice thickness of shallow sub-Arctic lakes using space-borne optical and SAR data. *Int J Remote Sens*. 2003;24(3):475-489.
21. Weeks W, Fountain A, Bryan M, Elachi C. Differences in radar return from ice-covered North Slope Lakes. *J Geophys Res Oceans*. 1978;83(C8):4069-4073.
22. Elachi C, Bryan M, Weeks W. Imaging radar observations of frozen Arctic lakes. *Remote Sens Environ*. 1976;5:169-175.
23. Antonova S, Duguay CR, Kääb A, et al. Monitoring bedfast ice and ice phenology in lakes of the Lena River Delta using TerraSAR-X backscatter and coherence time series. *Remote Sens (Basel)*. 2016;8(11):903.
24. Ling F, Zhang T. Numerical simulation of permafrost thermal regime and talik development under shallow thaw lakes on the Alaskan Arctic Coastal Plain. *J Geophys Res Atmos*. 2003;108:D16.
25. Walter KM, Zimov S, Chanton JP, Verbyla D, Chapin FS. Methane bubbling from Siberian thaw lakes as a positive feedback to climate warming. *Nature*. 2006;443(7107):71-75.
26. Collins M, Knutti R, Arblaster J, et al. Long-term climate change: projections, commitments and irreversibility. In: IPCC, ed. *Climate Change 2013: The Physical Science Basis. IPCC Working Group I Contribution to AR5*. Cambridge: Cambridge University Press; Chapter 12:1033.
27. Arp CD, Jones BM, Urban FE, Grosse G. Hydrogeomorphic processes of thermokarst lakes with grounded-ice and floating-ice regimes on the Arctic coastal plain, Alaska. *Hydrol Process*. 2011;25(15):2422-2438.
28. Surdu C, Duguay C, Brown L, Fernández Prieto D. Response of ice cover on shallow lakes of the North Slope of Alaska to contemporary climate conditions (1950-2011): radar remote-sensing and numerical modeling data analysis. *The Cryosphere*. 2014;8(1):167-180.
29. Jolivel M, Allard M. Thermokarst and export of sediment and organic carbon in the Sheldrake River watershed, Nunavik, Canada. *J Geophys Res Earth*. 2013;118(3):1729-1745.
30. Allard M, Seguin MK. Le pergélisol au Québec nordique: bilan et perspectives. *Géog Phys Quatern*. 1987;41(1):141-152.
31. Payette S. The forest tundra and present tree-lines of the northern Québec-Labrador peninsula. *Nordicana*. 1983;47:3-23.
32. Payette S, Gagnon R. Tree-line dynamics in Ungava peninsula, northern Quebec. *Ecography*. 1979;2(4):239-248.
33. Canadian Historical Climate Data: Historical Data. 2018. http://climate.weather.gc.ca/historical_data/search_historic_data_e.html
34. Climate station data from the Umiujaq region in Nunavik, Quebec, Canada, v. 1.5 (1997-2017). *Nordicana D9*; 2018.
35. Calmels F, Allard M, Delisle G. Development and decay of a lithalsa in Northern Québec: a geomorphological history. *Geomorphology*. 2008;97(3-4):287-299.
36. Calmels F, Allard M. Segregated ice structures in various heaved permafrost landforms through CT Scan. *Earth Surf Process Landf*. 2008;33(2):209-225.
37. Calmels F, Allard M. Ice segregation and gas distribution in permafrost using tomodensitometric analysis. *Permafrost Periglacial Process*. 2004;15(4):367-378.
38. Bouchard F, Pienitz R, Ortiz JD, Francus P, Laurion I. Palaeolimnological conditions inferred from fossil diatom assemblages and derivative spectral properties of sediments in thermokarst ponds of subarctic Quebec, Canada. *Boreas*. 2013;42(3):575-595.
39. Lévesque R, Allard M, Séguin MK. Le pergélisol dans les formations quaternaires de la région des rivières Nastapoca et Sheldrake, Québec nordique. Centre d'études nordiques, Université Laval; 1988.
40. Fortier R. Groundwater monitoring network from the Umiujaq region in Nunavik, Quebec, Canada, v. 1.3 (2012-2016). *Nordicana D19*; 2017. <https://doi.org/10.5885/45309SL-15611D6EC6D34E23>
41. Airbus D. *Space, "Radiometric Calibration of TerraSAR-X Data: Beta Naught and Sigma Naught Coefficient Calculation"*. TSXX-ITD-TN-0049;2014.
42. Bruzzone L, Marconcini M, Wegmuller U, Wiesmann A. An advanced system for the automatic classification of multitemporal SAR images. *IEEE Trans Geosci Remote Sens*. 2004;42(6):1321-1334.
43. Quegan S, Le Toan T, Yu JJ, Ribbes F, Floury N. Multitemporal ERS SAR analysis applied to forest mapping. *IEEE Trans Geosci Remote Sens*. 2000;38(2):741-753.
44. Quegan S, Yu JJ. Filtering of multichannel SAR images. *IEEE Trans Geosci Remote Sens*. 2001;39(11):2373-2379.
45. Frost VS, Stiles JA, Shanmugan KS, Holtzman JC. A model for radar images and its application to adaptive digital filtering of multiplicative noise. *IEEE Trans Pattern Anal Mach Intell*. 1982;2:157-166.
46. Riegler G, Hennig SD, Weber M. WorldDEM - a Novel Global Foundation Layer. *ISPRS - Int Arch Photogramm, Remote Sens Spat Inf Sci*. 2015;XL-3/W2:183-187.
47. WorldDEM. *WorldDEM™ Technical Product Specification*. Available at: <http://www.geo-airbusds.com/worlddem/2015>.
48. AG, GAMMA Remote Sensing. *Differential Interferometry and Geocoding Software-DIFF&GEO, Version 1.3*. Gumliggen: Gamma Remote Sensing; 2008.
49. Wegmuller U. Automated terrain corrected SAR geocoding. Paper presented at: Geoscience and Remote Sensing Symposium, 1999. IGARSS'99 Proceedings. IEEE 1999 International 1999.
50. Santoro M, Wegmüller U, Lamarche C, Bontemps S, Defourny P, Arino O. Strengths and weaknesses of multi-year Envisat ASAR backscatter measurements to map permanent open water bodies at global scale. *Remote Sens Environ*. 2015;171:185-201.
51. Breton J. *Caractérisation limnologique et réactivité de la matière organique dissoute des mares de thermokarst*, Université du Québec, Institut national de la recherche scientifique; 2007.

52. Narancic B, Wolfe BB, Pienitz R, Meyer H, Lamhonwah D. Landscape-gradient assessment of thermokarst lake hydrology using water isotope tracers. *J Hydrol*. 2017;545:327-338.
53. Gibson J, Birks S, Yi Y, Vitt D. Runoff to boreal lakes linked to land cover, watershed morphology and permafrost thaw: a 9-year isotope mass balance assessment. *Hydrol Process*. 2015;29(18):3848-3861.
54. Zuidhoff FS, Kolstrup E. Changes in palsa distribution in relation to climate change in Laivadalen, northern Sweden, especially 1960–1997. *Permafr Periglac Process*. 2000;11(1):55-69.

How to cite this article: Wang L, Jolivel M, Marzahn P, Bernier M, Ludwig R. Thermokarst pond dynamics in subarctic environment monitoring with radar remote sensing. *Permafrost and Periglac Process*. 2018;1–15. <https://doi.org/10.1002/ppp.1986>

6 Conclusions and Outlook

6.1 Conclusions

This thesis work contributes to developing methods and strategies for sub-Arctic permafrost environment monitoring with SAR datasets. The research questions mentioned in Section 1.4 can be answered as follows.

1) Is the D-InSAR or MT-InSAR technique able to monitor surface ground motion caused by permafrost activities in the sub-Arctic environment? What are the influencing factors limiting the application of these techniques?

What are suitable datasets regarding wavelength and resolution (temporal and spatial)?

The application of D-InSAR is limited in the sub-Arctic environment due to the developed vegetation and heterogeneous landscape in comparison with the Arctic permafrost terrain. The well-developed vegetation originating from shrub and spruce cover strongly decorrelates the phase signal and deteriorates the displacement analysis.

Regarding the monitoring period, effective phase retrieval related to ground deformation is limited to only the thawing season from the beginning of June to the middle of October. Phase retrieval is possible during the freezing season after stable snow accumulation from approximately January to April. However, the “uplift” signal during the winter period is more likely related to the change in the metamorphic state of the snow (ice lens, depth, hardness, wetness) rather than frost heaving in the active layer of the permafrost. Affected by snow wetness and the land surface freeze/thaw cycle, the interferogram at the beginning of winter and beginning of spring is of low quality, and reliable phase retrieval is not possible.

The spatial resolution is especially a limiting factor over discontinuous permafrost terrain. A heterogeneous landscape requires a high spatial resolution of SAR datasets to reduce the phase decorrelation effect caused by multiple scatterers with variable phase within a resolution cell. Furthermore, the width of some permafrost mounds is on the order of 10-50 m. In the future, the C-band RADARSAT constellation mission may provide datasets having higher spatial resolution than those obtained using the Sentinel-1 IW mode.

Regarding the currently available SAR datasets of different wavelengths, the X-band dataset is not suitable for monitoring permafrost-caused ground surface motion in the sub-Arctic discontinuous permafrost environment. The C-band Sentinel-1 dataset using SBAS-InSAR, by virtue of its routine acquisitions with high temporal revisit cycle (a 6-day or 12-day span), can obtain good results in the sub-Arctic tundra environment below the tree line (tundra, tundra wetlands, and the less-developed shrub-tundra environment),

but the results and accuracy are not promising over well-developed shrub-tundra and especially forest-tundra environments. L-band datasets show a strong advantage in maintaining high coherence over a longer span, and the monitoring results are close to those of ground-measured displacement; thus, such datasets are suitable for interannual or long-term monitoring over well-developed shrub-tundra and especially forest-tundra environments. However, image availability could be limited by the ALOS-2 PALSAR data acquisition plan, and water content changes in the soil and vegetation canopy can substantially affect the phase of L-band D-InSAR data due to the deeper penetration of this band.

In conclusion, this doctoral study contributes to understanding the application conditions of D-InSAR in the discontinuous permafrost environment using the C-, X- and L-band SAR datasets.

2) Are multi-temporal SAR backscatter and interferometric coherence information able to classify heterogeneous sub-Arctic permafrost environments?

How can we classify heterogeneous discontinuous permafrost environments by using multi-temporal SAR images?

What are the most efficient features for classification?

In this study, multi-temporal SAR backscatter and interferometric coherence data show the ability to classify heterogeneous sub-Arctic permafrost environments. An overall accuracy of 98% is achieved when classifying rock and water bodies, and an accuracy of 79% is achieved when discriminating among different vegetation types with one year of single-polarized acquisitions. The accuracy is comparable with those of two previous studies in the same study area, which used VHR (0.15 m) aerial photographs with an object-based image analysis (OBIA) classification scheme (Provencher-Nolet 2014) (overall accuracy (OA) of 84%) and RADARSAT-2 fine quad-pol images (8 m) with an SVM classification scheme (OA of 75% with one quad-pol image; OA of 85% after adding a second image with a different date or incidence angle) (Duguay et al. 2016).

An original approach that synergistically uses OBIA and classification and regression tree (CART) analysis was developed for classification with multi-temporal SAR images. OBIA allows for easy fusion of the backscatter intensity and interferometric information. CART analysis effectively determines the most suitable features and threshold values for land cover classification from a variety of candidate features derived from multi-temporal/time-series backscatter intensity data and interferometric images.

Regarding the most efficient features for classification with multi-temporal SAR images, it is clear that only the coherence and temporal variability of the backscatter intensity (i.e., the temporal standard deviation of the backscatter) can discriminate among rock, water and vegetation. More features are required to discriminate among different vegetation types. For X-band data, the coherence properties in the winter are more engaged in vegetation classification than are the coherence properties in the summer.

This seasonal distinction is because strong decorrelation occurs over vegetated areas in the X-band data during the summer and because the coherence retains only a limited amount of information when the time span exceeds 22 days. For C-band and L-band data, deeper penetration through the canopy layer is achieved, and the levels of backscatter saturation and interferometric decorrelation are reduced; these characteristics are beneficial for achieving higher accuracy when distinguishing vegetation types.

In conclusion, during this doctoral research, an original approach that uses multi-temporal information regarding SAR backscatter and interferometric coherence was developed for classification with multi-temporal SAR images. An accuracy of 79% was achieved in the heterogeneous sub-Arctic permafrost environment. Interferometric coherence with a very short span is useful for discriminating among different vegetation types.

3) What is the distribution pattern of permafrost-caused seasonal thaw subsidence? Which area has larger seasonal thaw subsidence?

From the deformation monitoring results in the thawing season 2017 (2017-05-30 to 2017-10-21) based on SBAS-InSAR processing with Sentinel-1 time series, the wet terrain covered by herbaceous vegetation tends to have a larger seasonal thaw subsidence than the drier terrain covered by lichen. The thawing settlement already reaches the maximum value in August over the lichen-dominated terrain, however, reaches the maximum value in the first half of October over the herbaceous vegetated terrain. There is no distinctive subsidence between August and the beginning of October over lichen-dominated terrain; this phenomenon is suspected to be related with the transient zone at the bottom of active layer and above the permafrost table. The transient zone is abundant in ice, thawing such amounts of ice requires an increase in the energy budget.

Herbaceous and lichen vegetation are used as simplified indicators of surficial soil water content in this study. Although the discrimination of displacement characteristics over wet or dry terrain is clear, the quantitative correlation of displacement with soil water content could not be obtained in this study and the relation is not always true because the thermal state in the vertical profile of active layer could have a substantial difference.

In conclusion, by SBAS-InSAR derived displace time series, the study firstly detected that the wet regions and the drier areas tend to exhibit different seasonal thaw subsidence patterns. The wet region has a larger thaw subsidence and reaches the maximum subsidence 1-2 month later than the drier region.

4) What are the ice-cover regime characteristics in the discontinuous permafrost zone of the sub-Arctic?

Could the state of permafrost degradation be assessed from the coverage percentage of all thermokarst ponds consisting of floating ice?

The thermokarst pond distribution and its winter ice-cover regime show large variability in the study area. Generally, the number of thermokarst ponds and the proportion of thermokarst ponds with floating ice cover in winter increase with increasing permafrost degradation state. Specifically, when the percentage of permafrost degradation exceeds 30%, the percentages of the number and coverage area of floating ice increase.

The relationship between floating ice coverage and permafrost degradation is not simply linear in the study area. The thermokarst ponds are developed as follows. In the first stage, many small shallow ponds (grounded ice in winter) appear. Then, all ponds reach “maturity” (i.e., become fully developed), and the average pond depth across the landscape increases, as does the proportion of ponds with floating ice. Last, aging thermokarst ponds shrink and turn back to the grounded ice regime if the underlying soil is permeable, which facilitates the internal drainage. However, over impermeable deposits, the drainage speed is very low, and the thermokarst ponds are more likely to remain and merge with other ponds.

In conclusion, this study confirms that the permafrost degradation state is difficult to directly access from the coverage area of floating ice in ponds and the percentage of all thermokarst ponds consisting of such floating ice in a single year. The study also confirms the assumption of the development process of thermokarst ponds.

6.2 Outlook

The developed SAR-based monitoring methods were tested in the Nunavik (Eastern Canada), but show large application promise in the other sub-Arctic region as well as the Arctic region. Sentinel-1 provides cryospheric researchers with the information of high temporal and spatial resolution SAR datasets. The datasets of high spatial resolution is an ideal source for land cover mapping in northern high latitude permafrost regions considering that it is independent of cloud cover and solar illumination. The SBAS-InSAR processing with Sentinel-1 time series can be applied to map seasonal thaw subsidence and to detect geohazards (i.e., landslide and subsidence) over pan-Arctic regions. Processing of huge amount of scenes with large file size is a challenge for continental and pan-Arctic monitoring. Thus, data processing in cloud computing environments is an area in developing.

This thesis shows monitoring result of one-year to two-year period. Long-term monitoring is suggested, e.g., long-term land cover change is an indication of the change in the near-surface permafrost extent, multi-year seasonal thaw subsidence change is an indication of the change in the active layer thickness and the permafrost thermal state, shift of lakes with bedfast-ice and floating-ice regimes is an indication of the permafrost thermal state and climatic conditions.

This study mainly employs the temporal information of SAR time series; less attention is given to polarimetric analyses. Several polarimetric decomposition methods have been developed for dual - polarized or quad - polarized datasets (Ullmann et al. 2017). Polarimetric information is assumed to provide more information about the vegetation. The inclusion of polarimetric information into a multi-temporal/time-series analysis is recommended for future studies.

7 Bibliography

- Allard, M., Lemay, M., Barrette, C., L'Hérault, E., Sarrazin, D., Bell, T., & Doré, G. (2012). Permafrost and climate change in Nunavik and Nunatsiavut: Importance for municipal and transportation infrastructures. In M. Allard, & M. Lemay (Eds.), *Nunavik and Nunatsiavut: From science to policy. An Integrated Regional Impact Study (IRIS) of climate change and modernization* (pp. 171-197). Quebec City, Canada: ArcticNet Inc.
- Allard, M., & Pollard, E.W. (2011). Permafrost and climate change in northern coastal Canada. In (p. 16). 2012-2013 Annual Research Compendium
- Allard, M., Sarrazin, D., & L'Hérault, E. (2016). Borehole and near-surface ground temperatures in northeastern Canada, v. 1.4 (1988-2016). In. Nordicana D8, Centre d'études nordiques. <http://www.cen.ulaval.ca/nordicanad/dpage.aspx?doi=45291SL-34F28A9491014AFD>
- Allard, M., & Seguin, M. (1985). La déglaciation d'une partie du versant hudsonien québécois: bassins des rivières Nastapoca, Sheldrake et à l'Eau Claire. *Géographie physique et Quaternaire*, 39, 13-24
- Allard, M., & Seguin, M.K. (1987a). The Holocene evolution of permafrost near the tree line, on the eastern coast of Hudson Bay (northern Quebec). *Canadian Journal of Earth Sciences*, 24, 2206-2222
- Allard, M., & Seguin, M.K. (1987b). Le pergélisol au Québec nordique: bilan et perspectives. *Géographie physique et Quaternaire*, 41, 141-152
- Anisimov, O.A., Vaughan, D.G., Callaghan, T.V., Furgal, C., Marchant, H., Prowse, T.D., Vilhjálmsson, H., & Walsh, J.E. (2007). Polar regions (arctic and antarctic). In M.L. Parry, O.F. Canziani, J.P. Palutikof, P.J. van der Linden, & C.E. Hanson (Eds.), *Climate Change 2007: Impacts, Adaptation and Vulnerability. Contribution of Working Group II to the Fourth Assessment Report of the Intergovernmental Panel on Climate Change* (pp. 653-685). Cambridge: Cambridge University Press
- Antonova, S., Duguay, C.R., Käab, A., Heim, B., Langer, M., Westermann, S., & Boike, J. (2016). Monitoring Bedfast Ice and Ice Phenology in Lakes of the Lena River Delta Using TerraSAR-X Backscatter and Coherence Time Series. *Remote Sensing*, 8, 903
- Antonova, S., Sudhaus, H., Strozzi, T., Zwieback, S., Käab, A., Heim, B., Langer, M., Bornemann, N., & Boike, J. (2018). Thaw Subsidence of a Yedoma Landscape in Northern Siberia, Measured In Situ and Estimated from TerraSAR-X Interferometry. *Remote Sensing*, 10, 494
- Arp, C.D., Jones, B.M., Lu, Z., & Whitman, M.S. (2012). Shifting balance of thermokarst lake ice regimes across the Arctic Coastal Plain of northern Alaska. *Geophysical Research Letters*, 39
- Arp, C.D., Jones, B.M., Urban, F.E., & Grosse, G. (2011). Hydrogeomorphic processes of thermokarst lakes with grounded - ice and floating - ice regimes on the Arctic coastal plain, Alaska. *Hydrological Processes*, 25, 2422-2438
- Ballantyne, C.K. (2018). *Periglacial Geomorphology*. John Wiley & Sons

- Banks, S., Millard, K., Pasher, J., Richardson, M., Wang, H., & Duffe, J. (2015). Assessing the potential to operationalize shoreline sensitivity mapping: Classifying multiple Wide Fine Quadrature Polarized RADARSAT-2 and Landsat 5 scenes with a single Random Forest model. *Remote Sensing*, 7, 13528-13563
- Banks, S.N., King, D.J., Merzouki, A., & Duffe, J. (2014a). Assessing RADARSAT-2 for mapping shoreline cleanup and assessment technique (SCAT) classes in the Canadian Arctic. *Canadian Journal of Remote Sensing*, 40, 243-267
- Banks, S.N., King, D.J., Merzouki, A., & Duffe, J. (2014b). Characterizing scattering behaviour and assessing potential for classification of arctic shore and near-shore land covers with fine quad-pol RADARSAT-2 data. *Canadian Journal of Remote Sensing*, 40, 291-314
- Beck, I., Ludwig, R., Bernier, M., Lévesque, E., & Boike, J. (2015a). Assessing Permafrost Degradation and Land Cover Changes (1986-2009) using Remote Sensing Data over Umiujaq, Sub-Arctic Québec. *Permafrost and Periglacial Processes*, 26, 129-141
- Beck, I., Ludwig, R., Bernier, M., Strozzi, T., & Boike, J. (2015b). Vertical movements of frost mounds in subarctic permafrost regions analyzed using geodetic survey and satellite interferometry. *Earth Surface Dynamics*, 3, 409-421
- Bense, V., Kooi, H., Ferguson, G., & Read, T. (2012). Permafrost degradation as a control on hydrogeological regime shifts in a warming climate. *Journal of Geophysical Research: Earth Surface*, 117
- Berardino, P., Fornaro, G., Lanari, R., & Sansosti, E. (2002). A new algorithm for surface deformation monitoring based on small baseline differential SAR interferograms. *Geoscience and Remote Sensing, IEEE Transactions on*, 40, 2375-2383
- Brown, J., Ferrians Jr, O., Heginbottom, J., & Melnikov, E. (1997). *Circum-Arctic map of permafrost and ground-ice conditions*. US Geological Survey Reston
- Bruzzo, L., Marconcini, M., Wegmuller, U., & Wiesmann, A. (2004). An advanced system for the automatic classification of multitemporal SAR images. *IEEE Transactions on Geoscience and Remote Sensing*, 42, 1321-1334
- Burn, C. (1998). The active layer: two contrasting definitions. *Permafrost and Periglacial Processes*, 9, 411-416
- Callaghan, T.V., Bergholm, F., Christensen, T.R., Jonasson, C., Kokfelt, U., & Johansson, M. (2010). A new climate era in the sub - Arctic: Accelerating climate changes and multiple impacts. *Geophysical Research Letters*, 37
- Calmels, F., Allard, M., & Delisle, G. (2008). Development and decay of a lithalsa in Northern Québec: a geomorphological history. *Geomorphology*, 97, 287-299
- Chang, L., & Hanssen, R.F. (2015). Detection of permafrost sensitivity of the Qinghai-Tibet railway using satellite radar interferometry. *International Journal of Remote Sensing*, 36, 691-700
- Chen, F., Lin, H., Li, Z., Chen, Q., & Zhou, J. (2012). Interaction between permafrost and infrastructure along the Qinghai-Tibet Railway detected via jointly analysis of C-and L-band small baseline SAR interferometry. *Remote Sensing of Environment*, 123, 532-540
- Chen, F., Lin, H., Zhou, W., Hong, T., & Wang, G. (2013). Surface deformation detected by ALOS PALSAR small baseline SAR interferometry over permafrost environment of Beiluhe section, Tibet Plateau, China. *Remote Sensing of Environment*, 138, 10-18

- ClarivateAnalytics (2018). 2017 Journal Citation Reports. In. <https://clarivate.com/products/journal-citation-reports/>
- Collins, M., Knutti, R., Arblaster, J., Dufresne, J.-L., Fichet, T., Friedlingstein, P., Gao, X., Gutowski, W., Johns, T., & Krinner, G. (2013). Long-term climate change: projections, commitments and irreversibility. In T.F. Stocker, D. Qin, G.-K. Plattner, M. Tignor, S.K. Allen, J. Boschung, A. Nauels, Y. Xia, V. Bex, & P.M. Midgley (Eds.), *Climate Change 2013: The Physical Science Basis. Contribution of Working Group I to the Fifth Assessment Report of the Intergovernmental Panel on Climate Change* (pp. 1029-1136). Cambridge, United Kingdom and New York, NY, USA: Cambridge University Press
- Connon, R.F., Quinton, W.L., Craig, J.R., & Hayashi, M. (2014). Changing hydrologic connectivity due to permafrost thaw in the lower Liard River valley, NWT, Canada. *Hydrological Processes*, 28, 4163-4178
- Cyr, S., & Payette, S. (2010). The origin and structure of wooded permafrost mounds at the arctic treeline in eastern Canada. *Plant Ecology & Diversity*, 3, 35-46
- Daout, S., Doin, M.P., Peltzer, G., Socquet, A., & Lasserre, C. (2017). Large - scale InSAR monitoring of permafrost freeze - thaw cycles on the Tibetan Plateau. *Geophysical Research Letters*, 44, 901-909
- Demers, A.-M., Banks, S.N., Pasher, J., Duffe, J., & Laforest, S. (2015). A comparative analysis of object-based and pixel-based classification of RADARSAT-2 C-band and optical satellite data for mapping shoreline types in the Canadian arctic. *Canadian Journal of Remote Sensing*, 41, 1-19
- Derksen, C., Xu, X., Dunbar, R.S., Colliander, A., Kim, Y., Kimball, J.S., Black, T.A., Euskirchen, E., Langlois, A., & Lorant, M.M. (2017). Retrieving landscape freeze/thaw state from Soil Moisture Active Passive (SMAP) radar and radiometer measurements. *Remote Sensing of Environment*, 194, 48-62
- Duguay, C., & Lafleur, P. (2003). Determining depth and ice thickness of shallow sub-Arctic lakes using space-borne optical and SAR data. *International Journal of Remote Sensing*, 24, 475-489
- Duguay, C.R., Pultz, T.J., Lafleur, P.M., & Drai, D. (2002). RADARSAT backscatter characteristics of ice growing on shallow sub - Arctic lakes, Churchill, Manitoba, Canada. *Hydrological Processes*, 16, 1631-1644
- Duguay, Y., Bernier, M., Lévesque, E., & Domine, F. (2016). Land cover classification in SubArctic regions using fully polarimetric RADARSAT-2 data. *Remote Sensing*, 8, 697
- Elger, K., Opel, T., Topp-Jørgensen, J.E., & Rasch, M. (2012). *INTERACT station catalogue*. Aarhus University, Danish Centre for Environment and Energy (DCE)
- Elmendorf, S.C., Henry, G.H., Hollister, R.D., Björk, R.G., Bjorkman, A.D., Callaghan, T.V., Collier, L.S., Cooper, E.J., Cornelissen, J.H., & Day, T.A. (2012a). Global assessment of experimental climate warming on tundra vegetation: heterogeneity over space and time. *Ecology letters*, 15, 164-175
- Elmendorf, S.C., Henry, G.H., Hollister, R.D., Björk, R.G., Boulanger-Lapointe, N., Cooper, E.J., Cornelissen, J.H., Day, T.A., Dorrepaal, E., & Elumeeva, T.G. (2012b). Plot-scale evidence of tundra vegetation change and links to recent summer warming. *Nature Climate Change*, 2, 453-457

- Engram, M., Anthony, K., Meyer, F., & Grosse, G. (2013). Characterization of L-band synthetic aperture radar (SAR) backscatter from floating and grounded thermokarst lake ice in Arctic Alaska. *The Cryosphere*, 7, 1741-1752
- Ferretti, A., Prati, C., & Rocca, F. (2001). Permanent scatterers in SAR interferometry. *Geoscience and Remote Sensing, IEEE Transactions on*, 39, 8-20
- Fortier, R., & Bolduc, M. (2008). Thaw settlement of degrading permafrost: A geohazard affecting the performance of man-made infrastructures at Umiujaq in Nunavik (Québec). In, J. Locat, D. Perret, D. Turmel, D. Demers and Leroueil, S. 2008. *Proceedings of the 4th Canadian Conference on Geohazards: From Causes to Management. Presse de l'Université Laval, Québec* (pp. 279-286)
- Fortier, R., LeBlanc, A.-M., Allard, M., Buteau, S., & Calmels, F. (2008). Internal structure and conditions of permafrost mounds at Umiujaq in Nunavik, Canada, inferred from field investigation and electrical resistivity tomography. *Canadian Journal of Earth Sciences*, 45, 367-387
- Fortier, R., LeBlanc, A.-M., & Yu, W. (2011). Impacts of permafrost degradation on a road embankment at Umiujaq in Nunavik (Quebec), Canada. *Canadian geotechnical journal*, 48, 720-740
- Frey, K.E., & McClelland, J.W. (2009). Impacts of permafrost degradation on arctic river biogeochemistry. *Hydrological Processes: An International Journal*, 23, 169-182
- Gangodagamage, C., Rowland, J.C., Hubbard, S.S., Brumby, S.P., Liljedahl, A.K., Wainwright, H., Wilson, C.J., Altmann, G.L., Dafflon, B., & Peterson, J. (2014). Extrapolating active layer thickness measurements across Arctic polygonal terrain using LiDAR and NDVI data sets. *Water resources research*, 50, 6339-6357
- Grosse, G., & Jones, B. (2011). Spatial distribution of pingos in northern Asia. *The Cryosphere*, 5, 13
- Grosse, G., Jones, B., & Arp, C. (2013). Thermokarst lakes, drainage, and drained basins
- Günther, F., Overduin, P.P., Yakshina, I.A., Opel, T., Baranskaya, A.V., & Grigoriev, M.N. (2015). Observing Muostakh disappear: permafrost thaw subsidence and erosion of a ground-ice-rich island in response to arctic summer warming and sea ice reduction. *The Cryosphere*, 9, 151-178
- Harris, S.A., French, H.M., Heginbottom, J.A., Johnston, G.H., Ladanyi, B., Sego, D.C., & van Everdingen, R.O. (1988). Glossary of permafrost and related ground-ice terms. *Associate Committee on Geotechnical Research, National Research Council of Canada, Ottawa*, 156
- Hinkel, K., Doolittle, J., Bockheim, J., Nelson, F., Paetzold, R., Kimble, J., & Travis, R. (2001). Detection of subsurface permafrost features with ground - penetrating radar, Barrow, Alaska. *Permafrost and Periglacial Processes*, 12, 179-190
- Hirose, T., Kapfer, M., Bennett, J., Cott, P., Manson, G., & Solomon, S. (2008). Bottomfast Ice Mapping and the Measurement of Ice Thickness on Tundra Lakes Using C - Band Synthetic Aperture Radar Remote Sensing 1. *JAWRA Journal of the American Water Resources Association*, 44, 285-292
- Hooper, A. (2008). A multi-temporal InSAR method incorporating both persistent scatterer and small baseline approaches. *Geophysical Research Letters*, 35

- Humlum, O., & Matsuoka, N. (2004). A handbook on periglacial field methods. *International Permafrost Association, the Working Group on Periglacial Proc. and Environment*, 82
- Im, S., & Kharuk, V. (2015). Dynamics of water mass in the Central Siberia permafrost zone based on gravity survey from the grace satellites. *Izvestiya, Atmospheric and Oceanic Physics*, 51, 806-818
- Jeffries, M., Morris, K., & Liston, G. (1996). A method to determine lake depth and water availability on the North Slope of Alaska with spaceborne imaging radar and numerical ice growth modelling. *Arctic*, 367-374
- Jeffries, M., Morris, K., Weeks, W., & Wakabayashi, H. (1994). Structural and stratigraphic features and ERS 1 synthetic aperture radar backscatter characteristics of ice growing on shallow lakes in NW Alaska, winter 1991-1992. *Journal of Geophysical Research: Oceans*, 99, 22459-22471
- Jolivel, M., & Allard, M. (2013). Thermokarst and export of sediment and organic carbon in the Sheldrake River watershed, Nunavik, Canada. *Journal of Geophysical Research: Earth Surface*, 118, 1729-1745
- Jones, B.M., Grosse, G., Arp, C., Jones, M., Walter Anthony, K., & Romanovsky, V. (2011). Modern thermokarst lake dynamics in the continuous permafrost zone, northern Seward Peninsula, Alaska. *Journal of Geophysical Research: Biogeosciences*, 116
- Jones, B.M., Gusmeroli, A., Arp, C.D., Strozzi, T., Grosse, G., Gaglioti, B.V., & Whitman, M.S. (2013a). Classification of freshwater ice conditions on the Alaskan Arctic Coastal Plain using ground penetrating radar and TerraSAR-X satellite data. *International Journal of Remote Sensing*, 34, 8267-8279
- Jones, B.M., Stoker, J.M., Gibbs, A.E., Grosse, G., Romanovsky, V.E., Douglas, T.A., Kinsman, N.E., & Richmond, B.M. (2013b). Quantifying landscape change in an arctic coastal lowland using repeat airborne LiDAR. *Environmental Research Letters*, 8, 045025
- Jorgenson, M.T., & Grosse, G. (2016). Remote sensing of landscape change in permafrost regions. *Permafrost and Periglacial Processes*, 27, 324-338
- Juszk, I., Eugster, W., Heijmans, M.M., & Schaepman-Strub, G. (2016). Contrasting radiation and soil heat fluxes in Arctic shrub and wet sedge tundra. *Biogeosciences*, 13, 4049-4064
- Kalantaria, P., Berniera, M., McDonalb, K., & Poulina, J. (2015). Using Smos Passive Microwave Data to Develop Smap Freeze/thaw Algorithms Adapted for the Canadian Subarctic. *ISPRS-International Archives of the Photogrammetry, Remote Sensing and Spatial Information Sciences*, 365-368
- Kelley, A.M., Epstein, H.E., & Walker, D.A. (2004). Role of vegetation and climate in permafrost active layer depth in arctic tundra of northern Alaska and Canada. *Journal of Glaciology and Geocryology*, 26, 269-274
- Kim, Y., Kimball, J.S., Zhang, K., & McDonald, K.C. (2012). Satellite detection of increasing Northern Hemisphere non-frozen seasons from 1979 to 2008: Implications for regional vegetation growth. *Remote Sensing of Environment*, 121, 472-487
- Kneisel, C., Hauck, C., Fortier, R., & Moorman, B. (2008). Advances in geophysical methods for permafrost investigations. *Permafrost and Periglacial Processes*, 19, 157-178

- Kokelj, S.V., & Jorgenson, M. (2013). Advances in thermokarst research. *Permafrost and Periglacial Processes*, 24, 108-119
- Kozlenko, N., & Jeffries, M.O. (2000). Bathymetric mapping of shallow water in thaw lakes on the North Slope of Alaska with spaceborne imaging radar. *Arctic*, 306-316
- Lajeunesse, P. (2008). Early Holocene deglaciation of the eastern coast of Hudson Bay. *Geomorphology*, 99, 341-352
- Lajeunesse, P., & Allard, M. (2003). Late quaternary deglaciation, glaciomarine sedimentation and glacioisostatic recovery in the Rivière Nastapoka area, eastern Hudson Bay, Northern Québec. *Géographie physique et Quaternaire*, 57, 65-83
- Lanari, R., Lundgren, P., Manzo, M., & Casu, F. (2004). Satellite radar interferometry time series analysis of surface deformation for Los Angeles, California. *Geophysical Research Letters*, 31
- Lantuit, H., Overduin, P., & Wetterich, S. (2013). Recent progress regarding permafrost coasts. *Permafrost and Periglacial Processes*, 24, 120-130
- Lantuit, H., & Pollard, W. (2008). Fifty years of coastal erosion and retrogressive thaw slump activity on Herschel Island, southern Beaufort Sea, Yukon Territory, Canada. *Geomorphology*, 95, 84-102
- Lavoie, C., Allard, M., & Duhamel, D. (2012). Deglaciation landforms and C-14 chronology of the Lac Guillaume-Delisle area, eastern Hudson Bay: a report on field evidence. *Geomorphology*, 159, 142-155
- Lavoie, C., Allard, M., & Hill, P.R. (2002). Holocene deltaic sedimentation along an emerging coast: Nastapoka River delta, eastern Hudson Bay, Quebec. *Canadian Journal of Earth Sciences*, 39, 505-518
- Lévesque, R., Allard, M., & Séguin, M.K. (1988). *Le pergélisol dans les formations quaternaires de la région des rivières Nastapoka et Sheldrake, Québec nordique*. Centre d'études nordiques, Université Laval
- Li, Z., Zhao, R., Hu, J., Wen, L., Feng, G., Zhang, Z., & Wang, Q. (2015). InSAR analysis of surface deformation over permafrost to estimate active layer thickness based on one-dimensional heat transfer model of soils. *Scientific reports*, 5
- Liljedahl, A.K., Boike, J., Daanen, R.P., Fedorov, A.N., Frost, G.V., Grosse, G., Hinzman, L.D., Iijma, Y., Jorgenson, J.C., & Matveyeva, N. (2016). Pan-Arctic ice-wedge degradation in warming permafrost and its influence on tundra hydrology. *Nature Geoscience*, 9, 312
- Liu, L., Jafarov, E.E., Schaefer, K.M., Jones, B.M., Zebker, H.A., Williams, C.A., Rogan, J., & Zhang, T. (2014a). InSAR detects increase in surface subsidence caused by an Arctic tundra fire. *Geophysical Research Letters*, 41, 3906-3913
- Liu, L., Schaefer, K., Chen, A., Gusmeroli, A., Zebker, H., & Zhang, T. (2015). Remote sensing measurements of thermokarst subsidence using InSAR. *Journal of Geophysical Research: Earth Surface*, 120, 1935-1948
- Liu, L., Schaefer, K., Gusmeroli, A., Grosse, G., Jones, B.M., Zhang, T., Parsekian, A.D., & Zebker, H.A. (2014b). Seasonal thaw settlement at drained thermokarst lake basins, Arctic Alaska. *Atmospheric Chemistry and Physics*, 8, 815

- Liu, L., Schaefer, K., Zhang, T., & Wahr, J. (2012). Estimating 1992–2000 average active layer thickness on the Alaskan North Slope from remotely sensed surface subsidence. *Journal of Geophysical Research: Earth Surface*, 117
- Liu, L., Zhang, T., & Wahr, J. (2010). InSAR measurements of surface deformation over permafrost on the North Slope of Alaska. *Journal of Geophysical Research: Earth Surface*, 115
- Mackay, J. (2000). Thermally induced movements in ice-wedge polygons, western Arctic coast: a long-term study. *Géographie physique et Quaternaire*, 54, 41-68
- Mackay, J.R. (1973). A frost tube for the determination of freezing in the active layer above permafrost. *Canadian geotechnical journal*, 10, 392-396
- Massonnet, D., Briole, P., & Arnaud, A. (1995). Deflation of Mount Etna monitored by spaceborne radar interferometry. *Nature*, 375, 567
- Massonnet, D., Rossi, M., Carmona, C., Adragna, F., Peltzer, G., Feigl, K., & Rabaute, T. (1993). The displacement field of the Landers earthquake mapped by radar interferometry. *Nature*, 364, 138
- May, I. (2011). Using in-field and remote sensing data to monitor permafrost dynamics in Northern Québec. In: Ph. D. thesis, Ludwig-Maximilians-Universität München, Munich
- McClelland, J.W., Déry, S.J., Peterson, B.J., Holmes, R.M., & Wood, E.F. (2006). A pan - arctic evaluation of changes in river discharge during the latter half of the 20th century. *Geophysical Research Letters*, 33
- McClelland, J.W., Holmes, R.M., Peterson, B.J., & Stieglitz, M. (2004). Increasing river discharge in the Eurasian Arctic: Consideration of dams, permafrost thaw, and fires as potential agents of change. *Journal of Geophysical Research: Atmospheres*, 109
- Ménard, É., Allard, M., & Michaud, Y. (1998). Monitoring of ground surface temperatures in various biophysical micro-environments near Umiujaq, eastern Hudson Bay, Canada. In, *Proceedings of the 7th International Conference on Permafrost. Yellowknife, Canada* (pp. 723-729)
- Mohr, J.J., Reeh, N., & Madsen, S.N. (1998). Three-dimensional glacial flow and surface elevation measured with radar interferometry. *Nature*, 391, 273
- Moreira, A., Prats-Iraola, P., Younis, M., Krieger, G., Hajnsek, I., & Papathanassiou, K.P. (2013). A tutorial on synthetic aperture radar. *Geoscience and Remote Sensing Magazine, IEEE*, 1, 6-43
- Morris, K., Jeffries, M., & Weeks, W. (1995). Ice processes and growth history on Arctic and sub-Arctic lakes using ERS-1 SAR data. *Polar Record*, 31, 115-128
- Muskett, R.R., & Romanovsky, V.E. (2011). Alaskan permafrost groundwater storage changes derived from GRACE and ground measurements. *Remote Sensing*, 3, 378-397
- Myers-Smith, I.H., Elmendorf, S.C., Beck, P.S., Wilkming, M., Hallinger, M., Blok, D., Tape, K.D., Rayback, S.A., Macias-Fauria, M., & Forbes, B.C. (2015). Climate sensitivity of shrub growth across the tundra biome. *Nature Climate Change*, 5, 887
- Myers-Smith, I.H., Forbes, B.C., Wilkming, M., Hallinger, M., Lantz, T., Blok, D., Tape, K.D., Macias-Fauria, M., Sass-Klaassen, U., & Lévesque, E. (2011). Shrub expansion in tundra ecosystems: dynamics, impacts and research priorities. *Environmental Research Letters*, 6, 045509

- Nelson, F., Shiklomanov, N., & Mueller, G. (1999). Variability of active-layer thickness at multiple spatial scales, north-central Alaska, USA. *Arctic, Antarctic, and Alpine Research*, *31*, 179-186
- Nelson, F.E., Anisimov, O.A., & Shiklomanov, N.I. (2001). Subsidence risk from thawing permafrost. *Nature*, *410*, 889
- Nguyen, T.N., Burn, C., King, D., & Smith, S. (2009). Estimating the extent of near - surface permafrost using remote sensing, Mackenzie Delta, Northwest Territories. *Permafrost and Periglacial Processes*, *20*, 141-153
- Olthof, I., Fraser, R.H., & Schmitt, C. (2015). Landsat-based mapping of thermokarst lake dynamics on the Tuktoyaktuk Coastal Plain, Northwest Territories, Canada since 1985. *Remote Sensing of Environment*, *168*, 194-204
- Payette, S. (1983). The forest tundra and present tree-lines of the northern Québec-Labrador peninsula. *Nordicana*, *47*, 3-23
- Payette, S., Delwaide, A., Caccianiga, M., & Beauchemin, M. (2004). Accelerated thawing of subarctic peatland permafrost over the last 50 years. *Geophysical Research Letters*, *31*
- Payette, S., & Gagnon, R. (1979). Tree - line dynamics in Ungava peninsula, northern Quebec. *Ecography*, *2*, 239-248
- Pelletier, M. (2015). Geomorphological, ecological and thermal time phase of permafrost degradation, Tasiapik, Nunavik (Québec, Canada). In, *Géographiques*. Québec, Canada: University of Laval
- Pissart, A. (2002). Palsas, lithalsas and remnants of these periglacial mounds. A progress report. *Progress in Physical Geography*, *26*, 605-621
- Provencher-Nolet, L. (2014). Détection de changement à court terme de la toundra arbustive à partir de photographies aériennes, région d'Umiujaq, Nunavik (Québec, Canada). In: Université du Québec
- Riordan, B., Verbyla, D., & McGuire, A.D. (2006). Shrinking ponds in subarctic Alaska based on 1950-2002 remotely sensed images. *Journal of Geophysical Research: Biogeosciences*, *111*
- Romanovsky, V.E., Smith, S.L., & Christiansen, H.H. (2010). Permafrost thermal state in the polar Northern Hemisphere during the international polar year 2007-2009: a synthesis. *Permafrost and Periglacial Processes*, *21*, 106-116
- Rowland, J., Jones, C., Altmann, G., Bryan, R., Crosby, B., Hinzman, L., Kane, D., Lawrence, D., Mancino, A., & Marsh, P. (2010). Arctic landscapes in transition: responses to thawing permafrost. *Eos, Transactions American Geophysical Union*, *91*, 229-230
- Rudy, A.C., Lamoureux, S.F., Treitz, P., Short, N., & Brisco, B. (2018). Seasonal and multi-year surface displacements measured by DInSAR in a High Arctic permafrost environment. *International Journal of Applied Earth Observation and Geoinformation*, *64*, 51-61
- Rykhus, R.P., & Lu, Z. (2008). InSAR detects possible thaw settlement in the Alaskan Arctic Coastal Plain. *Canadian Journal of Remote Sensing*, *34*, 100-112

- Schuur, E., McGuire, A.D., Schädel, C., Grosse, G., Harden, J., Hayes, D., Hugelius, G., Koven, C., Kuhry, P., & Lawrence, D. (2015). Climate change and the permafrost carbon feedback. *Nature*, 520, 171
- Serreze, M.C., & Barry, R.G. (2011). Processes and impacts of Arctic amplification: A research synthesis. *Global and planetary change*, 77, 85-96
- Shiklomanov, N.I., Streletskiy, D.A., & Nelson, F.E. (2012). Northern hemisphere component of the global circumpolar active layer monitoring (CALM) program. In, *Proc. 10th Int. Conf. on Permafrost* (pp. 377-382)
- Short, N., Brisco, B., Couture, N., Pollard, W., Murnaghan, K., & Budkewitsch, P. (2011). A comparison of TerraSAR-X, RADARSAT-2 and ALOS-PALSAR interferometry for monitoring permafrost environments, case study from Herschel Island, Canada. *Remote Sensing of Environment*, 115, 3491-3506
- Short, N., LeBlanc, A.-M., Sladen, W., Oldenborger, G., Mathon-Dufour, V., & Brisco, B. (2014). RADARSAT-2 D-InSAR for ground displacement in permafrost terrain, validation from Iqaluit Airport, Baffin Island, Canada. *Remote Sensing of Environment*, 141, 40-51
- SILA, S.o.c.d.U. (2018). Summary of climate data Umiujaq SILA. In. Développement durable, Environnement et Lutte contre le changements climatiques Québec <http://www.mddelcc.gouv.qc.ca/climat/donnees/OOMultiple.asp>
- Smith, L.C., Sheng, Y., MacDonald, G., & Hinzman, L. (2005). Disappearing arctic lakes. *Science*, 308, 1429-1429
- Smith, S., Romanovsky, V., Lewkowicz, A., Burn, C., Allard, M., Clow, G., Yoshikawa, K., & Throop, J. (2010). Thermal state of permafrost in North America: a contribution to the international polar year. *Permafrost and Periglacial Processes*, 21, 117-135
- Sobiech, J., & Dierking, W. (2013). Observing lake-and river-ice decay with SAR: advantages and limitations of the unsupervised k-means classification approach. *Annals of Glaciology*, 54, 65-72
- soundwavesUSGS. Second Phase of Photo and Video Portal Completed. In. <https://soundwaves.usgs.gov/2016/03/outreach.html>
- St. Jacques, J.M., & Sauchyn, D.J. (2009). Increasing winter baseflow and mean annual streamflow from possible permafrost thawing in the Northwest Territories, Canada. *Geophysical Research Letters*, 36
- Streletskiy, D., Anisimov, O., & Vasiliev, A. (2015a). Permafrost degradation. *Snow and Ice-Related Hazards, Risks and Disasters* (pp. 303-344): Elsevier
- Streletskiy, D.A., Shiklomanov, N.I., Little, J.D., Nelson, F.E., Brown, J., Nyland, K.E., & Klene, A.E. (2017). Thaw subsidence in undisturbed tundra landscapes, Barrow, Alaska, 1962-2015. *Permafrost and Periglacial Processes*, 28, 566-572
- Streletskiy, D.A., Tananaev, N.I., Opel, T., Shiklomanov, N.I., Nyland, K.E., Streletskaya, I.D., & Shiklomanov, A.I. (2015b). Permafrost hydrology in changing climatic conditions: seasonal variability of stable isotope composition in rivers in discontinuous permafrost. *Environmental Research Letters*, 10, 095003
- Surdu, C., Duguay, C., Brown, L., & Fernández Prieto, D. (2014). Response of ice cover on shallow lakes of the North Slope of Alaska to contemporary climate conditions (1950-2011): radar remote-sensing and numerical modeling data analysis. *The Cryosphere*, 8, 167-180

- Surdu, C.M., Duguay, C.R., & Fernández Prieto, D. (2016). Evidence of recent changes in the ice regime of lakes in the Canadian High Arctic from spaceborne satellite observations. *The Cryosphere*, 10, 941-960
- Surdu, C.M., Duguay, C.R., Pour, H.K., & Brown, L.C. (2015). Ice Freeze-up and Break-up Detection of Shallow Lakes in Northern Alaska with Spaceborne SAR. *Remote Sensing*, 7, 6133-6159
- Tanase, M.A., Santoro, M., Wegmüller, U., de la Riva, J., & Pérez-Cabello, F. (2010). Properties of X-, C-and L-band repeat-pass interferometric SAR coherence in Mediterranean pine forests affected by fires. *Remote Sensing of Environment*, 114, 2182-2194
- TheTuktoyaktukPingos. The Tuktoyaktuk Pingos. In. <https://www.atlasobscura.com/places/tuktoyaktuk>
- Ullmann, T., Banks, S.N., Schmitt, A., & Jagdhuber, T. (2017). Scattering characteristics of X-, C-and L-Band polsar data examined for the tundra environment of the Tuktoyaktuk Peninsula, Canada. *Applied Sciences*, 7, 595
- Ullmann, T., Schmitt, A., & Jagdhuber, T. (2016). Two Component Decomposition of Dual Polarimetric HH/VV SAR Data: Case Study for the Tundra Environment of the Mackenzie Delta Region, Canada. *Remote Sensing*, 8, 1027
- Ullmann, T., Schmitt, A., Roth, A., Duffe, J., Dech, S., Hubberten, H.-W., & Baumhauer, R. (2014). Land cover characterization and classification of arctic tundra environments by means of polarized synthetic aperture X-and C-Band Radar (PolSAR) and Landsat 8 multispectral imagery—Richards Island, Canada. *Remote Sensing*, 6, 8565-8593
- Usai, S. (2003). A least squares database approach for SAR interferometric data. *Geoscience and Remote Sensing, IEEE Transactions on*, 41, 753-760
- Vaughan, D.G., Comiso, J.C., Allison, I., Carrasco, J., Kaser, G., Kwok, R., Mote, P., Murray, T., Paul, F., Ren, J., Rignot, E., Solomina, O., Steffen, K., & Zhang, T. (2013). Observations: cryosphere. In T.F. Stocker, D. Qin, G.-K. Plattner, M. Tignor, S.K. Allen, J. Boschung, A. Nauels, Y. Xia, V. Bex, & P.M. Midgley (Eds.), *Climate Change 2013: The Physical Science Basis. Contribution of Working Group I to the Fifth Assessment Report of the Intergovernmental Panel on Climate Change* (pp. 317-382). Cambridge, United Kingdom and New York, NY, USA: Cambridge University Press
- Velicogna, I., Tong, J., Zhang, T., & Kimball, J.S. (2012). Increasing subsurface water storage in discontinuous permafrost areas of the Lena River basin, Eurasia, detected from GRACE. *Geophysical Research Letters*, 39
- Walvoord, M.A., & Striegl, R.G. (2007). Increased groundwater to stream discharge from permafrost thawing in the Yukon River basin: Potential impacts on lateral export of carbon and nitrogen. *Geophysical Research Letters*, 34
- Wang, Z., & Li, S. (1999). Detection of winter frost heaving of the active layer of Arctic permafrost using SAR differential interferograms. In, *Geoscience and Remote Sensing Symposium, 1999. IGARSS'99 Proceedings. IEEE 1999 International* (pp. 1946-1948): IEEE
- Westermann, S., Duguay, C.R., Grosse, G., & Käab, A. (2015a). Remote sensing of permafrost and frozen ground
- Westermann, S., Østby, T., Gislås, K., Schuler, T., & Etzelmüller, B. (2015b). A ground temperature map of the North Atlantic permafrost region based on remote sensing and reanalysis data. *The Cryosphere*, 9, 1303-1319

- Widhalm, B., Bartsch, A., Leibman, M., & Khomutov, A. (2017). Active-layer thickness estimation from X-band SAR backscatter intensity. *The Cryosphere*, *11*, 483
- Wolfe, S.A., Short, N.H., Morse, P.D., Schwarz, S.H., & Stevens, C.W. (2014). Evaluation of RADARSAT-2 DInSAR seasonal surface displacement in discontinuous permafrost terrain, Yellowknife, Northwest Territories, Canada. *Canadian Journal of Remote Sensing*, *40*, 406-422
- Wu, Q., Zhang, T., & Liu, Y. (2012). Thermal state of the active layer and permafrost along the Qinghai-Xizang (Tibet) Railway from 2006 to 2010. *The Cryosphere*, *6*, 607-612
- Xu, X., Dunbar, R.S., Derksen, C., Colliander, A., Kimball, J., & Kim, Y. (2016). Landscape freeze/thaw products from Soil Moisture Active/Passive (SMAP) radar and radiometer data. In, *Geoscience and Remote Sensing Symposium (IGARSS), 2016 IEEE International* (pp. 132-135): IEEE
- Yoshikawa, K., & Hinzman, L.D. (2003). Shrinking thermokarst ponds and groundwater dynamics in discontinuous permafrost near Council, Alaska. *Permafrost and Periglacial Processes*, *14*, 151-160
- Zhang, T., Barry, R., Knowles, K., Heginbottom, J., & Brown, J. (2008). Statistics and characteristics of permafrost and ground-ice distribution in the Northern Hemisphere. *Polar Geography*, *31*, 47-68
- Zhao, R., Li, Z.-w., Feng, G.-c., Wang, Q.-j., & Hu, J. (2016). Monitoring surface deformation over permafrost with an improved SBAS-InSAR algorithm: With emphasis on climatic factors modeling. *Remote Sensing of Environment*, *184*, 276-287
- Zhou, X., Chang, N.-B., & Li, S. (2009). Applications of SAR interferometry in earth and environmental science research. *Sensors*, *9*, 1876-1912
- Zimov, S.A., Schuur, E.A., & Chapin, F.S. (2006). Permafrost and the global carbon budget. *Science*, *312*, 1612-1613

8 Curriculum Vitae

Personal Information

Name: Lingxiao Wang
Date of birth: 29.09.1988
Place of birth: Chuzhou, Anhui, China
Nationality: China
Email: l.wang@iggf.geo.uni-muenchen.de

Education

2012 - 2018 Ph.D studies at the Department of Geography, LMU Munich
2009 - 2012 Master of Science in Cartography and Geographic Information Science
Nanjing University, Nanjing, China
Master thesis: Satellite Snow Extraction in Rugged Mountain Terrain in Manasi River Basin, Tianshan Mountains, China
2005 - 2009 Bachelor of Science in Geographic Information Science,
and Bachelor of Engineering in Computer Science
South China Normal University, Guangzhou, China
2002 - 2005 No. 1 Senior High School of Chuzhou, Anhui, China
1999 - 2002 No. 3 Middle School of Chuzhou, Anhui, China

Scientific career

2017 - 2018 Student researcher at the Department of Geography, LMU in Project MULTIscale SENTINEL land surface information retrieval Platform (European Commission Program)
2015 - 2018 Student researcher at the Department of Geography, LMU in Project Freeze/Thaw cycle monitoring using multi-scale SMAP products and hydrothermal modeling over the Canadian tundra (Canadian Space Agency Program)
2011 - 2012 Student researcher at the Department of Geographic Information Science, Nanjing University in Project of Large-scale land use /cover changes and its impact on regional climate in East Asia (Chinese National "973" Program)

Publications and communications

Publications

Wang, L., Marzahn, P., Bernier, M. and Ludwig, R.. High temporal resolution deformation monitoring over discontinuous permafrost terrain using Sentinel-1 time series. *Remote Sensing of environment*, under review.

Wang, L., Jolivel, M., Marzahn, P., Bernier, M. and Ludwig, R., 2018. Thermokarst pond dynamics in subarctic

environment monitoring with radar remote sensing. *Permafrost and Periglacial Processes*, 1-15.

Wang, L., Marzahn, P., Bernier, M. and Ludwig, R., 2018. Mapping permafrost landscape features using object-based image classification of multi-temporal SAR images. *ISPRS Journal of Photogrammetry and Remote Sensing*, 141, pp.10-29.

Wang, L., Marzahn, P., Bernier, M., Jacome, A., Poulin, J. and Ludwig, R., 2017. Comparison of TerraSAR-X and ALOS PALSAR differential interferometry with multisource DEMs for monitoring ground displacement in a discontinuous permafrost region. *IEEE Journal of Selected Topics in Applied Earth Observations and Remote Sensing*, 10(9), pp.4074-4093.

Li, H., Xiao, P., Feng, X., Yang, Y., **Wang, L.**, Zhang, W., Wang, X., Feng, W. and Chang, X., 2017. Using land long-term data records to map land cover changes in China over 1981–2010. *IEEE Journal of Selected Topics in Applied Earth Observations and Remote Sensing*, 10(4), pp.1372-1389.

Wang, L., Xiao, P., Feng, X., Li, H., Zhang, W. and Lin, J., 2014. Effective compositing method to produce cloud-free AVHRR image. *IEEE Geoscience and Remote Sensing Letters*, 11(1), pp.328-332.

Communications

Wang, L., Ludwig, R., Marzahn, P., Chen, Y., Bernier, M., Poulin, J. and Touati, C., 2018. Monitoring freeze/thaw cycles using Sentinel-1 time-series. Geophysical Research Abstracts, Vol. 20, EGU2018-10985-1, EGU General Assembly 2018, Vienna, Austria, 04. 2018.

Wang, L., Bernier, M. and Ludwig, R., 2017. Climate change, permafrost decline and its hydrological impact in the Sheldrake catchment (Québec, Canada). 3rd WaSiM user conference, Munich, Germany, 10. 2017.

Wang, L., Marzahn, P., Bernier, M. and Ludwig, R., 2016. Characterizing permafrost landscape features using object-based classification of Terrasar-X imagery. ArcticNet's 12th Annual Scientific Meeting (ASM2016), Winnipeg, Canada, 12. 2016.

Wang, L., Bernier, M. and Ludwig, R., 2016. Climate change, permafrost decline and its hydrological impact in Northern Québec, Canada. 11th International Conference on Permafrost (ICOP 2016), Potsdam, Germany, 06. 2016.

Wang, L., Marzahn, P., Bernier, M. and Ludwig, R., 2016. Differential SAR interferometry monitoring of ground displacement in the discontinuous permafrost region. 11th International Conference on Permafrost (ICOP 2016), Potsdam, Germany, 06. 2016.

Wang, L., Ludwig, R. and Bernier, M., 2013. Using remote sensing for the monitoring and modeling of permafrost decline in northern Québec. ArcticNet's 9th Annual Scientific Meeting (ASM2013), Halifax, Canada, 12. 2013.